

**Developments in the  
Transmission-Line Modelling Method  
for  
Electromagnetic Compatibility Studies**

by  
Jonathan L. Herring, M.Eng.

Thesis submitted to the University of Nottingham  
for the degree of Doctor of Philosophy, May 1993.

# Contents

Abstract	v
Acknowledgements	vi
List of symbols	vii
<b>1 Introduction</b>	
1.1 Electromagnetic compatibility	1
1.2 Numerical modelling	3
1.3 The role of modelling	5
1.4 Overview	6
<b>2 Transmission-Line Modelling Method</b>	
2.1 Basic method	8
2.2 Twelve-port node	9
2.3 Stub-loaded node	13
2.3.1 Stub parameters	14
2.3.2 Scattering properties	16
2.4 Hybrid node	19
2.4.1 Link-line and stub parameters	20
2.4.2 Scattering properties	22
2.4.3 Connect procedure	23
2.5 Boundary conditions	23
2.5.1 Short-circuit node	23
2.5.2 External boundaries	24
2.5.3 Internal boundaries	26
2.6 Outputs	26
2.6.1 Field at a node	26
2.6.2 Field on a link-line	27
2.6.3 Comparison between node and link-line outputs	27
2.7 Excitation	28
2.7.1 Impulse excitation of fields at a node	28
2.7.2 Impulse excitation of fields on a link-line	29
2.7.3 Voltage and current sources	29

<b>3</b>	<b>Signal Analysis</b>	
3.1	Frequency domain transformation	31
3.2	Windowing	34
3.3	Convolution	39
3.4	Ideal filters	40
3.5	Moving average filters	42
<b>4</b>	<b>Features of the TLM Method</b>	
4.1	Continuous excitation	44
4.2	Steady-state solution	47
4.2.1	Solution at d.c.	47
4.2.2	Solution above d.c.	48
4.3	Field at nodes and on link-lines	50
4.4	Energy considerations	52
4.5	Modelling with stubs	53
4.5.1	Dispersion	54
4.5.2	Excitation	55
4.5.3	Outputs	57
4.6	Plane wave propagation	58
4.6.1	Wave travelling parallel to an axis	58
4.6.2	Wave travelling at an arbitrary angle	60
<b>5</b>	<b>Multigrid Method</b>	
5.1	Introduction	62
5.2	Diakoptics	63
5.3	Basic concepts	65
5.3.1	Fine/coarse mesh interface	65
5.3.2	Characteristic impedance in 2-dimensions	66
5.3.3	Charge and energy considerations	66
5.4	Initial attempts	68
5.5	Interface conditions	69
5.6	Conversion methods	72
5.6.1	Slow conversion	72
5.6.2	Running sum conversions	74

5.6.3	Fast conversion	76
5.6.4	Fast conversions with energy conservation	76
5.6.5	Other methods	78
5.7	Conversion enhancements	78
5.7.1	Calculation order	78
5.7.2	Reducing the coarse mesh timestep	81
5.8	Choice of conversion method	81
5.8.1	Steady-state solution	82
5.8.2	Transient solution	84
5.8.3	Comparison	85
5.9	Three-dimensional systems	87
5.10	Energy considerations	89
5.11	Fine features	93
5.12	Open boundaries	96
5.13	Discussion	98
<b>6</b>	<b>Implementation Issues</b>	
6.1	Introduction	101
6.2	Run-time and storage efficiency	102
6.3	Calculation order	104
6.4	Virtual memory	104
6.5	Problem definition	109
6.5.1	Coordinates	109
6.5.2	Input file	110
6.5.3	Multigrid problem definition	111
6.5.4	Graded mesh problem definition	113
6.6	Output data	114
<b>7</b>	<b>Bounded systems</b>	
7.1	Simple cavity	116
7.2	Effect of a conducting bench	120
7.3	Sensitivity to small changes in position	125
7.4	Determination of Q factor	127
7.4.1	Method	127



7.4.2	Validation	132
7.5	Room damping	135
7.5.1	Optimum material properties	135
7.5.2	Actual material properties	137
7.5.3	Q factor of damped room	139
7.5.4	Optimum RAM arrangement	140
7.6	Field-to-wire coupling	142
7.7	TEM cell	147
<b>8</b>	<b>Unbounded systems</b>	
8.1	Wire antennas	152
8.2	Slot antennas	158
8.3	Spherical dipole	161
8.4	Radiation resistance	166
8.5	Proximity effects	169
8.6	Simulated device under test	174
8.7	Electromagnetic properties of a vehicle body	177
8.8	Current induced by a simplified table top device	180
<b>9</b>	<b>Discussion and Conclusions</b>	
9.1	Numerical modelling method	185
9.2	Development of the TLM method	187
9.3	Application of the TLM method	190
9.4	Future work	192
9.5	Overall conclusions	193
	<b>References</b>	194
	<b>Publications</b>	202
	<b>Appendices</b>	
A.1	Conservation of flux linkage	204
A.2	Optimised paging	207
A.3	Graded mesh parameters	208
A.4	Computer resources	210
A.5	List of programs	212

# Abstract

The transmission-line modelling (TLM) method is applied to 3-dimensional problems in electromagnetic compatibility (EMC). The method is found to be a versatile tool which is ideally suited to the modelling of many EMC systems.

A new way of deriving the scattering properties of the TLM node is presented and the derivation of mesh parameters, the application of boundary conditions and methods of applying excitation and of taking outputs are described. Issues regarding the efficient implementation of the TLM algorithm and a way of running very large simulations are reported. A multigrid method is introduced which allows meshes of different resolutions to be connected together to form a complete system. The method is used to apply fine resolution only in areas where it is required and to move numerical boundaries away from the region of interest. Comparisons are made with the more traditional graded mesh technique, using the hybrid node.

Results are presented for a number of different systems with particular emphasis on the environment in which radiated emission tests are undertaken, although more general systems are also considered. The consequences of making measurements in an unlined screened room are discussed and ways of damping resonances are investigated. Wire, slot and spherical dipole antennas are modelled. Field-to-wire coupling, the TEM cell, a simplified device under test, the shielding properties of a vehicle body and the current induced by a simplified table-top device are also considered. Techniques are developed to obtain the Q factor of a screened room loaded with radiation absorbing material (RAM) and to obtain the radiation resistance of an antenna in free-space and also in close proximity to conducting surfaces.

# Acknowledgments

Firstly, I would like to thank my supervisor, Prof. C. Christopoulos, for invoking the project, for his help and support during the course of the work and for answering my many questions. I would also like to thank the many colleagues who have given helpful advice during the project, in particular, A. P. Duffy for numerous discussions on experimental aspects and TLM, R. A. Scaramuzza for discussions on the hybrid node and Dr P. Naylor.

Much of the work presented here has been performed as part of a collaborative programme between the National Physical Laboratory (NPL), the University of York and the University of Nottingham, aimed at producing a draft emission calibration procedure for screened rooms. I would therefore like to thank the Defence Research Agency (DRA) for providing the funding. I also wish to acknowledge the input provided by the consortium members: Dr R. J. Cook, M. J. Alexander and Dr P. S. Bansal at NPL and Dr A. C. Marvin, G. Simpson and S. M. Mann at York.

# List of symbols

The following symbols are used throughout this thesis:

$c$	speed of light	$R$	magnetic loss stub impedance
$f$	frequency	$R_m$	resistive part of surface impedance
$j$	$\sqrt{-1}$	$R_r$	radiation resistance
$k$	timestep (iteration) number	$S$	scattering matrix
$l$	multigrid spatial reduction ratio	$S$	Poynting vector
$n$	total number of pulses (multigrid)	$T$	1 / relative $\Delta t$ (multigrid)
$q$	placed charge	$V$	voltage
$s$	standard deviation in terms of $\Delta t$	$W$	stored energy
$s$	Laplace transform variable	$Y$	admittance
$t$	time	$Y_0$	characteristic admittance
$t$	multigrid temporal reduction ratio	$Z$	impedance
$w$	total energy density	$Z_0$	characteristic impedance
$w_e$	electric energy density	$Z_b$	impedance of medium
$w_m$	magnetic energy density	$Z_l$	impedance of link-line
$z$	Z transform variable	$\mathcal{E}$	energy carried by pulses
$B$	magnetic flux density	$\alpha$	decay rate
$C$	capacitance	$\alpha$	multigrid energy ratio
$C$	connection matrix	$\delta$	decrement (damped oscillations)
$C$	number of conversions (multigrid)	$\delta_e$	electric loss angle
$D$	electric displacement	$\delta_s$	skin depth
$E$	electric field	$\epsilon$	absolute permittivity
$G$	conductance	$\epsilon'$	real part of permittivity
$G$	electric loss stub admittance	$\epsilon''$	imaginary part of permittivity
$H$	magnetic field	$\epsilon_0$	permittivity of free space
$I$	current	$\epsilon_r$	relative permittivity
$I$	identity matrix	$\epsilon_{r0}$	background relative permittivity
$L$	inductance	$\eta$	rate of energy dissipation
$L$	1 / relative $\Delta l$ (multigrid)	$\lambda$	flux linkage
$N$	number of timesteps (iterations)	$\lambda$	wavelength
$P$	power	$\mu$	absolute permeability
$Q$	charge carried by pulses	$\mu_0$	permeability of free space
$Q$	quality factor	$\mu_r$	relative permeability
$R$	resistance	$\mu_{r0}$	background relative permeability

$\rho_l$	link-line reflection coefficient	$\Delta f$	frequency step
$\rho_w$	wave reflection coefficient	$\Delta l$	node spacing
$\sigma$	conductivity	$\Delta t$	timestep
$\sigma$	standard deviation	$\Delta x$	node spacing in $x$ -direction
$\sigma_e$	electric conductivity	$\Delta y$	node spacing in $y$ -direction
$\sigma_m$	magnetic conductivity	$\Delta z$	node spacing in $z$ -direction
$\omega$	angular frequency	$\Lambda$	logarithmic decrement

Additional symbols are used to clarify such quantities as stub parameters, voltages and currents. These symbols are generally defined where they are used but they are listed here for completeness.

### Prefixed

A subscript prefix is used to denote the timestep (iteration) number.

### Suffixes

The following superscript suffixes are used:

- $i$  pulse incident upon a node
- $r$  pulse scattered from a node
- $s$  stub parameter (as distinct from a link-line parameter)

Subscript suffixes are often used to denote a direction. In the case of a multiple character suffix, the last character gives the polarisation and, for link-lines, the first character gives the direction parallel to the link-line. The following suffixes are also used:

- $c$  coarse mesh quantity (multigrid)
- $e$  electric field quantity / electric loss stub
- $f$  fine mesh quantity (multigrid)
- $m$  magnetic field quantity / magnetic loss stub
- $o$  open-circuit stub
- $s$  short-circuit stub

### Accents

The  $\hat{\phantom{x}}$  symbol is used to denote a normalised quantity.

# Chapter 1

## Introduction

### 1.1 Electromagnetic compatibility

The subject of electromagnetic compatibility (EMC) is concerned with the ability of systems to function correctly in their electromagnetic (EM) environment without generating interference which might cause other systems to fail. It is concerned with a wide variety of systems ranging from the human body to large electrical power systems, such as the national grid, which are subject to interference from sources as diverse as radio and television transmissions, lightning and electrostatic discharge. Subject areas within EMC include biological effects, emission tests, susceptibility tests, coupling to and from external fields and equipment design. The work reported here is mainly concerned with the radiated emission and susceptibility of moderately sized electrical and electronic equipment.

Originally, EMC was an activity largely associated with military projects, with commercial and domestic EMC mainly confined to Germany and the United States [1]. Limits were initially set for radio interference but as more sensitive equipment was developed, susceptibility limits were also established [2,3]. Later, the study of EMC in small systems and between systems became important so that the subject encompassed all types of electrical and electronic equipment during the design, development, production, installation and operational phases. With the growth of large scale consumer and commercial electronics, the need to design EMC into products has intensified so that it meets regulatory requirements, such as the European Community EMC Directive [4]. The potential biological health effects from power lines, common household appliances and radio frequency fields are also a matter of increasing interest [5].

EMC problems can be decomposed into a source of electromagnetic interference (EMI), a piece of equipment subjected to EMI and a coupling channel by which EMI couples into the equipment. Equipment will generally be surrounded by some form of metallic enclosure, or *shield*, which may contain holes through which EM radiation can penetrate and couple into the wires and circuits

within. EM radiation can also couple into equipment through other entry points, such as power cables. The susceptibility to EMI is determined by the strength of signals coupled into the equipment and the effect they have on its operation. Emission from the equipment is determined by the radiation from wires and circuits inside the shield and its propagation through the shield to the external environment.

The increasing presence of electronic equipment in many aspects of life in the modern world has made EMC a necessity. For example, modern computers have clock frequencies which can exceed 100 MHz. The most common enclosures are sheet metal which only allow small apertures, in order to retain the required shielding level, but this can result in thermal and acoustic problems [6]. In addition, there is the very dense packaging of a computer system which can cause electrically active components to be in close proximity to apertures in the shield. As another example, consider the increasing use of electronics in cars. Traditionally, most control and all safety critical functions were implemented through mechanical linkages and any electrical systems only had an auxiliary role. Electronics is now being applied to safety critical systems such as anti-lock braking, steering, suspension and engine management systems and it is obviously imperative that such systems are unaffected by external influences and indeed are also unaffected by internal influences, such as mobile telephones.

A significant proportion of EMC conformance testing is carried out in unlined screened rooms [7,8]. Emission measurements are often made with the receiving antenna placed 1 m from the equipment under test (EUT) with the antenna very close to the room walls, in small rooms. Such tests are unreliable and the results obtained quite often vary by at least 20 dB from one screened room to another. This is partly because the room behaves as a resonant cavity at high frequencies and a short-circuited transmission-line at low frequencies. Even in semi-anechoic or fully anechoic rooms, the measurement process can itself introduce changes in the environment which may be critical to the interpretation of results. This unsatisfactory state of affairs has led to the establishment of a programme of work, sponsored by the Defence Research Agency (DRA), to investigate techniques of reducing the measurement uncertainties of screened room radiated emission

measurements to acceptable levels. Many of the results presented here are concerned with identifying and quantifying factors affecting such electromagnetic measurements.

## 1.2 Numerical modelling

Numerical modelling is concerned with the representation of physical systems by specific quantities which are obtained by numerical methods. For electromagnetic systems, it is generally required to obtain the electric and magnetic field within a volume of space, subject to appropriate boundary conditions. The increase of computer power over the last 20 years has made the tools for numerical modelling widely accessible but although computation is well understood, modelling is still in its infancy [9]. This is because the view has prevailed that phenomena are governed by equations; once the relevant equations are known, it is a simple matter of computation to find the solution. It is now becoming more accepted that the equations are themselves models of the real system and they may not be the most appropriate way of expressing a problem which then has to be solved numerically because the analytical solution is intractable. The use of computer graphics allows electromagnetic field behaviour to be observed directly and the speed of computation makes it possible to use numerical methods as experimental tools both for visualising fields, in a way which cannot be done from measurements, and to undertake sensitivity studies which would otherwise be unacceptably expensive.

There are many different methods which can be used to solve 3-dimensional electromagnetic problems. A convenient although not exhaustive classification<sup>1</sup> is to divide them into integral and differential methods [10]. Integral equation methods, for example the method of moments (MoM), start with the selection of an appropriate Green's function<sup>2</sup> which is manipulated analytically so that it incorporates the boundary conditions and then a solution is sought. Differential equation methods, for example finite difference techniques, exploit Maxwell's equations in differential form and require a minimum of analytical manipulation.

---

<sup>1</sup> Examples of methods which do not fall into this classification are geometric theory of diffraction (GTD) and geometric optics (GO) which use optical techniques to obtain a solution.

<sup>2</sup> A Green's function gives the field due to a point source.



Some of the advantages and disadvantages of the two approaches are given below.

	integral	differential
inhomogeneous materials	difficult	easy
non-linearities time variations	difficult	easy <sup>3</sup>
open boundaries	easy	difficult
number of nodes	required only on certain surfaces	whole workspace has to be filled
maths.	complex (e.g. invert large matrices)	simple

An alternative classification is to consider time and frequency domain methods. Time domain methods typically obtain the impulse response (which contains information at all frequencies) and frequency domain methods obtain the transfer function at a specific frequency. A comparison of the two methods is given below.

	time domain	frequency domain
output at single frequency	bad	good
output at many frequencies	good	bad
frequency dependent parameters	bad	good
non-linearities time-variations	good	bad

The method adopted for this work is the transmission-line modelling (TLM) method which can be classed as a differential time domain method although a frequency domain formulation has recently been proposed [11]. TLM has a number of features which make it ideally suited to EMC problems.

- The method is expressed in terms of circuit concepts which are familiar to the engineer.

<sup>3</sup> Easy for time domain differential methods only.

- In the absence of any active components stability problems do not arise.
- Increased resolution can be applied only in areas where it is required.
- A single calculation will give information over a wide range of frequencies.
- Both the internal and external environments can be modelled simultaneously.
- Complex shapes can be included.
- Inhomogeneous materials can be described.
- Source regions with non-linearities can be represented.

There are several features which make it less suitable, although these are areas of current research.

- There are problems in representing features which are smaller than a node e.g. wire-like structures.
- Completely general open boundaries, or *radiation boundaries*, have yet to be implemented

### 1.3 The role of modelling

If modelling is to gain acceptance along with the existing analytical and measurement techniques then it must offer something which the other methods do not. A high degree of certainty can be placed in results predicted by analytical methods but only very simple systems can be dealt with in this way. Gross simplifications are necessary for more complex systems and the effect that these have on the results is often unknown. In order to perform measurements, the equipment to be tested must first be built and it may be difficult to make necessary alterations without significant effort. In addition, uncertainties are introduced by the measuring process itself. Numerical modelling offers the potential for obtaining accurate results for complex systems without the problems of the other two methods. Currently, models can only be used for relatively simple systems, although the complexity of these nearly always exceeds that which can be handled analytically. It is therefore appropriate to invest in the development of modelling

methods so that their full potential can be exploited in the future.

It is perhaps more appropriate to consider modelling as complementary rather than competing with analytical and experimental methods. It is now nearing the stage where it can be used as a cost effective tool in improving understanding and accuracy of testing and it can reduce test time by aiding in the selection of worst case conditions and providing guidance on the impact of design changes [12]. It can also be used, for example, to give the current distribution in an inaccessible region [13] and it is ideally suited to testing for sensitivity to parameter variations and in finding optimum solutions. In addition, discrepancies between modelled and experimental results can be investigated further so that it is less likely that anything is missed.

## 1.4 Overview

The purpose of this section is to describe the structure of the work presented in the following chapters. The work can be divided into two areas: development of the method and application of the method. Results are presented throughout to illustrate specific points but the major results for EMC systems have been placed together in chapters 7 and 8. An attempt has been made to present information in an order which prevents forward references but this has not been possible in all cases.

**Chapter 2** reviews the theory of 3-dimensional TLM models and presents a new way of deriving the scattering properties of the node. The derivation of mesh parameters, the application of boundary conditions and the way in which excitation is applied and outputs are taken are also presented.

**Chapter 3** is concerned with the analysis of the time domain data output from a TLM calculation. Fourier transform techniques, windowing, convolution and filtering are described.

**Chapter 4** describes some features of the TLM method with particular emphasis on the most appropriate excitation and outputs.

**Chapter 5** describes a new development in TLM, the multigrid technique,

which allows a fine mesh region to be connected to a coarse mesh without the disadvantages of using a graded mesh. The method is developed in 2-dimensions and is then extended to 3-dimensions and some applications are presented.

**Chapter 6** is concerned with ways in which the TLM algorithm can be implemented efficiently and a new way of running large problems on virtual memory systems is presented. Issues regarding the way in which problems are defined and the way outputs are taken are also described.

**Chapters 7 and 8** are the main results sections, which have been divided into bounded and unbounded systems purely for convenience. Chapter 7 is mainly concerned with screened room simulations and a method for obtaining the Q factor of a cavity is presented. Chapter 8 is mainly concerned with antennas and a method for obtaining the radiation resistance is described.

# Chapter 2

## Transmission-Line Modelling Method

### 2.1 Basic method

The modelling of electromagnetic fields with the TLM technique can be regarded as the application of a discrete version of Huygen's continuous wave model [14,15]. TLM is a discrete model which can be solved exactly — approximations are only introduced at the discretisation stage. This is to be contrasted with the traditional approach in which an idealised continuous model is first obtained and then this model is solved approximately [16].

In TLM, space is modelled by a network of transmission-lines. The point at which the transmission-lines, or *link-lines*, intersect is referred to as a node. The most commonly used node for 3-dimensional work, and that used exclusively in this thesis, is the symmetrical condensed node (SCN). The SCN is a development of earlier expanded [17] and asymmetrical nodes [18].

The structure of the node and the characteristic impedances of the link-lines are chosen so that the voltage and current give information on the electric and magnetic fields in each part of space. At each timestep,  $k$ , voltage pulses,  $[{}_kV']$ , are incident upon the node from each of the link-lines. These pulses are then scattered to produce a set of scattered voltages,  $[{}_kV']$ , which become incident on adjacent nodes at the next timestep. The processes of *scatter* and *connect* may be written as

$$[{}_kV'] = [S][{}_kV']$$
$$\text{and } [{}_{k+1}V'] = [C][{}_kV']$$

where  $[S]$  is the scattering matrix and  $[C]$  is the connection matrix, and they are repeated for as many timesteps as required. Voltage pulses are initially introduced into the system in a manner consistent with the desired excitation and outputs can be taken where needed. An impulse excitation is generally used so that information at all frequencies is obtained at the outputs.

The TLM algorithm is explicit, computationally simple and is unconditionally stable since it is a passive network which is solved exactly. A further useful feature

is that the transmission-lines can be considered as distributed models of capacitors, inductors and resistors. The user therefore has a good grasp of the properties and behaviour of the model, the nature and significance of errors and the manner in which material properties may be introduced.

## 2.2 Twelve-port node

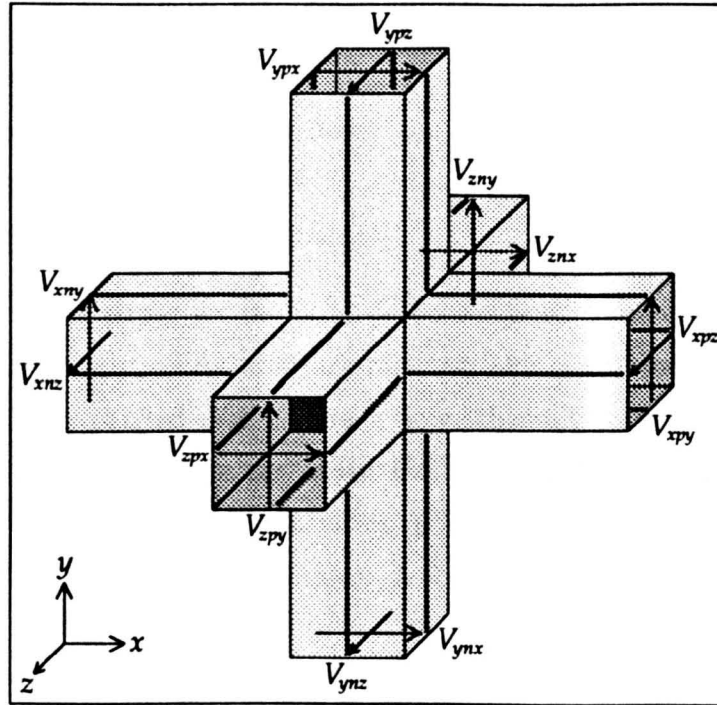


Fig. 2.1 – 12-port symmetrical condensed node

In its basic form, termed the 12-port node, the node is the intersection of twelve transmission-lines, each of total length  $\Delta l$  and characteristic impedance  $Z_0$ , as shown in fig. 2.1. The two polarisations in any direction of propagation are carried on two pairs of transmission-lines which do not couple with each other. The scattering matrix was originally obtained by Johns [19] from Maxwell's equations using the concepts of charge and energy conservation. This method is unwieldy as it depends on the solution of non-linear simultaneous equations and it is not easy to appreciate the underlying conditions which have been imposed. Attempts have been made to obtain an equivalent circuit [20] but this is complex and difficult to solve. An alternative method has been suggested by Włodarczyk [21] in which ports are placed diagonally on the six arms of the node and these ports carry the sum and difference of the signals on the original ports.

In this section, the scattering matrix of the SCN will be derived from first principles and, although based on a knowledge of the scattering matrix originally obtained by Johns, the conditions imposed are reasonable and give insight into the underlying properties of the node. To overcome the problem of obtaining an equivalent circuit, the centre of the node is treated as an undefined region in which the link-lines from adjacent nodes converge. The four principles which will be exploited are

- conservation of charge
- conservation of magnetic flux
- continuity of electric field
- continuity of magnetic field

In his original paper on the SCN, Johns assigned numbers to each of the twelve ports in an apparently arbitrary manner (although these may have been derived from the expanded node). Here, a new scheme is introduced where each port is assigned a three-character name: the first character gives the direction parallel to the link-line, the second is "n" or "p" indicating the port on the negative or positive side of the node and the third gives the polarisation. For example,  $V_{ynx}$  (port 1 in the original scheme) refers to the voltage pulse on the link-line parallel to the  $y$ -axis, on the negative side of the node, polarised in the  $x$ -direction.

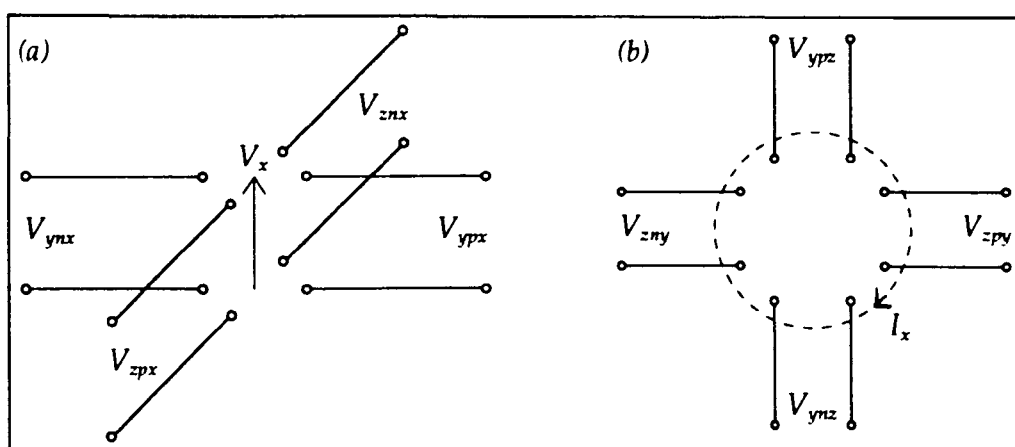


Fig. 2.2 – 12-port node (a) electric field (b) magnetic field

#### i) conservation of charge

Consider the link-lines contributing to the  $x$ -component of the electric field, as shown in fig. 2.2a. Equating the total incident charge with the total scattered charge

gives

$$\frac{1}{2}C(V_{ynx}^i + V_{ypr}^i + V_{znx}^i + V_{zpr}^i) = \frac{1}{2}C(V_{ynx}^r + V_{ypr}^r + V_{znx}^r + V_{zpr}^r)$$

where  $\frac{1}{2}C$  is the capacitance associated with each of the four half link-lines. Similar equations may be obtained for the other field components giving

$$V_{ynx}^i + V_{ypr}^i + V_{znx}^i + V_{zpr}^i = V_{ynx}^r + V_{ypr}^r + V_{znx}^r + V_{zpr}^r \quad (2.1)$$

$$V_{zny}^i + V_{zpy}^i + V_{xny}^i + V_{xpy}^i = V_{zny}^r + V_{zpy}^r + V_{xny}^r + V_{xpy}^r \quad (2.2)$$

$$V_{xnz}^i + V_{xpr}^i + V_{ynz}^i + V_{ypr}^i = V_{xnz}^r + V_{xpr}^r + V_{ynz}^r + V_{ypr}^r \quad (2.3)$$

## ii) conservation of magnetic flux

Consider the link-lines contributing to the x-component of the magnetic field, as shown in fig. 2.2b. Equating the total magnetic flux linked with the incident pulses to the total magnetic flux linked with the scattered pulses [22]<sup>1</sup> gives

$$\frac{1}{2}L(I_{ynz}^i + I_{zpy}^i - I_{ypr}^i - I_{znx}^i) = \frac{1}{2}L(I_{ynz}^r + I_{zpy}^r - I_{ypr}^r - I_{znx}^r)$$

where  $\frac{1}{2}L$  is the inductance associated with each of the four half link-lines and the current pulses are related to the voltage pulses by  $I^i = Y_0 V^i$  and  $I^r = -Y_0 V^r$  ( $Y_0 = 1/Z_0$ ). Similar equations may be obtained for the other field components giving

$$V_{ynz}^i + V_{zpy}^i - V_{ypr}^i - V_{znx}^i = -(V_{ynz}^r + V_{zpy}^r - V_{ypr}^r - V_{znx}^r) \quad (2.4)$$

$$V_{znx}^i + V_{xpr}^i - V_{zpy}^i - V_{xny}^i = -(V_{znx}^r + V_{xpr}^r - V_{zpy}^r - V_{xny}^r) \quad (2.5)$$

$$V_{xny}^i + V_{ypr}^i - V_{xpy}^i - V_{ynx}^i = -(V_{xny}^r + V_{ypr}^r - V_{xpy}^r - V_{ynx}^r) \quad (2.6)$$

## iii) continuity of electric field

For the structure shown in fig. 2.2a, equating the electric field (or equivalently the total voltage) across link-lines parallel to the y-axis with that across link-lines parallel to the z-axis gives

$$V_{ynx} + V_{ypr} = V_{znx} + V_{zpr}$$

The total voltage on each port is given by  $V = V^i + V^r$  and the equations for all three directions are

$$(V_{ynx}^i + V_{ypr}^i) - (V_{znx}^i + V_{zpr}^i) = -(V_{ynx}^r + V_{ypr}^r) + (V_{znx}^r + V_{zpr}^r) \quad (2.7)$$

$$(V_{zny}^i + V_{zpy}^i) - (V_{xny}^i + V_{xpy}^i) = -(V_{zny}^r + V_{zpy}^r) + (V_{xny}^r + V_{xpy}^r) \quad (2.8)$$

$$(V_{xnz}^i + V_{xpr}^i) - (V_{ynz}^i + V_{ypr}^i) = -(V_{xnz}^r + V_{xpr}^r) + (V_{ynz}^r + V_{ypr}^r) \quad (2.9)$$

<sup>1</sup> For further details on conservation of flux linkage see appendix 1.



#### iv) continuity of magnetic field

For the structure shown in fig. 2.2b, equating the magnetic field (or equivalently the total current) on link-lines parallel to the y-axis with that on link-lines parallel to the z-axis gives

$$I_{y\pi z} - I_{y\pi x} = I_{z\pi y} - I_{z\pi x}$$

The total current on each port is given by  $I = Y_0(V^i - V^r)$  and the equations for all three directions are

$$(V_{y\pi z}^i - V_{y\pi x}^i) - (V_{z\pi y}^i - V_{z\pi x}^i) = (V_{y\pi z}^r - V_{y\pi x}^r) - (V_{z\pi y}^r - V_{z\pi x}^r) \quad (2.10)$$

$$(V_{x\pi z}^i - V_{x\pi y}^i) - (V_{y\pi z}^i - V_{y\pi x}^i) = (V_{x\pi z}^r - V_{x\pi y}^r) - (V_{y\pi z}^r - V_{y\pi x}^r) \quad (2.11)$$

$$(V_{x\pi y}^i - V_{x\pi x}^i) - (V_{y\pi x}^i - V_{y\pi z}^i) = (V_{x\pi y}^r - V_{x\pi x}^r) - (V_{y\pi x}^r - V_{y\pi z}^r) \quad (2.12)$$

The twelve equations (2.1)–(2.12) are linearly independent and when solved for the scattered pulses yield the required scattering matrix. Note that energy is conserved ( $\sum(V^r)^2 = \sum(V^i)^2$ ) even though this condition was not explicitly enforced. This is a general result which is true for any linear network subject to the usual voltage and current constraints [23]. A consequence of the fact that energy is conserved is that the scattering matrix is unitary [24 pp248–254] i.e.  $[S]^T [S] = [I]$ . This condition was fundamental to Johns' original derivation.

Although the scattering procedure can be expressed concisely in matrix notation, it is not appropriate, as far as computational efficiency is concerned, to implement the procedure in this form since there are a large number of zeros in the scattering matrix. The following expressions may be evaluated directly in order to obtain the scattered pulses in an efficient manner.

$$V_{y\pi x}^r = \frac{1}{2}(V_{x\pi z}^i + V_{x\pi y}^i + V_{x\pi y}^i - V_{x\pi y}^i)$$

$$V_{y\pi x}^r = \frac{1}{2}(V_{z\pi x}^i + V_{z\pi x}^i + V_{x\pi y}^i - V_{x\pi y}^i)$$

$$V_{z\pi x}^r = \frac{1}{2}(V_{y\pi x}^i + V_{y\pi x}^i + V_{x\pi z}^i - V_{x\pi z}^i)$$

$$V_{z\pi x}^r = \frac{1}{2}(V_{y\pi x}^i + V_{y\pi x}^i + V_{x\pi z}^i - V_{x\pi z}^i)$$

$$V_{z\pi y}^r = \frac{1}{2}(V_{x\pi y}^i + V_{x\pi y}^i + V_{y\pi z}^i - V_{y\pi z}^i)$$

$$V_{z\pi y}^r = \frac{1}{2}(V_{x\pi y}^i + V_{x\pi y}^i + V_{y\pi z}^i - V_{y\pi z}^i)$$

$$V_{x\pi y}^r = \frac{1}{2}(V_{z\pi y}^i + V_{z\pi y}^i + V_{y\pi x}^i - V_{y\pi x}^i)$$

$$V_{x\pi y}^r = \frac{1}{2}(V_{z\pi y}^i + V_{z\pi y}^i + V_{y\pi x}^i - V_{y\pi x}^i)$$

$$\begin{aligned}
V_{xnx}^r &= \frac{1}{2} (V_{ynz}^i + V_{ytx}^i + V_{znx}^i - V_{ztx}^i) \\
V_{xtx}^r &= \frac{1}{2} (V_{ynz}^i + V_{ytx}^i + V_{ztx}^i - V_{znx}^i) \\
V_{ytx}^r &= \frac{1}{2} (V_{xnx}^i + V_{xtx}^i + V_{ztx}^i - V_{zny}^i) \\
V_{ytx}^r &= \frac{1}{2} (V_{xnx}^i + V_{xtx}^i + V_{ztx}^i - V_{zny}^i)
\end{aligned}$$

A single array is sufficient to store both incident and scattered voltage pulses (provided that local storage is used to prevent overwriting of the incident pulses as the scattered pulses are computed).

The 12-port node can be used to model regions of space with a uniform mesh. The intrinsic impedance of the medium is determined by the characteristic impedance of the link-lines. The timestep can be determined by equating the total capacitance and inductance of the link-lines to the capacitance and inductance of the block of space represented by each node. For a complete transmission-line of length  $\Delta l$ , with total inductance  $L$  and total capacitance  $C$ , the characteristic impedance and the speed of propagation of a voltage pulse are given by

$$Z_0 = \sqrt{\frac{L}{C}} \quad \text{and} \quad \frac{\Delta l}{\Delta t} = \frac{\Delta l}{\sqrt{LC}}$$

combining these equations gives  $C = Y_0 \Delta t$  and  $L = Z_0 \Delta t$ . In total, four half link-lines must be taken into account. The capacitance and inductance in the  $x$ -direction are given by

$$C_x = \epsilon \frac{\Delta y \Delta z}{\Delta x} = 2 Y_0 \Delta t \quad \text{and} \quad L_x = \mu \frac{\Delta y \Delta z}{\Delta x} = 2 Z_0 \Delta t$$

For a uniform mesh,  $\Delta l = \Delta x = \Delta y = \Delta z$ , and so the timestep can be written as

$$\Delta t = \frac{\Delta l}{2c} \quad \text{where} \quad c = \frac{1}{\sqrt{\mu \epsilon}}$$

The velocity of waves on the transmission-line structure is therefore half the velocity of the pulses on the individual link-lines.

## 2.3 Stub-loaded node

The addition of stubs to the node allows the modelling of different material properties within the same mesh. They can also be used to independently alter the shape of each node so that a graded mesh can be used. In this thesis, only the

hybrid node (described in §2.4) has been used to implement a graded mesh. Open-circuit and short-circuit stubs were originally added by Johns to model increased permittivity and permeability and the same characteristic impedance was used for all link-lines. Loss stubs were subsequently added to model both electric [25] and magnetic losses [26]. Three of each type of stub are connected to the node so that they couple only with the field components in each of the coordinate directions. The open-circuit and electric-loss stubs couple with the electric field whilst the short-circuit and magnetic-loss stubs couple with the magnetic field.

### 2.3.1 Stub parameters

#### i) open-circuit stubs

Consider the capacitance of the block of space represented by the node in the  $x$ -direction,  $C_x$ . This is to be modelled as distributed capacitance on the link-lines and an open-circuit stub, of capacitance  $C_x^s$ , at the node.

$$C_x = \epsilon \Delta l = 2 Y_0 \Delta t + C_x^s$$

Making use of the relation  $\epsilon_0 = Y_0 / c$ , gives

$$C_x^s = Y_0 \left( \frac{\epsilon_r}{c} \Delta l - 2 \Delta t \right)$$

The round trip time for a pulse scattered from the node into the stub, to become incident again, is set to be the same as the transit time between nodes,  $\Delta t$ , and the length is set to  $\frac{1}{2}\Delta l$ . The required stub admittance, normalised to  $Y_0$ , is given by

$$\begin{aligned} \hat{Y}_x^s &= \frac{2 C_x^s}{Y_0 \Delta t} \\ &= 2 \left( \frac{\epsilon_r}{c} \frac{\Delta l}{\Delta t} - 2 \right) \end{aligned}$$

To guarantee stability, the stub admittance must be positive so that it represents a passive component. This means that  $\Delta t$  is determined by the lowest value of  $\epsilon_r$  for any node in the mesh. Taking the background relative permittivity as unity and writing  $\Delta t = \Delta l / 2 c$  gives

$$\hat{Y}_x^s = 4 (\epsilon_r - 1)$$

For any other background relative permittivity,  $\epsilon_{r0}$

$$\hat{Y}_x^s = 4 \left( \frac{\epsilon_r}{\epsilon_{r0}} - 1 \right)$$

For isotropic materials, the stub admittances are the same in all three directions. Note that this analysis ignores the error inductance,  $L_{error} = \Delta t^2 / C$ , which is a second order effect and is not significant.

## ii) short-circuit stubs

Consider the inductance of the block of space represented by the node in the x-direction,  $L_x$ . Equating  $L_x$  with the distributed inductance of the link-lines and a short-circuit stub of inductance  $L_x^s$ , gives

$$\begin{aligned} L_x &= \mu \Delta l = 2 Z_0 \Delta t + L_x^s \\ \Rightarrow L_x^s &= Z_0 \left( \frac{\mu_r}{c} \Delta l - 2 \Delta t \right) \end{aligned}$$

The required normalised stub impedance is given by

$$\begin{aligned} \hat{Z}_x^s &= \frac{2 L_x^s}{Z_0 \Delta t} \\ &= 4(\mu_r - 1) \quad \text{for background relative permeability of unity} \\ &= 4 \left( \frac{\mu_r}{\mu_{r0}} - 1 \right) \quad \text{for background relative permeability of } \mu_{r0} \end{aligned}$$

Note that the stub is terminated by a short-circuit so that the pulse scattered into the stub will be incident (after time  $\Delta t$ ) with the opposite sign.

## iii) electric losses

Electric loss stubs can be treated as either infinitely long, or, terminated with their own impedance; in either case, the energy scattered into the stub is removed from the system and there is no incident pulse. This means that no additional storage is required for pulses on loss stubs. In general, for a material with complex permittivity  $\epsilon = \epsilon' - j \epsilon''$  and conduction conductivity  $\sigma$ , the total effective conductivity is given by  $\sigma_e = \omega \epsilon'' + \sigma$ . The loss tangent may be written as [24 pp23–28]

$$\tan \delta_e = \frac{\sigma_e}{\omega \epsilon_r \epsilon_0}$$

If  $\sigma_e$  has a significant frequency dependence then either an average value must be taken, or the function must be approximated in a piecewise fashion (requiring separate simulations for each value). The required normalised stub admittance, for

a stub in the x-direction, is given by

$$\begin{aligned}\hat{G}_x &= \sigma_e Z_0 \frac{\Delta y \Delta z}{\Delta x} \\ &= \sigma_e Z_0 \Delta l \quad \text{for a uniform mesh}\end{aligned}$$

#### iv) magnetic losses

Magnetic loss stubs operate in a similar way, but the energy removed from the system is proportional to the magnetic field rather than the electric field <sup>2</sup>. The required normalised stub impedance, for a stub in the x-direction, is given by

$$\hat{R}_x = \sigma_m Y_0 \frac{\Delta y \Delta z}{\Delta x}$$

### 2.3.2 Scattering properties

The scattering matrix may be derived in a similar manner as for the 12-port node.

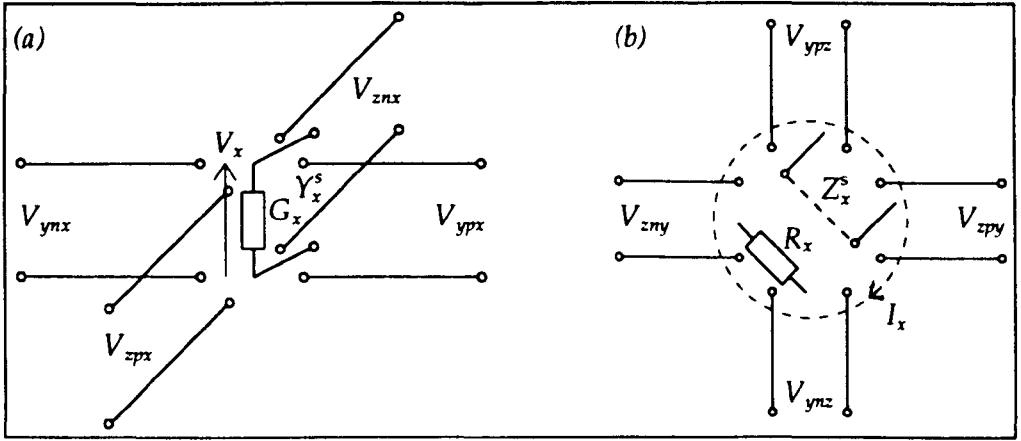


Fig. 2.3 – Stub-loaded node (a) electric field (b) magnetic field

#### i) conservation of charge

Equating the incident and scattered charge for transmission-lines contributing to the x-component of the electric field, as shown in fig. 2.3a, gives

$$\begin{aligned}V_{ynx}^i + V_{ypx}^i + V_{znx}^i + V_{zpx}^i + \hat{Y}_x V_{ox}^i &= \\ V_{ynx}^r + V_{ypx}^r + V_{znx}^r + V_{zpx}^r + \hat{Y}_x V_{ox}^r + \hat{G}_x V_{ex}^r\end{aligned}\quad (2.13)$$

where  $V_{ox}$  and  $V_{ex}$  denote the voltages on the open-circuit and electric-loss stubs, respectively.

<sup>2</sup> Improved magnetic losses for the modelling of ferrite materials have recently been proposed [27]. In this approach, the loss stub is placed in parallel with the inductive stub rather than in series.

## ii) conservation of magnetic flux

Equating the flux linked with the incident pulses with the flux linked with the scattered pulses for transmission-lines contributing to the x-component of the magnetic field, as shown in fig. 2.3b, gives

$$\begin{aligned}
 I'_{ymz} + I'_{zpy} - I'_{ypz} - I'_{zmy} + \hat{Z}_x^s I'_{sx} &= \\
 I'_{ymz} + I'_{zpy} - I'_{ypz} - I'_{zmy} + \hat{Z}_x^s I'_{sx} + \hat{R}_x I'_{mx} &= \\
 \Rightarrow V'_{ymz} + V'_{zpy} - V'_{ypz} - V'_{zmy} + V'_{sx} &= \\
 -(V'_{ypz} + V'_{zpy} - V'_{ypz} - V'_{zmy} + V'_{sx} + V'_{mx}) & \quad (2.14)
 \end{aligned}$$

where  $V_{sx}$  and  $V_{mx}$  denote the voltages on the short-circuit and magnetic-loss stubs.

## iii) continuity of field

The continuity of the electric and magnetic fields is enforced in the same manner as for the 12-port node (conditions (iii) and (iv) in §2.2). The stubs do not enter into the equations since they are not associated with any direction (apart from their polarisation).

## iv) electric field stubs

The voltage pulses scattered into the open-circuit and electric-loss stubs may be found from equations of the form

$$V'_{ox} = V_x - V'_{\alpha x} \quad (2.15)$$

$$\text{and } V'_{\alpha x} = V_x \quad (2.16)$$

where  $V_x$  is the total voltage across the node. Note that  $V'_{\alpha x}$  need not be calculated unless the magnitude of the losses is required.  $V_x$  may be found as the voltage across the total capacitance of the node,  $C_x$ . Equating the charge on  $C_x$  and the sum of the charges on the contributing transmission-lines gives

$$V_x = \frac{V_{ymx} + V_{ypx} + V_{zmx} + V_{zpx} + \hat{Y}_x^s V_{\alpha x}}{4 + \hat{Y}_x^s} \quad (2.17)$$

$V_x$  may be expressed solely in terms of incident pulses (which are known) by substituting the scattered pulses from (2.13) into (2.17) and making use of equations (2.15) and (2.16).

$$V_x = \frac{2}{4 + \hat{Y}_x^s + \hat{G}_x} (V_{ynx}^i + V_{y\eta x}^i + V_{znx}^i + V_{z\eta x}^i + \hat{Y}_x^s V_{sx}^i)$$

Note that  $V_x$  may also be calculated from the Thévenin equivalent circuit obtained when the transmission-lines are connected in parallel. This circuit is misleading, however, since it is inconsistent with the pulses scattered into the link-lines.

#### v) magnetic field stubs

The voltage pulses scattered into the short-circuit and magnetic-loss stubs may be found from equations of the form

$$V_{sx}^r = Z_0 \hat{Z}_x^s I_x + V_{sx}^i \quad (2.18)$$

$$\text{and } V_{mx}^r = Z_0 \hat{R}_x I_x \quad (2.19)$$

where  $I_x$  is the total current circulating around the node. The sign of the current is chosen to be consistent with the magnetic field. Equating the flux linkage on the total inductance,  $L_x$ , with the sum of flux linkage on the contributing transmission-lines gives

$$I_x = \frac{I_{y\eta x} + I_{z\eta y} - I_{y\eta z} - I_{z\eta y} - \hat{Z}_x^s I_{sx}}{4 + \hat{Z}_x^s} \quad (2.20)$$

$I_x$  may be expressed solely in terms of incident pulses by substituting the scattered pulses from (2.14) into (2.20) and making use of equations (2.18) and (2.19).

$$I_x = \frac{2}{Z_0 (4 + \hat{Z}_x^s + \hat{R}_x)} (V_{y\eta x}^i + V_{z\eta y}^i - V_{y\eta z}^i - V_{z\eta y}^i - V_{sx}^i)$$

$I_x$  may be obtained from the Thévenin equivalent circuit obtained when the transmission-lines are connected in series. This circuit is, however, inconsistent with the scattered pulses, as before.

Solving equations (2.13), (2.14), (2.7), (2.10), the equations for the pulses scattered into the stubs and the corresponding equations for the other directions gives the scattering matrix. Naylor and Ait-Sadi [28] have found that the scattering procedure is most efficiently implemented by first calculating the nodal voltages ( $V_x, V_y, V_z$ ) and the loop currents ( $I_x, I_y, I_z$ ) from the incident pulses. The voltage pulses scattered into the stubs can then be directly obtained and the voltage pulses scattered into the link-lines can be found from the following expressions.

$$V_{ynx}^r = V_x - Z_0 I_z - V_{ynx}^i$$

$$V_{ynx}^r = V_x + Z_0 I_z - V_{ynx}^i$$

$$V_{znx}^r = V_x + Z_0 I_y - V_{znx}^i$$

$$V_{znx}^r = V_x - Z_0 I_y - V_{znx}^i$$

$$V_{zny}^r = V_y - Z_0 I_x - V_{zny}^i$$

$$V_{zny}^r = V_y + Z_0 I_x - V_{zny}^i$$

$$V_{xny}^r = V_y + Z_0 I_z - V_{xny}^i$$

$$V_{xny}^r = V_y - Z_0 I_z - V_{xny}^i$$

$$V_{xnz}^r = V_z - Z_0 I_y - V_{xnz}^i$$

$$V_{xnz}^r = V_z + Z_0 I_y - V_{xnz}^i$$

$$V_{ynz}^r = V_x + Z_0 I_x - V_{ynz}^i$$

$$V_{ynz}^r = V_x - Z_0 I_x - V_{ynz}^i$$

Some manipulation is necessary to get the equations into this form. The method can also be used for the 12-port and the hybrid nodes although there may be no computational advantage in the case of the former.

## 2.4 Hybrid node

In the stub-loaded node, the characteristic impedance of all link-lines in the mesh is kept constant. In the hybrid node, this restriction is removed so that the characteristic impedance can take different values with respect to both link-lines on the same node and link-lines on other nodes. This idea was explored by Wright [29] and was implemented for the expanded node by Voelker and Lomax [30]. In the scheme devised for the SCN by Scaramuzza and Lowery [31], used here, the inductance of the link-lines is altered so that they model all of the required inductance, removing the need for short-circuit stubs. Open-circuit stubs are still required since the capacitance of the link-lines is chosen to maintain time synchronism. Alternative schemes, of equal validity, may also be devised; for example, all of the required capacitance (rather than inductance) could be modelled by the link-lines, or, the impedances of the link-lines could be assigned in an alternative manner. The hybrid node was originally developed to overcome the



limitation on maximum timestep, encountered for certain types of grading, with the stub-loaded node and is used exclusively for graded meshes in this thesis.

### 2.4.1 Link-line and stub parameters

Three distinct values of characteristic impedance are used for the 12 link-line ports on each node and these are assigned to the three sets of link-lines contributing to the three components of the magnetic field. The impedance is constant along half of each link-line; there is an impedance discontinuity at the mid-point due to the different impedances associated with adjacent nodes. The mesh parameters will be derived for the general case of a node of dimensions  $\Delta x \times \Delta y \times \Delta z$ . The time taken for a voltage pulse to travel between any two nodes,  $\Delta t$ , is kept constant and so the bulk wave must be slowed down with stubs.

Consider the link-lines associated with the z-component of the magnetic field. The characteristic impedance and the total inductance of the two pairs of orthogonal link-lines are chosen to be the same, i.e.

$$\sqrt{\frac{L_{xy}}{C_{xy}}} = \sqrt{\frac{L_{yx}}{C_{yx}}} \quad \text{and} \quad L_{xy} \Delta x = L_{yx} \Delta y$$

where  $L_{xy}$  and  $L_{yx}$  are values of distributed inductance and  $C_{xy}$  and  $C_{yx}$  are values of distributed capacitance, with the first subscript giving the direction parallel to the link-line and the second subscript giving the polarisation. The total inductance is to be modelled as distributed inductance on the link-lines. For example,  $L_z$

$$\begin{aligned} L_z &= \mu \frac{\Delta x \Delta y}{\Delta z} = L_{xy} \Delta x + L_{yx} \Delta y \\ \Rightarrow L_{yx} &= \frac{1}{2} \mu \frac{\Delta x}{\Delta z} \end{aligned} \quad (2.20)$$

The total capacitance is to be modelled as distributed capacitance on the link-lines and an open-circuit stub at the node. For example,  $C_x$

$$\begin{aligned} C_x &= \epsilon \frac{\Delta y \Delta z}{\Delta x} = C_{yx} \Delta y + C_{zx} \Delta z + C_x^s \\ \Rightarrow C_x^s &= \epsilon \frac{\Delta y \Delta z}{\Delta x} - C_{yx} \Delta y - C_{zx} \Delta z \end{aligned} \quad (2.21)$$

It is necessary to express  $C_x^s$  in terms of  $\Delta t$  so that a limit on the maximum timestep can be determined. To do this,  $C_{yx}$  and  $C_{zx}$  must first be expressed in terms of  $\Delta t$ .  $C_{yx}$

can be found by considering the speed of propagation of a pulse on a link-line parallel to the  $y$ -axis.

$$\frac{\Delta y}{\Delta t} = \frac{1}{\sqrt{C_{yx} L_{yx}}}$$

$$\Rightarrow C_{yx} = \frac{2}{\mu} \frac{\Delta z}{\Delta x} \frac{\Delta t^2}{\Delta y^2}$$

where  $L_{yx}$  is taken from (2.20). Similarly, for propagation on a link-line parallel to the  $z$ -axis

$$C_{zx} = \frac{2}{\mu} \frac{\Delta y}{\Delta x} \frac{\Delta t^2}{\Delta z^2}$$

Substituting  $C_{yx}$  and  $C_{zx}$  into (2.21) gives

$$C_x^s = \frac{1}{\mu \Delta x \Delta y \Delta z} (\mu \epsilon \Delta y^2 \Delta z^2 - 2 \Delta y^2 \Delta t^2 - 2 \Delta z^2 \Delta t^2)$$

$$\Rightarrow \Delta t < \frac{1}{c} \Delta y \Delta z \sqrt{\frac{\mu_r \epsilon_r}{2 \Delta y^2 + 2 \Delta z^2}}$$

This inequality, and similar ones for the other two directions, must be satisfied at all nodes in the mesh to guarantee stability. Once the timestep is known, the mesh parameters can be determined. For example, the normalised admittance of the link-lines associated with the  $z$ -component of the magnetic field is given by

$$\hat{Y}_z = \frac{1}{Y_0} \sqrt{\frac{C_{yx}}{L_{yx}}}$$

$$= \frac{2 c \Delta t \Delta z}{\mu_r \Delta x \Delta y}$$

and the normalised admittance of the open-circuit stub polarised in the  $x$ -direction is given by

$$\hat{Y}_x^s = \frac{2 C_x^s}{\Delta t Y_0}$$

$$= \frac{2 \epsilon_r}{c \Delta t} \frac{\Delta y \Delta z}{\Delta x} - \frac{4 c \Delta t}{\mu_r \Delta x \Delta y \Delta z} (\Delta y^2 + \Delta z^2)$$

These expressions can also be written in terms of the smallest node dimension,  $\Delta l_{min}$ , by making use of the expression  $\Delta t = \Delta l_{min} / 2 c$ . Values for the impedance of loss stubs are obtained in the same way as for the stub-loaded node.

## 2.4.2 Scattering properties

The derivation of the scattering matrix is similar in form to the two previous cases; only the form of the equations will therefore be given. The original derivation by Scaramuzza and Lowery was based on the unitary principle. The relevant transmission-lines are shown in fig. 2.4.

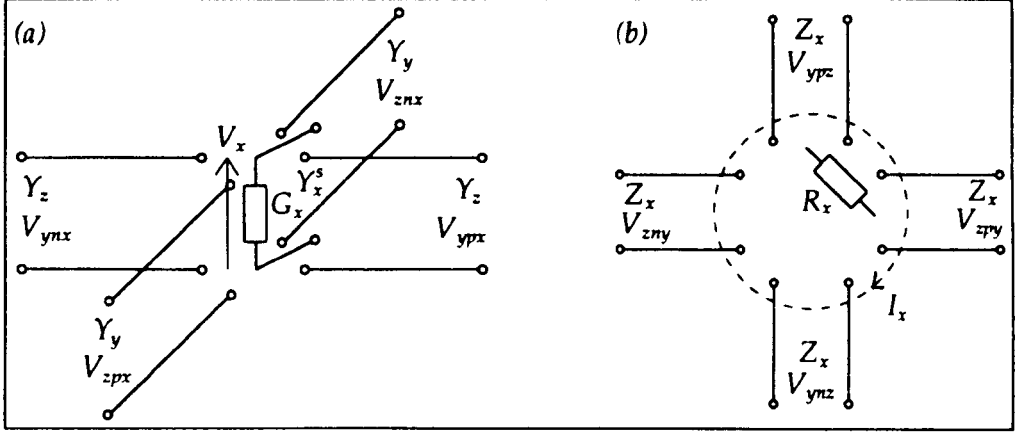


Fig. 2.4 - Hybrid node (a) electric field (b) magnetic field

### i) conservation of charge

$$\hat{Y}_z(V'_{ynx} + V'_{ypx}) + \hat{Y}_y(V'_{znx} + V'_{zpx}) + \hat{Y}_x V'_{ox} + \hat{G}_x V'_{ox} =$$

$$\hat{Y}_z(V^i_{ynx} + V^i_{ypx}) + \hat{Y}_y(V^i_{znx} + V^i_{zpx}) + \hat{Y}_x V^i_{ox}$$

### ii) conservation of magnetic flux

$$V'_{ynz} + V'_{zpy} - V'_{ypz} - V'_{zny} + V'_{mx} = -(V^i_{ynz} + V^i_{zpy} - V^i_{ypz} - V^i_{zny})$$

### ii) continuity of field

The equations for the continuity of the electric and magnetic fields are the same as for the 12-port and stub-loaded nodes since all four magnetic field link-lines have the same admittance and the admittance is irrelevant for the electric field.

### iii) electric field stubs

$$V_x = \frac{\hat{Y}_z(V_{ynx} + V_{ypx}) + \hat{Y}_y(V_{znx} + V_{zpx}) + \hat{Y}_x V_{ox}}{2\hat{Y}_y + 2\hat{Y}_z + \hat{Y}_x}$$

$$= \frac{2\hat{Y}_z(V^i_{ynx} + V^i_{ypx}) + 2\hat{Y}_y(V^i_{znx} + V^i_{zpx}) + 2\hat{Y}_x V^i_{ox}}{2\hat{Y}_y + 2\hat{Y}_z + \hat{Y}_x + \hat{G}_x}$$

#### iv) magnetic field stubs

$$I_x = \frac{1}{4}(I_{y\eta z} + I_{z\eta y} - I_{y\eta z} - I_{z\eta y})$$

$$= \frac{2}{Z_0(4\hat{Z}_x + \hat{R})}(V_{y\eta z}^i + V_{z\eta y}^i - V_{y\eta z}^i - V_{z\eta y}^i)$$

### 2.4.3 Connect procedure

For the stub-loaded node, the connect procedure consists simply of swapping voltage pulses from adjacent nodes. For the hybrid node, account must be taken of the possibility of differences in link-line impedance. The required transmission and reflection coefficients can be readily obtained from the Thévenin equivalent circuit and the two polarisations on each arm of the node must be treated separately.

## 2.5 Boundary conditions

Boundary conditions may be imposed at nodes and on link-lines. In this section, short-circuit nodes and resistive boundaries, placed at the mid-point of link-lines will be discussed. Boundaries at nodes are implemented in the scatter procedure whilst boundaries on link-lines are implemented in the connect procedure. The restriction on placing boundaries at the mid-point of link-lines ensures that the transit time is the same for a pulse transmitted through the boundary to the adjacent node, as for a pulse reflected back to the same node.

### 2.5.1 Short-circuit node

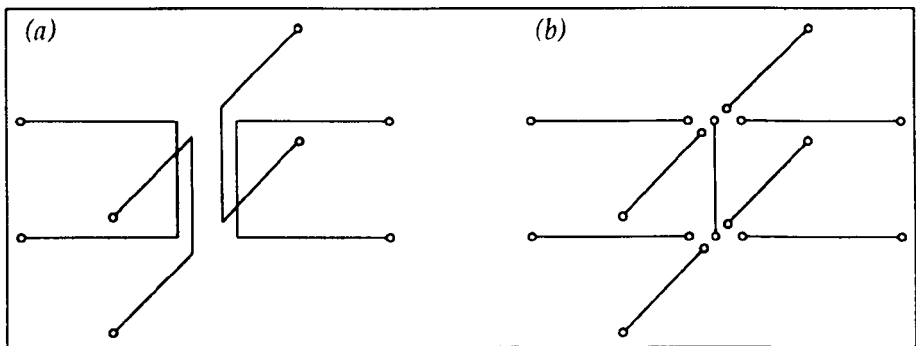


Fig. 2.5 – (a) short circuit node (b) zero resistance “lossy” node

The short-circuit node can be used to place perfectly conducting metal objects into the mesh. The scattering matrix is zero everywhere except on the leading diagonal, where all elements are  $-1$ . Note that this scattering matrix differs from

that obtained from a “lossy” node in which the electrical resistance is reduced to zero. This is a consequence of the fact that there is no direct connection between the link-lines and the loss stub. The connection of link-lines contributing to a single component of the electric field is shown schematically in fig. 2.5. Contrast the scattered pulses for the 12-port node (2.22), the short-circuit node (2.23) and the zero resistance “lossy” node (2.24).

$$V_{y\eta x}^r = \frac{1}{2} (V_{x\eta x}^i + V_{x\eta x}^i + V_{x\eta y}^i - V_{x\eta y}^i) \quad (2.22)$$

$$V_{y\eta x}^r = -V_{y\eta x}^i \quad (2.23)$$

$$V_{y\eta x}^r = \frac{1}{2} (V_{x\eta y}^i - V_{x\eta y}^i - V_{y\eta x}^i - V_{y\eta x}^i) \quad (2.24)$$

If a conducting surface is modelled using a “lossy” node then pulses will be transmitted through it. For example, if a pulse of unit magnitude is incident, then two pulses (over two iterations) are reflected back, both of value  $-\frac{1}{2}$  and two pulses are transmitted through the node, of values  $-\frac{1}{2}$  and  $+\frac{1}{2}$ . The total charge is therefore correct and the energy of the transmitted pulses is well above the working frequency of the mesh. In practice there is found to be very little difference between the two methods.

## 2.5.2 External boundaries

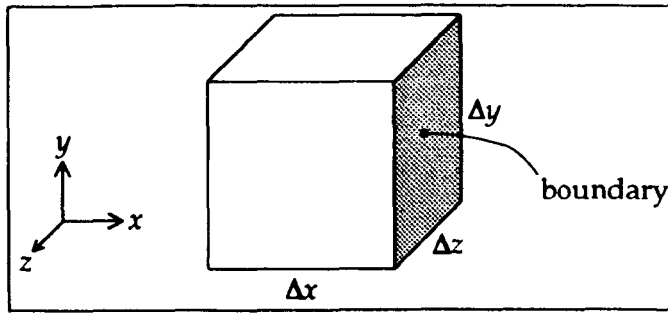


Fig. 2.6 – External boundary

External boundaries of arbitrary reflection coefficient may be modelled by terminating the link-lines on the edge of the problem space with an appropriate load. The properties of the boundary may be expressed as a reflection coefficient, as a resistivity or as a skin depth. Resistivity can be converted to reflection coefficient from a knowledge of the node dimensions and the intrinsic impedance of the material. Skin depth can be converted into resistance if the frequency is known. Once the required reflection coefficient,  $\rho_w$ , is known, the reflection coefficient

needed to terminate each link-line,  $\rho_l$ , can be determined.

Consider the block of space represented by a node of dimensions  $\Delta x \times \Delta y \times \Delta z$ , as shown in fig. 2.6. For a pulse travelling towards the boundary polarised in the  $y$ -direction, the characteristic impedance of the medium is

$$\begin{aligned} Z_b &= \sqrt{\frac{L_z}{C_y}} \\ &= \frac{\Delta y}{\Delta z} Z_0 \sqrt{\frac{\mu_r}{\epsilon_r}} \end{aligned}$$

The resistance needed to terminate a transmission-line of characteristic impedance  $Z_b$ , in order to give reflection coefficient  $\rho_w$  is

$$R = Z_b \left( \frac{1 + \rho_w}{1 - \rho_w} \right)$$

The link-line reflection coefficient,  $\rho_l$ , is found by terminating the link-line, of characteristic impedance  $Z_l$ , with this same resistance.

$$\begin{aligned} \rho_l &= \frac{R - Z_l}{R + Z_l} \\ &= \frac{Z_b (1 + \rho_w) - Z_l (1 - \rho_w)}{Z_b (1 + \rho_w) + Z_l (1 - \rho_w)} \end{aligned}$$

German *et al* [32] have used the concept of effective material constants to obtain the same result.

To model a short-circuit, or *electric wall*,  $\rho_w = -1$  and  $\rho_l = -1$ . For an open-circuit, or *magnetic wall*,  $\rho_w = 1$  and  $\rho_l = 1$ . Both electric and magnetic walls can be used to exploit symmetry. For other values of  $\rho_w$ ,  $\rho_l$  will depend on  $Z_l$ . For example, consider a matched boundary,  $\rho_w = 0$ , used to match the mesh to free-space.

$$\text{for the stub-loaded node, } Z_l = Z_0 \Rightarrow \rho_l = \frac{\sqrt{\mu_r} - \sqrt{\epsilon_r}}{\sqrt{\mu_r} + \sqrt{\epsilon_r}}$$

$$\text{for the hybrid node, } Z_l = Z_0 \frac{\mu_r \Delta x \Delta y}{2 \Delta t \Delta z} \Rightarrow \rho_l = \frac{2 c \Delta t - \Delta x \sqrt{\mu_r \epsilon_r}}{2 c \Delta t + \Delta x \sqrt{\mu_r \epsilon_r}}$$

Note that for a graded mesh using the hybrid node, the same value of  $\rho_l$  is used for both polarisations; different values must be used for a graded mesh using the stub-loaded node. Matched boundaries may be used to approximate radiation boundaries. They work perfectly when a wave is normally incident but work less

well for a wave incident at an angle.

### 2.5.3 Internal boundaries

Internal boundaries of arbitrary resistance can be placed at the mid-point of link-lines and the required reflection and transmission coefficients can be readily obtained from the Thévenin equivalent circuit. Internal boundaries differ from external ones in that they are connected to both halves of the link-line.

## 2.6 Outputs

The TLM method yields information on incident and scattered voltage pulses. This information may be readily transformed to give any required field quantity. Fields may be obtained either at a node or on the individual link-lines.

### 2.6.1 Field at a node

The electric field is proportional to the total voltage across the node. For example, the x-component of the electric field for the 12-port node is given by

$$\begin{aligned} E_x &= -\frac{V_x}{\Delta x} \\ &= -\frac{V_{ynx}^i + V_{ypx}^i + V_{znx}^i + V_{zpx}^i}{2 \Delta l} \end{aligned}$$

The electric field at stub-loaded or hybrid nodes can be found by substituting values of  $V_x$  obtained in §2.3 and §2.4. The field can equally well be expressed in terms of scattered pulses. The magnetic field is proportional to the current circulating in the node. For example, the z-component of the magnetic field for the 12-port node is given by

$$\begin{aligned} H_z &= \frac{I_z}{\Delta z} \\ &= \frac{V_{ynx}^i + V_{xpy}^i - V_{ypx}^i - V_{xny}^i}{2 Z_0 \Delta z} \end{aligned}$$

The current flowing through a lossy or short-circuit node may also be readily calculated.

### 2.6.2 Field on a link-line

The electric and magnetic fields on a link-line can be found, in a straightforward manner, from the two voltage pulses from the adjacent nodes. For example, for the 12-port or stub-loaded nodes,

$$E_y = -\frac{1}{\Delta y} [V'_{xpy}(x) + V'_{xny}(x+1)]$$

$$H_z = \frac{1}{Z_0 \Delta z} [V'_{xny}(x+1) - V'_{xpy}(x)]$$

For the hybrid node,

$$E_y = -\frac{2[\hat{Y}_z(x) V'_{xpy}(x) + \hat{Y}_z(x+1) V'_{xny}(x+1)]}{\Delta y [\hat{Y}_z(x) + \hat{Y}_z(x+1)]}$$

$$H_z = \frac{2\hat{Y}_z(x) \hat{Y}_z(x+1) [V'_{xny}(x+1) - V'_{xpy}(x)]}{\Delta z Z_0 [\hat{Y}_z(x) + \hat{Y}_z(x+1)]}$$

### 2.6.3 Comparison between node and link-line outputs

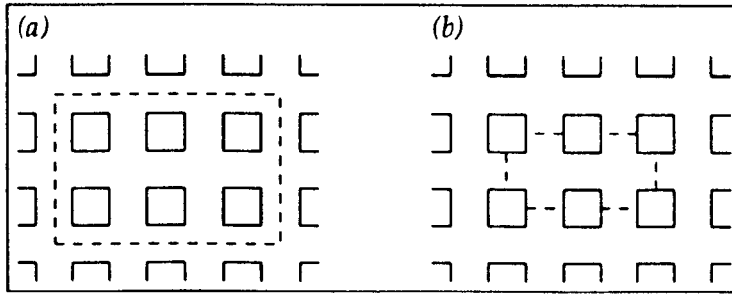


Fig. 2.7 – Surface formed from (a) node outputs (b) link-line outputs

In general, there is found to be very little difference between outputs taken at nodes and on link-lines (beyond any expected spatial variation)<sup>3</sup> and the choice is essentially one of convenience. There is a time difference of  $\frac{1}{2}\Delta t$  between pulses leaving the centre of the node and arriving at the mid-point of a link-line, but this can be neglected in most cases. The field at a node can be considered as an average of the field on the appropriate transmission-lines and is applicable when several field components are required at the same point. The field on a link-line is convenient when dealing with closed surfaces, since the corners do not enter into the problem; this is shown schematically in fig. 2.7. Link-line outputs are also more

<sup>3</sup> This is a consequence of the fact that, in the derivation, the field on orthogonal pairs of link-lines is forced to be the same (conditions (iii) and (iv) in §2.2) and the field at a node is obtained from pulses on both sets of link-lines.



appropriate when dealing with the energy stored in the system.<sup>4</sup>

## 2.7 Excitation

Energy is generally introduced into a simulation by means of an impulse excitation either at nodes or on link-lines. This means that the output data contains information at all frequencies (up to some maximum). Energy can also be introduced with voltage and current sources.

The expressions given in this section for the hybrid node have been obtained as an extension of those used for the stub-loaded node and, under certain circumstances, they have been found to give unpredictable results. These expressions should therefore be treated with caution and should be the subject of further study. Additional details can be found in §4.5.2. However, for most of the work presented in this thesis, the excitation has been applied in free-space at the smallest node dimension and, in these situations, no problems have been observed.

### 2.7.1 Impulse excitation of fields at a node

If the excitation is specified in terms of field quantities, then the equivalent voltage pulses must be found. At a node, there are 6 field quantities and 12 voltage pulses (18 for the stub-loaded node) and it is apparent that there is a non-unique mapping from the field to the voltage pulses. For the 12-port case, it follows from symmetry that each of the four pulses introduced into the four link-lines (associated with the field) should be equal. When stubs are present the question arises as to whether pulses should be applied to the stubs. If it is assumed that open-circuit and short-circuit stubs are present solely to slow down wave propagation then these stubs need not be excited. This is different to Johns' original derivation in which these stubs were included in the excitation. In practice, there is often found to be little difference between the two methods. As far as loss stubs are concerned, if incident pulses are excited then they are irrelevant (since there can be no incident pulse from a loss stub) and if scattered pulses are excited they can be disregarded if no loss is assumed to take place during the first iteration. The voltage pulses which must be applied to the link-lines for electric and magnetic fields are given below for the case when incident pulses are excited. For the hybrid

---

<sup>4</sup> Further details can be found in §4.4

node,  $Y_1$  and  $Y_2$  are the admittances of the two pairs of link-lines associated with the electric field and  $Y$  is the admittance of the magnetic field link-lines.

$$\text{electric-field on stub-loaded node, } V' = -\Delta l \left[ \frac{4 + \hat{Y}^s + \hat{G}}{8} \right] E$$

$$\text{electric-field on hybrid node, } V' = -\Delta l \left[ \frac{2(\hat{Y}_1 + \hat{Y}_2) + \hat{Y}^s + \hat{G}}{4(\hat{Y}_1 + \hat{Y}_2)} \right] E$$

$$\text{magnetic field on stub-loaded node, } V' = \pm \Delta l Z_0 \left[ \frac{4 + \hat{Z}^s + \hat{R}}{8} \right] H$$

$$\text{magnetic field on hybrid node, } V' = \pm \Delta l Z_0 \left[ \frac{4 + \hat{Y} \hat{R}}{8 \hat{Y}} \right] H$$

### 2.7.2 Impulse excitation of fields on a link-line

On a link-line, the required field must be obtained by exciting two voltage pulses and, from symmetry, these pulses should be equal. The voltage pulses required for electric and magnetic fields are given below for the case when scattered pulses are excited. For the hybrid node,  $Y_1$  and  $Y_2$  are the link-line admittances from the adjacent nodes.

$$\text{electric-field (stub-loaded and hybrid nodes), } V' = -\frac{1}{2} \Delta l E$$

$$\text{magnetic-field (stub-loaded node), } V' = \pm \frac{1}{2} \Delta l Z_0 H$$

$$\text{magnetic field (hybrid node), } V' = \pm \frac{\Delta l Z_0 (\hat{Y}_1 + \hat{Y}_2)}{4 \hat{Y}_1 \hat{Y}_2}$$

### 2.7.3 Voltage and current sources

Both voltage and current sources can be placed at the mid-point of link-lines. These link-lines may be internal to the mesh or may be incomplete link-lines on the edge of the mesh. In general, voltage sources may have a series resistance and current sources may have a shunt conductance. The required voltage pulses may be obtained from the Thévenin equivalent circuit. The difference between applying an impulse excitation and a source is that there are no pulses existing in the mesh in the first case case, whereas existing pulses must be taken into account in the source calculation. The source function can be an impulse but is, more usefully, a continuous function such as a sinusoid or a Gaussian pulse. A phase difference may be introduced between several source points by including a time delay. In

principle, sources can be applied at a node although this has not been done for work in this thesis.

The calculation for sources on link-lines can be considered as the general case of the connect procedure (although it would be inefficient to implement such a general procedure at all points in the mesh). It is convenient to first obtain the total voltage across the source and then subtract the scattered pulses to obtain the pulses which will be incident upon the node in the next iteration. The total voltage for a voltage source,  $V_s$ , with series resistance  $R$  and a current source,  $I_s$ , with shunt conductance  $G$  are given below for the hybrid node. For a complete link-line

$$\text{voltage source, } V = \frac{2R(\hat{Y}_1 V_1' + \hat{Y}_2 V_2') + Z_0 V_s}{R(\hat{Y}_1 + \hat{Y}_2) + Z_0}$$

$$\text{current source, } V = \frac{2(\hat{Y}_1 V_1' + \hat{Y}_2 V_2') - Z_0 I_s}{\hat{Y}_1 + \hat{Y}_2 + G Z_0}$$

For an incomplete link-line on the edge of the mesh

$$\text{voltage source, } V = \frac{2R\hat{Y}_1 V_1' + Z_0 V_s}{R\hat{Y}_1 + Z_0}$$

$$\text{current source, } V = \frac{2\hat{Y}_1 V_1' - Z_0 I_s}{\hat{Y}_1 + G Z_0}$$

# Chapter 3

## Signal Analysis

### 3.1 Frequency domain transformation

The TLM method provides output information in the time domain and it is often necessary to transform this data into the frequency domain. Fourier transform techniques have traditionally been used for this purpose. If an impulse excitation is used then the impulse response is obtained and this is generally taken as valid from d.c. up to a maximum frequency corresponding to a wavelength of ten nodes. The discrete Fourier transform (DFT) is often used in preference to the fast Fourier transform (FFT) since it allows greater flexibility in the way it is used and the additional calculation time is generally negligible when compared with the total simulation time.

With the DFT, it is possible to obtain any number of points in the frequency domain from any number of points in the time domain (although the information content in the frequency domain will always be less than that of the time domain data). By increasing the number of points in the frequency domain, a better evaluation of the signal is obtained although there is no increase in resolution. Flexibility is necessary so that the same technique can be used to obtain, for example, a single frequency transform over a plane (to obtain the field profile of a particular resonance), or, a transform at many closely spaced frequencies (in order to accurately predict the frequency of a resonance). The problem with the FFT is that it produces output uniformly distributed over a large frequency bandwidth extending from d.c. to half the sampling frequency; well beyond the accepted maximum working frequency of the mesh.

The Fourier transform of a signal,  $x(t)$ , is written as

$$X(f) = \int_{-\infty}^{\infty} x(t) \exp(-j2\pi ft) dt$$

In discrete form (the DFT), this integral may be approximated by a summation (for small  $\Delta t$ ).

$$X(f) = \Delta t \sum_{n=0}^{N-1} x[n] \exp(-j2\pi fn\Delta t)$$

The function  $X(f)$  is an estimation of the spectral content of the complete time series  $x[n]$  based on the  $N$  available values of  $x[n]$ . This estimator is termed the periodogram. Suitable manipulation of the above expression shows that the value at a particular frequency is obtained by filtering the data with a band pass filter (or more specifically, a notch filter) and then resampling the output at time  $t = 0$ , where the filter characteristic is determined by the truncated complex exponential function  $\exp(j 2 \pi f n \Delta t)$  for  $-(N - 1) \leq n \leq 0$ . Analysis of the periodogram shows that although the mean converges to the correct value as the number of points is increased, the uncertainty of the estimate remains constant. The periodogram is therefore an unbiased but inconsistent estimator [33]. However, provided care is taken, the periodogram is extremely useful and it has been used exclusively for the work in this thesis.

In general, models can be described as low, medium or high loss systems. For low loss systems, the spectral content of the truncated time series is required since the amplitude of any resonances will increase in proportion to the number of iterations (tending to infinity in the limit). For high loss systems, in which the signal effectively decays to zero within the simulation time, the actual spectral content of the complete time series is obtained. Moderately damped systems present a problem since an excessive number of iterations would be required for the signal to decay significantly. In this case, the spectral content of the truncated time series is obtained as an estimation of the spectral content of the complete time series.

For low and medium loss systems, the time series,  $x[n]$ , must necessarily be truncated since the simulation can only proceed for a finite time interval. The frequency response obtained is therefore the convolution of the actual response and the response of the windowing function  $W(f)$ . If  $x[n]$  is simply truncated, at time  $t = N \Delta t$ , then  $W(f)$  describes a rectangular window and is given by

$$W(f) = N \Delta t \exp(-j\pi f N \Delta t) \text{sinc}(\pi f N \Delta t)$$

where  $\text{sinc}(x) = \sin(x) / x$ . For example, the time and frequency domain signals taken at a point in a 1 m<sup>3</sup> cavity are shown in fig. 3.1. The true frequency response would be an impulse function at each resonant frequency.

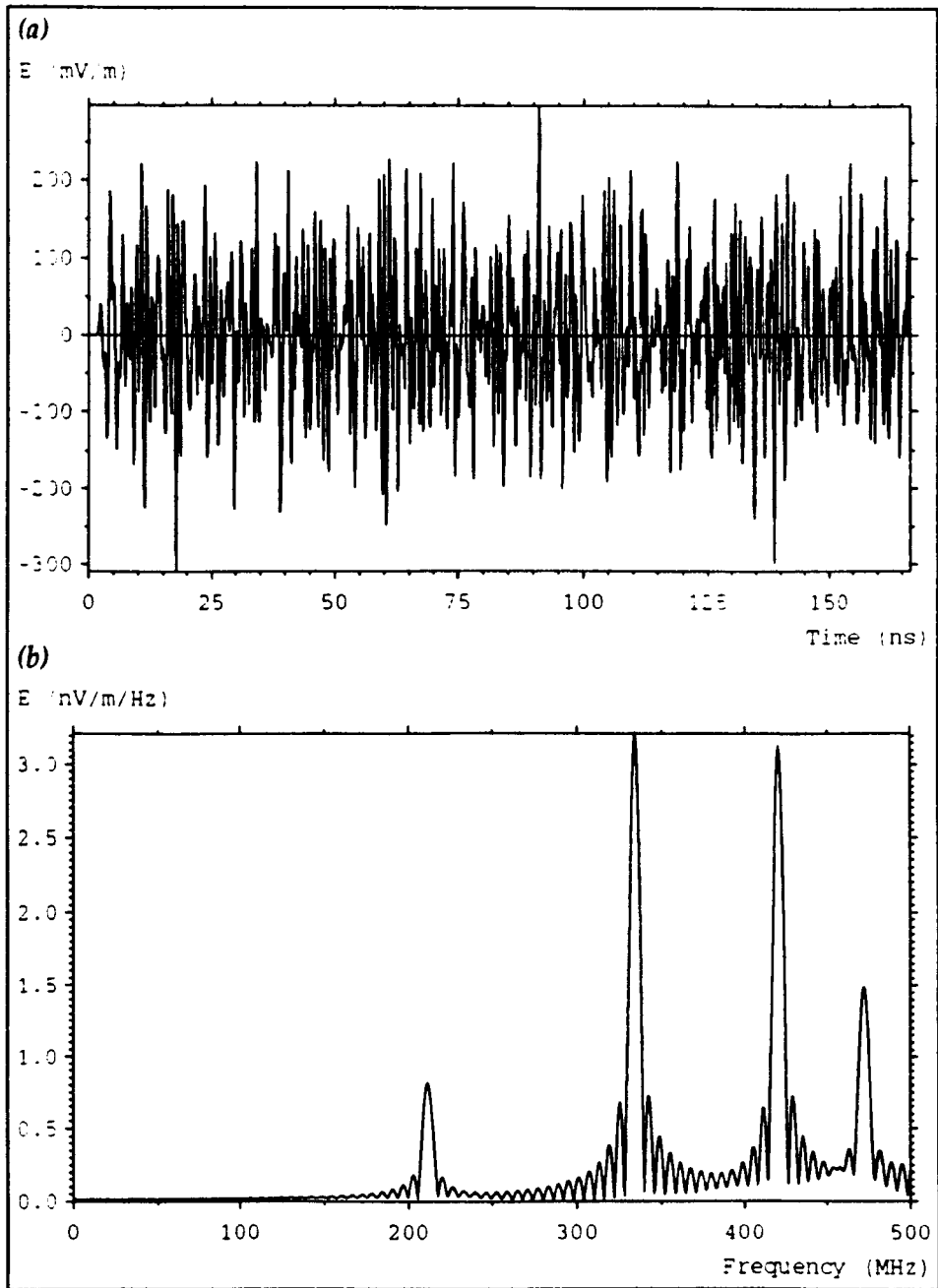


Fig. 3.1 –  $1\text{m}^3$  cavity (a) time domain (b) frequency domain

To predict resonant frequencies, the DFT is taken over the frequency range of interest with a frequency step of  $\Delta f$ . This frequency step must be sufficiently small so that the point of maximum amplitude on the *sinc* curve can be obtained. For example, the 3 dB point occurs when  $x \approx 1.392$  requiring that, at worst, the frequency step is selected such that

$$\Delta f < \frac{1.392}{\pi N \Delta t}$$

If the node spacing is 4 cm and 4000 iterations are performed then  $\Delta f$  must be smaller than 1.66 MHz. However, a much smaller frequency step was typically used, for example,  $\Delta f = 0.5$  MHz, giving a maximum error of 0.26 dB. Another problem which can arise is that of resolving closely spaced resonances. It can be shown [34] that, for two peaks of equal magnitude, the upper bound on the magnitude of the error,  $f_{err}$ , of a resonance, due to truncation is

$$f_{err} = \frac{3}{\Delta F \Delta t^2 N^2 \pi^2}$$

where  $\Delta F$  is the difference in frequency between the desired resonance and the neighbouring resonance <sup>1</sup>. If a long simulation time is used then the window function is a narrow feature in the frequency domain and hence does not cause significant interference between adjacent peaks. However, if the window function is narrow then the frequency step must be small in order to accurately predict the point of maximum amplitude.

The DFT is only one technique which can be used to transform data into the frequency domain. Recently, Prony's method has been used and it has been possible to reduce the number of iterations required by an order of magnitude [35,36]. In this technique, the signal is approximated by a superposition of damped sinusoids and it is the frequencies of these sinusoids which are obtained. There are also a large number of digital filtering and modern spectral estimation techniques which can be employed [37]. Although these techniques undoubtedly give good results, experience is required to make best use of them, for example, in the choice of model order.

### 3.2 Windowing

If the time domain signal has a significant high frequency content, which does not decay with time, then the DFT will produce very poor results. Features of this are a significant *sinc* presence and a noise level which is highly dependant on the number of iterations. This problem may be reduced by applying a standard single-sided window function, such as the Bartlett (triangular) or Hanning (raised cosine) windows [33], rather than the implicit rectangular window. The window should be

---

<sup>1</sup> In [34] this equation is expressed in terms of the normalised frequency  $\hat{f}$ , where  $\hat{f} = f \Delta t$ .

single-sided since the data near  $t=0$  makes a significant contribution to the impulse response. The disadvantage of these windows is that any resonance peaks will be broadened and their amplitude reduced. A better solution is to only reduce the magnitude of the last  $n$  values, where  $n$  is much less than the number of iterations. The idea is to minimise the effect of the truncation whilst keeping as much data as possible unaffected.

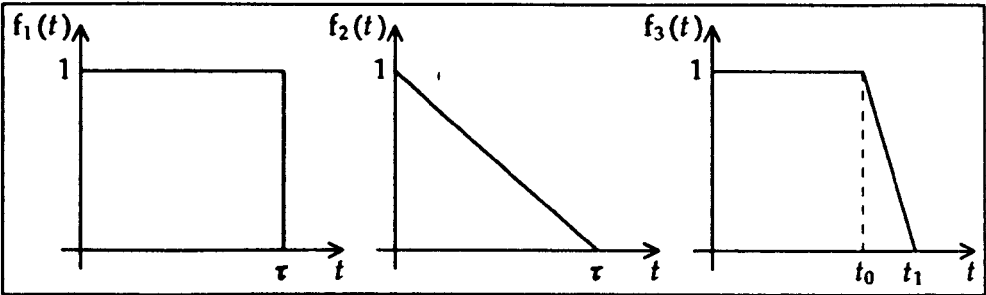


Fig. 3.2 – Window functions

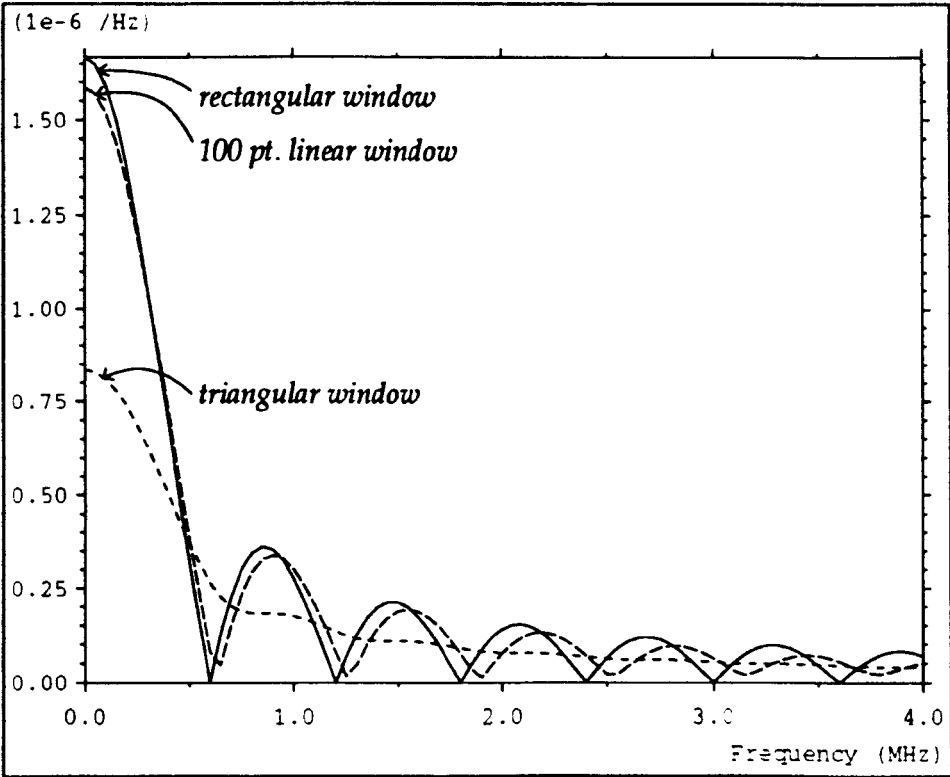


Fig. 3.3 – Frequency response of window functions

The time domain responses of rectangular, triangular and  $n$ -point linear (where  $n$  refers to the number of values reduced) window functions are shown in fig. 3.2 and expressions for the frequency domain response are given below <sup>2</sup>, in

<sup>2</sup> The expression for the rectangular window is the same as that given in §3.1 for  $W(f)$  although it is expressed in a slightly different form.



terms of  $\omega$  (where  $\omega = 2\pi f$ ) .

$$\text{Rectangular, } F_1(\omega) = \frac{2}{\omega} \sin\left(\frac{\omega \tau}{2}\right) \exp\left(-j \frac{\omega \tau}{2}\right)$$

$$\text{Triangular, } F_2(\omega) = \frac{4}{\omega^2 \tau} \sin^2\left(\frac{\omega \tau}{2}\right)$$

$$n\text{-point linear, } F_3(\omega) = \frac{4}{\omega^2 \tau} \sin^2\left(\frac{\omega \tau}{2}\right) \exp(-j \omega t_0) + \frac{2}{\omega} \sin\left(\frac{\omega t_0}{2}\right) \exp\left(-j \frac{\omega t_0}{2}\right)$$

where, for the last expression,  $\tau = t_1 - t_0$ . The frequency characteristics are shown in fig. 3.3 for the case when the windows are applied to a data set consisting of 1000 unit pulses with a timestep of 1.67 ns ( $\Delta l = 1$  m in 3-dimensions). The curve for a particular window will be superimposed on any impulse functions in the required frequency response and will also be introduced, although to a lesser extent, by any other sharp features. It can be seen that, for the  $n$ -point linear window, the value at d.c. is much greater than for the triangular window. This means that the reduction in amplitude of any resonances will be small. However, the *sinc* presence is also more significant. It may be necessary to adopt a trial and error procedure to determine the optimum window width. Two examples will now be considered to show how  $n$ -point linear windows can be successfully applied.

#### Example 1 - electrically small excitation

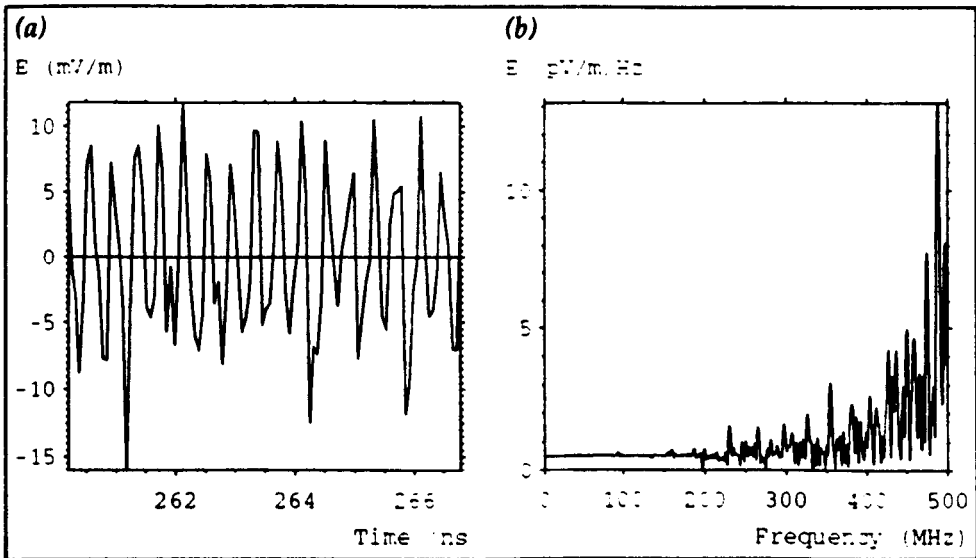
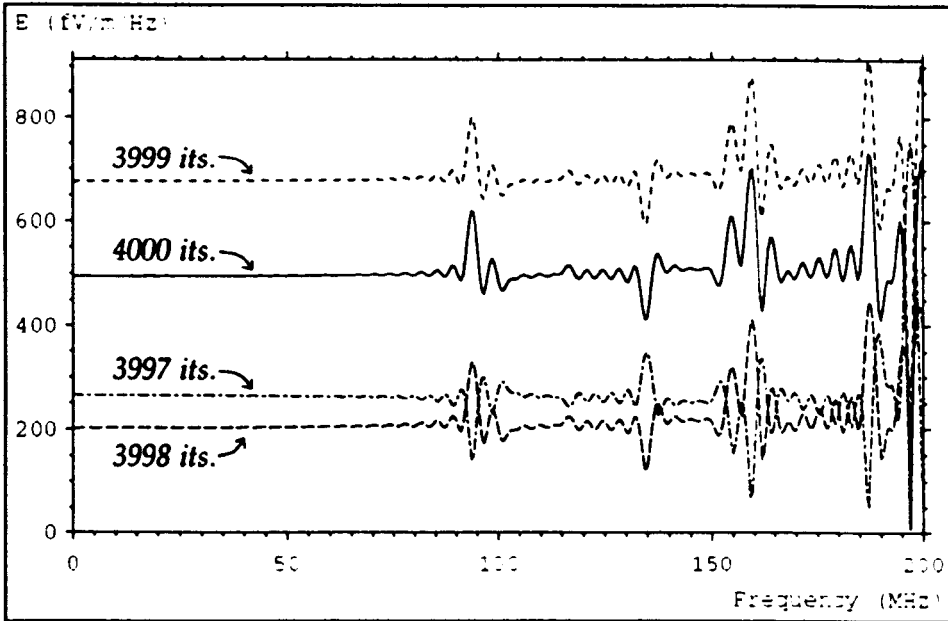
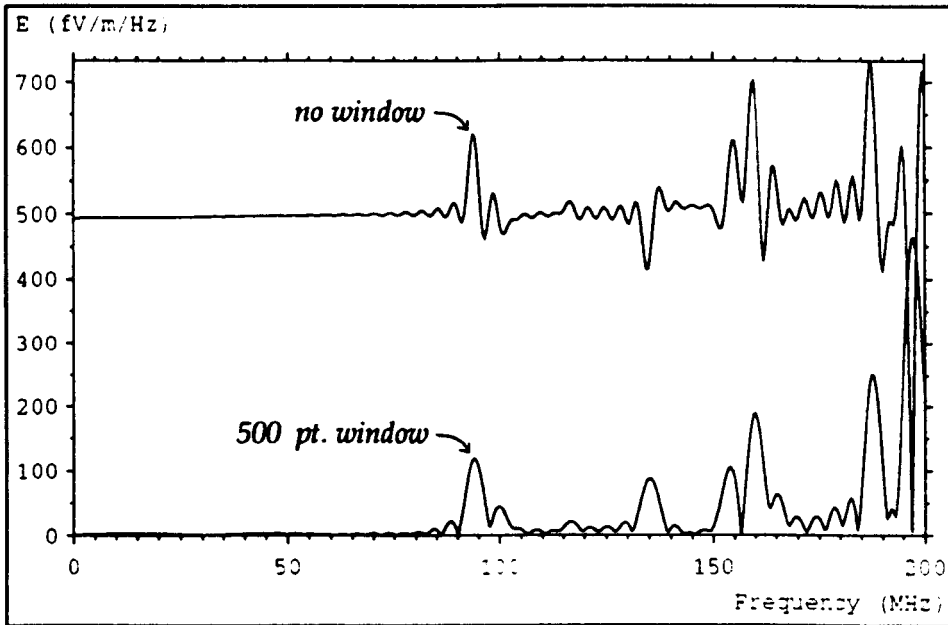


Fig. 3.4 – (a) last 100 iterations (b) frequency response



**Fig. 3.5 – Effect of changing number of iterations**



**Fig. 3.6 – Effect of 500 point single-sided linear window**

This data was obtained from an undamped screened room simulation, excited by an electrically small source. The small size of the source means that most energy is injected at high frequencies. The last 100 time domain values are shown in fig. 3.4a and the frequency response obtained from 4000 iterations is shown in fig. 3.4b. It is found that the noise level, observable in the range 0→200 MHz is highly dependant on the number of iterations and some resonance peaks are inverted. Fig. 3.5 shows the frequency response over this frequency range when the number of

iterations is varied from 3997 to 4000. The problem arises because the value at each successive time point is large compared to the running sums used in the DFT, so that the addition of one more value causes a significant change. Fig. 3.6 shows the effect of a 500 point single-sided linear window. The noise level has effectively been removed and the resonances are all maxima. In addition, the same curve is obtained if the number of iterations is changed slightly.

**Example 2 - output taken close to impulse excitation**

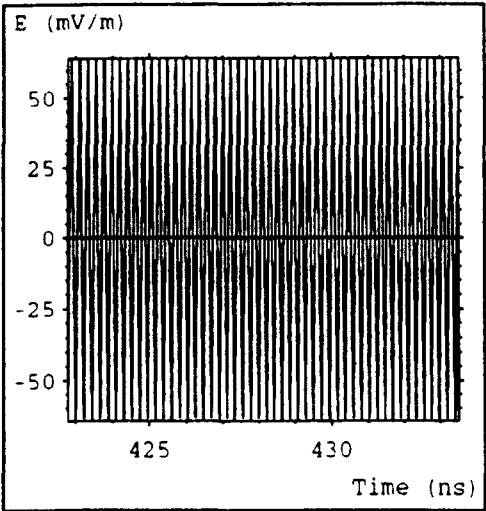


*Fig. 3.7 – Last 100 iterations*

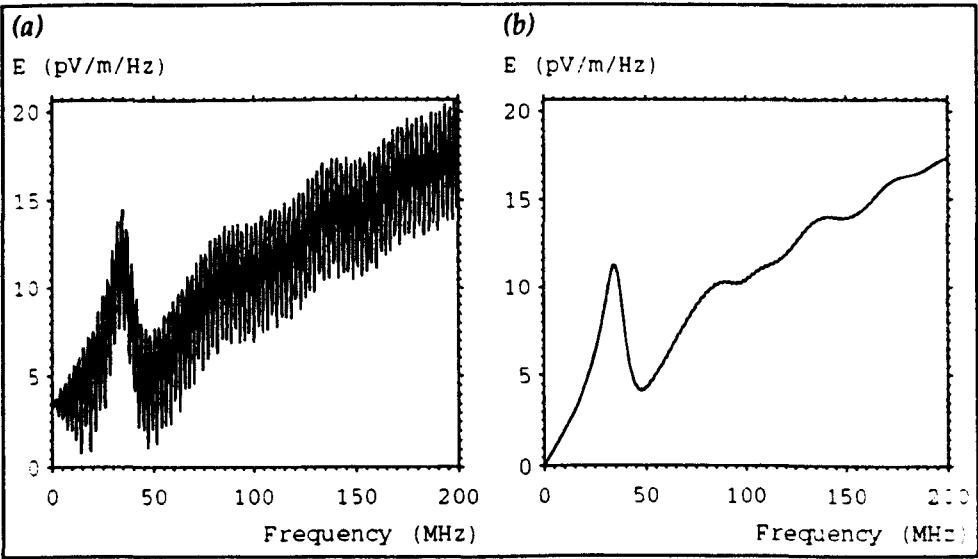


*Fig. 3.8 – Effect of 50-point single-sided linear window*

This data was obtained from a damped screened room simulation in which the output was taken coincident with the impulse excitation. The last 100 time domain values (out of 4000) are shown in fig. 3.7. The output takes large positive

and negative values on alternate iterations which do not decay with time, despite the presence of losses in the system. This phenomenon is often observed near to an impulse excitation. The frequency of the oscillation is much greater than the maximum working frequency of the mesh (and is therefore of no interest) and it decays within the space of a few nodes. However, in the frequency domain, the required signal is masked by *sinc* presence, as shown in fig. 3.8a. The effect of a 50 point single-sided linear window is shown in fig. 3.8b.

### 3.3 Convolution

An impulse excitation is generally used to introduce energy into a system. The response to any other waveform, for example, the double exponential pulse used for electromagnetic pulse (EMP) studies [38], can be obtained by convolution. Convolution can also be used to apply filtering operations (see §3.4).

In discrete form, the convolution process can be written as

$$\begin{aligned} y[n] &= x[n] * f[n] \\ &= \sum_{i=0}^{N-1} x[i] f[n-i] \end{aligned}$$

where  $x[n]$  is the TLM output data, which is non-zero in the interval  $0 \leq n \leq N-1$ , and  $f[n]$  is the sampled convolution function. If  $f[n]$  is non-zero for all values of  $n$  then  $y[n]$  is also non-zero for all  $n$ . If  $f[n]$  decays for large  $n$ , and can be considered as zero for  $|n| > N_0$  (where  $N_0$  is a constant) then  $y[n]$  need only be calculated in the interval  $-N_0 \leq n \leq N_0 + N - 1$ .

As an example, if  $f[n] = \cos(2\pi f n \Delta t)$  for  $-\infty < n < \infty$ , then  $y[n]$  is a harmonic wave of amplitude  $x / \Delta t$  where  $x$  is the amplitude obtained from the DFT. This follows from the interpretation of the DFT as the convolution of the input signal and the response of a notch filter. The amplitude must be divided by  $\Delta t$  because a multiplying factor of  $\Delta t$  was included in the DFT and this is not present in the convolution<sup>3</sup>.

<sup>3</sup> The inclusion of the  $\Delta t$  factor in the DFT means that if the same system is modelled with a different resolution (and hence with a different timestep), the same values will be output from the DFT (neglecting any change due to the improved accuracy of the model).

Convolution is generally more computationally intensive than the DFT. If  $f[n]$  is an analytical function which is computationally expensive (e.g. contains sines or cosines) then it may be advantageous to store values of  $f[n]$  rather than evaluate each value several times. Note, however, that the time taken to perform a convolution will generally be much smaller than the time taken for the TLM simulation.

### 3.4 Ideal filters

An ideal filter allows the distortionless transmission of a certain band of frequencies and suppresses the remaining frequencies. Such a filter may be implemented by convolving the input signal with the filter impulse response. Note that these filters are non-causal i.e.  $f[n]$  is non-zero for  $n < 0$ . This does not present a problem if the complete time series is known before the convolution is applied (which will always be the case for a post-processing activity). If the filter is to be applied as the TLM calculation proceeds then an ideal filter can be closely realised at the cost of introducing a delay [39] but this requires storage for previous output values and this requirement may be excessive.

The impulse response of a low pass filter is

$$f[n] = 2f_1 \Delta t \operatorname{sinc}(2\pi f_1 n \Delta t)$$

where  $f_1$  is the bandwidth. The impulse response of a band pass filter is

$$f[n] = 2f_1 \Delta t \operatorname{sinc}(\pi f_1 n \Delta t) \cos(2\pi f_2 n \Delta t)$$

where  $f_1$  is the bandwidth and  $f_2$  is the centre frequency. If the bandwidth is narrow, then care must be taken to allow the filter transients to decay. As a general rule, for a low pass filter, choose

$$\begin{aligned} 2\pi f_1 N_0 \Delta t &> 100 \\ \Rightarrow N_0 &> \frac{100}{2\pi f_1 \Delta t} \end{aligned}$$

where  $N_0$  is defined in §3.3. However, a value of 50 may be adequate in many cases and this limit can be relaxed further if the time series decays significantly before truncation. Inclusion of transients is particularly important if the data is subsequently transformed into the frequency domain.

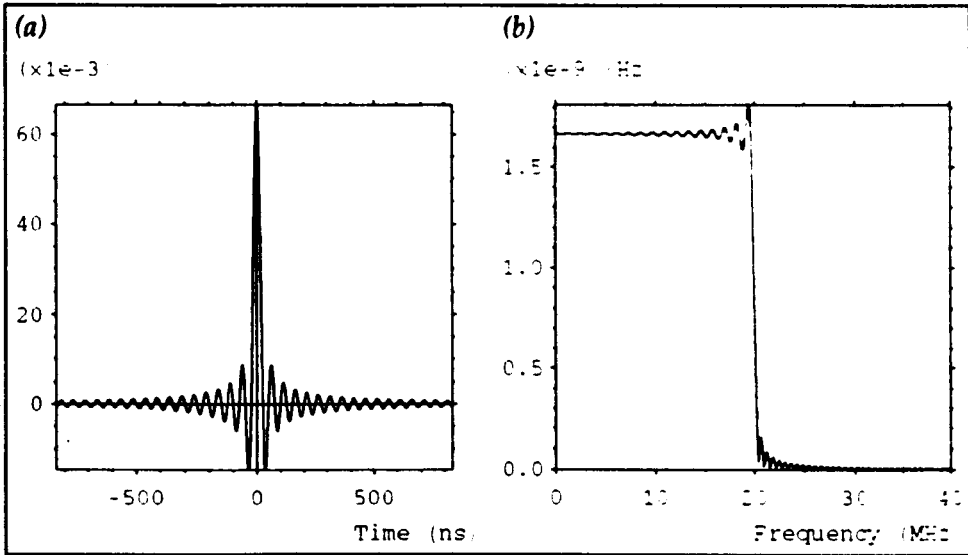


**Fig. 3.9 – Low pass filter (a) time domain (b) frequency domain**

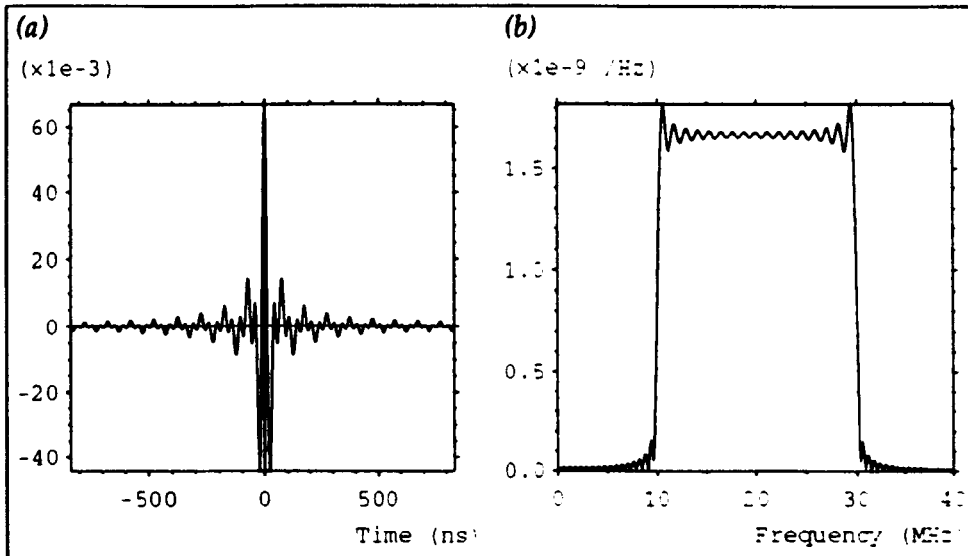


**Fig. 3.10 – Band pass filter (a) time domain (b) frequency domain**

The time and frequency responses of ideal low pass and band pass filters are shown in figs. 3.9 and 3.10 for the case when the input data is a single unit pulse of duration 1.67 ns and a total of 1001 time domain values have been output. For the low pass filter, the effect of not allowing transients to decay sufficiently is shown in fig. 3.11a, for the case when 201 points have been used, and the effect of omitting negative time is shown in fig. 3.11b. In the first case, the cutoff is less sharp and the *sinc* oscillation is more significant and in the second case, the response is completely wrong.

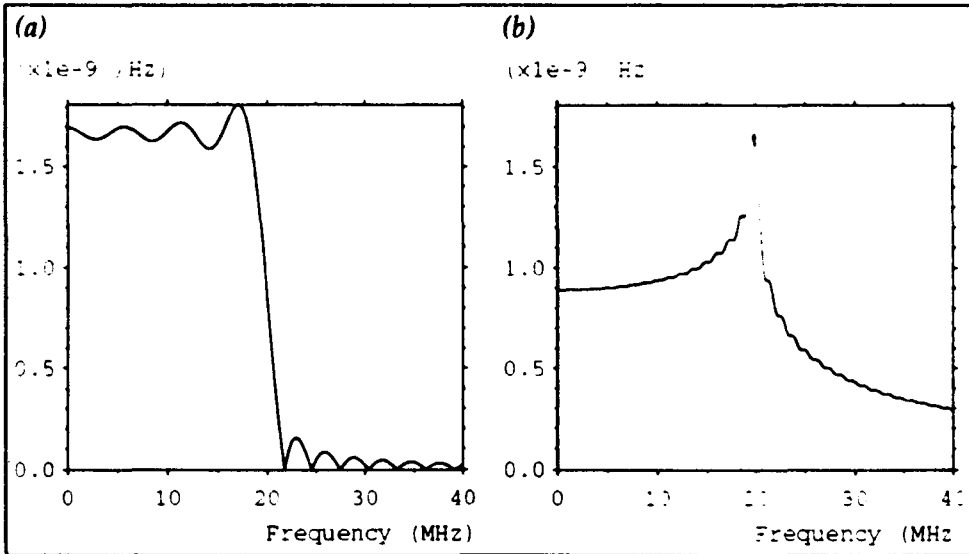


Fig. 3.11 – Low pass filter (a) severe truncation (b) omission of negative time

An ideal low pass filter cannot be used to solve the problems highlighted in §3.2. In such situations, the time domain output from the filter contains large transients at the end (and possibly also at the beginning) of the original data window, and the output from the DFT is exactly the same (within the pass band) as if no filter was applied.

### 3.5 Moving average filters

If a low pass filter of large bandwidth is required, and the maximum frequency of interest is much less than the bandwidth, then a moving average filter may be conveniently employed. The moving average filter is simple to implement and is computationally inexpensive.

The autoregressive form of an  $N$ -point moving average filter is given by

$$y[n] = y[n-1] + \frac{1}{N}(x[n] - x[n-N])$$

The transfer function is

$$H(z) = \frac{1}{N} \left( \frac{1 - z^{-N}}{1 - z^{-1}} \right)$$

where  $z = e^{s\Delta t}$ . The frequency response is

$$|H(e^{j\omega\Delta t})| = \frac{\sin\left(\frac{N\omega\Delta t}{2}\right)}{N \sin\left(\frac{\omega\Delta t}{2}\right)}$$

The disadvantage of the moving average filter is that there is no sharp cutoff and significant attenuation can occur, within the frequency range of interest, for large  $N$ . However, a two or four point moving average can be used, as an alternative to a window function, to remove high frequency oscillation introduced into the mesh by an impulse excitation, as for example 2 in §3.2. When the problem is at a slightly lower frequency, as for example 1, a larger value of  $N$  is required and this causes problems with attenuation; in this case, the windowing method is the most appropriate.

The frequency responses of two and four point moving average filters are shown in fig 3.12, for input data consisting of a single pulse of duration 1.67 ns.

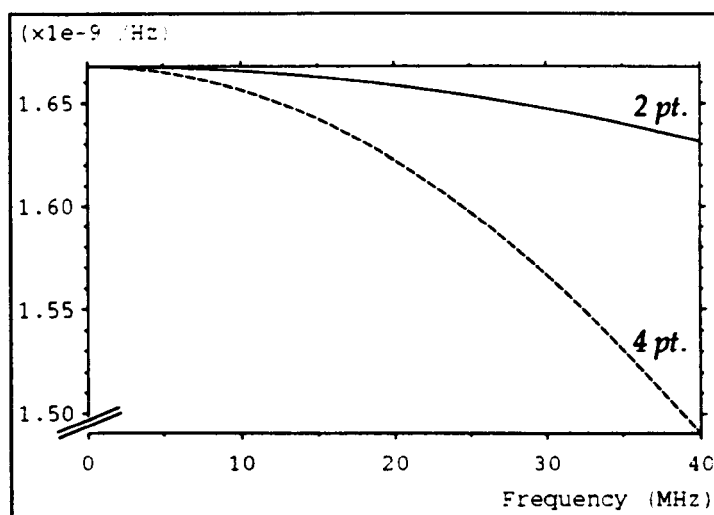


*Fig. 3.12 – Frequency response of 2 and 4-point moving average filters*



# Chapter 4

## Features of the TLM Method

### 4.1 Continuous excitation

An impulse excitation introduces energy at frequencies well above the accepted maximum working frequency of the mesh. This is unimportant in many cases but there are situations in which this high frequency energy causes problems and an alternative excitation waveform must be used. Such waveforms may be readily applied by means of voltage or current sources placed at the mid-point of link-lines, as described in §2.7.3.

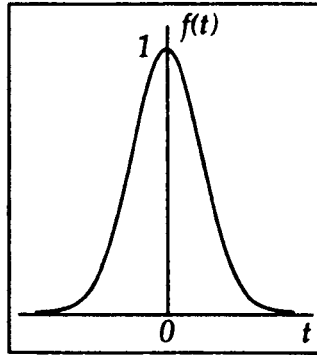


*Fig. 4.1 – Gaussian pulse*

One of the most useful excitation waveforms is the Gaussian pulse, shown in fig. 4.1. The time and frequency characteristics are given, respectively, by

$$f(t) = \exp\left(-\frac{t^2}{2\sigma^2}\right)$$

and  $F(\omega) = \sigma\sqrt{2\pi} \exp\left(-\frac{\omega^2\sigma^2}{2}\right)$

where  $\sigma$  is the standard deviation. In discrete form,  $f(t)$  can be written as

$$f[n] = \exp\left(-\frac{n^2}{2s^2}\right)$$

where the standard deviation is given in terms of the timestep, such that  $\sigma = s\Delta t$ . This function must be offset by  $n_0$  iterations so that the negative tail of the pulse is not significantly truncated. If the value of  $f[-n_0]$  is to be  $10^{-7}$  (which is less than the accuracy of single precision real numbers) then

$$n_0 > s\sqrt{-2\ln 10^{-7}}$$

$$\Rightarrow n_0 \geq 5.7 s$$

The standard deviation is chosen so that a significant signal is injected at the highest frequency of interest and this signal falls off rapidly as the frequency is increased further. A lower limit may be imposed so that the energy at the frequency  $f_{max}$ , corresponding to a wavelength of  $2 \Delta l$  is negligible.

$$f_{max} = \frac{c}{\lambda} = \frac{c}{2 \Delta l}$$

writing  $\Delta l = 2c \Delta t$  gives

$$f_{max} = \frac{1}{4 \Delta t}$$

If the value of  $F(\omega)$  at  $\omega = 2\pi f_{max}$  is to be  $10^{-7}$  then

$$s \geq \frac{2}{\pi} \sqrt{-2 \ln 10^{-7}}$$

$$\Rightarrow s \geq 3.7$$

For most of the work in this thesis, where the highest frequency of interest was less than that corresponding to a wavelength of  $10 \Delta l$ , a standard deviation of  $10 \Delta t$  with an offset of 60 iterations was found to be convenient. For example, if the timestep is 1.67 ns ( $\Delta l=1m$ ) then the amplitude is reduced by half at 11 MHz and is essentially zero above 50 MHz. The time and frequency characteristics of several Gaussian pulses, with different standard deviations, are shown in fig. 4.2. It would be possible to normalise the pulse so that the d.c. level is independent of the standard deviation. It is, however, more useful to normalise the data in the frequency domain to give a flat response over the frequency range of interest.

Gaussian pulse excitation is widely used in the finite-difference time-domain method to prevent instability caused by high frequency energy [40]. In TLM, for the range of systems considered, it has been found that effectively the same result is obtained for a Gaussian pulse excitation as for an impulse excitation (over the frequency range of interest) provided that suitable signal processing (e.g. windowing) is used in the latter case. However, it is obviously better to avoid introducing high frequency energy in the first place, particularly with single precision real numbers when the required signal is masked by high frequency oscillation.

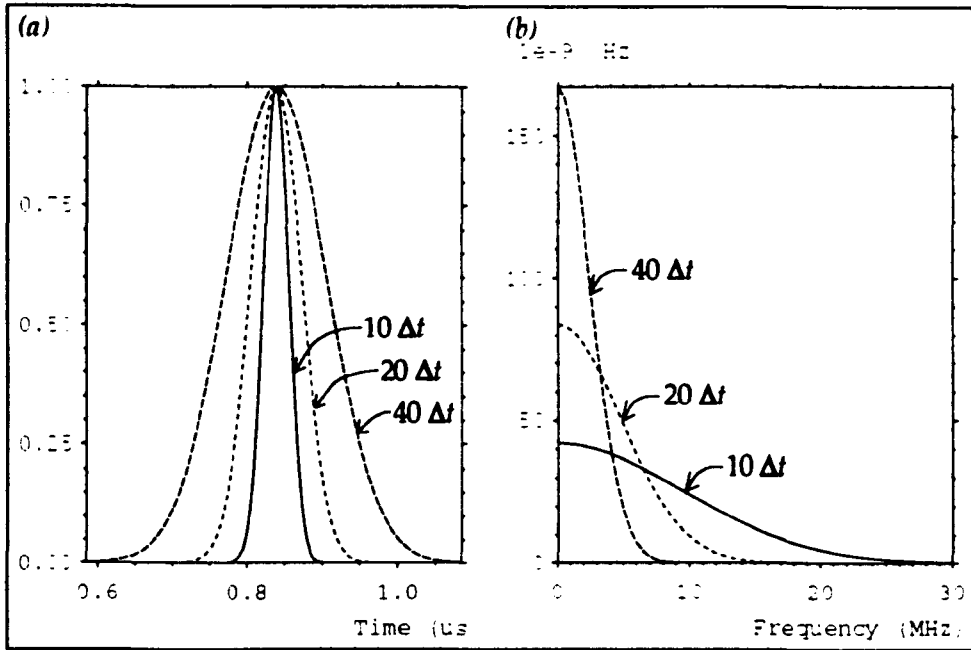


Fig. 4.2 – Characteristics of Gaussian pulses (a) time domain (b) frequency domain

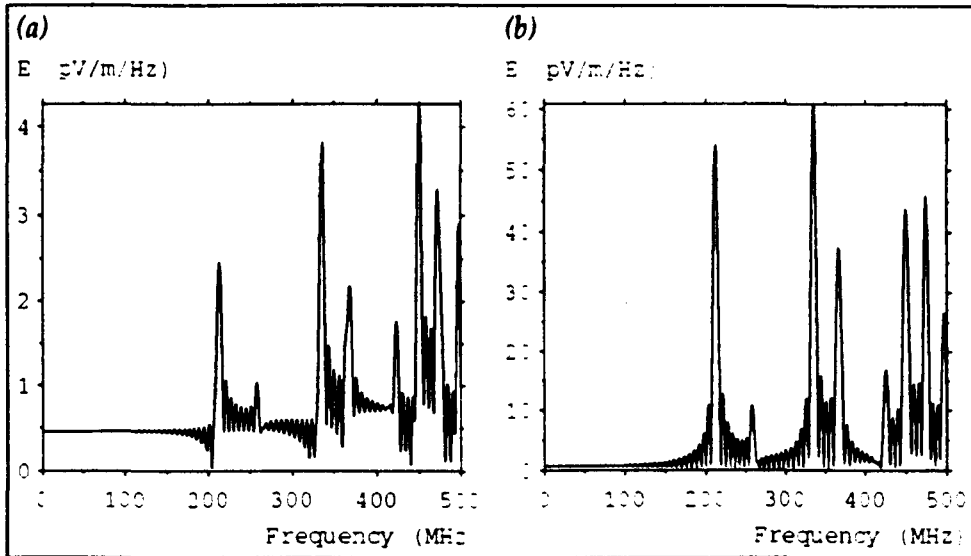


Fig. 4.3 – Exciting with (a) impulse (b) Gaussian pulse

### Example

This data was obtained from a  $1\text{m}^3$  cavity with  $\Delta l=2.5\text{cm}$ , excited by two voltage sources in series. Fig. 4.3a shows the electric field at the output point, transformed into the frequency domain, when an impulse excitation is used. Fig. 4.3b shows the same output point when a  $10 \Delta t$  Gaussian pulse is used. Note the reduction in amplitude caused by the tail-off of the frequency response of the Gaussian pulse. The noise level in the first case can be removed by applying a 500 point single-sided linear window before the DFT but this is not necessary in the

second case.

## 4.2 Steady-state solution

TLM is generally used to perform transient analysis. It is however possible to obtain the steady-state solution to many problems directly. This can be done at d.c. by introducing an arbitrary excitation and then waiting for the transients to decay or it may be done at a particular frequency by injecting a continuous sinusoidal signal. The fact that the steady-state solution can be found in this way is of no practical benefit unless it is known that the transients decay rapidly. In particular, care must be taken to ensure that the excitation does not introduce a high frequency oscillation which decays slowly.

### 4.2.1 Solution at d.c.

If losses are present in the system then the steady-state solution will be obtained after the transients have decayed. Losses may be introduced into a lossless system by replacing any short-circuit boundaries with resistive boundaries since both will form an equipotential surface in the steady-state. Care must be taken if outputs are taken prematurely because the electric field will not be normal to the boundary if there is any current flow. Boundaries which are not to become an equipotential must be modelled by open-circuits [41]. To obtain the same solution using transient analysis, the real part of the DFT at d.c. is calculated from the time domain data; this is equivalent to taking a time average of all the data.

#### Example

Consider, in 2-dimensions, a point charge placed inside a square conduit. This was modelled using the SCN with open-circuit boundaries defining a plane of  $10 \times 10$  nodes, surrounded by matched boundaries. The system was excited with an impulse electric field extending from the bottom boundary to the centre of the mesh. Fig. 4.4 shows the two electric field components at a point near the charge, for the first 1000 iterations. As the calculation proceeds, the electric field settles to a constant value and the magnetic field decays to zero. Fig. 4.5 shows the steady-state solution, where the arrows show the magnitude and direction of the field. The same solution may be obtained by using the DFT except that the magnitude will be

greater by a factor of  $N \Delta t$  where  $N$  is the number of iterations. In this case, fewer iterations are required and the technique will also work for lossless systems.

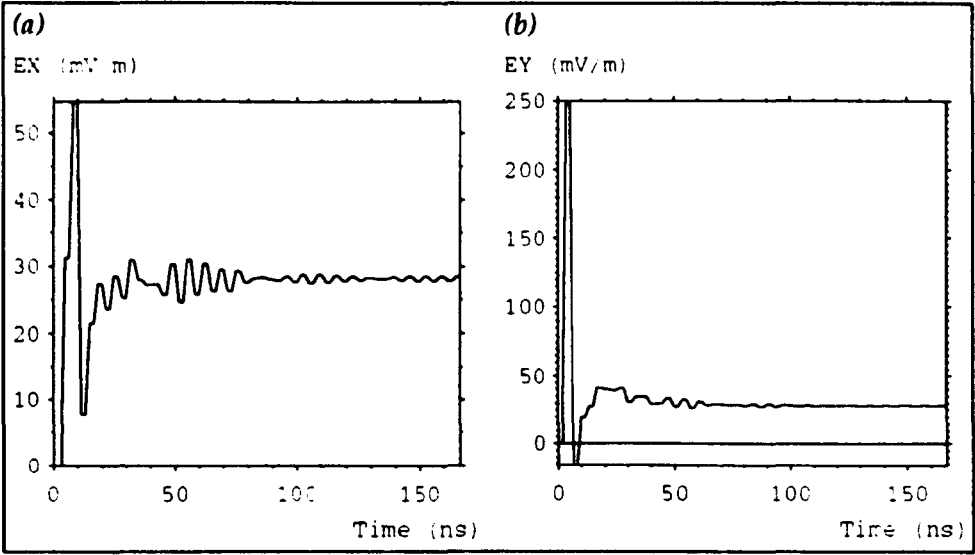


*Fig. 4.4 – Electric field at a point near the charge*

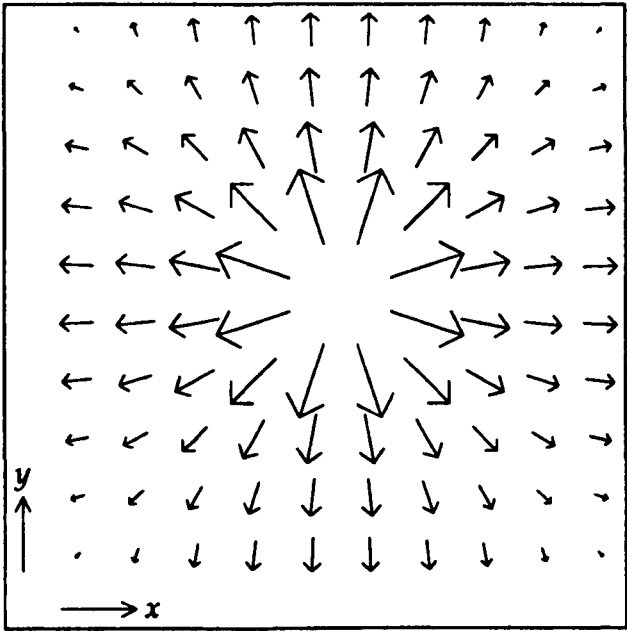


*Fig. 4.5 – Electric field in the steady-state*

### 4.2.2 Solution above d.c.

The steady-state solution at a particular frequency is obtained by injecting a sinusoidal signal of the required frequency. However, the energy introduced into the mesh will not be restricted to a single frequency since the excitation cannot exist for  $t < 0$ . It is therefore necessary to let the calculation proceed for a number of iterations to allow the transients to decay. To obtain the same solution by transient

analysis, the DFT is taken at the required frequency. The complex data output from the DFT can be converted into magnitude data or the phase information can be used to obtain the output at a particular time.

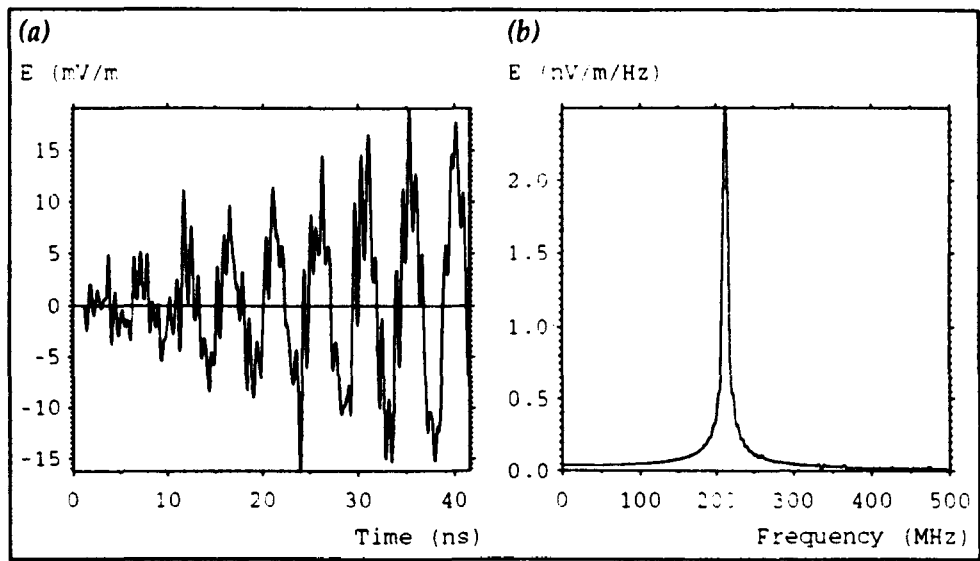


Fig. 4.6 – Sinusoidal excitation (a) time domain (b) frequency domain

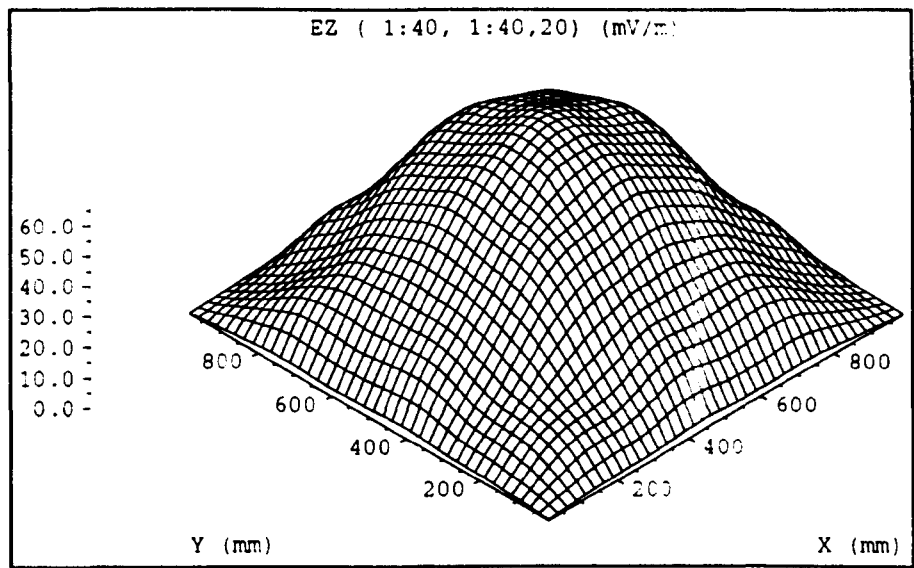


Fig. 4.7 – Field profile on iteration 3902

**Example**

For the  $1\text{m}^3$  cavity used for the example in §4.1, a 212 MHz sinusoidal source was used to excite the first resonance (the  $\text{TE}_{110}$  mode). The first 500 iterations are shown in fig. 4.6a and the frequency response obtained from 4000 iterations is shown in fig. 4.6b. There are no losses in the system so the amplitude increases with the number of iterations. The magnitudes of the other resonances are insignificant

compared to the main resonance. The field profile at a field maximum (obtained on iteration 3902) is shown in fig. 4.7. The overall shape is as expected but undulations are apparent. If the DFT is used to obtain the field profile after the same number of iterations then no undulations are observed since the DFT effectively averages the data over the whole calculation. If the system is excited off-resonance then the field at the excitation frequency is concentrated around the source and at points away from the source the actual resonances can be observed.

### 4.3 Field at nodes and on link-lines

In general, as far as the magnitude of the field is concerned, there is found to be very little difference between taking the field at a node and taking the field on a link-line, for both excitation and output purposes. Fields at a node are less prone to high frequency oscillations but fields on link-lines should be used if the energy stored in the field is to be considered (see §4.4).

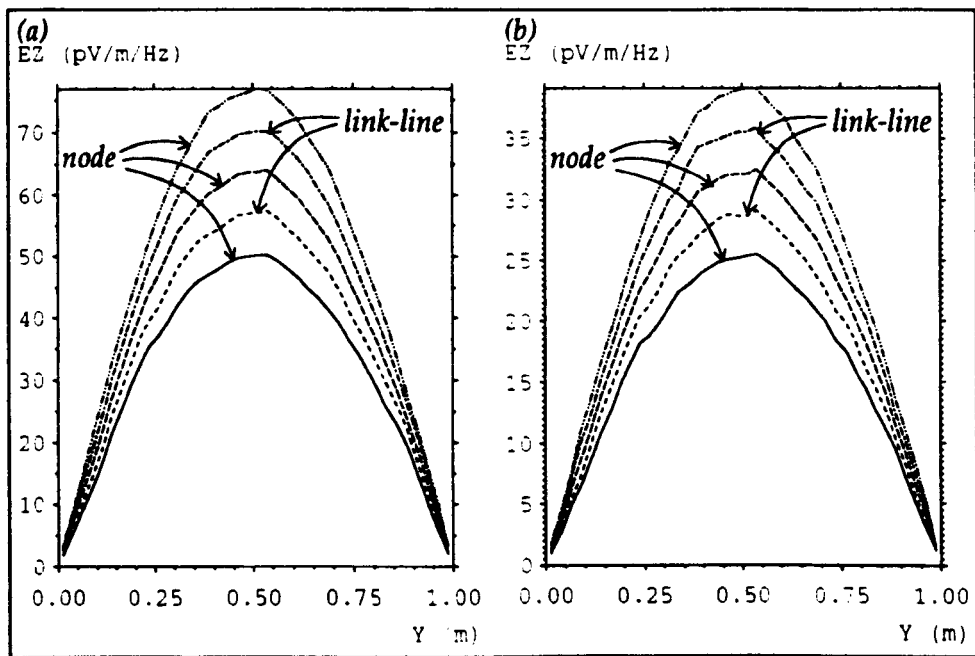


Fig. 4.8 – Field profile for (a) node excitation (b) link-line excitation

#### Example 1

This data was obtained from a 1m<sup>3</sup> cavity, with  $\Delta l=2.5\text{cm}$ , excited by an impulse electric field, polarised in the z-direction, extending along a line parallel to the z-axis, between two walls. Fig. 4.8a shows a cross-section of the field profile, taken along the y-axis, at points taken alternately on nodes and link-lines parallel to

the x-axis. The curves show the expected field variation, which increases when the output points approach the centre of the cavity <sup>1</sup>. Fig. 4.8b shows the corresponding curves when a set of link-lines parallel to the x-axis are excited. The curves are essentially the same apart from a scaling factor. Note that the field is equally valid on link-lines parallel to the y-axis, even though they were not explicitly excited.

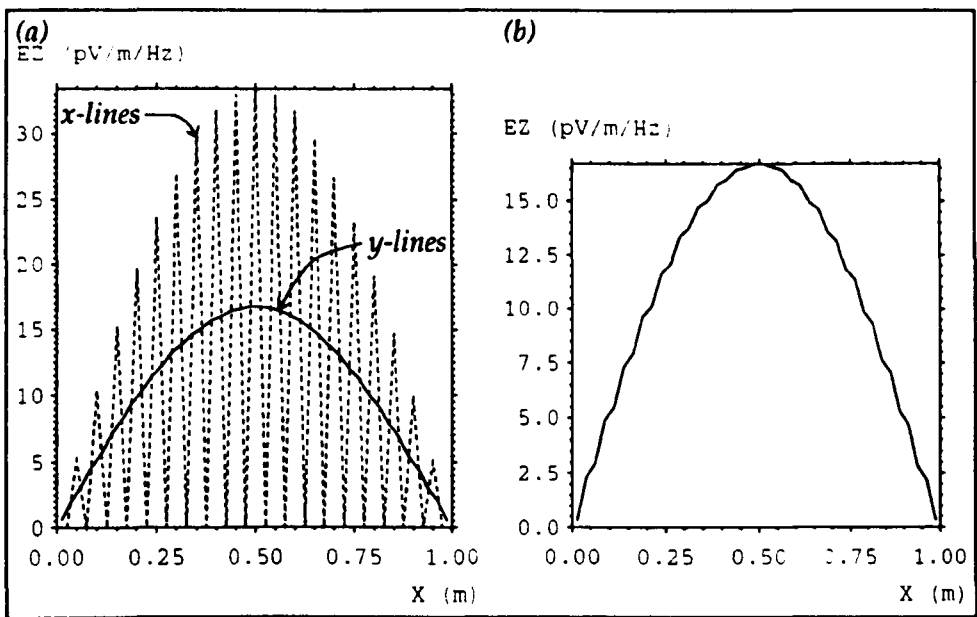


Fig. 4.9 – Single source (a) link-line outputs (b) node output

### Example 2

This example highlights the problems which can occur when the system is excited on link-lines. The data was obtained for the same system as for example 1, but it was excited by a single Gaussian voltage source, on a link-line parallel to the x-axis. The same problem arises if an impulse excitation is used. It is found that the voltage pulses introduced into the mesh cancel so that there are no pulses on alternate link-lines parallel to the source link-line, along a line passing through the source. The problem is reduced away from this line but it is still significant. Fig. 4.9a shows a cross-section of the field profile for link-lines parallel to both the x and y-axes. The field obtained from nodes is approximately correct but oscillates slightly, as shown in fig. 4.9b. It is therefore important not to use a single source to excite a system unless the output is taken on orthogonal link-lines or at nodes and the oscillation is considered acceptable. This problem does not arise for excitation at

<sup>1</sup> A degree of asymmetry is apparent resulting from the off-centre excitation. This asymmetry varies as the number of iterations is changed, but the error is small and can be usually be neglected. The asymmetry can be removed by applying a suitable window function before the DFT.



a single node nor if the length of the source is increased to an even number of nodes. In practice it is important to test a particular excitation rather than assuming that it will work as expected.

## 4.4 Energy considerations

The fact that the field at a node can be considered as an average of the field on the appropriate link-lines has important implications when calculating the energy stored in a system. This is due to the fact that, when several quantities are considered, the sum of the squares is not equal to the square of the sum. Values of energy calculated from fields at a node will, in general, be very different to those calculated from fields on link-lines, even though the magnitudes of the fields are similar.

Consider a single link-line, with voltage pulses  $V_1$  and  $V_2$  (these may be incident or reflected pulses). The electric and magnetic fields are given by

$$E = -\frac{1}{\Delta l}(V_1 + V_2) \quad \text{and} \quad H = \pm \frac{1}{Z_0 \Delta l}(V_1 - V_2)$$

The electric and magnetic energy densities  $w_e$  and  $w_m$  are given, respectively, by

$$w_e = \frac{1}{2} \epsilon E^2 = \frac{\epsilon}{2 \Delta l^2} (V_1 + V_2)^2$$

$$\text{and } w_m = \frac{1}{2} \mu H^2 = \frac{\mu}{2 Z_0^2 \Delta l^2} (V_1 - V_2)^2$$

The total energy density,  $w$ , is given by

$$w = w_e + w_m$$

writing  $\epsilon = 1 / c Z_0$  and  $\mu = Z_0 / c$  gives

$$\begin{aligned} w &= \frac{1}{2 c Z_0 \Delta l^2} [(V_1 + V_2)^2 + (V_1 - V_2)^2] \\ &= \frac{1}{c Z_0 \Delta l^2} (V_1^2 + V_2^2) \end{aligned}$$

The stored energy, calculated from fields on link-lines is therefore proportional to the total energy of the individual voltage pulses and, because the scattering matrix is unitary, the stored energy will be the same on successive iterations, provided that no losses are present. This condition is not met if the energy is calculated from

fields on nodes. However, at low frequencies, where the field variation is small, similar results may be obtained from both link-line and node outputs.

### Example

Consider an unbounded mesh <sup>2</sup> excited by an impulse electric field on a single node. Fig. 4.10 shows the energy stored in the electric and magnetic fields calculated from link-lines and from nodes <sup>3</sup>. It is apparent that for the link-lines, the same energy is stored in the magnetic field as in the electric field and the energy remains constant. For the nodes, the energy is lower than it should be and it varies with time.

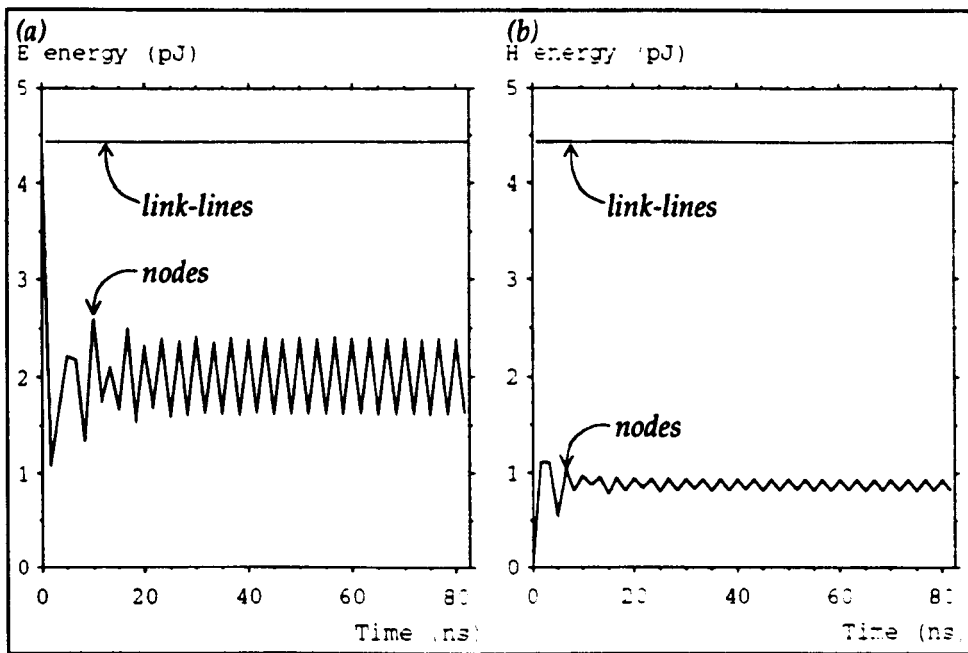


Fig. 4.10 – Stored energy (a) electric (b) magnetic

## 4.5 Modelling with stubs

Stubs are added to the node so that regions of increased permittivity or permeability and non-cubic nodes can be modelled. The effect of stubs can be conveniently studied by reducing the background permittivity and permeability below unity and then adding stubs to model free-space conditions <sup>4</sup>. An alternative

<sup>2</sup> An unbounded mesh is implemented by using a very large mesh with the number of iterations limited so that reflections from the edge do not occur.

<sup>3</sup> Problems with single precision numbers on some machines can cause a steady increase in energy with time.

<sup>4</sup> This technique has also found practical application in the modelling of wires where it is used to provide a local reduction in permittivity and permeability around the wire [42].

interpretation, which is more useful when considering the hybrid node and graded meshes, is to consider reducing the timestep below its maximum value.

### 4.5.1 Dispersion

The addition of stubs to the node inevitably introduces additional dispersion. This is because the stubs only act to reduce the speed of the bulk wave; some energy will always arrive too soon and some will arrive too late. In a cavity, dispersion will alter the observed resonant frequencies.

#### Example

This data was obtained from a  $1\text{m}^3$  cavity, modelled with a  $10\times 10\times 10$  node mesh. The table below shows the frequencies of the first three resonances, obtained when the background permittivity and permeability are reduced below unity, for both the stub-loaded and hybrid nodes. The total simulation time has been kept constant in both cases.

	iterations	TE <sub>110</sub> (MHz)		TE <sub>210</sub> (MHz)		TE <sub>220</sub> (MHz)	
		stub.	hybrid	stub.	hybrid	stub.	hybrid
analytical	–	212.0		335.2		424.0	
$\epsilon_r=1, \mu_r=1$	1000	211.5		334.5		420.5	
$\epsilon_r=0.5, \mu_r=0.5$	2000	212.5	212.5	334.5	337.5	425.5	425.5
$\epsilon_r=0.1, \mu_r=0.1$	10000	213.5	212.5	336.5	337.5	435.5	427.0
$\epsilon_r=0.05, \mu_r=0.05$	20000	213.5	212.5	344.0	337.5	437.0	427.0

For background relative permittivity and permeability of 0.5, the results are more accurate but when these values are reduced further, higher frequencies are obtained. The results for the hybrid node are better than those for the stub-loaded node. Note, however, that at ten nodes per wavelength, the frequency is 300 MHz and any errors below this frequency are small.

## 4.5.2 Excitation

When the electric field at a node is excited there is a choice, for both the stub-loaded and hybrid nodes, as to whether a voltage pulse is introduced into the open-circuit stub. If the background permittivity and permeability are not too low, for example 0.5, then very little difference is observed but any differences increase as these values are reduced further.

### Example

This data was obtained from a large mesh, with matched boundaries, in which the excitation was applied along a line ten nodes in length. The node spacing was 10 cm. Outputs were taken at the centre of the excitation and at a point away from the excitation. The ratio between the output obtained with background values of  $\epsilon_r = 0.1$ ,  $\mu_r = 0.1$  and the output obtained with unit background values was then taken over the interval 0→500 MHz.

Fig. 4.11 shows the results obtained with the stub-loaded node when the excitation is applied to the four link-lines only. The ratio is approximately unity at d.c. but falls off slightly as the frequency is increased. Fig. 4.12 shows the results when equal excitation pulses are applied to the four link-lines and the stub. The second output is similar to the previous case but the output coincident with the excitation is erroneous. These results suggest that, for the stub-loaded node, it is better not to excite the stub.

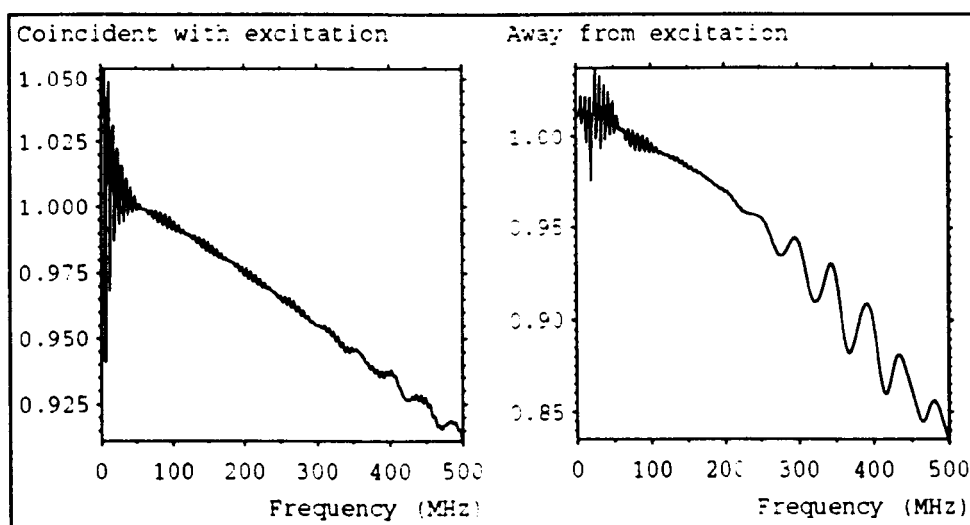


*Fig. 4.11 – Stub-loaded node, excite link-lines only*

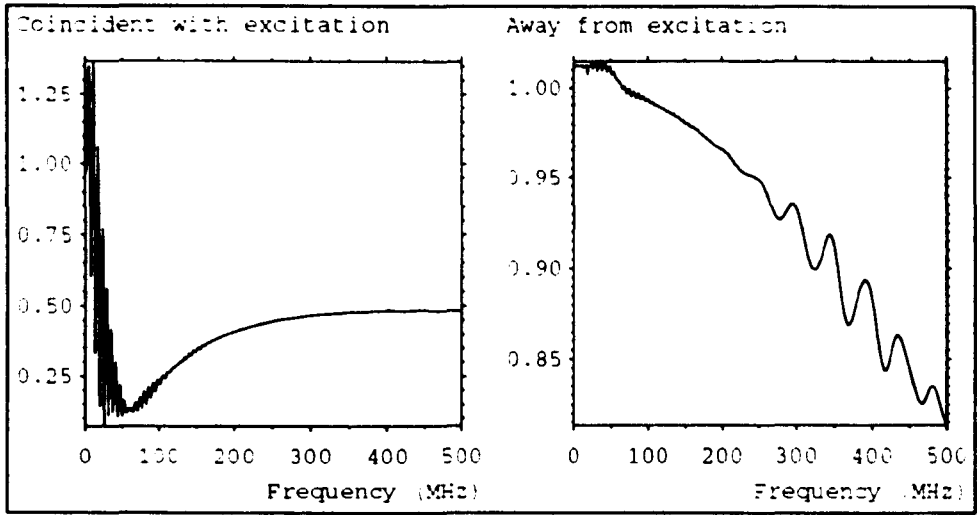


**Fig. 4.12 – Stub-loaded node, excite link-lines and stub**

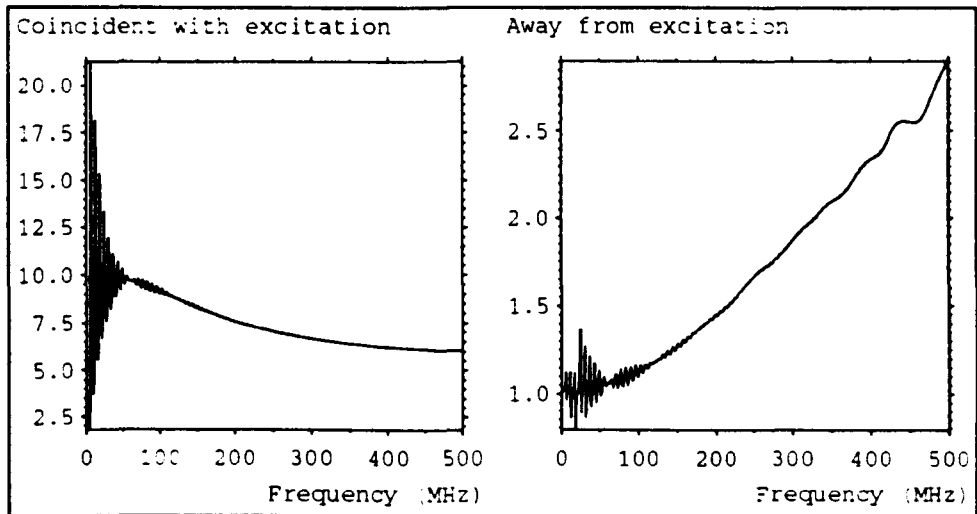


**Fig. 4.13 – Hybrid node, excite link-lines only**

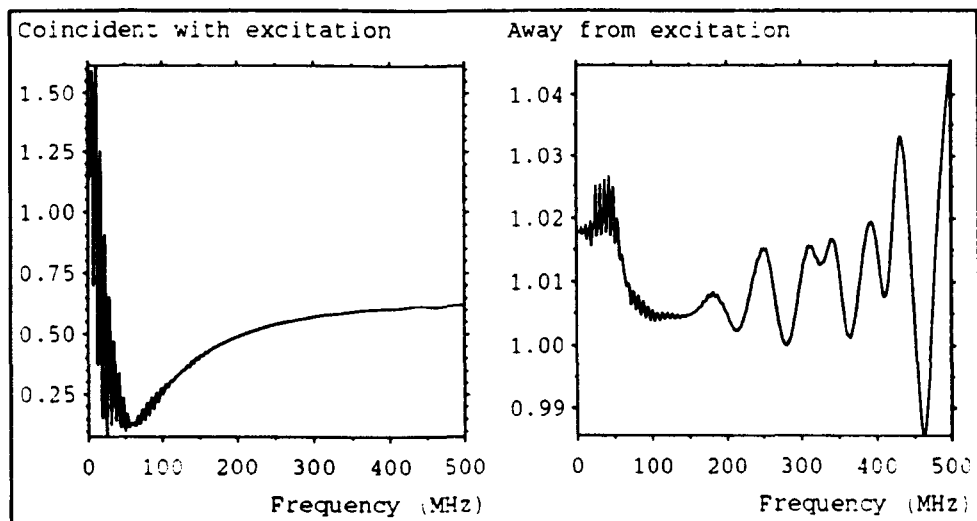


**Fig. 4.14 – Hybrid node, excite link-lines and stub**

Fig. 4.13 shows the results obtained with the hybrid node when the excitation is applied to the four link-lines only. The first output is ten times too large at d.c. and the second output, although correct at d.c., increases dramatically as the frequency is increased. Fig. 4.14 shows the results when equal pulses are applied to the link-lines and the stub. Both curves are similar to the corresponding curves for the stub-loaded node. These results suggest that, for the hybrid node, it may be more appropriate to excite the stub.

It should be noted that, in all cases, the excitation calculation is consistent with the output calculation i.e. in the time domain, the first output value is equal to the applied field. Further work is needed to fully identify factors affecting excitation in the presence of stubs.

### 4.5.3 Outputs

Field quantities calculated on link-lines are consistent with those obtained on nodes even when stubs are added to the node, for both uniform and graded meshes.

#### Example 1 – uniform mesh

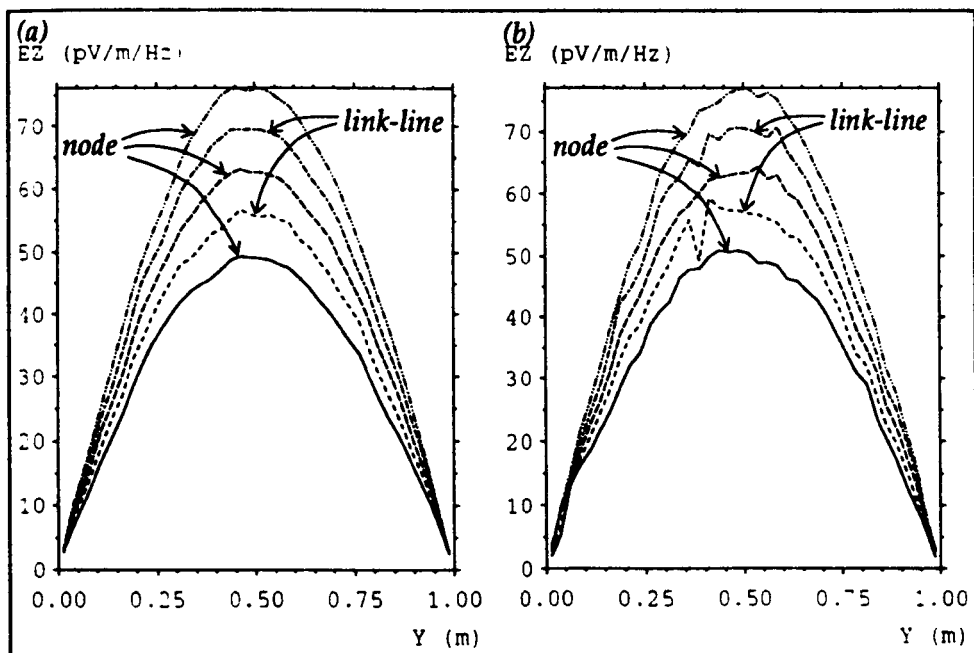


Fig. 4.15 – Field profile for (a) stub-loaded node (b) hybrid node

This data, which should be compared with example 1 in §4.3, was obtained from a  $1\text{m}^3$  cavity with  $\Delta l = 2.5\text{cm}$  and background values of  $\epsilon_r = 0.25$ ,  $\mu_r = 0.25$ . Fig.

4.15a shows a cross-section of the field profile at points taken alternately on nodes and link-lines. Fig. 4.15b shows the corresponding curves for the hybrid node. The curves can be made smooth by applying a suitable window.

### Example 2 – graded mesh

This data was obtained from a  $1\text{m}^3$  cavity in which the node spacing, along each axis, was set to be 10 nodes of 1 cm, 10 nodes of 2 cm, 10 nodes of 3 cm and 10 nodes of 4 cm. Fig. 4.16 shows the field profile of the first resonance after windowing. The expected field distribution is obtained even though the node spacing varied.

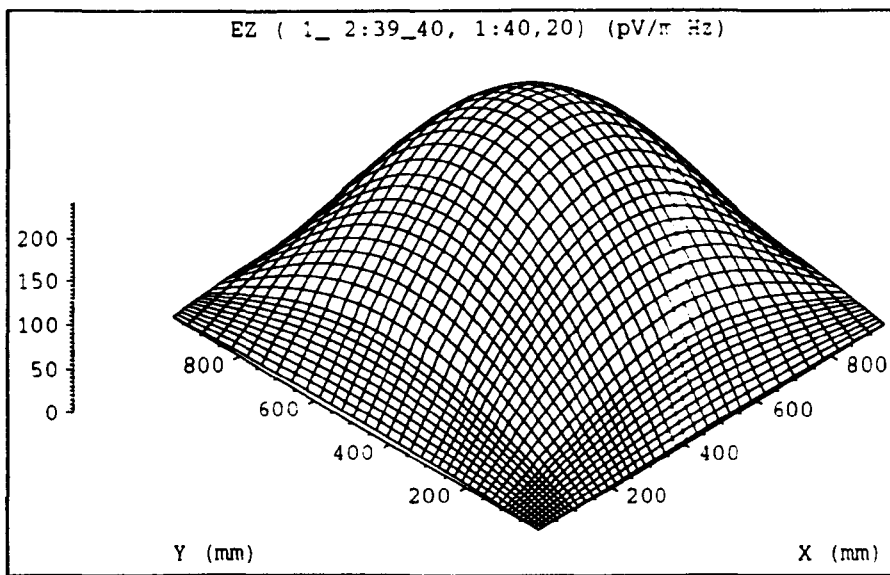


Fig. 4.16 – Field profile in graded mesh

## 4.6 Plane wave propagation

### 4.6.1 Wave travelling parallel to an axis

In the absence of stubs, a plane wave travelling parallel to one of the axes, subject to the appropriate boundary conditions, will propagate without dispersion. This is essentially a 1-dimensional problem, with boundary conditions shown schematically in fig. 4.17, for a  $y$ -polarised wave travelling in the  $x$ -direction. A unit pulse incident from the left will produce the scattered pulses shown in fig. 4.18a. The pulses incident on the node during the next iteration are then scattered to produce the single pulse shown in fig. 4.18b.

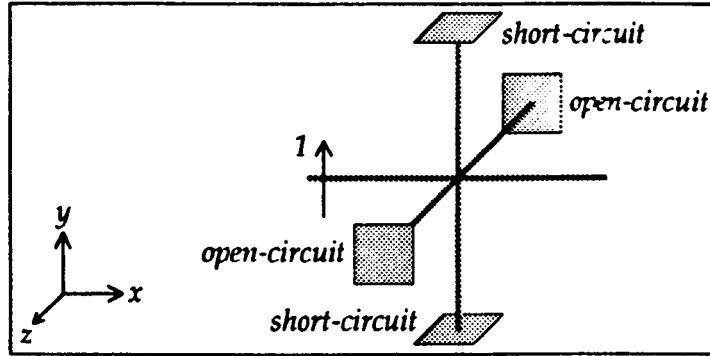


Fig. 4.17 – Boundary conditions for plane wave

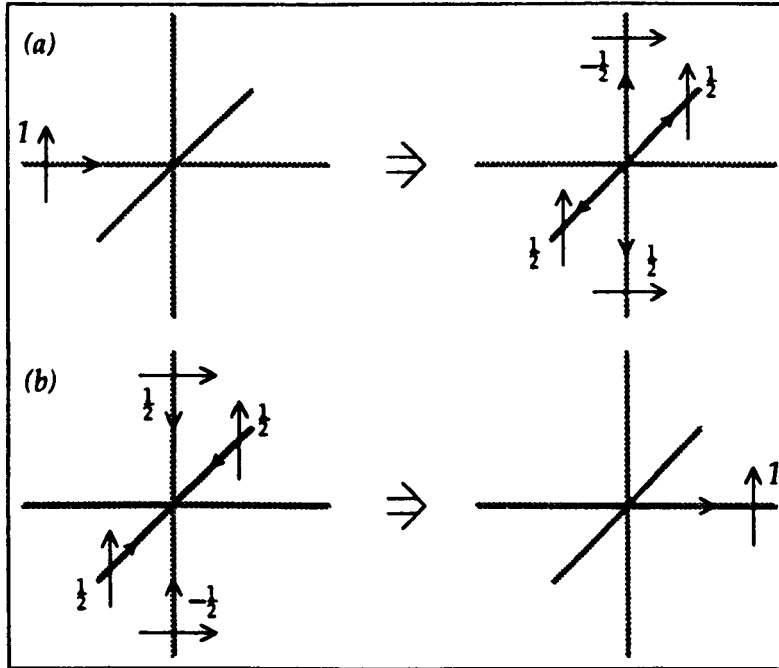


Fig. 4.18 – Propagation of a plane wave

If the wave is excited by applying an impulse electric field across a link-line, then a forward and backward travelling wave, each of duration  $\Delta t$ , will be produced. If required, the backward wave can be completely absorbed with a matched boundary, or, alternatively, only the forward travelling voltage pulse can be introduced. If the wave is excited by applying the field at a node, then a pulse of duration  $2\Delta t$  will be produced, as shown in fig. 4.19.

If the boundary conditions are not consistent with plane wave propagation then dispersion will occur. This is illustrated in fig. 4.20 for a  $10 \times 10$  impulse excitation placed in an unbounded mesh, after intervals of 10 and 20 iterations. The arrows show the directions of propagation of the wavefronts. Both the forward and backward waves are shown and, although some of the features in the centre of the



mesh will be due to remnants of the excitation, it is apparent that dispersion does occur.

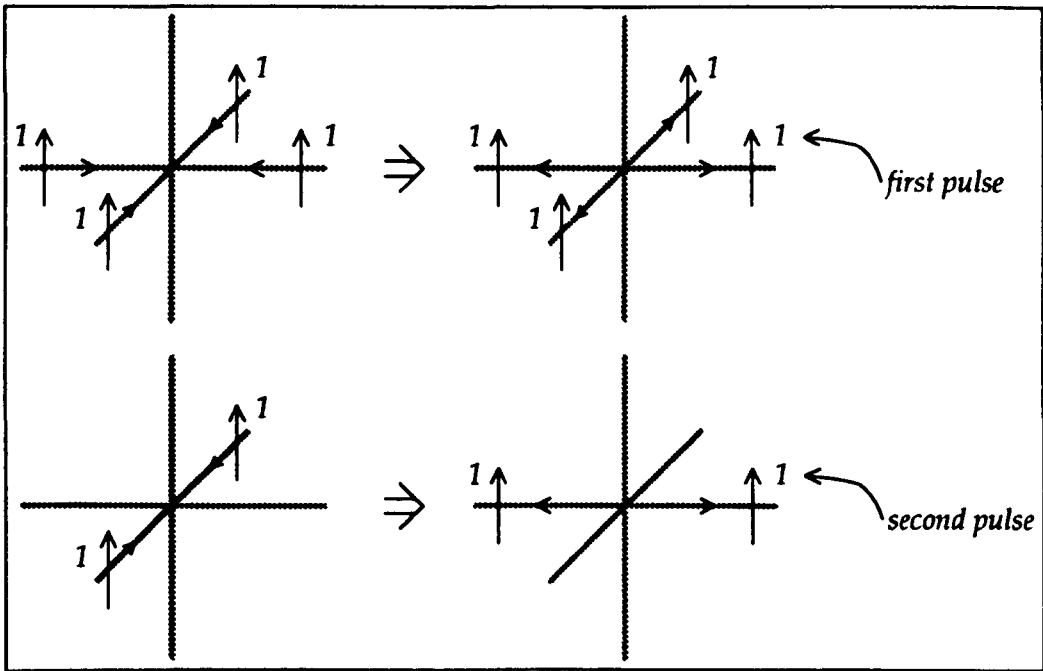


Fig. 4.19 – Propagation of a plane wave excited at a node

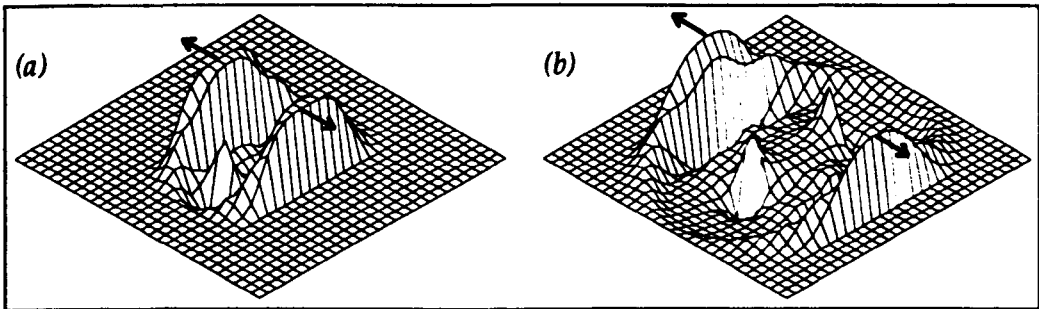


Fig. 4.20 – Plane wave dispersion

### 4.6.2 Wave travelling at an arbitrary angle

When a plane wave is propagating parallel to one of the axes, it is possible to place boundary conditions which will maintain the wave without dispersion. This cannot be done when the wave is travelling at an arbitrary angle and so such waves will be subject to increased dispersion. A 45° wave may be introduced by exciting two electric field components on a diagonal, as shown in fig. 4.21. Fig 4.22 shows a single field component, in an unbounded mesh, after 10 and 20 iterations. It is apparent that although the wavefront is at 45°, there is a lot of following noise. This may not be important if the data is subsequently transformed into the frequency

domain.

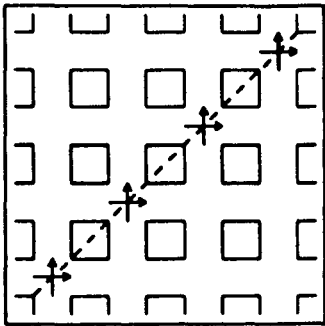


Fig. 4.21 – Excitation of a 45° wave

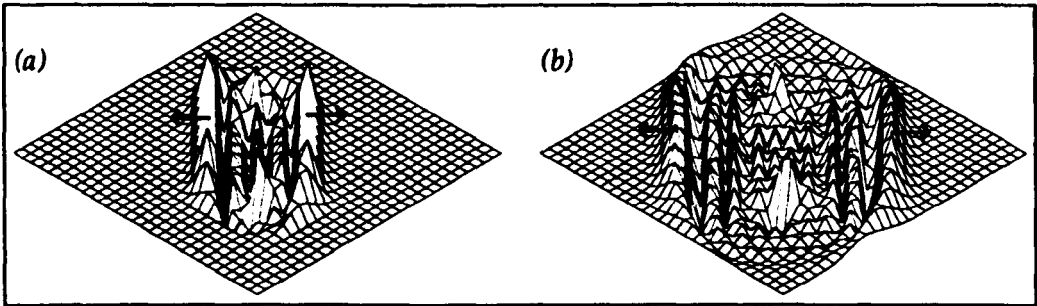


Fig. 4.22 – 45° plane wave dispersion

# Chapter 5

## Multigrid Method

### 5.1 Introduction

The multigrid technique has been developed to overcome the following limitations encountered when modelling EMC type systems with a uniform mesh:

- Regions in which fields vary rapidly (e.g. around a thin wire) require a fine spatial description but this can rarely be used throughout the entire problem space due to computer storage and run-time restrictions.
- Regions in which an accurate knowledge of the field is not necessary (e.g. the space near numerical boundaries in open boundary problems) must often be modelled with an excessively fine spatial description.

The traditional approach to this problem is to use a graded mesh, in which the shape of the nodes is distorted to give increased resolution in certain areas. The mesh is uniquely defined by specifying the node dimensions along each of the three coordinate axes and this is also applicable to orthogonal curvilinear coordinates [43]. This is a restricted case of a mesh formed in general curvilinear coordinates. The addition of stubs slows down the speed of propagation for the larger nodes so that time synchronism between voltage pulses is maintained. Both the stub-loaded and hybrid nodes can be used but the latter has been found to be more efficient and accurate [44].

In the multigrid technique, the principles of synchronism and connectivity are violated so that separate meshes of different spatial resolution can be connected together to form a complete system. At the interface between these meshes, there is an abrupt change in mesh size. This is to be contrasted with a graded mesh, in which the mesh size changes gradually. A feature of the graded mesh is that regions of fine spatial description cannot be completely localised from the rest of the problem space. For example, fig. 5.1a shows the grading which might be employed for describing the cross-section of two wires. Using the multigrid

method, separate fine mesh regions may be employed, embedded in a large coarse mesh, as shown in fig. 5.1b. The saving in storage requirement is obvious. In addition, there is a run-time saving to be made, especially if the coarse mesh operates at a slower speed. With the graded mesh, the same small timestep must be used throughout the problem space and this is dependant on the smallest node dimension.

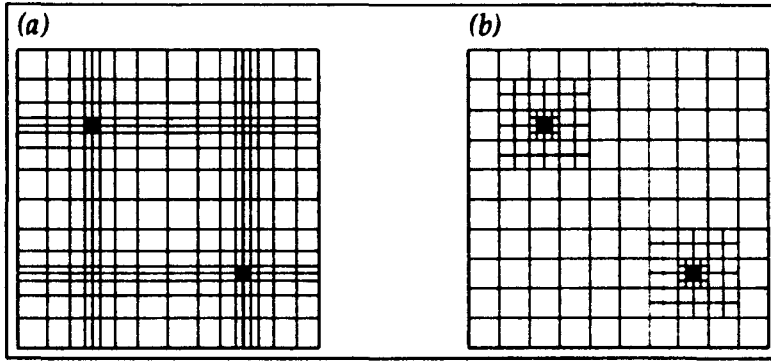


*Fig. 5.1 – Comparison of (a) grading and (b) multigrid method*

The multigrid method, as described here, is a restricted case of a more general method in which several grids, each in a different coordinate system, come together and overlap in an irregular fashion. Such systems have been used with finite difference schemes for modelling transonic flow around complex geometries [45].

Initial work on the multigrid technique used a 2-dimensional series connected mesh [46,47]. Once the basic concepts had been explored, all later work was done in 3-dimensions by adding additional code to a standard TLM program. This meant that use could be made of more flexible input and output options without a significant investment in program development. 2-dimensional systems could still be investigated by defining a plane of nodes with appropriate boundary conditions.

## 5.2 Diakoptics

The principles behind the multigrid method are similar to those used in the time domain diakoptic method developed by Johns and Akhtarzad [48,49,50] although the reasons for the development are subtly different. The diakoptic method was developed to overcome the following limitations:

- For systems containing large volumes of homogeneous material it is

necessary to iterate over these volumes for each separate system.

- Several systems in which there are only small differences must each be solved in their entirety.

The technique operates by splitting a network into sub-networks which are solved individually, to obtain the impulse response, and then subsequently connected together by convolution. This involves applying an impulse excitation to each of the severed link-lines and recording the outputs on all of these link-lines when they are terminated with a matched load. The idea was to build up a library of presolved blocks, describing standard geometries, and then connect them together to solve new geometries with minimum computational effort. The big disadvantage is the huge storage requirement needed to store the impulse response for each link-line on the surface of the block. Both space and time approximations must be made to reduce this requirement to acceptable limits and these approximations reduce the accuracy and hence the utility of the method. However, once it is accepted that such approximations must be made, this opens up the possibility of connecting sub-networks of differing mesh coarseness and timestep.

Space approximation may be effected by using a simple scheme such as interpolating between adjacent points or by fitting the amplitude of the pulses to a particular polynomial. Johns and Akhtarzad found, in tests on a rectangular waveguide, that quadratic approximation gave much better results than linear approximation [48]. However, the fact that pulses are changed to fit a polynomial means that conservation of power, in a loss free structure, cannot be guaranteed and it is possible that such approximations may cause the signal to fade away or build up to very large values over a large number of iterations.

Time approximation is effected by first filtering (to ensure that the signal is appropriately band-limited) and then re-sampling at the new sampling rate. The fact that sub-structures are completely solved before the connect process means that a non-causal filter, such as the ideal low-pass filter, can be employed.

In a practical system, it is necessary to truncate the sub-structure impulse response. Fortunately, this will decay with time even for a loss-less system due to the matched loads introduced onto the severed link-lines. Care has to be taken

when connecting sub-networks, during the convolution process, to avoid unnecessary truncation, which can lead to spurious results [50].

In the multigrid technique, the complete system can still be regarded as a number of sub-systems but these are solved simultaneously so that there is no significant storage overhead. Space and time approximations are made purely to connect regions of different node spacing and timestep.

## **5.3 Basic concepts**

### **5.3.1 Fine/coarse mesh interface**

The main decision to be made, when implementing the multigrid procedure, is the location of the interface between fine and coarse mesh regions. If the interface passes through the centre of nodes, then new scattering matrices must be devised and special account has to be taken of corner nodes. If the interface cuts across link-lines, then there is no change in scattering procedure and the entire surface of the interface can be treated in a consistent manner. In either case, the transfer of voltage pulses across the interface must be given careful consideration. Ideally, this transfer should be subject to the following constraints:

- charge conservation
- energy conservation
- no reflection
- zero delay

The first two items follow from the fact that, in an infinite mesh containing no features, the total charge carried by the voltage pulses (in one iteration) and the total energy remain constant. No reflection means that the interface appears transparent to the adjacent nodes and zero delay means that information from pulses incident upon the interface must be immediately transferred across. In addition, the interface must be seen to enforce continuity of fields. In a practical system, it will not be possible to meet all constraints exactly and approximations must be made.

### 5.3.2 Characteristic impedance in 2-dimensions

In the 2-dimensional case, it can be argued that the fine mesh link-lines should have half the characteristic impedance of the coarse mesh link-lines so that they model the same “depth”. For example, the characteristic impedance of a link-line parallel to the x-axis carrying a voltage pulse polarised in the y-direction is given by

$$Z_0 = \frac{\Delta y}{\Delta z} \sqrt{\frac{\mu}{\epsilon}}$$

In the coarse mesh,  $\Delta y = \Delta z = \Delta l$ , giving  $Z_0 = \sqrt{\frac{\mu}{\epsilon}}$ .

In the fine mesh,  $\Delta y = \frac{1}{2}\Delta l$ ,  $\Delta z = \Delta l$ , giving  $Z_0 = \frac{1}{2}\sqrt{\frac{\mu}{\epsilon}}$ .

This scaling can be introduced if required but it is really unnecessary as the effect cancels when field quantities are obtained. Indeed, it is perhaps physically more meaningful to regard the depth as irrelevant in a 2-dimensional system. This “problem” does not arise in 3-dimensions.

### 5.3.3 Charge and energy considerations

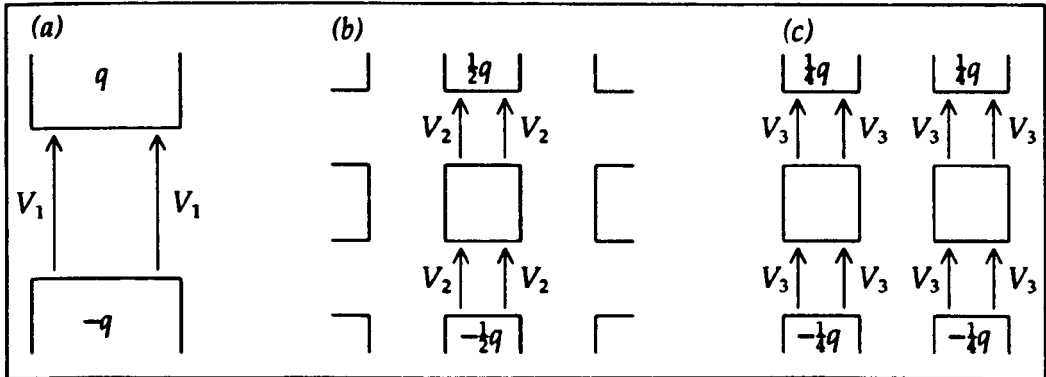


Fig. 5.2 – Placing charge in (a) coarse mesh (b) fine mesh (c) distributed in fine mesh

Care has to be taken when applying the concepts of charge and energy conservation in regions of different node spacing and/or timestep. For example, consider a 2-dimensional series mesh with node spacing  $\Delta l$ , timestep  $\Delta t$ <sup>1</sup> and link-line characteristic impedance  $Z_0$ . To place a charge  $q$ , two voltage pulses<sup>2</sup>, each of value  $V_1$ , must be introduced, as shown in fig. 5.2a, where

<sup>1</sup> For a 2-dimensional mesh,  $\Delta t = \Delta l / \sqrt{2} c$ .

<sup>2</sup> The system can be excited with a single pulse but two pulses ensure a symmetrical excitation.

$$V_1 = \frac{Z_0 c q}{\sqrt{2} \Delta l}$$

The total charge,  $Q_1$ , and energy,  $\mathcal{E}_1$ , introduced into the mesh are

$$Q_1 = 2 \frac{V_1}{Z_0} \Delta t = q$$

$$\mathcal{E}_1 = 2 \frac{V_1^2}{Z_0} \Delta t = \frac{Z_0 c q^2}{\sqrt{2} \Delta l}$$

If a mesh of twice the resolution is now used, with properties  $\frac{1}{2}\Delta l$ ,  $\frac{1}{2}\Delta t$  and  $Z_0$  then a charge of  $\frac{1}{2}q$  must be placed in order to model the equivalent system, so that the charge per unit length is the same. Four pulses, each of value  $V_2$ , must be introduced, as shown in fig. 5.2b.

$$V_2 = \frac{Z_0 c \left(\frac{q}{2}\right)}{\sqrt{2} \left(\frac{\Delta l}{2}\right)} = V_1$$

The total charge,  $Q_2$ , and energy,  $\mathcal{E}_2$ , are the same as before.

$$Q_2 = 4 \frac{V_2}{Z_0} \frac{\Delta t}{2} = Q_1$$

$$\mathcal{E}_2 = 4 \frac{V_2^2}{Z_0} \frac{\Delta t}{2} = \mathcal{E}_1$$

Alternatively, if the charge is to be distributed over a larger area, as shown in fig. 5.2c, in order to be more consistent with the coarse mesh model, then the total charge,  $Q_3$ , will be the same but the energy,  $\mathcal{E}_3$ , will be different.

$$V_3 = \frac{1}{2}V_1$$

$$Q_3 = Q_1$$

$$\mathcal{E}_3 = \frac{1}{2}\mathcal{E}_1$$

At the interface separating these two meshes it would therefore be appropriate to transfer the same charge but the energy needs further consideration. If the fine mesh is to model an equivalent system to the coarse mesh then charge should be distributed over the same area as in the coarse mesh so that the energy in the fine mesh is half that in the coarse mesh. Alternatively, if the greater resolution of the fine mesh is to be exploited then the charge should be placed in the smallest possible area and the energy in the fine mesh will be the same as that in the coarse mesh. In addition, for an ungraded system, it is not necessary to use the node



spacing when calculating field quantities (provided consistency is maintained between the excitation and output calculations) and this may also have to be taken into consideration.

In 3-dimensions, the same charge  $q$  must be placed in both the coarse and fine mesh models. In this case, the charge carried by the voltage pulses in the fine mesh is twice that carried by the pulses in the coarse mesh.

### 5.4 Initial attempts

The first approach considered is shown schematically in fig. 5.3, in which use is made of 3-port nodes shaped like a "T". It was felt, however, that the "T" nodes would introduce spurious reflections. Some work was done on 2-dimensional nodes with a double port, as shown in fig. 5.4, but no satisfactory results were obtained. The method adopted for all later work was to place the interface at the mid-point of link-lines. This approach is consistent with the diakoptic method described in §5.2 and is shown schematically in fig. 5.5, where each square represents a node.

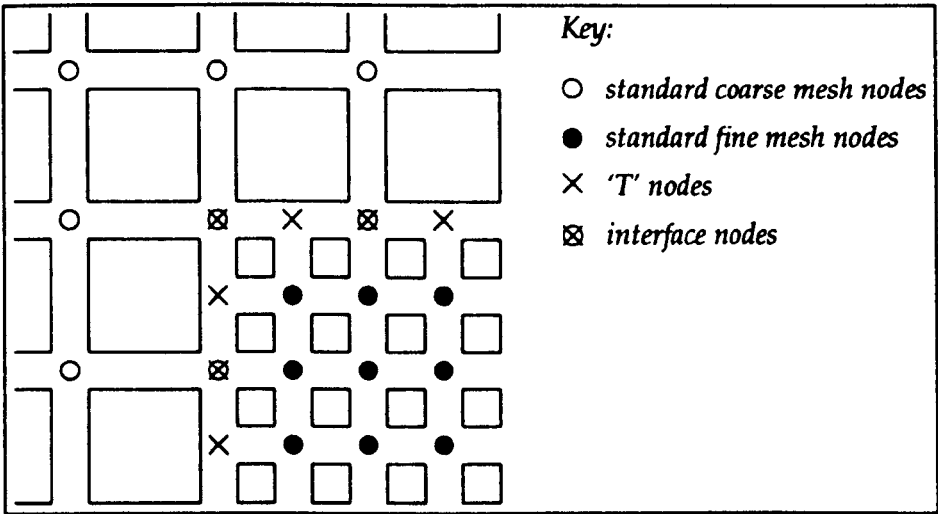


Fig. 5.3 - First approach

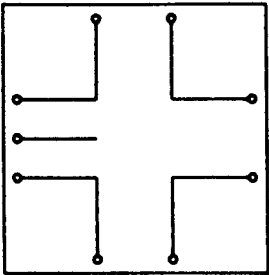


Fig. 5.4 - Double port node

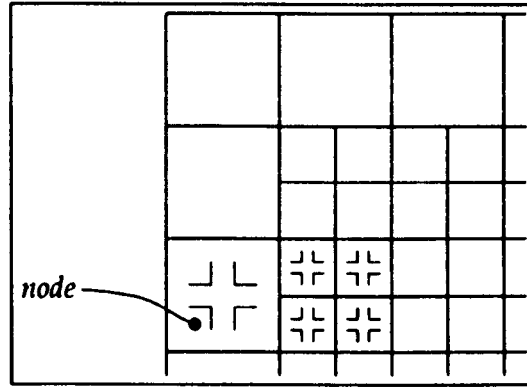


Fig. 5.5 – Interface at the mid-point of link-lines

## 5.5 Interface conditions

When the interface is placed at the mid-point of link-lines, the problem reduces to that of transferring  $n_1$  pulses on  $l_1$  link-lines, in each direction, from region (1) to  $n_2$  pulses on  $l_2$  link-lines in region (2), where the restriction is imposed that  $n_1$ ,  $l_1$ ,  $n_2$  and  $l_2$  are the smallest possible integers. This process is repeated over the surface of the interface. In 2-dimensions,  $n_i = l_i t_i$ , where  $t_i$  is the temporal reduction ratio (which need not be the same as the spatial reduction ratio). In 3-dimensions,  $n_i = l_i^2 t_i$ , and the two polarisations on each of the six pairs of link-lines are treated separately.

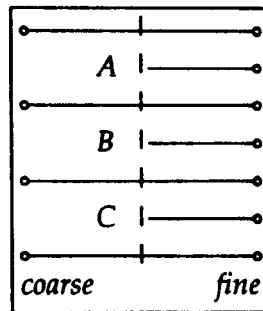


Fig. 5.6 – Fine/coarse mesh interface

For example, consider a 2-dimensional system in which there is a 2:1 reduction in both space and time. In this case, if region (1) is the coarse mesh and region (2) is the fine mesh,  $l_1 = 1$ ,  $t_1 = 1$ ,  $l_2 = 2$  and  $t_2 = 2$ . Part of the interface is shown in fig. 5.6. The interface is divided into sections (labelled A, B and C) so that a single coarse mesh link-line is connected to two fine mesh link-lines. For every coarse mesh iteration there must be two fine mesh iterations and for every coarse mesh pulse,  $V_c$ , there must be four fine mesh pulses,  $V_{f1}$ ,  $V_{f2}$ ,  $V_{f3}$  and  $V_{f4}$ , as shown

in fig. 5.7.

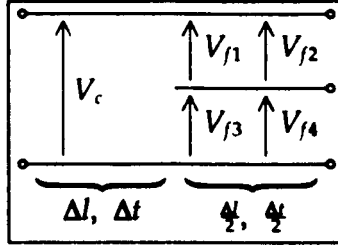


Fig. 5.7 – Pulses transferred across the interface

Consider now, for the general case, how the constraints mentioned in §5.3.1 are imposed on this system. The following equations can be applied either to the conversion from the fine mesh to the coarse mesh or to the conversion from the coarse mesh to the fine mesh.

#### i) charge conservation

For the 2-dimensional case with a 2:1 reduction ratio, it was shown in §5.3.3 that the charge in the fine mesh must be the same as that in the coarse mesh i.e.

$$\frac{\Delta t}{Z_0} V_c = \frac{(\frac{\Delta t}{2})}{Z_0} \sum_{i=1}^4 V_{fi}$$

$$\Rightarrow V_c = \frac{1}{2} \sum_{i=1}^4 V_{fi}$$

This condition is the same as ensuring continuity of fields. For example, the electric field due to pulse  $V_c$  is

$$E_c = -\frac{V_c}{\Delta l}$$

and the average electric field (with respect to both space and time) due to pulses  $V_{fi}$  is

$$E_f = -\frac{1}{4} \sum_{i=1}^4 \frac{V_{fi}}{(\frac{\Delta l}{2})}$$

The total electric and magnetic fields between nodes (due to part of a coarse mesh link-line and parts of two fine mesh link-lines) can be written as

$$E = E_c + E_f'$$

$$H = \pm \frac{1}{Z_0} (E_c - E_f')$$

where the prime indicates the field due to the independent set of pulses from the

adjacent node. Both the electric and magnetic fields are therefore continuous across the interface i.e. the field is the same if it is calculated from pulses incident upon the interface or if it is calculated from the converted pulses transferred across the interface. In general, conservation of charge means that the ratio of the charge carried by voltage pulses in each region must be kept constant and this ratio is not necessarily unity. In this case, it is preferable to explicitly enforce continuity of fields rather than conservation of charge. Taking the space and time average of the electric field on each side of the interface gives

$$\frac{1}{n_1} \sum_{i=1}^{n_1} \frac{V_{1i}}{(\Delta l_1)} = \frac{1}{n_2} \sum_{j=1}^{n_2} \frac{V_{2j}}{(\Delta l_2)}$$

$$\Rightarrow \frac{l_1}{n_1} \sum_{i=1}^{n_1} V_{1i} = \frac{l_2}{n_2} \sum_{j=1}^{n_2} V_{2j}$$

where  $\Delta l$  is some base value of node spacing, common to both regions.

## ii) energy conservation

If the energy of the pulses in region (1) is related to the energy of the pulses in region (2) by a constant  $\alpha$ , then conservation of energy is enforced when

$$\sum_{i=1}^{n_1} V_{1i}^2 = \alpha \sum_{j=1}^{n_2} V_{2j}^2$$

The constant  $\alpha$  must be used in a consistent manner for both the fine→coarse and the coarse→fine conversions. Appropriate values of  $\alpha$  will be given in the following sections. If both charge and energy conservation are enforced then it is apparent that it is not possible to convert many pulses from the fine mesh to a single coarse mesh pulse.

## iii) no reflection

This condition is approximated by running the fine→coarse and coarse→fine conversions separately so that the apparent “reflection” is solely due to scattered pulses from the adjacent node. It is an approximation in the sense that an average must be taken over the fine-mesh link-lines. For example, a node in the fine mesh may send a pulse across the interface. This pulse will become incident on a coarse mesh node on the other side of the interface where scattering will take place. A new coarse mesh pulse will then be incident upon the interface where it will be

converted into several fine mesh pulses. These pulses will then be incident upon the original fine mesh node and also on adjacent fine mesh nodes and it is on the adjacent nodes where the error is introduced. However, if the reduction ratio is not too large then pulses sent across the interface from adjacent nodes will be similar and the error will not be great. This method of working is to be contrasted with treating the interface as a scattering junction where, for example, a coarse mesh pulse transferred across the interface depends on the incident coarse mesh pulse as well as on the incident fine mesh pulses.

#### **iv) zero delay**

The delay is minimised by transferring pulses across the interface as soon as possible. If the coarse mesh is run at a slower speed than the fine mesh then there will inevitably be some delay in transferring fine mesh pulses to the coarse mesh since it is necessary to wait for several fine mesh iterations before any information can be transferred.

Note that the above constraints are not all compatible. For example, it is possible to have both charge and energy conservation at the expense of increased delay. The methods devised to reduce the approximations needed and establish an optimum procedure are described in the following sections.

## **5.6 Conversion methods**

This section describes some of the early work done for a 2-dimensional series mesh with a 2:1 reduction ratio. The principles can be readily extended to 3-dimensions and different reduction ratios if required. The conversion methods described below are principally concerned with the fine→coarse conversion since this is where most problems arise. Many variations on these methods, in which the order of the pulses transferred across the interface is altered, have also been tried.

### **5.6.1 Slow conversion**

For this conversion method it was assumed that charge and energy conservation were more important than a small delay.

Many pulses from the fine mesh cannot be converted into a single coarse

mesh pulse whilst conserving both charge and energy. However, they can be converted into two coarse mesh pulses if the constant  $\alpha$  is chosen appropriately. The conversion process must therefore wait for two coarse mesh iterations and four fine mesh iterations before any information is transferred. The relevant equations are

$$\sum_{i=1}^2 V_{ci} = \frac{1}{2} \sum_{j=1}^8 V_{fj}$$

and

$$\sum_{i=1}^2 V_{ci}^2 = \alpha \sum_{j=1}^8 V_{fj}^2$$

Pulses incident upon the interface are added to the quantities  $\sum V$  and  $\sum V^2$  and when these sums are complete, new pulses are introduced into the adjacent region. The equations must be solved for  $V_{ci}$  for the fine→coarse conversion and must be solved for  $V_{fj}$  for the coarse→fine conversion. Solving for  $V_{ci}$  gives

$$V_{ci} = \frac{1}{4} \sum_{j=1}^8 V_{fj} \pm \frac{1}{4} \sqrt{8\alpha \sum_{j=1}^8 V_{fj}^2 - \left( \sum_{j=1}^8 V_{fj} \right)^2}$$

where the positive sign is taken for one solution and the negative sign is taken for the other. The quantity under the square root will be positive for  $\alpha > 1^3$ .

For the coarse→fine conversion it is apparent that there is a non-unique solution for the eight fine mesh pulses. The restriction is imposed that these pulses are divided into two groups of four, with the pulses in each group taking the same value. The equations to solve then become

$$V_{fa} + V_{fb} = \frac{1}{2} \sum_{i=1}^2 V_{ci}$$

and

$$V_{fa}^2 + V_{fb}^2 = \frac{1}{4\alpha} \sum_{i=1}^2 V_{ci}^2$$

where  $V_{fa}$  and  $V_{fb}$  are the two unique values. The solution is

$$V_{fa}, V_{fb} = \frac{1}{4} \sum_{i=1}^2 V_{ci} \pm \frac{1}{4} \sqrt{\frac{2}{\alpha} \sum_{i=1}^2 V_{ci}^2 - \left( \sum_{i=1}^2 V_{ci} \right)^2}$$

---

<sup>3</sup> In general,  $n \sum_{i=1}^n V_i^2 - \left( \sum_{i=1}^n V_i \right)^2 > 0$ .

The proof of this follows directly from the relation  $n \sum_{i=1}^n V_i^2 - \left( \sum_{i=1}^n V_i \right)^2 = n \sum_{i=1}^n (V_i - \bar{V})^2$

where  $\bar{V}$  is the mean,  $\bar{V} = \frac{1}{n} \sum_{i=1}^n V_i$

provided  $\alpha \leq 1$ .

The conversion process will work provided that  $\alpha$  is chosen to be unity. This value means that  $\sum V^2$  is the same in each mesh, for a constant field, when the pulses are all equal. Or, equivalently, when transferring pulses across the interface, the energy in the fine mesh must be half that in the coarse mesh. It was decided that the pulse of largest magnitude would be sent across the interface first. This was done by setting the sign of the second quantity in the above expressions to be the same as the sign of  $\sum V$ . The calculation order was arranged as follows:

- calculate coarse mesh, inserting  $V_{c1}$  pulses along the interface
- calculate coarse mesh, inserting  $V_{c2}$  pulses along the interface
- calculate fine mesh, inserting  $V_{fa}$  pulses along the interface
- calculate fine mesh, inserting  $V_{fa}$  pulses along the interface
- calculate fine mesh, inserting  $V_{fb}$  pulses along the interface
- calculate fine mesh, inserting  $V_{fb}$  pulses along the interface
- convert coarse→fine
- convert fine→coarse

Sending the fine mesh pulses in this order avoids introducing high frequency energy which cannot be represented in the coarse mesh.

### 5.6.2 Running sum conversions

For this class of conversion methods an attempt was made to minimise the delay whilst still maintaining charge and energy conservation.

In this method, for the fine→coarse conversion, a pulse is transferred across the interface after two fine mesh iterations, rather than waiting for four. Running sums are maintained for the total charge,  $\sum V_f$ , and the total energy,  $\sum V_f^2$ <sup>4</sup>. These quantities are increased when pulses are incident from the fine mesh and are decreased when a pulse is sent into the coarse mesh. Each coarse mesh pulse must be chosen so that the remaining charge and energy can be transmitted in the event of no further pulses from the fine mesh. This means that it would not be advisable

---

<sup>4</sup> The notation  $\sum V_f$  and  $\sum V_f^2$  is used in a *loose* manner and does not strictly imply sum of a sequence. However, the values of  $\sum V_f$  and  $\sum V_f^2$  will always be consistent with and indistinguishable from a true sum.

to send the pulse of largest magnitude since this would leave either zero charge or zero energy and no subsequent pulse could be transmitted. It is also desirable that the number of subsequent pulses be minimised with magnitudes falling rapidly to zero. This requirement implies that, if  $\sum V_f$  and  $\sum V_f^2$  can be converted exactly into into two coarse mesh pulses (neglecting the trivial case when they can be converted into a single coarse mesh pulse), then it is these pulses which should be transmitted. The main disadvantage of this method is that it cannot be guaranteed that some charge and energy will not remain at the interface for a significant number of iterations.

One scheme which was devised for the fine→coarse conversion was to solve the equations given in §5.6.1 and then send the pulse of largest magnitude. i.e.

$$V_c = \frac{1}{4} \sum V_f \pm \frac{1}{4} \sqrt{8 \sum V_f^2 - \left( \sum V_f \right)^2}$$

with the sign of the second term chosen to be the same as the sign of  $\sum V_f$ . If the quantity under the square root was negative then just the first term was used. The running sums are then altered to reflect the new values of charge and energy

$${}_{k+1}\sum V_f = {}_k\sum V_f - 2{}_kV_c$$

$$\text{and } {}_{k+1}\sum V_f^2 = {}_k\sum V_f^2 - {}_kV_c^2$$

where the preceding subscript denotes the coarse mesh iteration number. The factor of 2 in the first expression arises because the charge in the fine mesh must equal the charge in the coarse mesh. For example,

$$\text{if } {}_1\sum V_f = 6 \text{ and } {}_1\sum V_f^2 = 5 \text{ then } {}_1V_c = 2$$

$${}_2\sum V_f = 2 \text{ and } {}_2\sum V_f^2 = 1 \text{ then } {}_2V_c = 1$$

$${}_3\sum V_f = 0 \text{ and } {}_3\sum V_f^2 = 0$$

assuming that there are no further pulses from the fine mesh.

For the coarse→fine conversion, four fine mesh pulses of equal magnitude may be obtained from

$$V_{fi} = \frac{1}{2}V_c \quad i = 1, 2, 3, 4$$



In addition to the above method, numerous other schemes which make use of running sums may be devised. For example, if it is apparent that  $\sum V_f$  and  $\sum V_f^2$  cannot be converted exactly into two coarse mesh pulses then it may be more appropriate to convert to three or four pulses and then transfer one of these. However, none of the additional methods tested were found to have any significant advantage.

### 5.6.3 Fast conversion

For this conversion method it was assumed that charge conservation and minimum delay were more important than energy conservation.

If energy conservation is not important then multiple pulses from the fine mesh can be converted into a single coarse mesh pulse using charge conservation.

$$V_c = \frac{1}{2} \sum_{i=1}^4 V_{fi}$$

The coarse→fine conversion is the same as for the running sum conversions.

The main disadvantage of this method is that, for the fine→coarse conversion, the interface behaves as a low pass filter with respect to both space and time. The other conversion methods also suffer from this problem, to a certain extent, but the problem is more acute here as it is obvious that there is loss of energy. Tests must be performed to check that there is no significant loss of energy below the highest frequency of interest.

### 5.6.4 Fast conversions with energy conservation

For this class of conversion methods the storage requirement for the coarse mesh was doubled so that charge conservation, energy conservation and minimum delay could be achieved simultaneously. The increased storage means that the space savings are reduced from four to two when compared with a uniform fine mesh. Three different approaches were considered.

#### Method 1

The problem with the conversion method described in §5.6.1 is the excessive delay. The delay may be reduced by running the coarse mesh at double speed. The

ways in which this may be done are described in §5.7.2.

## Method 2

Convert the four fine mesh pulses into two coarse mesh pulses and inject these pulses into two separate identical coarse meshes which are run in parallel. The only communication between these meshes occurs at the interface. Excitation and outputs in the coarse region must consider the pulses in both meshes. The relevant equations are

$$\sum_{i=1}^2 V_{ci} = \sum_{j=1}^4 V_{fj}$$

$$\text{and } \sum_{i=1}^2 V_{ci}^2 = \alpha \sum_{j=1}^4 V_{fj}^2$$

The required solutions are, for the fine→coarse conversion

$$V_{ci} = \frac{1}{2} \sum_{j=1}^4 V_{fj} \pm \frac{1}{2} \sqrt{2\alpha \sum_{j=1}^4 V_{fj}^2 - \left( \sum_{j=1}^4 V_{fj} \right)^2}$$

If the fine mesh pulses are to take two unique values,  $V_{fa}$  and  $V_{fb}$  then

$$V_{fa} V_{fb} = \frac{1}{4} \sum_{i=1}^2 V_{ci} \pm \frac{1}{4} \sqrt{\frac{4}{\alpha} \sum_{i=1}^2 V_{ci}^2 - \left( \sum_{i=1}^2 V_{ci} \right)^2}$$

For both square roots to be real,  $\alpha$  must be 2. This means that when transferring pulses across the interface, the energy in both coarse meshes must be four times that in the fine mesh.

## Method 3

When the four fine mesh pulses are converted into a single coarse mesh pulse, an additional quantity,  $\mathfrak{Z}$ , is used to store the energy which has been lost. This quantity is then allowed to propagate through the coarse mesh until it is incident again upon the interface. For the fine→coarse conversion

$$V_c = \frac{1}{2} \sum_{j=1}^4 V_{fj}$$

$$\mathfrak{Z} = \alpha \sum_{j=1}^4 V_{fj}^2 - V_c^2$$

For the coarse→fine conversion, the equations to be solved are

$$V_{fa} + V_{fb} = V_c$$

$$\text{and } V_{fa}^2 + V_{fb}^2 = \frac{1}{2\alpha} (V_c^2 + \mathfrak{E})$$

giving solution

$$V_{fa} V_{fb} = \frac{1}{2} V_c \pm \frac{1}{2} \sqrt{\left(\frac{1}{\alpha} - 1\right) V_c^2 + \frac{\mathfrak{E}}{\alpha}}$$

Choosing  $\alpha$  to be unity means that  $\mathfrak{E}$  is always positive and the square root is always real. Within the coarse mesh, the  $\mathfrak{E}$  quantities may be propagated by dividing the sum  $\Sigma \mathfrak{E}$  at each node in proportion to the square of the scattered voltage pulses. The big disadvantage of the method is that additional scattering procedures have to be implemented.

### 5.6.5 Other methods

One technique which was not tried was to fit the pulses to a particular polynomial. This is not an appropriate method for a 2:1 reduction ratio since there are only a limited number of voltage pulses. It might be possible to use the method for higher reduction ratios but there is always the possibility of instability.

## 5.7 Conversion enhancements

### 5.7.1 Calculation order

For the conversion methods in which one coarse mesh iteration is performed for every fine mesh iteration (i.e. all methods in §5.6 apart from that in §5.6.1) the calculation order, for a 2:1 reduction ratio (in either 2 or 3-dimensions), may be written as

- calculate fine
- calculate fine
- calculate coarse
- convert coarse→fine
- convert fine→coarse

More specifically, the calculation for each mesh (either fine or coarse) can be written as

- insert pulses travelling out of interface (pulses which have been

converted)

- perform one iteration (scatter, connect, boundaries *etc.*)
- remove pulses travelling into interface (pulses to be converted)

The pulses are removed to a temporary location (e.g. incorporated into  $\sum V$  and  $\sum V^2$  for the running sum conversions) where they are kept until the conversion takes place. After the conversion, the new pulses are stored in a separate place until they are injected into the mesh on the other side of the interface.

It is possible to change the calculation order to compensate for any conversion delay. Changing the order to

- calculate fine
- calculate fine
- convert fine→coarse
- calculate coarse
- convert coarse→fine

overcompensates. The optimum calculation order can be written as

- calculate fine
- convert fine→coarse
- calculate fine
- calculate coarse
- convert coarse→fine

As an example, compare the idealised propagation of a pulse through a multigrid region with a uniform coarse mesh, as shown in fig. 5.8. The propagation is idealised in the sense that, in 3-dimensions, it takes a pulse two iterations to traverse a node (see §4.6.1); the principles are the same, however. There is only one calculation order in which the coarse mesh pulse is perfectly regenerated at the correct time. Other calculation orders will cause the pulse to appear at the wrong time or will split it into two pulses of half the value.

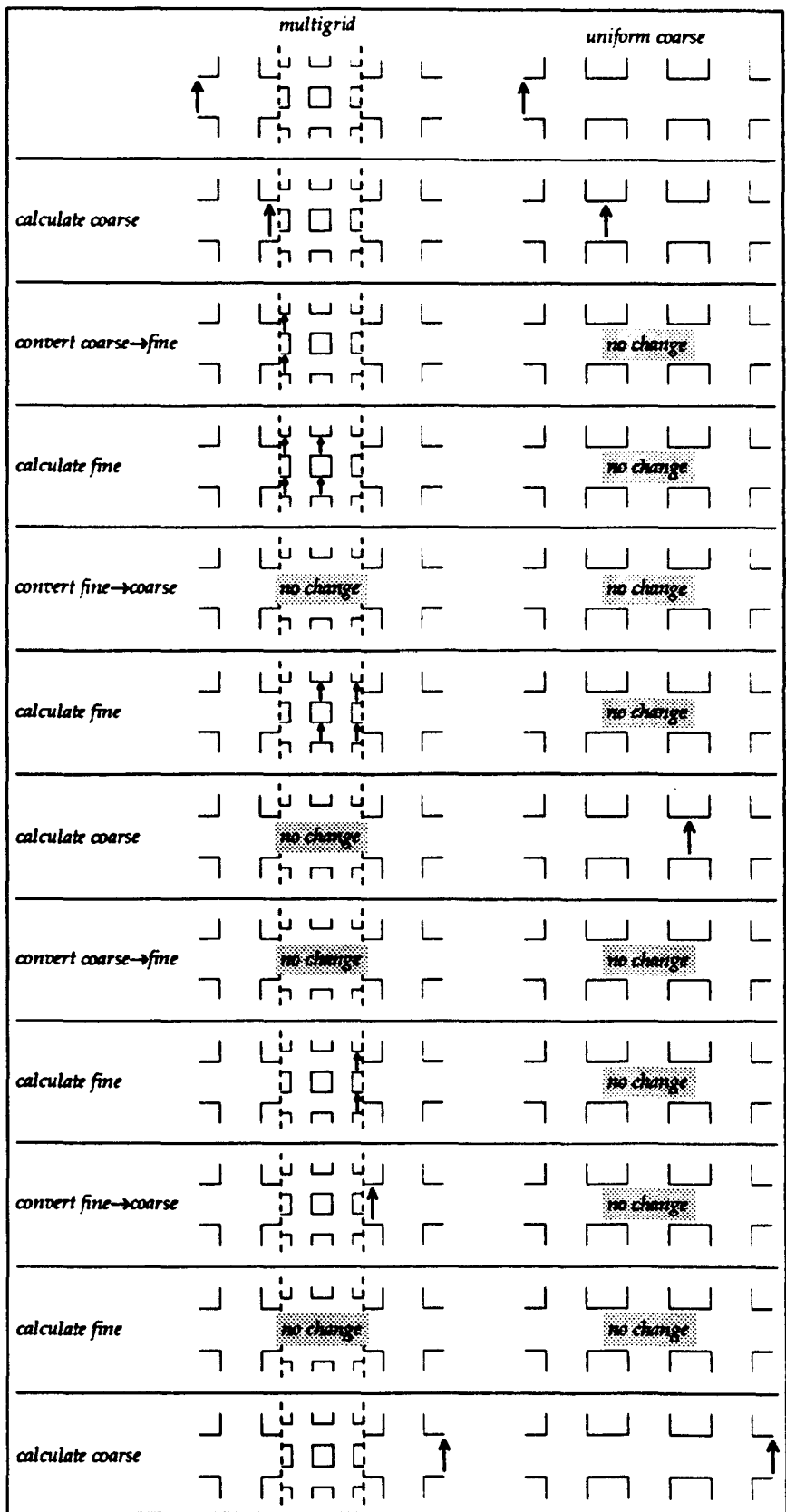


Fig. 5.8 - Optimum calculation order

### 5.7.2 Reducing the coarse mesh timestep

It is possible to minimise the loss of information when pulses pass into the coarse mesh by running the coarse mesh at a higher speed. This can be done by adding stubs to the node to slow down the speed of the bulk wave (see §4.5) or it can be done by making use of additional storage. The first approach was not considered as it reduces some of the advantages that the multigrid technique has over the use of a graded mesh. In particular, for the types of problem considered, there are large regions of free-space and it is desirable to model these with the 12-port node in both fine and coarse mesh regions.

In the method used, the speed of propagation on the link-lines is kept constant so that, if the coarse mesh timestep is reduced by half, it takes two timesteps for a pulse to travel between nodes. This is in addition to the time it takes for a pulse to traverse the node. Additional storage is then required for the pulse at the centre of each link-line but the overall storage requirement is still less than that required for a uniform fine mesh <sup>5</sup>. In 2-dimensions, the space saving is reduced from a factor of four to two and in 3-dimensions, the space saving is reduced from eight to four. Similar reductions are obtained in the run-time saving, since the number of scattering operations is increased. The coarse mesh timestep may be reduced further but there is no advantage in doing this unless higher space reduction ratios are used.

For a 2:1 space reduction, in which the coarse mesh is run at double speed, the calculation order is simply

- calculate fine
- calculate coarse
- convert fine→coarse
- convert coarse→fine

### 5.8 Choice of conversion method

This section describes some of the results obtained with a 2-dimensional

---

<sup>5</sup> Intermediate storage locations have been used by Saguet [51] in the so-called "memory technique" for implementing graded meshes.

series mesh and a 2:1 reduction ratio for the conversion methods described in §5.6 with and without the enhancements described in §5.7. A limited number of the conversion methods were implemented in 3-dimensions but the conclusions were the same. The results shown in this section are for the following conversion methods

- (i) slow conversion
- (ii) running sum conversion with original calculation order
- (iii) fast conversion (without energy conservation) with optimum calculation order
- (iv) fast conversion with energy conservation (method 2) and optimum calculation order

### 5.8.1 Steady-state solution

The basic test used to indicate whether the conversion process was working correctly was to place a fine mesh in the centre of a coarse mesh, with a matched boundary, and then apply appropriate excitation to place a charge in the centre of the fine mesh, as shown in fig. 5.9. Typically, an  $8 \times 8$  fine mesh was used inside a  $16 \times 16$  coarse mesh. The simulation was then run until the steady-state was reached. A graph of the electric field at the output point gives an indication of the rate of convergence.

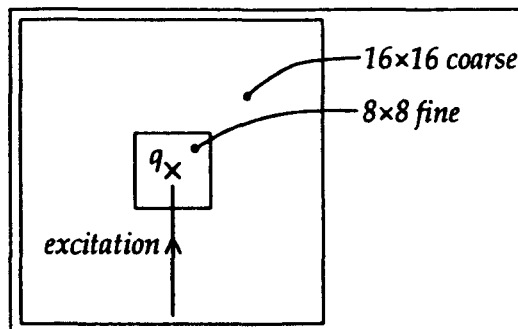


*Fig. 5.9 – Charge in centre of fine mesh*

Graphs showing the vertical component of the electric field at a point directly below the charge are shown in fig. 5.10 for a time corresponding to 500 fine mesh iterations. The result for a uniform coarse mesh is shown in fig. 5.10a and the results for methods (i), (iii) and (iv) are shown in figs. 5.10b–d. It is apparent that the graph for the uniform mesh is very different in character: the field alternates

between values above and below its final value with a slowly diminishing envelope (this oscillation can be removed with a 2-point moving average filter). In contrast, the responses obtained from the multigrid technique jump about the final value in an apparently chaotic manner with the rate of convergence determined by the conversion method. The field obtained from the uniform mesh is half that obtained from the multigrid systems because the charge density is less in the coarse mesh than in the fine mesh.

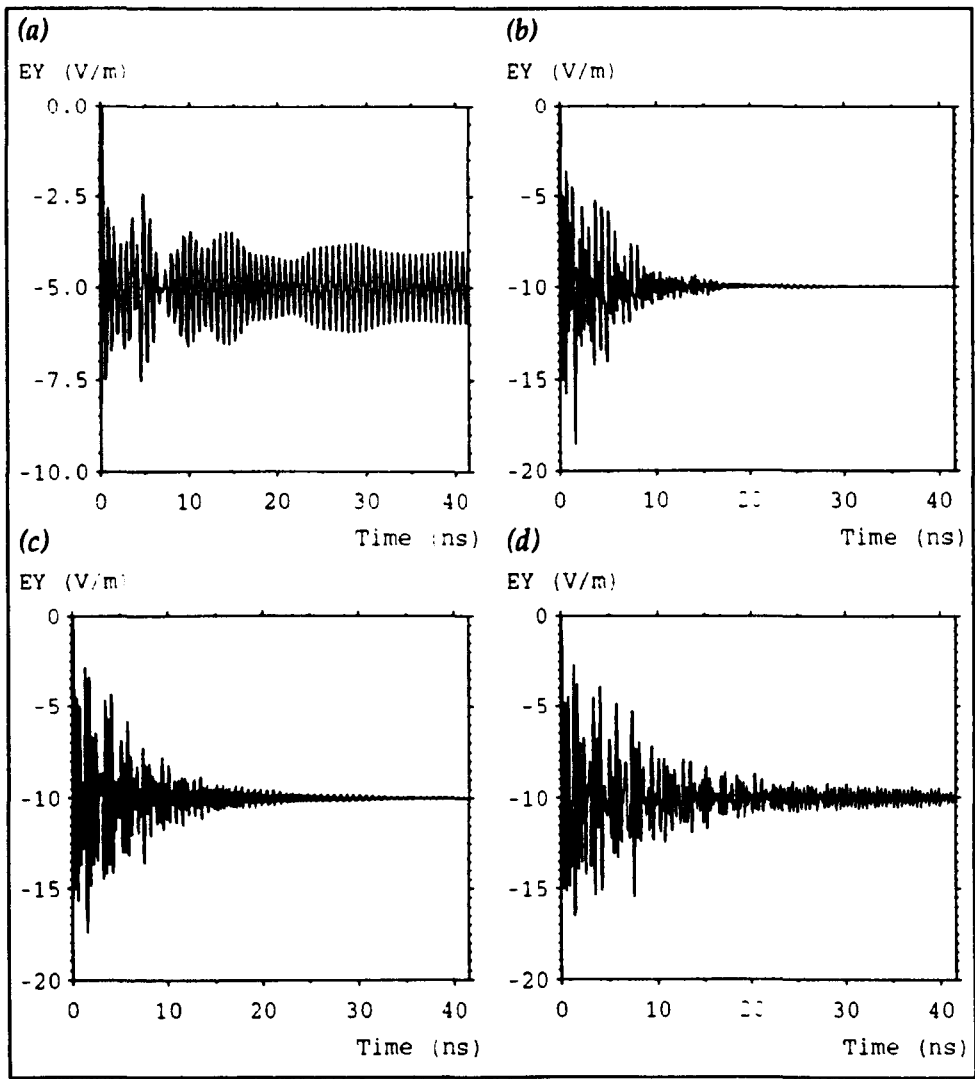


*Fig. 5.10 – Electric field below central charge*

If the steady-state field over the whole mesh is symmetrical (left to right and top to bottom) then this indicates that the conversion method is operating correctly since a symmetrical field distribution is obtained from an asymmetrical excitation. The field may be compared with that obtained from a uniform mesh. For example,



consider the vertical component of the electric field along a line extending from the bottom boundary to the central charge.

coarse	fine	(i)	(ii)	(iii)	(iv)
5.000	10.000 4.536	10.002 4.546	10.002 4.544	10.000 4.536	10.002 4.536
2.268	2.676 1.870	2.728 1.996	2.696 1.876	2.676 1.834	2.676 1.834
1.342	1.438 1.174	1.095	1.254	1.267	1.267
0.944	0.994 0.864	0.860	0.921	0.923	0.923
0.739	0.770 0.696	0.708	0.732	0.732	0.732
0.623	0.642 0.598	0.610	0.620	0.620	0.620
0.558	0.568 0.544	0.552	0.556	0.557	0.557
0.528	0.530 0.524	0.524	0.527	0.527	0.527

The results show that the multigrid technique can be used to obtain the field around a charge more accurately than for a uniform coarse mesh. Method (ii) appears to be better than method (i) and methods (iii) and (v) are better than method (ii). Method (iii) has the faster convergence so it can be regarded as the favoured method based on these results.

## 5.8.2 Transient solution

Another test which may be used is to look for resonances inside a 2-dimensional cavity. This is readily achieved by extending the excitation up to the top boundary and changing the matched boundary conditions to short-circuits. When a uniform mesh of physical dimensions  $0.8 \times 0.8 \text{ m}^2$  is excited by an off-centre set of current sources, three resonances are observed in the interval  $0 \rightarrow 500 \text{ MHz}$ . These correspond to the  $TE_{10}$  (132 MHz),  $TE_{20}$  (265 MHz) and  $TE_{30}$  (397 MHz) modes. Cavity resonances are accurately predicted by TLM and there will be very little difference between the resonant frequencies obtained from models of different

resolutions, provided that there are enough nodes to describe the wavelength. The relative magnitudes are also largely independent of resolution, provided that the physical position of the excitation is kept constant.

In a multigrid system, any delay introduced at the interface will tend to make the cavity appear larger. The fine mesh will only fill part of the cavity and so it is possible that any genuine resonances may be split to form two separate resonances. This would be an undesirable feature, particularly in complex systems, where there are many closely spaced resonances. It is also important that degenerate modes are not resolved into two separate resonances. A second effect that may occur is that the addition of the fine mesh may alter the relative energy in each of the modes. This could occur if, at a particular point, the mesh does not appear isotropic. To test for this, the fine mesh may be moved to different positions in the cavity while the excitation and output are kept in the same position. Ideally, the relative magnitudes of the resonances will not be affected and will be the same as those obtained with a uniform mesh. Another possibility is that additional modes may be excited. Although these modes may well be genuine ones for the cavity it is considered desirable to make the multigrid system behave as much like a uniform mesh as possible, when the fine mesh contains no features.

Results are shown in fig. 5.11 for a  $16 \times 16$  coarse mesh in which a  $8 \times 8$  fine mesh is moved to three different positions (centre, top right and centre right) for method (ii). The excitation and output points are at fixed positions in the coarse mesh. It is apparent that the relative amplitudes vary with the position of the fine mesh and splitting is observed in one case. In addition, other modes are excited and there are some numerical artefacts between resonance peaks. The corresponding curves for method (iii) are shown in fig. 5.12. Only the three main peaks are present and there is very little change in relative amplitudes.

### 5.8.3 Comparison

Examination of the results from all of the conversion methods (and for many different pulse orders) suggests that the fast conversion with no energy conservation is the best choice. This method does not significantly introduce additional resonances and there is very little noise between resonant peaks. As far

as splitting is concerned, the optimum calculation order described in §5.7.1 must be used. Running the coarse mesh at a higher speed may give some improvement in results but this is offset by the additional storage and run-time requirement.

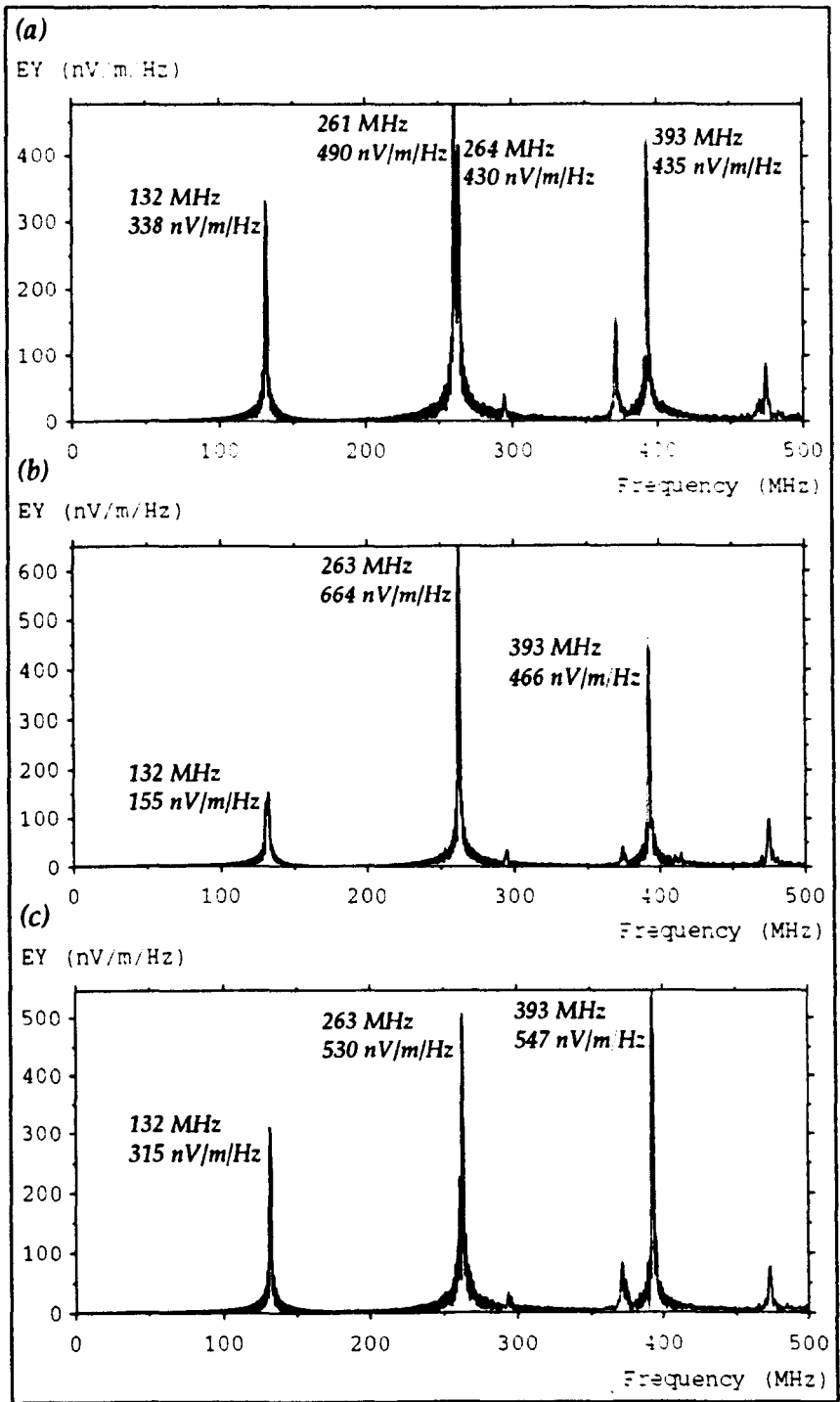
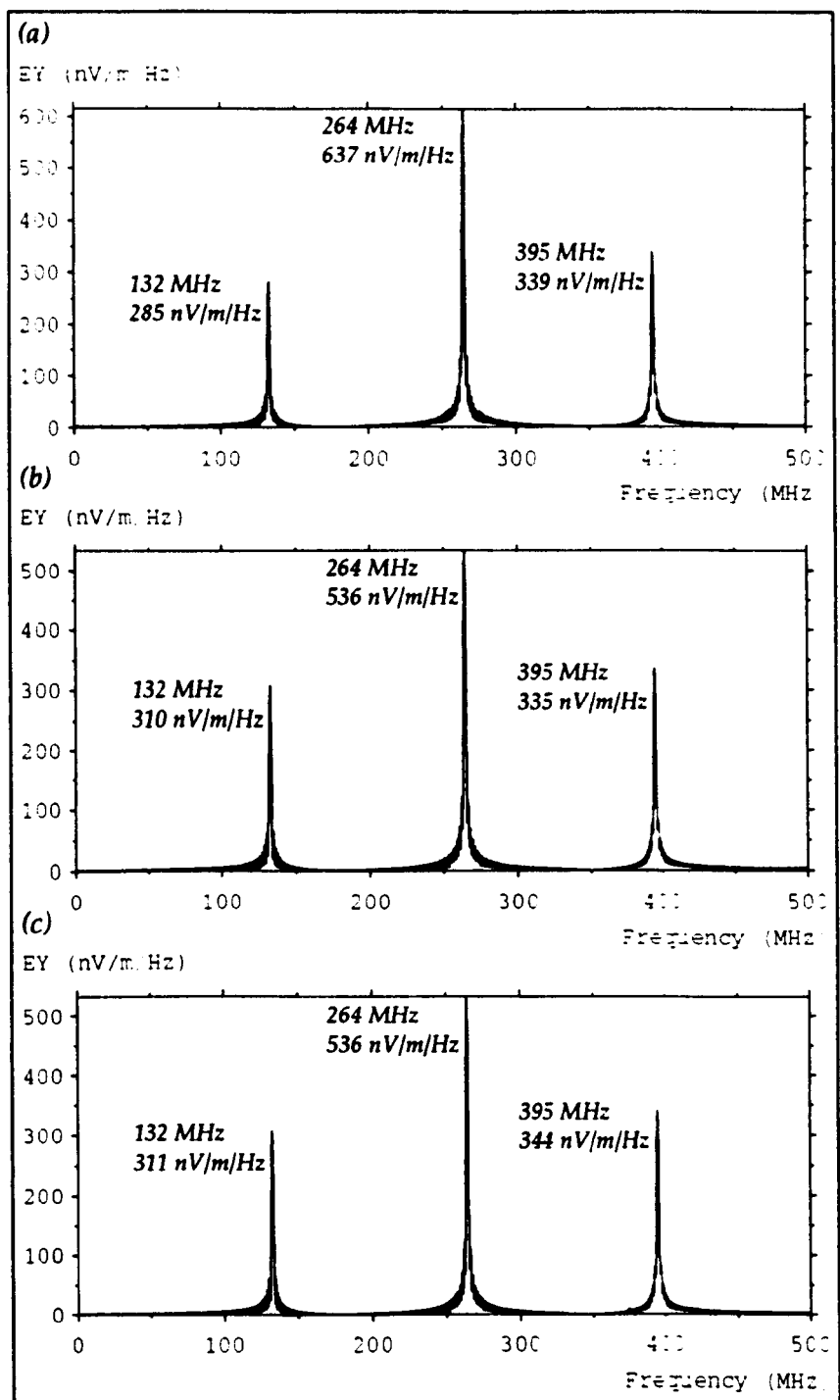


Fig. 5.11 – Cavity resonances for method (ii)



*Fig. 5.12 – Cavity resonances for method (iii)*

## 5.9 Three-dimensional systems

The purpose of this section is to summarise the work described in the previous sections to show how the multigrid technique can be applied, in a general way, to 3-dimensional systems. Fig. 5.13 shows a section of the interface for a 2:1

reduction in both space and time. In general,  $n_1$  pulses from region (1) must be converted into  $n_2$  pulses in region (2) and this must be done for both polarisations. The total number of pulses  $n_i$  is given by  $n_i = l_i^2 t_i$  where  $l_i$  is the number of link-lines in each direction (which is assumed to be the same in both directions) and  $t_i$  is the number of sets of  $l_i^2$  pulses which must be transferred in each conversion. If coarse mesh regions are run at increased speed then  $t_i$  will be greater than  $l_i$ . The conversion method is based on the fast conversion with no energy conservation. To enforce continuity of fields, the following condition must be met

$$\frac{l_1}{n_1} \sum_{i=1}^{n_1} V_{1i} = \frac{l_2}{n_2} \sum_{j=1}^{n_2} V_{2j}$$

For the conversion from region (2) to region (1), if the pulses  $V_{1i}$  are set to be equal then

$$V_{1i} = \frac{l_2}{n_2 l_1} \sum_{j=1}^{n_2} V_{2j}$$

writing  $n_2 = l_2^2 t_2$  gives

$$V_{1i} = \frac{1}{l_1 l_2 t_2} \sum_{j=1}^{n_2} V_{2j}$$

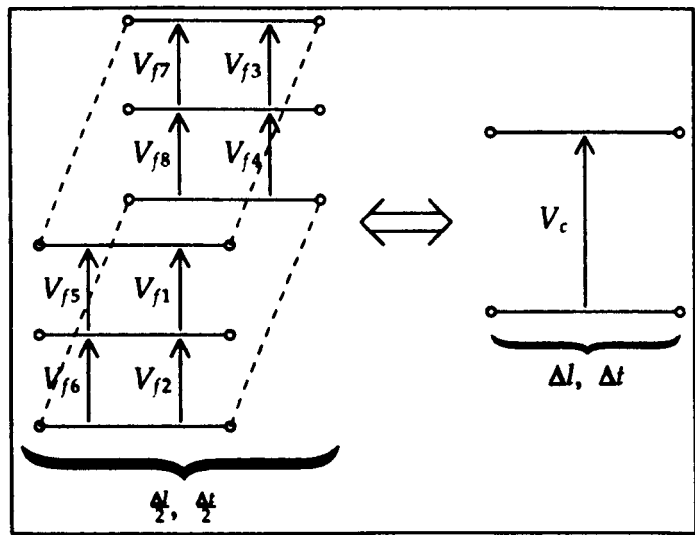


Fig. 5.13 – 2:1 reduction in 3-dimensions

For example, for a 2:1 reduction, if region (1) is the coarse mesh and region (2) is the fine mesh then  $l_1 = 1$ ,  $t_1 = 1$ ,  $l_2 = 2$  and  $t_2 = 2$ . For the fine→coarse conversion

$$V_1 = \frac{1}{l_1 l_2 t_2} \sum_{j=1}^{n_2} V_{2j} = \frac{1}{4} \sum_{j=1}^8 V_{2j}$$

For the coarse→fine conversion

$$V_2 = \frac{1}{l_2 l_1 t_1} \sum_{i=1}^{n_1} V_{1i} = \frac{1}{2} V_1 \quad j = 1, 2, \dots, 8$$

The calculation order is selected so that a plane wave will propagate perfectly if a fine mesh extending across the complete cross-section is inserted. A shorthand notation is adopted so that the correct calculation order for a 2:1 reduction ratio can be written as

$$F, F>C, F, C, C>F$$

where "F" denotes a fine mesh calculation, "C" denotes a coarse mesh calculation, "F>C" denotes the conversion of pulses from the fine mesh to the coarse mesh and "C>F" denotes the conversion from the coarse mesh to the fine mesh. The calculation orders for some higher reduction ratios are given below

$$3:1 \quad F, F, F>C, F, C, C>F$$

$$4:1 \quad F, F, F, F>C, F, C, C>F$$

$$5:1 \quad F, F, F, F, F>C, F, C, C>F$$

If the system contains more than two resolutions then the calculation order becomes more complex. For example, if there are three meshes "C", "F", "U" where the reduction ratio between "C" and "F" is 2:1 and the ratio between "F" and "U" is also 2:1 then the correct order can be written as

$$U, U>F, U, F, F>U, F>C, U, U>F, U, F, F>U, C, C>F$$

## 5.10 Energy considerations

In this section, the energy stored in the fine and coarse mesh regions is compared and the loss of energy in the fine→coarse conversion is considered to see whether it is a significant problem.

The energy density in a uniform mesh can be written as (see §4.4)

$$w = \frac{1}{c Z_0 \Delta l^2} \sum V^2$$

The total stored energy within the volume can then be written as

$$W = \frac{\Delta l}{c Z_0} \sum V^2$$

For multigrid systems,  $\Delta l$  must be replaced by  $\Delta l / l_i$  and, for the following results, the factor  $\Delta l / c Z_0$  has been omitted. The total stored energy is then proportional to  $W'$  where

$$W' = \frac{1}{l_i} \sum V^2$$

Two basic tests have been performed to look directly at the energy, and also at the amplitudes of resonances, in a lossless cavity. In a cavity, pulses must pass through the interface many times which leads to a continual loss of energy. The situation is less severe for open systems, where the pulses are not reflected from the boundaries.

**Test 1 – energy in a lossless cavity**

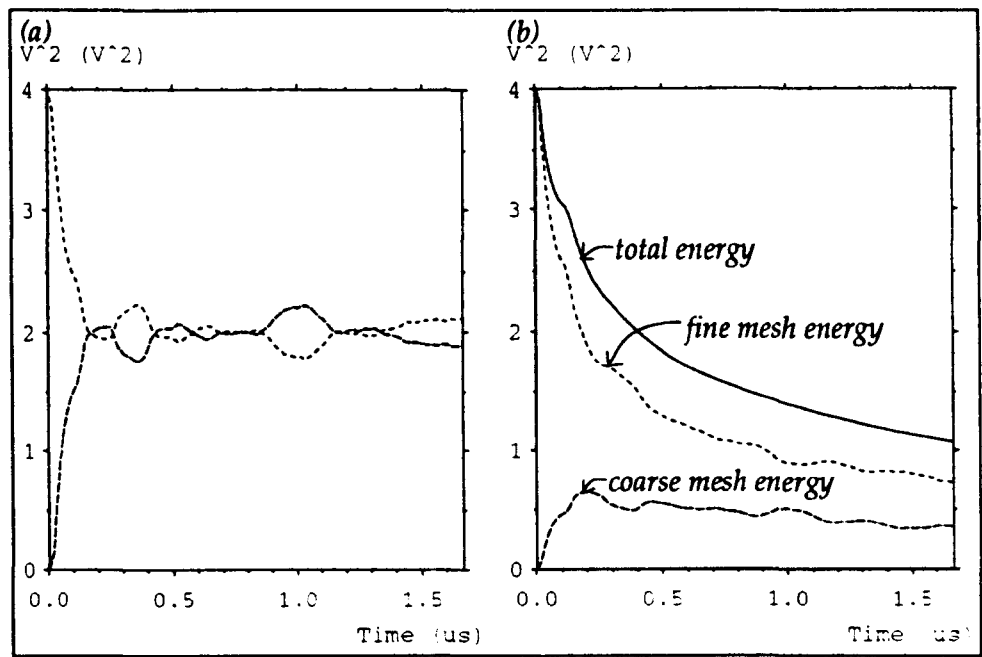


*Fig. 5.14 – Energy due to impulse excitation (a) uniform (b) multigrid*

Consider a 40 m<sup>3</sup> cavity modelled with a uniform fine mesh of node spacing 1 m. The total energy in the system remains constant. If the cavity is divided into two halves, with the excitation wholly contained in one half, then the energy in each half will be approximately equal but will vary slightly as the pulses travel across the cavity. Fig. 5.14a shows the energy in each half for the first 1000 iterations and an impulse excitation. If one half of the cavity is modelled with a coarse mesh of half the resolution and the excitation is in the fine mesh then the results obtained in fig. 5.14b are obtained. It is apparent that the total energy is

decaying exponentially and there is more energy in the fine mesh than in the coarse mesh. The fine mesh contains more energy because there are more degrees of freedom and this result is consistent with that observed for uniform meshes of different resolutions.

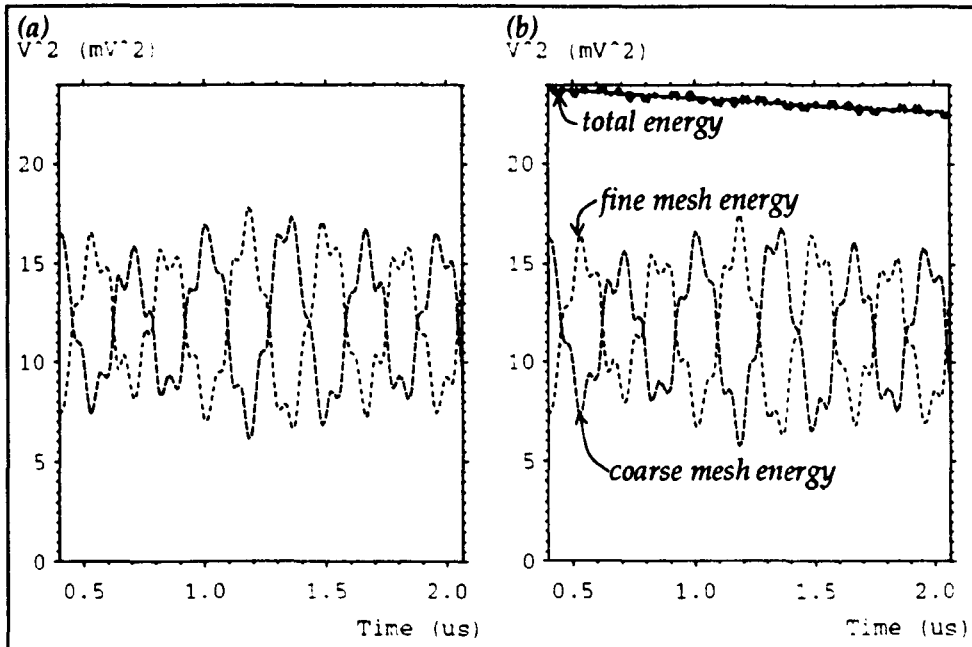


Fig. 5.15 – Energy due to Gaussian excitation (a) uniform (b) multigrid

The loss of energy at low frequencies can be found by injecting a Gaussian pulse. Fig. 5.15a shows the results for a uniform fine mesh for 1000 iterations after the excitation pulse has decayed. A standard deviation corresponding to 10 coarse mesh timesteps was used. The response is dominated by the first few resonances but the average energy in each half of the cavity is the same. The results for the multigrid system are shown in fig. 5.15b<sup>6</sup>. The average energy in the coarse and fine mesh are approximately the same and the decay rate for the total energy is much reduced. After 20000 fine mesh iterations the total energy is 11.5 and is reduced to 7.2 after 40000 iterations.

These and similar results show that at high frequencies there is a significant loss of energy and the fine mesh contains more energy than the coarse mesh. At low frequencies, the fine and coarse mesh contain approximately equal energy and there is very little loss of energy<sup>7</sup>. If the reduction ratio is increased then significant

<sup>6</sup> The slight oscillation in the total energy is due to the fact that some energy at the interface was not considered.

<sup>7</sup> The fact that there is no constant ratio between the energy in the coarse and fine mesh regions



energy loss will occur at lower frequencies. The rate of energy loss will depend on the system modelled, the location and extent of the interface and the reduction ratio. In lossy systems, the energy loss at the interface may well be insignificant when compared to the required losses. There is no problem with applying an impulse excitation in the fine mesh since the highest frequencies are immediately removed by the fine→coarse conversion.

**Test 2 – resonances in a lossless cavity**

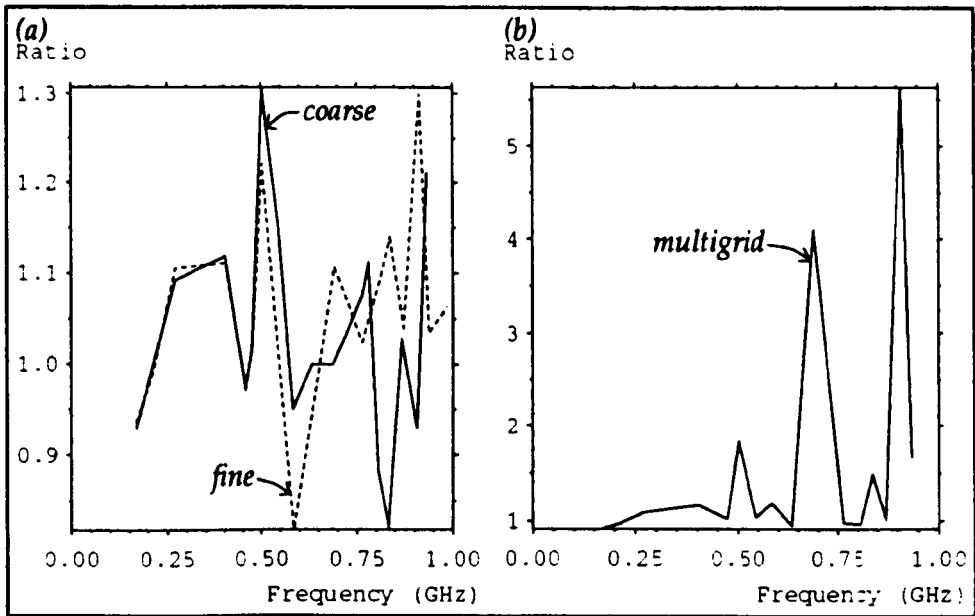


*Fig. 5.16 – Reduction in amplitude of resonances (a) uniform (b) multigrid*

Loss of energy will result in a reduced amplitude for the resonances. This was investigated for a  $2 \times 1 \times 1 \text{ m}^3$  cavity. This was modelled by a 2.5 cm fine mesh, a 5 cm coarse mesh and by the multigrid method with half of the cavity modelled at 2.5 cm and half at 5 cm. A total of 8000 fine mesh iterations were performed. The DFT was then taken for the first 4000 iterations and then for the last 4000 iterations and the ratio of the amplitudes (last÷first) of the resonances was taken. Fig. 5.16a shows the results for uniform fine and uniform coarse meshes. It shows that the amplitudes do change with time but this variation is not great. Fig. 5.16b shows the results for the multigrid case. There are three major peaks: the first corresponds to a peak in the uniform mesh case, the second arises because there are problems with closely spaced resonances and the third is potentially in error because the amplitudes of the resonances are very small (and there are problems with taking the ratio of two

---

means that it is impossible to correctly transfer energy between the meshes at all frequencies.

small numbers). The ratio is greater than unity for almost all of the resonances (indicating a loss of energy) but at frequencies below the  $10\Delta l$  limit for the coarse mesh (600 MHz), the results are acceptable.

## 5.11 Fine features

The multigrid technique should not be used at frequencies above the maximum working frequency of the coarse mesh so that waves passing from the fine mesh can be adequately resolved in the coarse mesh. However, the technique can be used to determine the low frequency properties of features which are smaller than the coarse mesh node spacing.

A known problem with TLM (and also with finite difference schemes) is in the modelling of thin wires<sup>8</sup>. This section is concerned with predicting the resonant frequencies of a 1m dipole in free-space; the prediction should become more accurate as the resolution is increased. The dipole was modelled by short-circuit boundaries at the mid-point of link-lines<sup>9</sup>, with a single node cross-section and it was excited by an impulse magnetic field around the circumference and along the full length. Exciting along the length means that the  $3\lambda/2$  resonance is observed at the output point. Matched boundaries were used to approximate the required open boundary conditions.

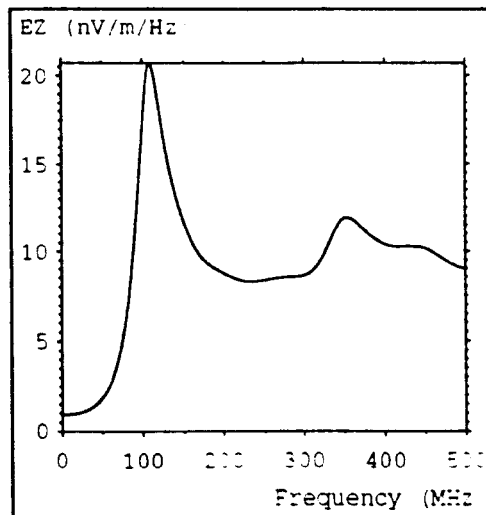


*Fig. 5.17 – Dipole resonances in a uniform coarse mesh*

<sup>8</sup> There are ways to get around this problem but it is the fact that the problem exists which is of interest here.

<sup>9</sup> When modelling dipoles, short-circuits at the mid-point of link-lines are found to give slightly better results than short-circuit nodes.

The electric field at a point away from the dipole is shown in fig. 5.17 for a uniform mesh of 10 cm node spacing. The two resonances occur at 109 MHz and 354 MHz. The analytical values for a thin dipole are 150 MHz and 450 MHz. The discrepancy can be attributed to the fact that the modelled dipole is not thin and there are errors in modelling a wire with a single node cross-section. A layer of fine mesh nodes may be placed around the dipole to increase the resolution. The results are poor if the cross-section of the fine mesh is only a single coarse mesh node. If the cross-section is increased to 3×3 coarse mesh nodes then the results are much better and they are relatively unaffected by any further increase in cross-section. Values for the first two resonances are given below for various reduction ratios and the data is shown graphically in fig. 5.18.

reduction	fine mesh	1st res. (MHz)	2nd res. (MHz)
uniform	–	109	354
2:1	6×6×24	118	377
3:1	9×9×36	122	388
4:1	12×12×48	125	395
5:1	15×15×60	127	400
6:1	18×18×72	128	404
9:1	27×27×108	131	411

For the smaller reduction ratios, a comparison can be made directly with a uniform mesh. For example, fig 5.19a shows the comparison for a 3:1 reduction ratio. The output point for the multigrid system is in the coarse mesh and occupies the same physical position as 27 nodes in the fine mesh (3 in each direction). The upper and lower solid lines show the maximum and minimum output values in this volume and the dashed line shows the multigrid result. There is good agreement between the resonant frequencies but the multigrid curve is slightly too low at some points. For the larger reduction ratios, a uniform fine mesh cannot be used and so comparisons must be made with a multigrid system using a reduction

ratio which is known to work (this implies a finer coarse mesh). Fig. 5.19b shows the comparison for a 9:1 reduction ratio with a coarse node spacing of 10 cm and a 3:1 reduction ratio with a 3.33 cm coarse node spacing. The 9:1 result is bounded by the maximum and minimum values of the 3:1 system for most of the range but the 9:1 result is slightly too low at some points.

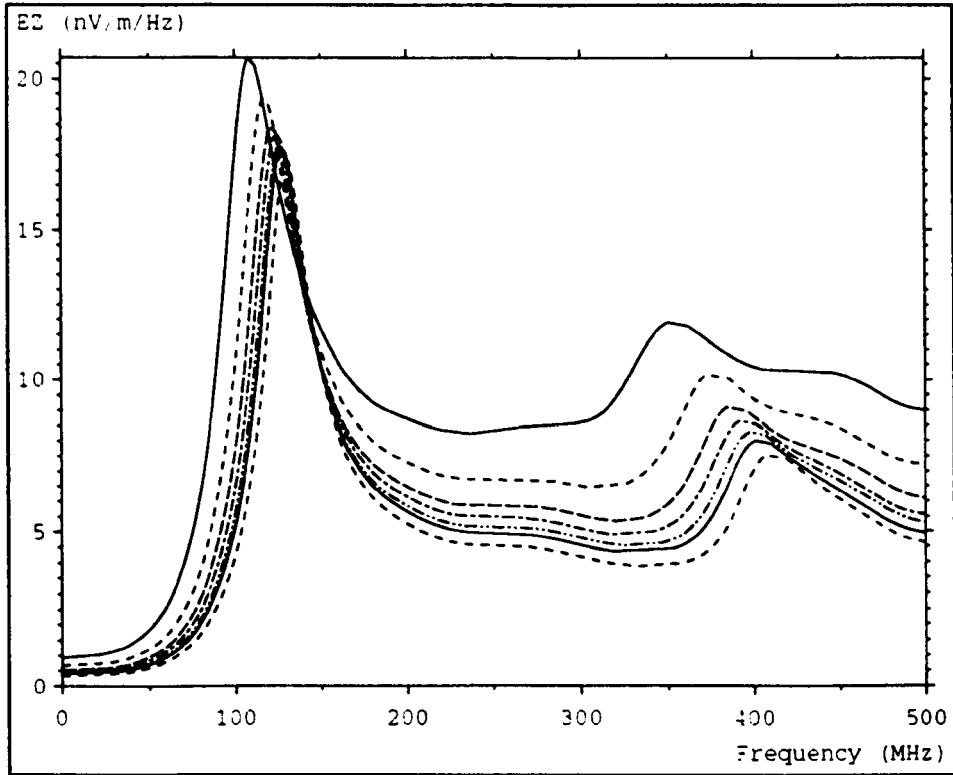


*Fig. 5.18 – Dipole resonances for various reduction ratios*

The results indicate that the multigrid technique can be used to model fine features with reduction ratios of at least 9:1. However, in closed systems, where pulses pass through the interface many times, it may be better to use lower ratios. Further work is needed to fully characterise the interface for a full range of reduction ratios. In particular, it has to be determined whether it is better to increase the resolution on one large step or in several smaller stages.

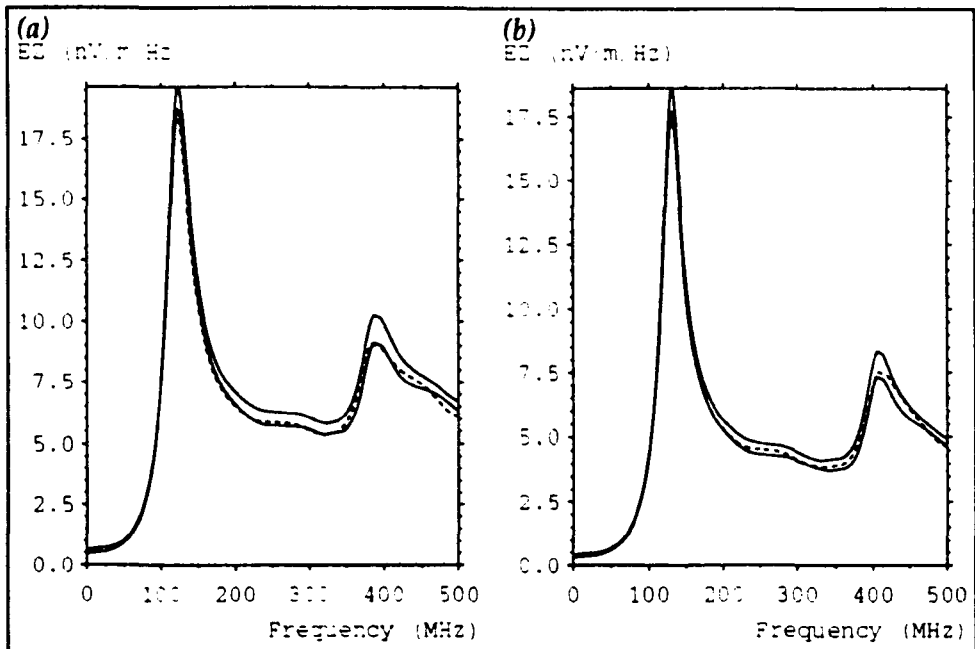


*Fig. 5.19 – Comparisons of (a) 3:1 and uniform (b) 9:1 and 3:1*

## 5.12 Open boundaries

Open boundaries may be approximated by terminating the link-lines adjacent to the boundary with a matched load. This method works perfectly when a plane wave is normally incident upon the boundary but works less well for waves incident at an angle. To minimise the effects of imperfect numerical boundaries, the volume modelled may be increased so that the boundaries are distant from the region of interest. The multigrid technique can be used to place a layer of coarse mesh nodes between the region of interest and the numerical boundary. This allows the boundaries to be placed further away without a significant increase in computer resources. This method may also be applicable when improved open boundary conditions are used and high accuracy is required.

The system considered in this section consists of a Gaussian point source in free-space, as shown in fig. 5.20. Symmetry has been exploited so that only one eighth of the total volume is modelled and the other boundaries are matched. Fig. 5.21a shows lines of constant electric field magnitude (logarithmic scale), at frequencies of 100 MHz and 200 MHz, for a mesh of  $40 \times 40 \times 40$  nodes with a node spacing of 10 cm. The lines should be a set of concentric circles but distortion is apparent in the top right corner (where the wave is incident at an angle) and this

distortion is worse at the higher frequency. The results for meshes of  $50^3$  and  $80^3$  nodes are shown in figs. 5.21b–c, for a  $40 \times 40$  node plane around the source. For the  $80^3$  node case, the distortion has disappeared at 100 MHz but it is still apparent at the higher frequency.

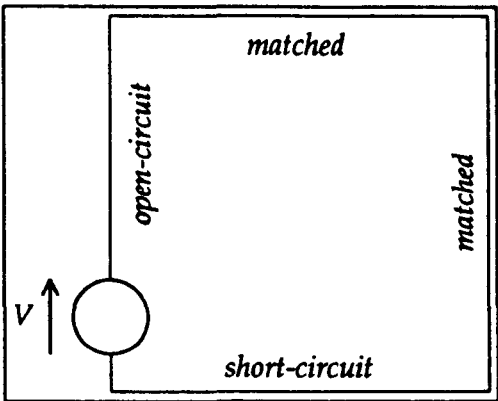


Fig. 5.20 – Point source in free-space

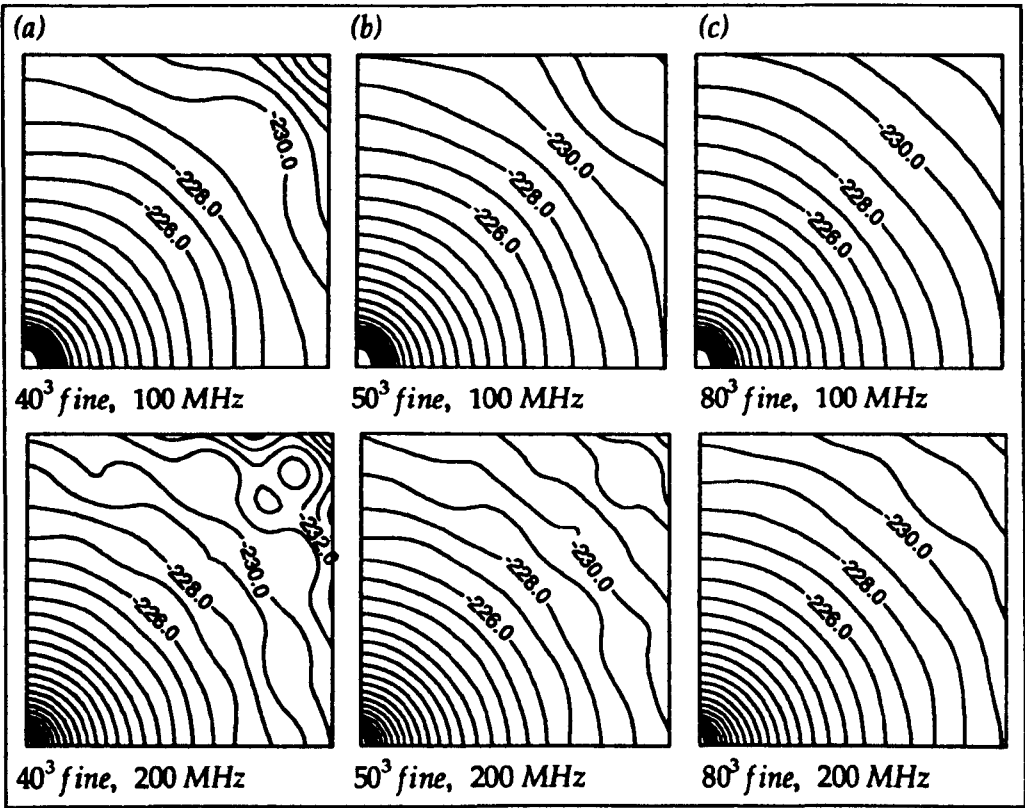


Fig. 5.21 – Matched boundaries with a uniform mesh

The results obtained when a layer of coarse mesh nodes is placed around the  $40^3$  fine mesh are shown in fig. 5.22, for the fine mesh region only. Reduction ratios of 2:1, 4:1 and 8:1 have been used. The results for the 2:1 case are similar to those obtained with a  $80^3$  fine mesh. The best results are obtained with the 4:1 reduction.

For the 8:1 case, the results at 100 MHz are reasonable but those at 200 MHz are completely unacceptable. This is because at 80 cm the  $10 \Delta l$  frequency limit is 38 MHz and at 200 MHz the coarse mesh cannot adequately describe the wave. Even for the 4:1 case, the  $10 \Delta l$  limit is 75 MHz but the method seems to work at 200 MHz.

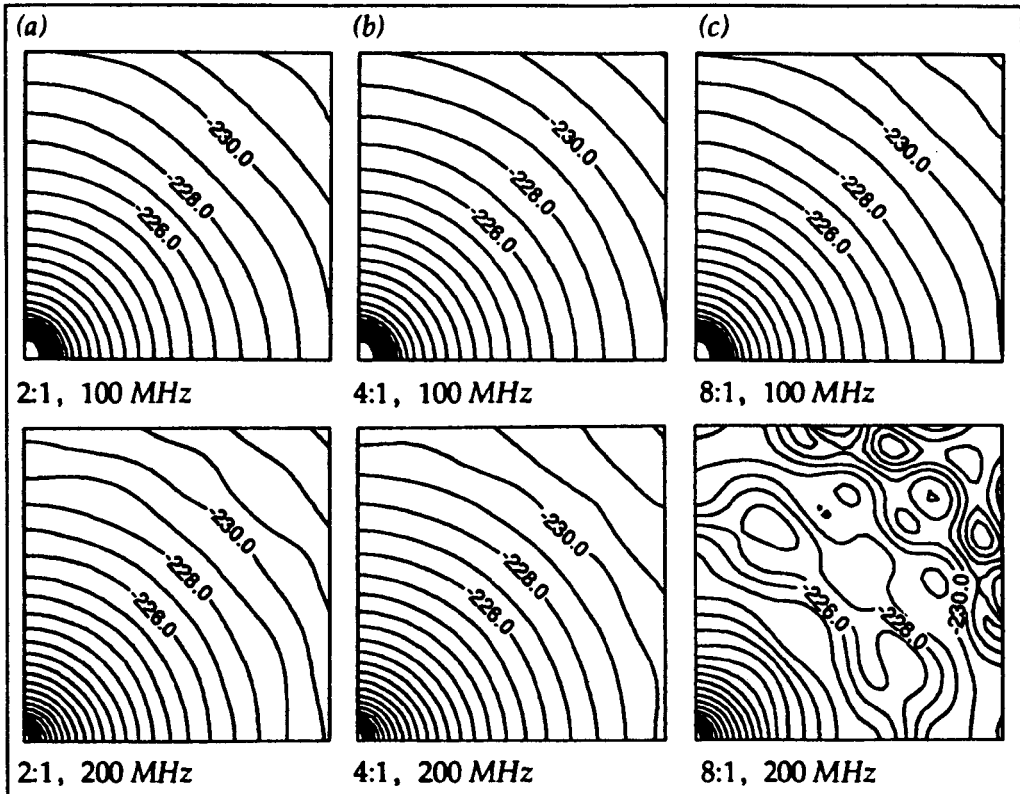


Fig. 5.22 – Matched boundaries with a multigrid mesh

The results show that the effects of imperfect boundaries can be effectively minimised. The relative run-time and storage (when compared to a  $40^3$  fine mesh) for the 4:1 multigrid system are 1.95 and 1.28, respectively. These values are to be compared with 8 (for both run-time and storage) for a  $80^3$  fine mesh in which the results are not as good.

### 5.13 Discussion

The method adopted for the transfer of pulses between the fine and coarse mesh regions is simply to force the average field across the interface to be constant. It has not been possible, and indeed it may not be possible, to obtain a satisfactory method of enforcing conservation of energy. This is because a fine mesh contains

more degrees of freedom and there will always be more (or at least equal) energy stored in the field than for the equivalent coarse mesh. For example, if the field on a single coarse mesh node is the average of the field on several fine mesh nodes then the energy in the fine mesh nodes (proportional to the sum of the square of the voltage pulses) will always be at least equal to the energy in the coarse mesh node (proportional to the square of the sum of the fine mesh voltage pulses). At higher frequencies, the fine mesh will contain a greater proportion of energy due to the increased field variation. If energy conservation was employed then any additional energy transferred into the coarse mesh (over that implicitly transferred when meeting the constant field criterion) would be redundant. It is only when this energy is transferred back into the fine mesh that any advantage is gained (in allowing greater field variations).

As implemented, the interface does not have a physical interpretation. This is a departure from the usual way of doing things in TLM. Methods have been proposed for connecting fine and coarse mesh regions using physical structures, for diffusion problems, in which an additional scattering stage is introduced [52,53]. Such methods are reasonable for spatial substructuring but when temporal substructuring is also employed some means of averaging the field, so that it is constant over a coarse mesh timestep, must be employed <sup>10</sup> and this is inherently a non-physical process.

It has been found that, under certain circumstances, a small d.c. offset is introduced on electric field outputs taken near the interface and this offset is consistent with a charge distribution over the interface. The nature of systems in which this offset is apparent and the mechanism by which charge can become stuck at the interface have yet to be investigated. However, a d.c. offset is not apparent in any of the multigrid results presented in this thesis and it is not considered to be a major problem since any error is only introduced at d.c. (although it may manifest itself over a finite frequency range due to *sinc* presence).

The most unsatisfactory part about the proposed conversion process is the loss of energy. It is inevitable that the fine→coarse mesh conversion must behave as

---

<sup>10</sup> In diffusion problems this is not necessary and it is possible to directly transfer pulses between the two meshes by assuming that the interface is a perfect insulator during certain parts of the calculation [53].



some form of low pass filter but this should ideally have a sharp cutoff so that frequencies of interest are not significantly attenuated. It may be possible to derive an improved conversion method but this must be computationally inexpensive with only a small storage requirement if the utility of the multigrid technique is to be maintained. By running the coarse mesh at a greater speed it is possible to reduce the loss of energy — in effect taking just a spatial average rather than both a spatial and temporal average, but this increases the storage requirement and does not appear to have any significant advantage, for the range of systems considered. Further work is needed to determine the maximum reduction ratio for a given error and to determine whether increasing the coarse mesh speed is worthwhile for the higher reduction ratios.

By adopting the correct calculation order, the problem of resonance splitting appears to have been removed. It is not possible to state that splitting definitely will not occur, but it does appear reasonable to suggest that splitting should only occur if the coarse mesh is operated near its upper frequency limit. However, in a symmetrical system, it would be advantageous to place the fine and coarse mesh regions symmetrically so that splitting is less likely to occur.

The multigrid technique has been derived and used for the restricted case of cubic nodes with the same reduction ratio in all three directions. In principle, the method can be extended to account for non-cubic nodes and different reduction ratios. This would enable a combined multigrid and graded mesh system to be defined and the method could be generalised to orthogonal curvilinear meshes. The use of stubs to slow down the speed of wave propagation means that the timestep in each region can be selected in a much more flexible way since it can then be chosen independently of the node spacing. There may be some advantage in allowing meshes to intersect at an arbitrary angle but this is likely to reduce the accuracy of the method.

# **Chapter 6**

## **Implementation Issues**

### **6.1 Introduction**

It is not appropriate to consider the application of TLM to EMC problems without considering how the method is actually implemented; theoretical concepts must be translated into real programs so that useful results can be obtained in an efficient manner. As with any numerical technique, the overall utility of the TLM method is limited by the available computer resources. Restrictions on memory and run-time have led to the development of graded mesh and multigrid techniques. These restrictions are particularly acute for EMC type problems where the requirement is to simultaneously represent both fine features and large volumes which sometimes extend to infinity. The development of more efficient algorithms opens up the possibility of using a uniform fine mesh without resorting to such techniques.

In the following sections, the basic algorithms and some of the features relevant to program efficiency will be described. Obviously, in a research environment, a compromise has to be made between development of the method, development of the code and obtaining actual results. However, when many hundreds of simulations have to be performed and each of these takes many hours to run, it is appropriate to invest in improving the efficiency of the actual TLM simulation as well as the efficiency of any pre- and post-processing activities.

Ideally, a TLM simulation program would consist of hand optimised machine code tailored to a specific problem definition. This could be achieved, at least to a certain extent, by writing a TLM compiler which would take the problem definition and output the code to run it. In practice, simulation programs are often compiled from a high level language and are completely general so as to avoid a proliferation of smaller programs which can only be used for a limited range of problems. The overall efficiency of the code is then limited by the compiler and the range of optimisations it supports. The disadvantage of using a general code is that simple problems may take longer to run. However, experience has shown that it is better

to implement things in a general way rather than imposing restrictions which have to be revised at a later date. In any case, provided that the key areas of the TLM calculation are well written, lack of efficiency in other areas will have negligible impact on overall performance.

It is likely that in the future greater use will be made of the emerging parallel processing technologies [36]. The nature of the TLM algorithm is such that it is ideally suited to direct implementation [54,55].

## 6.2 Run-time and storage efficiency

In a TLM calculation, most of the run-time is taken up in the scattering procedure. The procedures for connect, boundaries and outputs are much less computationally intensive. It is therefore advantageous to optimise the scattering algorithm as far as possible. Further gains can be made, particularly when there are large regions of empty space, by implementing several procedures of increasing generality since, for example, the scattered pulses for the 12-port node can be computed much more quickly than those for a node with stubs. The decision on which procedure to use can be made on a per node basis as the calculation proceeds.

The scattering procedure for the standard 12-port node requires 36 additions/subtractions and 12 multiplications by a constant if it is calculated directly from the equations in §2.2. The algorithm developed by Naylor and Ait-Sadi (see §2.3.2) would require 42 additions/subtractions and 6 multiplications by a constant. The total number of operations is the same and so the fastest method will depend on the relative efficiency of the addition and multiplication operations. This will depend upon machine architecture and on whether fixed or floating point arithmetic is used. Most modern computers perform floating point operations in hardware and so there may be little advantage in adopting a fixed point solution. For the work presented in this thesis, single precision floating point numbers have been used.

For a fully featured stub-loaded node, with both electric and magnetic losses, the new algorithm requires 54 additions/subtractions and 12 multiplications<sup>1</sup>,

---

<sup>1</sup> This assumes that the product of the loop current and  $Z_0$  is calculated rather than just the current (so that multiplications do not have to be performed for each scattered pulse) and that the product

provided that two quantities <sup>2</sup> (six for a graded mesh or for anisotropic materials) are stored for each node type. This is to be compared with 126 additions/subtractions and 144 multiplications which are required for direct implementation for a node without losses [56] <sup>3</sup>. When implementing the hybrid node, which is generally used for graded meshes, the storage required to store the scattering coefficients at every node is excessive and it may be necessary to recalculate the coefficients on each iteration. A choice also has to be made on whether the link-line and stub parameters are stored or recalculated.

There is an obvious tradeoff between storage and run-time efficiency as regards the scattering coefficients. For the hybrid node, if storage is required for both the link-line and stub admittances then a total of 21 quantities are required for each node. The situation is less severe for a uniform mesh in which there are only a small number of different material properties since the scattering coefficients need only be stored for each material type rather than for each node. This method can also be used with the graded mesh provided that the total number of distinct node sizes is small.

Space savings can be made by only allocating storage for stubs on nodes which actually require them. These savings will be significant for systems in which a large part of the volume is free-space. The disadvantage is that it becomes necessary to keep track of stub storage for each node. A compromise solution is to divide the problem space into a number of cuboid meshes (even for non-multigrid systems) in which stub storage is allocated on a per mesh basis. An additional connection stage is then required to join these meshes together.

The connection process is fairly inexpensive in terms of run-time. This means that it is reasonable to apply link-line boundary conditions in regions where they are needed and then subsequently apply the standard connect process over the whole mesh. The boundary conditions are applied in such a way that the correct pulses are obtained after connection. This avoids having to store boundary conditions for every link-line in the mesh. An alternative method, which was not implemented, would be to divide all of the link-lines into a set of cuboid regions

---

of the open-circuit stub voltage and the stub admittance is stored rather than just the voltage.

<sup>2</sup> These quantities are used to determine the node voltages and currents.

<sup>3</sup> The algorithm described in this paper has now been superseded.

and then apply the appropriate boundary condition or connection for each separate region.

### 6.3 Calculation order

The calculation order for uniform and graded mesh systems can be written as follows:

- apply node impulse excitation (first iteration only) and sources
- take node outputs (calculated from incident pulses)
- scatter
- apply link-line impulse excitation (first iteration only) and sources
- take link-line outputs (calculated from scattered pulses)
- apply link-line boundary conditions
- connect

These steps are repeated for the required number of iterations. Typically, either node or link-line excitation is used; it is unlikely that they would be used together. It is possible to express both node and link-line outputs solely in terms of either incident or scattered pulses but the above approach is more general. In particular, the correct output values are obtained on the first iteration, for both node and link-line outputs, when the output is coincident with the excitation.

Additional steps must be included for multigrid systems. Converted pulses moving out from the interface are inserted into the mesh before the node excitation is applied and pulses to be converted are removed from the interface after the link-line outputs are obtained. The capability of running the coarse mesh at higher speeds can conveniently (although not optimally) be implemented by swapping pulses to and from additional storage before the connect procedure. This avoids making major changes to the program for something which is only occasionally useful.

### 6.4 Virtual memory

Virtual memory systems map a large logical address space to a smaller physical address space by swapping pages to and from disk. This technique allows

a program to transparently access memory resident data structures whose storage requirement exceeds the physical memory capacity of the machine. In principle, code may be written to perform a TLM calculation on a very large mesh in exactly the same way as for a mesh which is wholly memory resident. However, if the code is written in a straightforward manner (e.g. scatter at all nodes then connect at all nodes) then the entire mesh must be brought into memory several times during each iteration, resulting in very inefficient operation. A more efficient method is to divide the mesh into a number of overlapping regions, each of which will fit into physical memory. A number of iterations are then performed in each region before the next is processed. The interface between any two regions moves within the overlap to take account of the temporary loss of connectivity.

The operation of the method is illustrated for a mesh which is divided into two regions with an overlap of two nodes, as shown in fig. 6.1<sup>4</sup>. The letters "B", "C", "D" and "E" are used to represent layers which are one node thick. The letters "A" and "F" represent layers of arbitrary thickness away from the interface. Three iterations are performed in each region before moving on to the other region. This is shown schematically in fig. 6.2. The shaded areas indicate where the calculation is performed and the numbers give the iteration. The nodes on which scattering takes place and the nodes between which connection takes place are also shown. For example, for the first stage, scattering takes place for all nodes in the range "A" to "D" (inclusive) and connection takes place on nodes in the range "A" to "C"; the pulses on node "D" are left until a later stage.

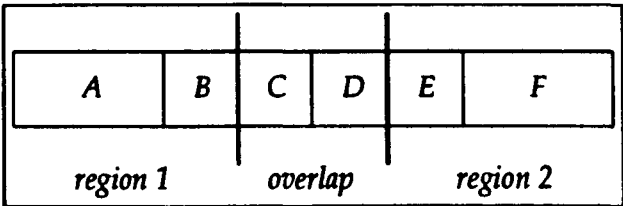


Fig. 6.1 – Mesh split into two regions

There is very little overhead in using this method although the code does become more complex. Care must be taken when dealing with features which intersect the overlap. For example, outputs must only be taken after the required number of iterations have been performed. In principle, the method can be

<sup>4</sup> The method is described in a more general way in appendix 2.

extended so that the mesh is divided into more than two regions in all three dimensions.

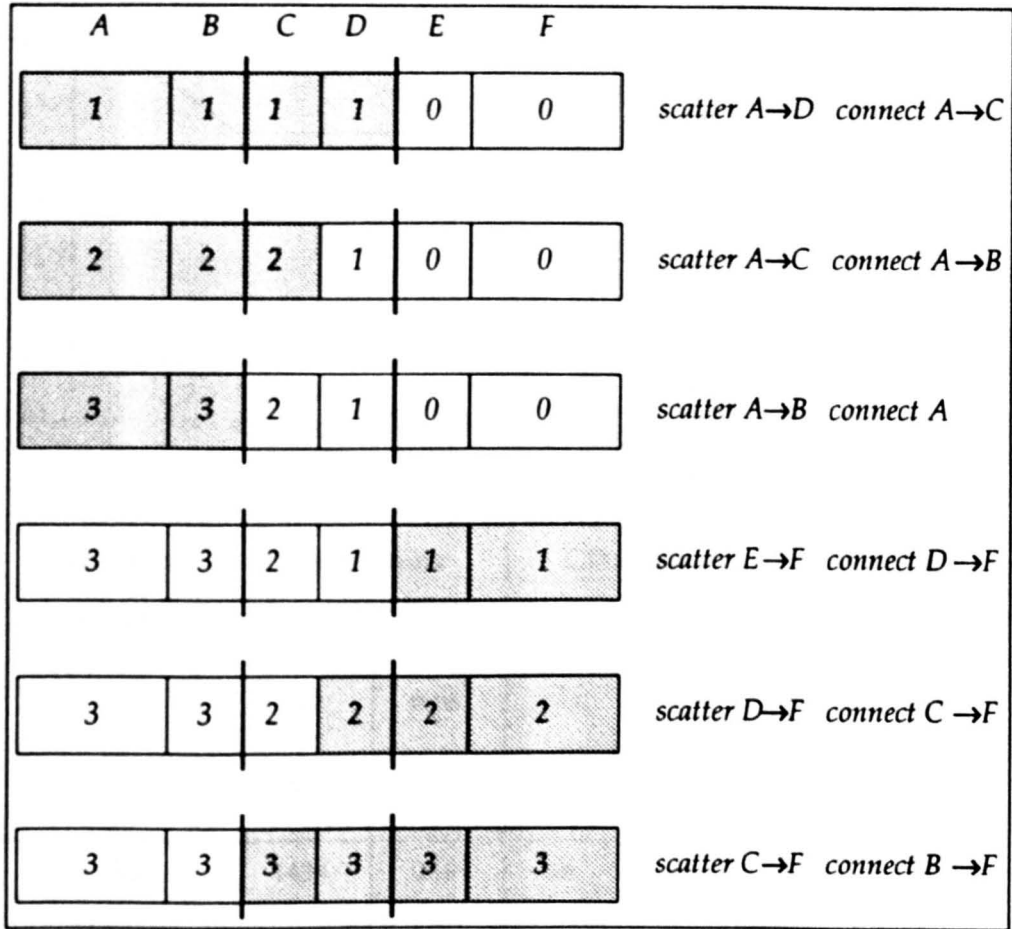


Fig. 6.2 – Operation of the method

Two basic tests have been performed to compare the standard method with the new method. The results are necessarily specific to a particular machine, in this case a VAXstation 3100 with 24 Mbyte of RAM running VMS 54. The program was written so that the entire mesh was stored on one large array with the dimensions arranged so that each region was contiguous in memory<sup>5</sup>. The paging mechanisms built into the operating system are not necessarily optimised for a single process with a large memory requirement [57] and although it may be possible to gain some improvement by tweaking the system parameters, it may be necessary to abandon transparent paging in favour of explicitly reading and writing parts of the array to and from disk. This may need to be done in a machine specific manner for maximum efficiency.

<sup>5</sup> For the new method, a slight performance improvement was gained by locking the section of the array corresponding to the overlap into the working set.

Test 1

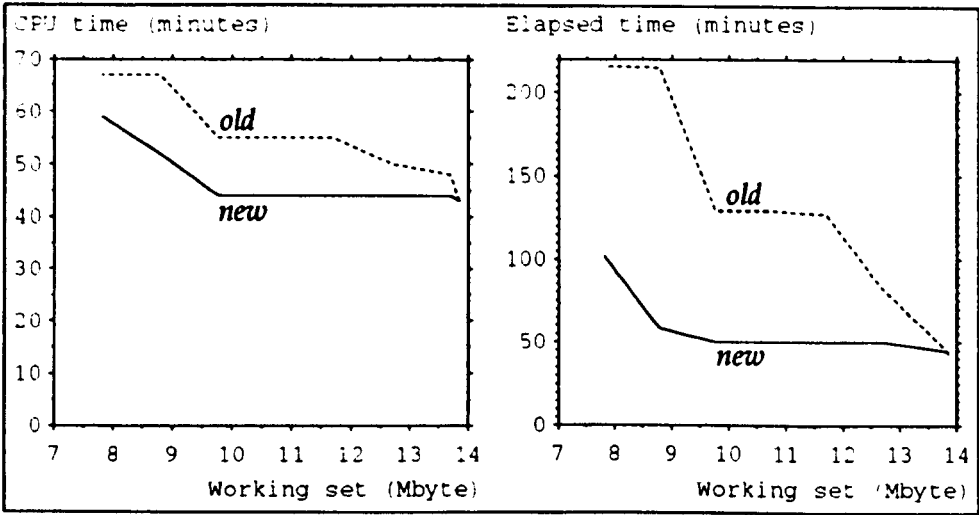


Fig. 6.3 – CPU and elapsed time against working set limit

working set (Mbyte)	page faults (1000's)		CPU time (minutes)		elapsed time (minutes)	
	old	new	old	new	old	new
—	50	53	43	43	43	44
13.7	1434	246	48	44	49	45
12.7	1881	245	50	44	82	50
11.7	2807	245	55	44	127	50
10.7	2809	245	55	44	129	50
9.77	2818	245	55	44	129	50
8.79	5565	2353	67	52	215	58
7.81	5567	4132	67	59	216	102

This test was done for a problem with a constant size of 13.85 Mbyte with a limit set on the maximum size of the working set. The machine was only lightly loaded at the time of the tests. The CPU and elapsed time are shown graphically in



fig. 6.3. It is apparent that when the working set size is reduced there is an increase in both CPU and elapsed time. The results for the new method are significantly better than for the standard algorithm.

### Test 2

This test was done for problems of increasing size with a constant working set limit. For the last case (marked with a star) the page fault cluster (the number of pages brought into memory on each page fault) was increased from the default value of 16 to 128. The results show that when the requirement increases beyond the available memory there is an increase in CPU time and a dramatic increase in elapsed time. Significant savings can be made by using the new method. In practice, the method was mainly used when the mesh was just too big to fit into memory; for larger problems the CPU time was unacceptable.

nodes (1000's)	page faults (1000's)		CPU time (minutes)		elapsed time (minutes)	
	old	new	old	new	old	new
295	50	53	43	43	43	44
386	504	334	57	57	59	58
420	649	78	87	62	308	79
420 *	597	81	86	63	299	80

A slightly different approach has recently been proposed for the finite difference time domain method [58] and this would also be suitable for implementation in TLM. In this approach, the calculation proceeds in a moving window and after each iteration a single node thick layer on one side of the window is written to disk and a new layer is read from disk on the other side. The main difference between this formulation and the one previously described is that disk operations occur on every iteration rather than occurring in a concentrated burst after several iterations. However, modern computers can be fitted with large amounts of memory and if such machines are available then code can be written in

a straightforward manner without resorting to such techniques.

## 6.5 Problem definition

### 6.5.1 Coordinates

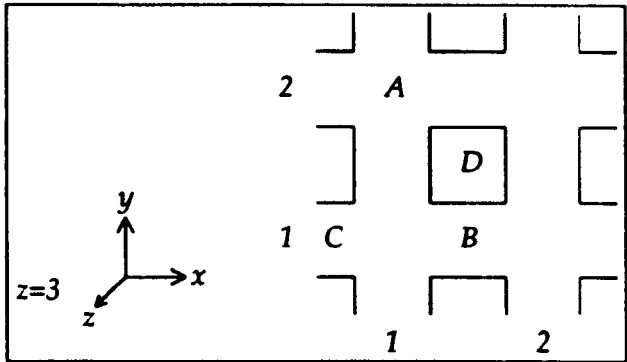


Fig. 6.4 – Plane through a 3-dimensional mesh

Within a 3-dimensional TLM mesh, it may be necessary to refer to nodes, link-lines and the space between nodes in which charge may reside. The position of a node may be defined in a straightforward manner by assigning integers along each of the coordinate axes. For example, the node marked "A" in fig. 6.4 is denoted by (1,2,3). The link-lines are placed between nodes in one direction (to which they are parallel) and are coincident with the centre of nodes in the other two directions. To avoid introducing additional coordinate systems for the link-lines, the coordinate in the direction parallel to the link-line may be replaced by two numbers giving the nodes between which the link-line is connected. For example, the link-line marked "B" is denoted by (1\_2,1,3). Note that there are two link-lines on each arm of the node and which link-line is required will be determined by the context in which the coordinates are used. For example, the z-component of the electric field can only be excited on the link-line polarised in the z-direction. At boundaries, only one half of the link-line exists and this is denoted by omitting the non-existent node number. For example, the incomplete link-line marked "C" is denoted by (\_1,1,3). This system readily extends to describing the space between nodes by using pairs of node numbers for all three coordinates. For example, if the point "D" is between nodes 3 and 4 in the z-direction then it may be denoted by (1\_2,1\_2,3\_4). A range of values may be specified by separating the minimum and maximum values with a colon. In this way, points, lines, planes and cuboids can all

be readily defined.

### 6.5.2 Input file

Ideally, a graphical user interface would be employed so that the user could enter details of a complex system and immediately see the resultant structure. However, the time needed to develop such an interface would be considerable. It is possible to make use of a commercial computer aided design (CAD) package [59] but it must be sufficiently flexible to support the full range of features required. In industry, it is likely that the simulation package will have access to the existing databases, which have been used to design the system under test, but some additional information will still be required to describe exactly how features are to be modelled, at least in the development stages of the model.

The approach adopted for the work in this thesis was to describe the system in a relatively user friendly manner by means of a text file. This file was then translated (as a pre-processing operation) to a new file which could be easily read by the calculation program. This approach has a number of advantages:

- Large simulations will typically be submitted to some form of batch queue to be run when the system load permits. It is important that the problem definition is verified before the simulation is performed so that the user can take corrective action.
- The size and complexity of the calculation program can be reduced since it does not have to process complicated problem definitions.
- Additional pre-processing operations for non-standard features can be easily included.
- The calculation program is, to some extent, independent of the pre-processing operations so that a more user friendly input format (e.g. CAD package) could be substituted in the future.

A simple example of an input file is given below for a 1 m<sup>3</sup> cavity. A mesh of 10×10×10 nodes is defined with a uniform node spacing of 10 cm and 1000 iterations are requested. Short-circuits are placed on all six external boundaries. The system is excited by an impulse electric field, of unit amplitude, extending across the problem space and a single electric field output is requested.

```

name = ex1;
title = "1.0*1.0*1.0 m^3 cavity";
mesh = 10*10*10;
dl = 0.1;
iterations = 1000;
(xmin) (ymin) (zmin) (xmax) (ymax) (zmax) :short;
(1:10,2,2) :excite=ex /amp=1.0;
(8,8,8) :output=ex;

```

### 6.5.3 Multigrid problem definition

In a general uniform mesh system, space is modelled by one or more uniform meshes which are connected together to produce the required volume. In a multigrid system, these meshes may have different node spacings and timesteps. There are two basic methods which can be used to define the geometry of a multigrid system:

- define the location of the fine mesh region in terms of the coarse mesh within which it is placed.
- define the location of the interface in each of the two meshes.

The first method allows easy definition of simple geometries, for example fig. 6.5a. The second method is more general in that it allows fine mesh regions which are not wholly embedded in a coarse mesh to be defined, for example fig. 6.5b. This method does however have the disadvantage that it is more difficult to determine the physical position of an arbitrary point and it is possible to define non-realisable systems. The second method was used for all later work in 3-dimensions.

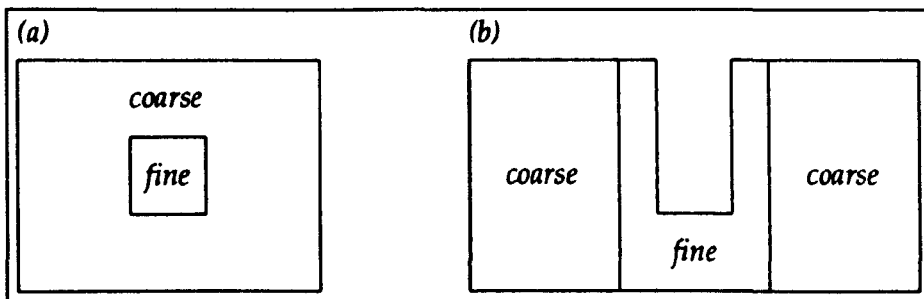


Fig. 6.5 – Examples of multigrid systems

The node spacing and timestep for each mesh are set to be fractions of the largest node spacing and timestep, which are specified in the same way as for a uniform mesh. The restriction is imposed that these fractions are the reciprocals of

integers. The interface is divided into a number of planes located at the mid-point (and normal to) link-lines. The number of link-lines enclosed by each plane and the relative node spacing and timestep determine the coefficients to be used in the conversion process. These coefficients will now be obtained for the case of a single coarse mesh link-line connected to many fine mesh link-lines and for a general plane with coordinates  $(x_{min}:x_{max}, y_{min}:y_{max}, z_{min}:z_{max})$  in which the minimum and maximum node numbers for the direction normal to the plane are equal. The spatial reduction ratio,  $l_i$ , is given by

$$l_i = \begin{cases} 1 & L_i \leq L_j \\ L_i / L_j & L_i > L_j \end{cases}$$

where  $1/L_i$  is the relative node spacing (with respect to the largest node spacing) and  $1/L_j$  is the corresponding quantity for the other interface plane. The number of connection points in each direction is then given by

$$x_{c_i} = (x_{max} - x_{min}) / l_i$$

$$y_{c_i} = (y_{max} - y_{min}) / l_i$$

$$z_{c_i} = (z_{max} - z_{min}) / l_i$$

The temporal reduction ratio,  $t_i$ , is given by

$$t_i = T_i / C_i$$

where  $1/T_i$  is the relative timestep and  $C_i$  is the number of conversions from level (i). For the more complicated conversion methods (abandoned for the later work), in the general case, the number of pulses taken from each link-line in one conversion may not be equal to the number of pulses inserted into each link-line. The number of pulses to insert into each link-line,  $t'_i$ , is given by

$$t'_i = T_i / C'_i$$

where  $C'_i$  is the number of conversions to level (i).

A simple example in which a fine mesh is used to describe a linear dipole is given below. Two meshes are defined: a  $51 \times 51 \times 68$  coarse mesh (denoted by "/1") and a  $15 \times 15 \times 110$  fine mesh (denoted by "/2"). The node spacing and number of iterations for the coarse mesh are set to be 5 cm and 2000, respectively. The relative node spacing and timestep for the fine mesh are both set to be  $\frac{1}{2}$ . The six external boundaries of the fine mesh are connected to the inside of a region in the coarse

mesh and the coarse mesh nodes within this volume are set to be *null* so that no time is wasted evaluating the scattered pulses. Matched boundaries are placed around the coarse mesh to approximate open boundary conditions. The dipole is modelled by short-circuits at the mid-point of link-lines and it is excited by introducing voltage pulses around the circumference and along the length. A single electric field output is taken in the coarse mesh.

```

name = ex2;
title = "1m dipole, excite length";
mesh = 51*51*68 /1;
mesh = 15*15*110 /2;
dl = 0.05;
iterations = 2000;
m_level = c :speed=1 :space=1 :mesh=1;
m_level = f :speed=5 :space=5 :mesh=2;
m_order = f, f, f, f, f>c, f, c, c>f;
m_connect ( 23_,24:26,24:45)/1 (xmin)/2;
m_connect ( _27,24:26,24:45)/1 (xmax)/2;
m_connect (24:26, 23_,24:45)/1 (ymin)/2;
m_connect (24:26, _27,24:45)/1 (ymax)/2;
m_connect (24:26,24:26, 23_)/1 (zmin)/2;
m_connect (24:26,24:26, _46)/1 (zmax)/2;
(24:26,24:26,24:45)/1 :null;
(xmin)/1 (ymin)/1 (zmin)/1
(xmax)/1 (ymax)/1 (zmax)/1 :matched;
(7_,8,6:105)/2 (_9,8,6:105)/2 (8,7_,6:105)/2
(8,_9,6:105)/2 (8,8,5_)/2 (8,8,_106)/2 :short;
(7,8,6:105)/2 :excite=vxpz /amp=1.0;
(9,8,6:105)/2 :excite=vxnz /amp=1.0;
(8,7,6:105)/2 :excite=vy pz /amp=1.0;
(8,9,6:105)/2 :excite=vynz /amp=1.0;
(7,25,33)/1 :output=e z;

```

#### 6.5.4 Graded mesh problem definition

In a graded mesh, the node size along each of the coordinate directions must be specified. This can be done by supplying the size of each node individually or by defining an arithmetic or geometric progression. It is more difficult to locate features by node numbers since the physical position will depend upon the preceding node dimensions.

## 6.6 Output data

If completely general output options are to be supported then a large number of different output types must be implemented. In addition to the standard electric and magnetic field outputs on nodes and link-lines, which must be implemented for field components and link-lines in all three directions, it may be necessary to output on incomplete link-lines or on link-lines with an internal boundary. Further outputs may be required for the current flowing through a short-circuit node or an internal or external boundary, the charge at a point, the power loss in a boundary or lossy node, the power flow through a surface or the stored energy. The method adopted was to only implement the most common output types but to allow individual voltage pulses to be output so that non-standard outputs could be synthesised as a post-processing operation. A large number of options are also required to allow general excitation but the problem is less severe, particularly for impulse excitation, where the required input can be imposed assuming that there are no other pulses in the mesh.

If a limited number of output points are specified then it is reasonable to write the time domain data to a file and then decide on what post-processing operations are required. For example, it is then possible to determine whether sufficient iterations have been performed or to find the most appropriate window width. If frequency domain output is required at many output points (e.g. over a plane) then the volume of time domain data may be too great. To overcome this, the DFT may be evaluated as the calculation proceeds by maintaining the appropriate running sums. In order to do this, the frequencies of interest and the characteristics of any window function must be known before the calculation starts. This means that it may be necessary to perform an additional simulation to first determine what frequencies are required.

Another area in which problems can arise is that of summing a quantity over a volume, for example, summing the square of the voltage pulses over the whole mesh will give the energy at a particular instant in time, or, evaluating the sum of the square of the modulus obtained from a DFT over a plane will give power flow. It has to be decided whether it is more efficient to output all of the data and then

sum or whether it is best to sum the data internally and only output the result. It is often necessary to use the second solution but in this case it is more difficult to see what has happened if the data is not as expected.

In general, it is possible to output both time and frequency domain data for points, lines, planes and cuboids. It is appropriate to extract as much data as possible from a single TLM run. This means that the format of the output file must be sufficiently flexible to deal with any output combination. In addition, it must be able to cope with complex data (from a DFT) and vector data (e.g. all three components of the electric field). It is also useful if the output file contains information on all pre- and post-processing operations so that checks can be made on which programs have been run if the data turns out to be erroneous.



# Chapter 7

## Bounded Systems

### 7.1 Simple cavity

The resonant frequencies of a lossless cavity can be predicted using TLM. This is done by placing short-circuit boundaries around the mesh, exciting the field inside the cavity and then transforming the time domain data obtained at the output point into the frequency domain. The peaks in the response correspond to the resonant frequencies. The prediction of resonances by this method is only useful for validation purposes since the exact frequencies can be obtained analytically from the formula [24, p501]

$$f_{nmp} = \frac{c}{2} \sqrt{\left(\frac{n}{x_1}\right)^2 + \left(\frac{m}{y_1}\right)^2 + \left(\frac{p}{z_1}\right)^2}$$

for a cavity of dimensions  $x_1 \times y_1 \times z_1$ , where  $n$ ,  $m$  and  $p$  are the number of half-sinusoidal variations in the standing wave pattern along each of the coordinate axes.

The cavity may be excited in a number of ways. It is appropriate to apply an impulse field excitation in free-space so that no additional structure is introduced into the system, which might alter the resonant frequencies. This excitation may be applied throughout the volume of the cavity, on a plane, along a line or at a point. The way in which the system is excited will determine which modes are observed at the output point. The positions of both the excitation and the output point must be chosen to avoid nulls in the standing wave pattern.

Consider a  $1 \text{ m}^3$  cavity modelled by a  $40^3$  node mesh. Fig. 7.1a shows the  $x$ -component of the electric field ( $E_x$ ) for node (25,25,25) when this same field component is excited uniformly throughout the problem space. The only modes observed are the  $TE_{0np}$  modes where  $n$  and  $p$  are both odd. Most of the energy is in the lower frequency modes. Fig. 7.1b shows the corresponding graph when the system is excited along the plane (1:40,1:40,16). In this case,  $p$  can take any value but  $n$  must still be odd and, also, there is more energy in the higher frequency modes. When the system is excited along the line (1:40,16,16), additional modes for which  $n$

is even are observed, as shown in fig. 7.1c. Fig. 7.1d shows the graph obtained when the excitation is at the point (16,16,16). In this case, all modes are excited and most energy is at the higher frequencies (above 500 MHz). The resonant frequencies obtained from the simulation are in very good agreement with those obtained analytically.

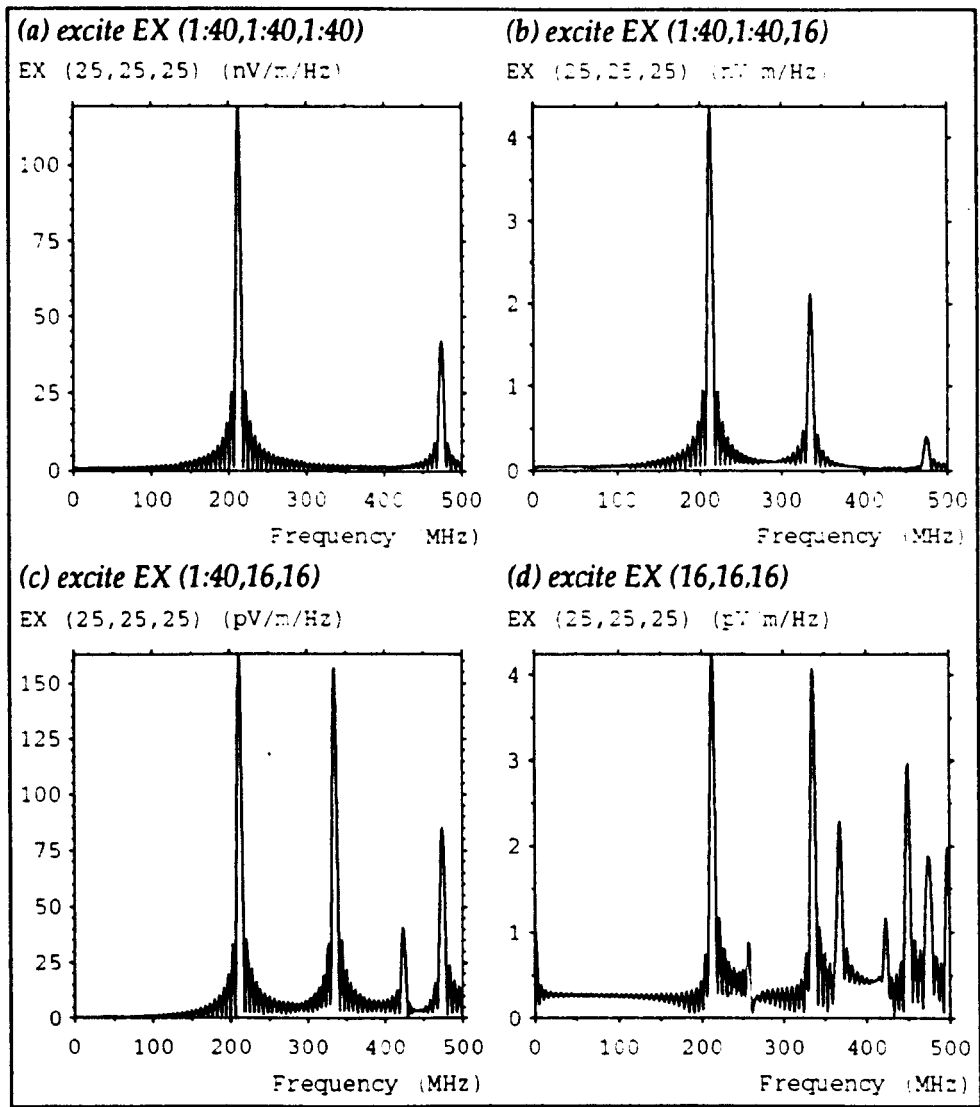


*Fig. 7.1 – Cavity resonances for different excitations*

Exciting the system by an electric field at a point does introduce problems. A d.c. offset is produced because the excitation inserts static charges into the mesh (when the excitation extends across the cavity these charges can flow around the boundary). This d.c. value can be ignored in many situations but if its presence cannot be tolerated then a voltage source with finite series resistance can be used to excite the system. This has the disadvantage of introducing additional structure

into the cavity but if the source is small the effects should be negligible. An alternative method is to excite the link-lines surrounding the node excitation so that there is no net charge at the ends of the excitation, but this does tend to introduce additional noise into the system. Another problem with excitation at a point is that the signal at the frequencies of interest may be masked by larger high frequency signals. This can be overcome by using a Gaussian pulse or by applying an appropriate window function.

The field profile for a particular resonance can easily be compared with that predicted analytically. Fig. 7.2 shows the field profile for  $E_x$ ,  $H_y$  and  $H_z$  on planes normal to the  $x$ -axis for the first resonance when the system is excited by  $E_x$  along a line. The field is constant along the  $x$ -axis and all other field components are zero. The electric field is of greatest magnitude in the centre of the cavity and so this is shown for a central plane. The magnetic field is of greatest magnitude near the walls and this is shown on a plane adjacent to the wall. It is apparent that the expected sinusoidal field variation is obtained in all cases.

If more than one field component is required then it is possible to excite multiple components in a single simulation. However, the amplitudes of the resonances for a particular field component may not be the same as if only that component is excited. For example, fig. 7.3 shows  $E_x$  for a cavity measuring  $1.0 \times 1.1 \times 1.2 \text{ m}^3$  with  $\Delta l = 5 \text{ cm}$ , excited by an impulse electric field at (7,7,7). Fig. 7.3a is for the case when  $E_x$  only is excited and fig. 7.3b is for the case when  $E_x$  and  $E_z$  are excited equally. It is apparent that the amplitudes of the modes which are not invariant in the  $x$ -direction (e.g. the  $TE_{111}$  mode at 237 MHz) do vary with the excitation. However, this is unlikely to be important unless the amplitudes of the resonances are required.

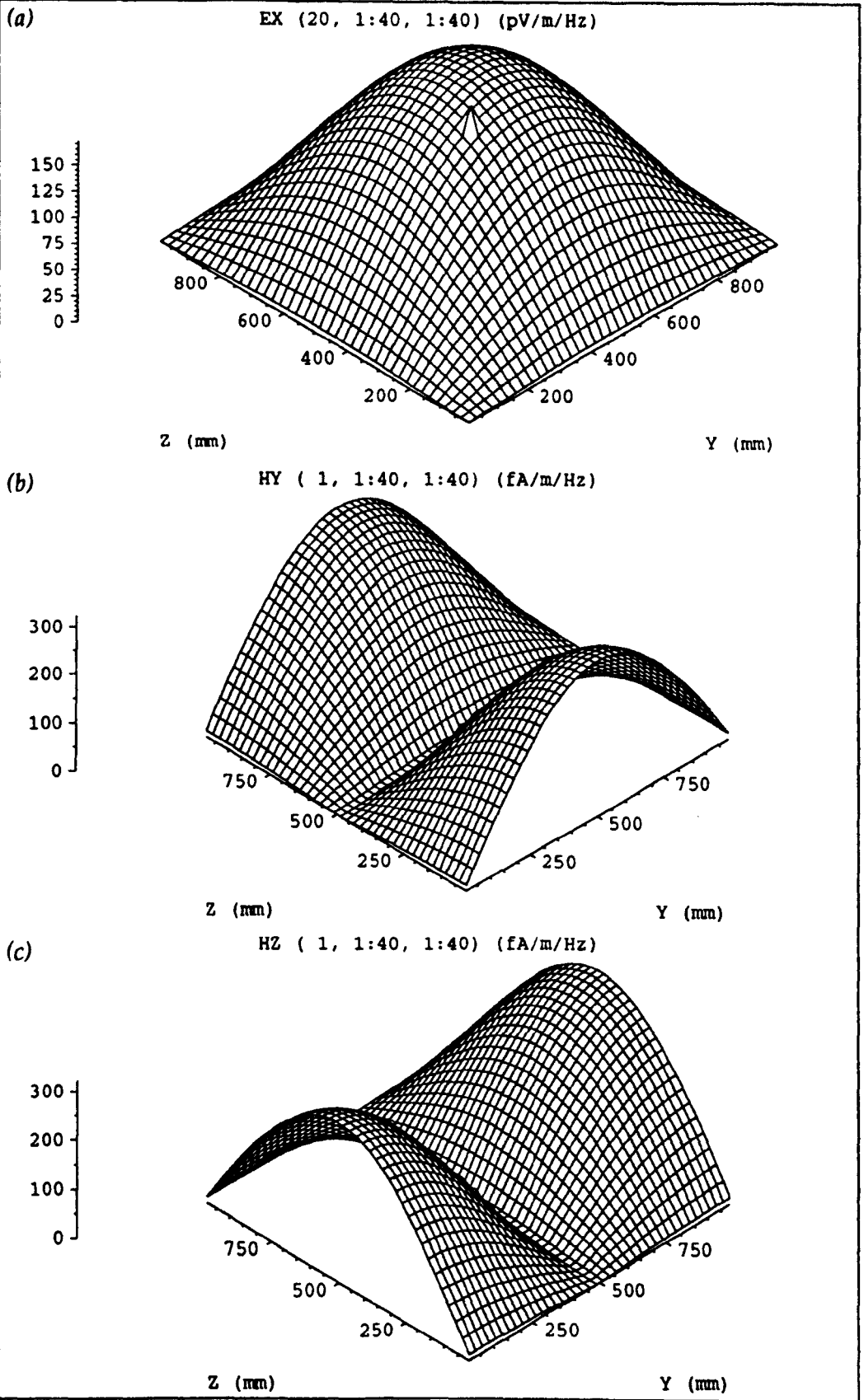


Fig. 7.2 - Electric and magnetic field at the first resonance

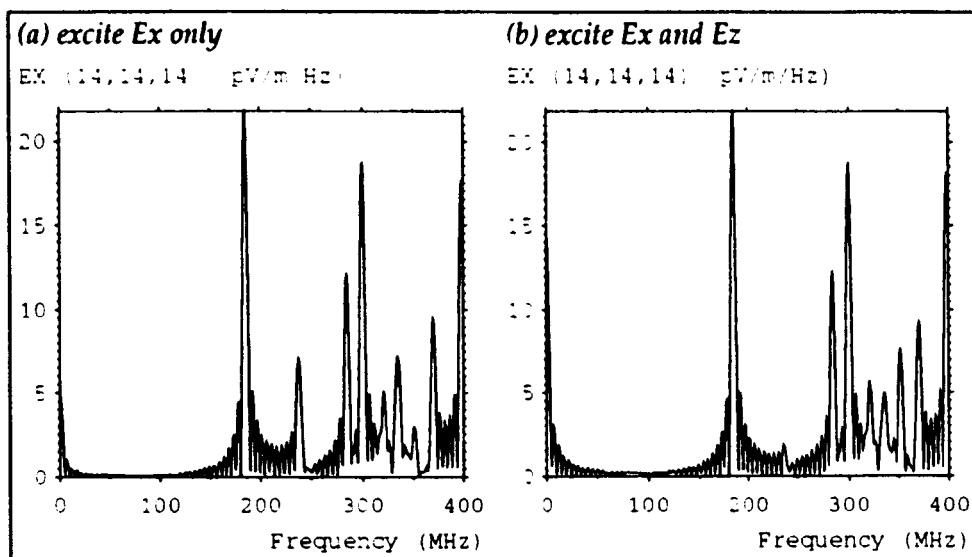


Fig. 7.3 – Excitation of more than one field component

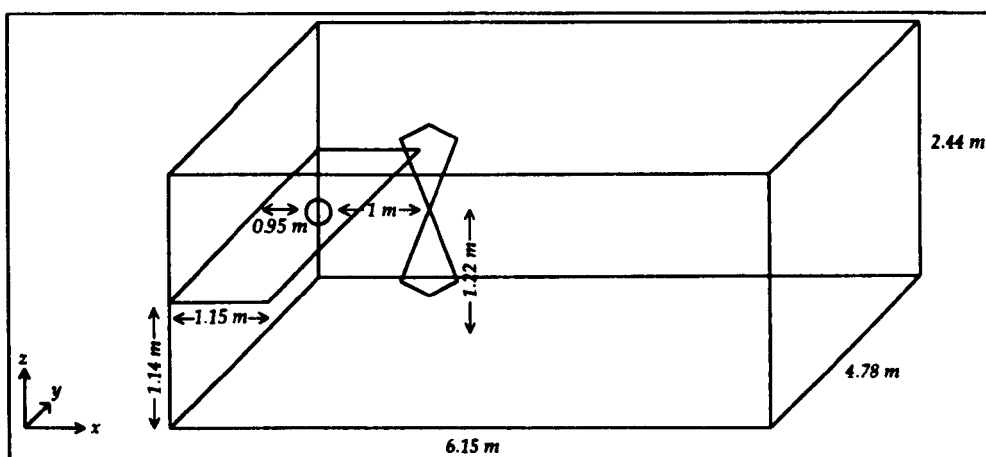


Fig. 7.4 – Screened room with a bench

## 7.2 Effect of a conducting bench

The procedure described in Defence Standard 59–41 [60], for measurements in a screened room, requires the use of a conducting bench onto which the equipment under test is electrically fixed. The presence of the bench complicates the field distribution within the room and causes the frequencies of some of the resonances to change. The effect of the bench on the room resonances can be easily investigated using TLM. This has been done for a room of dimensions  $6.15 \times 4.78 \times 2.44 \text{ m}^3$  with a conducting bench  $1.15 \text{ m}$  wide placed at a height of  $1.14 \text{ m}$ , as shown in fig. 7.4. This was modelled with a node spacing of  $6 \text{ cm}$  and the modelled room was slightly larger than the real room. The bench was modelled by short-circuit boundaries placed at the mid-point of link-lines. The system was excited by a small

source (Gaussian voltage source two nodes in length) placed above the bench and the output was taken at a distance of 1 m. Both the source and output points were taken away from symmetry planes to avoid nulls in the field profile.

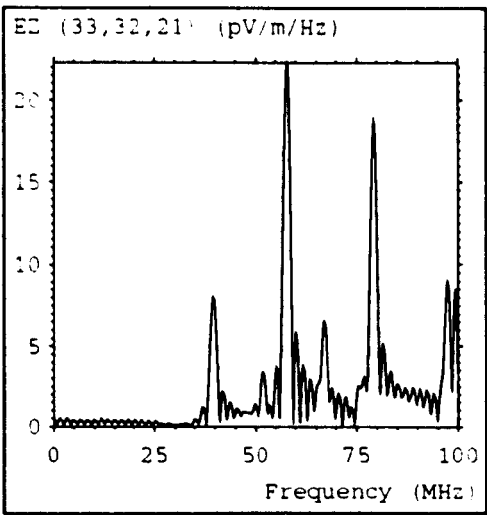


Fig. 7.5 – Vertical component of the electric field with bench

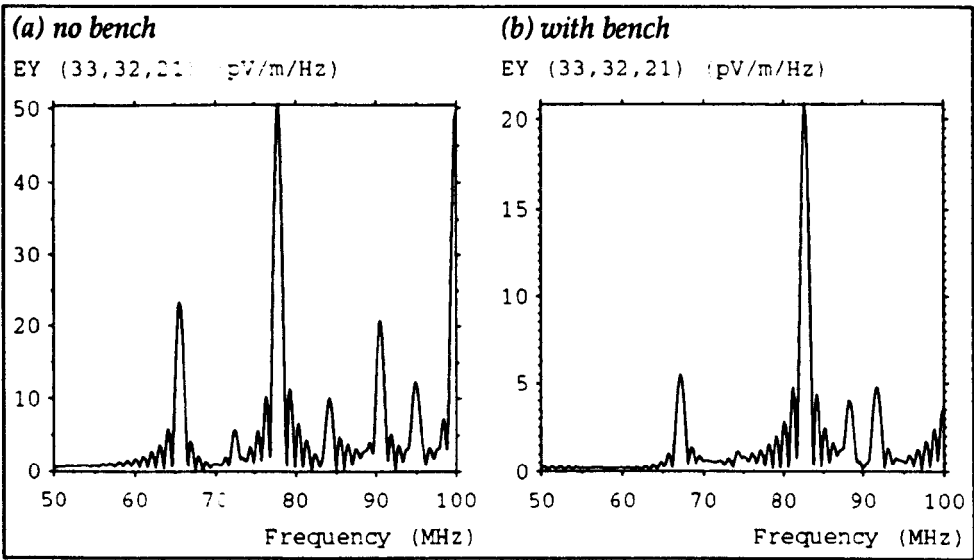


Fig. 7.7 – Horizontal component of the electric field with and without bench

The results for vertical polarisation, excited by a vertically polarised source with centre 12 cm above the bench are shown in fig. 7.5. With the exception of the peak at 52 MHz, the response is essentially the same as when no bench is present. The field profiles on a horizontal plane half way up the room are shown in fig. 7.6, for the first three resonances. The position of the source can be identified by the region of large field strength (which has been clipped above a certain value). The first and third plots show the expected field variation for the  $TE_{110}$  and  $TE_{210}$  modes,

although there is some variation in the vicinity of the bench. The second plot shows a bench specific resonance which does not occur in the empty room.

For the horizontal polarisation, the height of the source above the bench was increased to 33 cm and the number of iterations was increased (from 6000 to 10000) in order to resolve the more closely spaces resonances. The responses obtained with and without the bench are shown in fig. 7.7a and 7.7b, respectively. For this polarisation, the field is parallel to the bench and more variation (between the empty room and the room with the bench) is apparent. The field profiles for three of the resonances are shown in fig. 7.8. It can be seen that the field is very small in the vicinity of the bench (the output plane is just one node above the bench) which means that the standing wave pattern must be contained in a smaller volume of the room, which implies that the resonances should occur at higher frequencies. The resonant frequencies are listed below and are compared with experiment [61] for the two cases. It can be seen that, for equivalent resonances with and without the bench, there is an increase of a few MHz. Analytically, for a room of the exact dimensions used in the model, the frequency of the first resonance goes up from 65.6 MHz to 67.5 MHz when the length of the room is reduced by 1 m. The resonance at 74.1 MHz, obtained with the bench, is not well resolved when the source is placed above the bench but it becomes more prominent if the source is moved into the room.

No Bench (MHz)				Bench (MHz)	
mode	anal.	TLM	expt.	TLM	expt.
TE <sub>101</sub>	66.1	65.5	62.6	67.1	65.8
TE <sub>111</sub>	73.1	72.5	73.1	74.1	74.6
TE <sub>201</sub>	78.4	77.9	—	82.6	—
TE <sub>211</sub>	84.5	84.2	84.0	88.3	89.0
TE <sub>121</sub>	91.1	90.6	—	91.7	—
TE <sub>301</sub>	95.5	94.9	95.2		

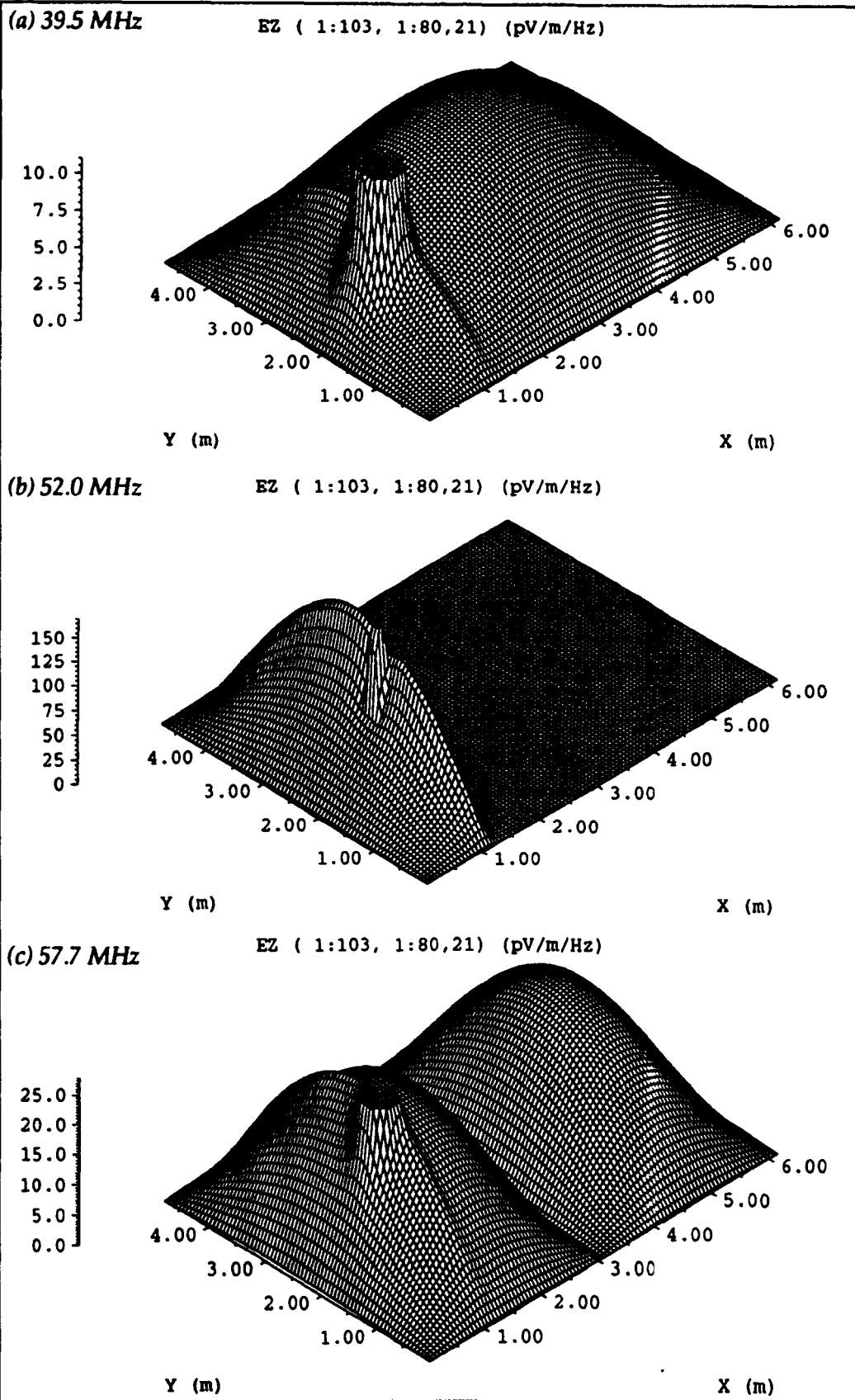


*Fig. 7.6 – Vertical component of the electric field for the first three resonances*



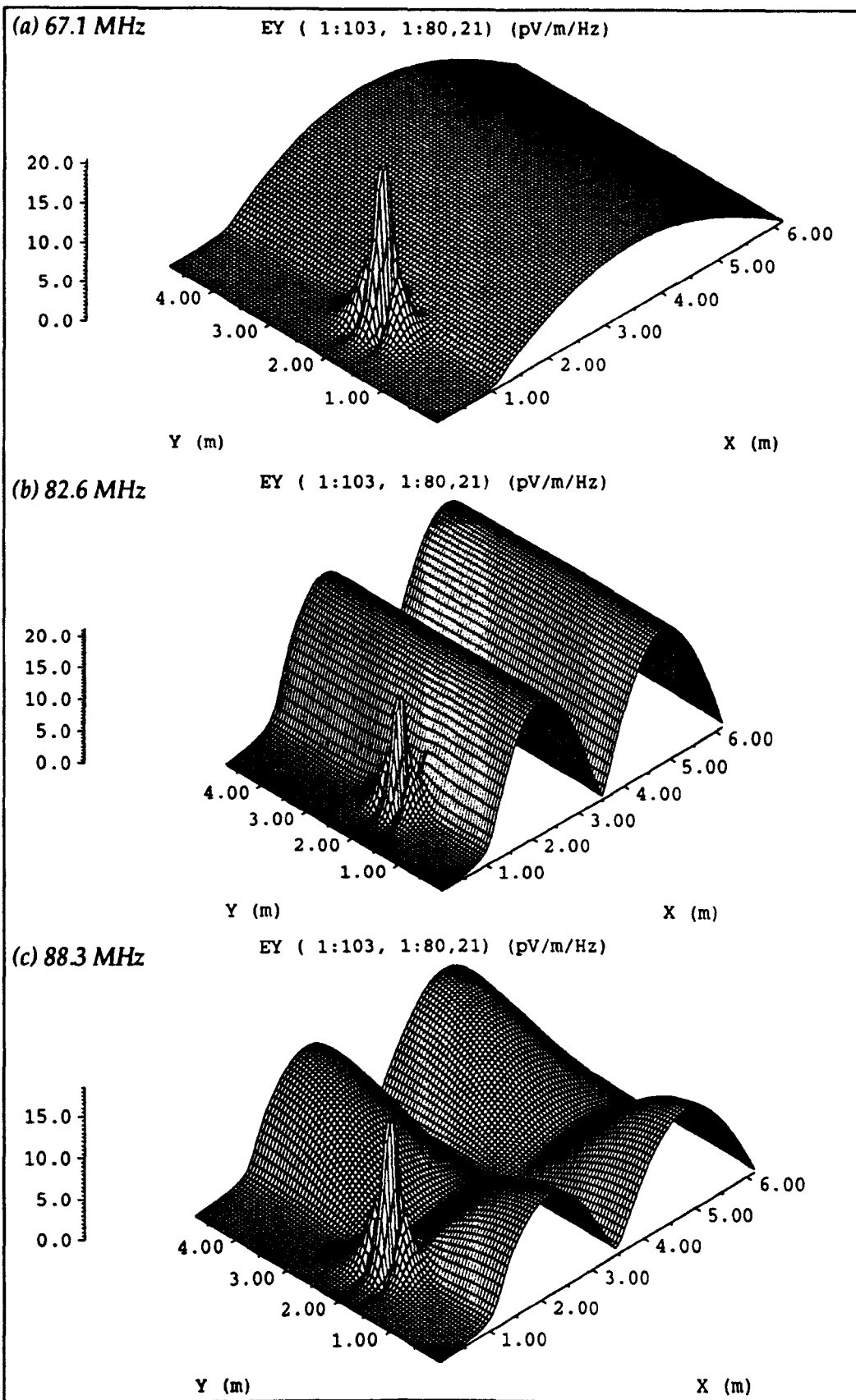


*Fig. 7.8 – Horizontal component of the electric field for three resonances*

In general, there is good agreement between the model and experiment. However, some resonances are not observed in the experimental data and there is some difference in frequency even when there is no bench present. The experimental data was obtained as a return loss measurement (so the source and output are in the same position) with the centre of the antenna placed in the same position as the output point in the model. Placing the source above the bench, as in the model, is more consistent with the way in which real measurements on equipment are obtained. A biconical antenna was used and it is likely that its presence would disturb the field. In addition, the room size differed slightly between the model and experiment and the real room had additional features such as cable conduits and ventilation ducts. It can be concluded that TLM is useful for obtaining resonant frequencies and in obtaining the field profile so that the nature of the resonances can be investigated.

### **7.3 Sensitivity to small changes in position**

Measurements made in a screened room, particularly an unlined room, are affected by changes in position of the equipment under test (EUT). Many of these effects are dominated by the location of power and instrumentation lines and it is difficult to distinguish the effects due to the EUT alone. This is important since the position of the EUT on a conducting bench and the placing of an antenna at a fixed distance (e.g. 1 m) cannot be specified with certainty, particularly when the EUT is of an irregular shape. A standard device under test (DUT) was considered, measuring  $48 \times 48 \times 12 \text{ cm}^3$ , which could be made to radiate in a number of ways. Further details on the modelling of this device and its radiation properties can be found in §8.6.

The DUT was placed on a conducting bench (1 m wide and 1 m high) in a screened room measuring  $4.56 \times 2.36 \times 2.44 \text{ m}^3$  and was made to radiate as an electric source by raising the lid and exciting between the body and the lid. The system was modelled with a node spacing of 4 cm and 8000 iterations were performed. The output was taken at a nominal distance of 1 m from the DUT and also at three additional points, each displaced by 8 cm along different axes. Fig. 7.9 shows the maximum, mean and minimum signals observed at all of the points over frequency

ranges of 200–250 MHz and 700–750 MHz. Log. scales have been used so that the power (in dB) is obtained <sup>1</sup>. It is apparent that small changes in the position of the output point do not cause significant variations in received signal below 250 MHz. However, in the 700–750 MHz range, where the mode density is much higher, variations as high as 30 dB are typical.

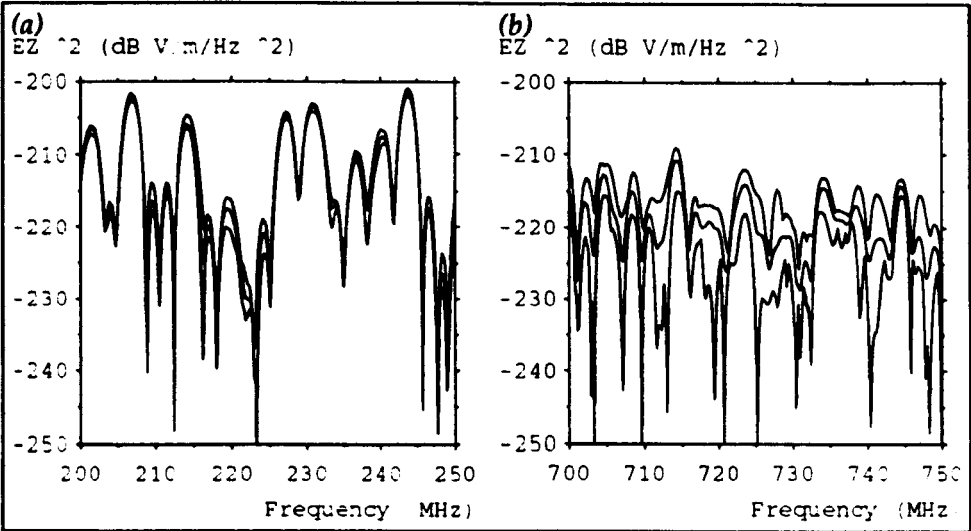


*Fig. 7.9 – Effect of small changes in position of the output point*

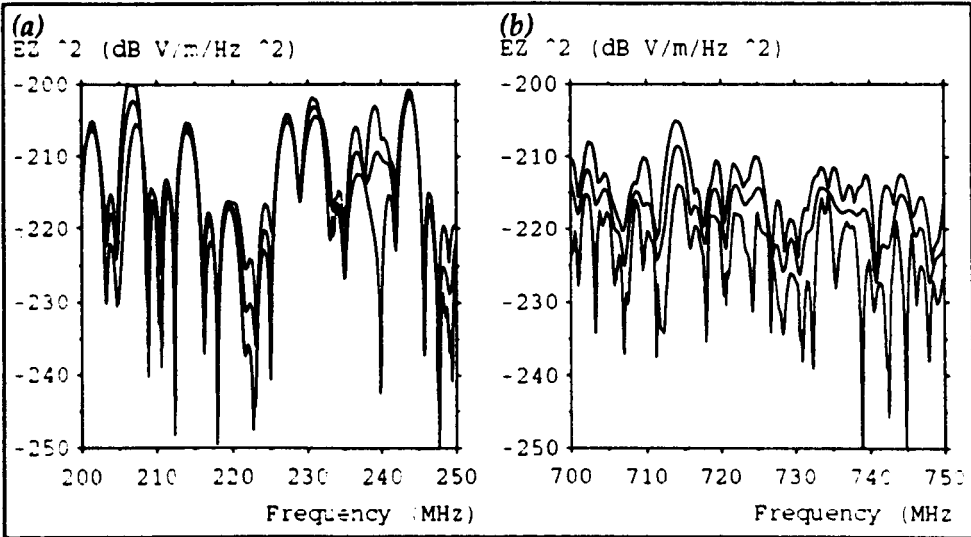


*Fig. 7.10 – Effect of small changes in the position of the DUT*

Another test which was performed was to move the DUT while keeping the output point in the same position with respect to the room. This requires separate simulations for each position of the DUT. The corresponding graphs are shown in fig. 7.10. A further variation on this theme is to move both the DUT and the output

<sup>1</sup> The power was calculated as  $20 \log_{10} E_z$  where  $E_z$  is the observed electric field. The values are very small because the  $\Delta t$  factor in the DFT has also been squared.

so that the output is in a constant position with respect to the DUT. The results are similar for all three cases and they show that in an undamped room, at the higher frequencies, substantial variations in received signal are obtained. This suggests that some form of room damping is essential in order to achieve repeatable results.

Note that the TLM results should be treated with some caution. The system has no imposed losses and so the width of the *sinc* waveform around each resonant peak will be inversely proportional to the number of iterations. The maxima and minima of the *sinc* waveforms will have some effect on the graphs, away from the resonant peaks, because the signal radiated by the DUT is very small, but at high frequencies, where the greatest variations are observed, the resonances are closely spaced and the effect should be minimal. The model can be considered to represent a real system with small losses because the width of the resonances is finite and it may be possible to set the number of iterations so that the Q factor of the resonances is the same as that observed experimentally.

## 7.4 Determination of Q factor

### 7.4.1 Method

The quality factor, or *Q factor*, is a measure of the frequency selectivity and general performance of a cavity resonator. For experimental purposes, it is a requirement that a screened room should not have any high Q resonances so that repeatable results can be obtained. A general definition of Q, which is applicable to all resonant systems is given by [24 p482]

$$Q = 2\pi f \frac{W_{av}}{\eta}$$

where  $W_{av}$  is a time average of the energy stored in the system and  $\eta$  is the rate of energy dissipation. The Q factor can also be expressed in terms of the 3 dB bandwidth<sup>2</sup>

$$Q = \frac{f}{2\Delta f}$$

where the bandwidth is  $2\Delta f$ . Or, it can be expressed in terms of the logarithmic

---

<sup>2</sup> The frequency range between points on each side of the peak where the field strength is  $1/\sqrt{2}$  of its maximum value, or alternatively, where the power is 1/2 of its maximum value.

decrement  $\Lambda$ .

$$Q = \frac{\pi}{\Lambda}$$

The logarithmic decrement is a measure of the decay rate of an exponentially damped oscillation. It is the natural log. of the decrement,  $\delta$ , which is the ratio of the amplitude of any of the damped oscillations to the following one. The amplitude of the oscillation, at a time after the source has been removed, can be written as

$$E = E_0 \exp(-\alpha t)$$

The decrement and Q factor are then given by

$$\delta = \exp\left(\frac{\alpha}{f}\right)$$

$$\text{and } Q = \frac{\pi f}{\alpha}$$

There are a number of ways in which the Q factor can be obtained from a TLM simulation. For example, it would be possible to record the total energy in the system or the power dissipated in all the boundary and lossy nodes, on each successive iteration. However, the Q factor will be required at a particular frequency and it would be computationally expensive to evaluate the DFT at each node (to obtain the total energy) or on each lossy element (to obtain the dissipated power). The method adopted was to apply an impulse excitation and then obtain the time domain output at a single point, where the field strength was known to be good.

In principle, the Q factor can be evaluated by measuring the 3 dB bandwidth of the resonant peak obtained after a DFT. However, truncation of the time series will also cause broadening of the peak so that, for small losses, the additional broadening is negligible. This is illustrated for test data consisting of a 40 MHz sinusoidal signal described by 1000 values with a timestep of 167 ps ( $\Delta l=10\text{cm}$  for the SCN) and for a decaying sinusoidal signal with a decay rate given by  $\exp(-5 \times 10^6 t)$ . The DFT of these signals is shown in fig. 7.11. The theoretical Q factor and bandwidth for the damped signal, assuming no truncation, are 25.1 and 1.6 MHz, respectively. The actual bandwidth of the undamped signal (i.e. the

bandwidth of the *sinc* function) is 5.3 MHz and the observed bandwidth for the damped signal is 5.6 MHz. It would be inaccurate to obtain the required bandwidth from such a small change in observed bandwidth.

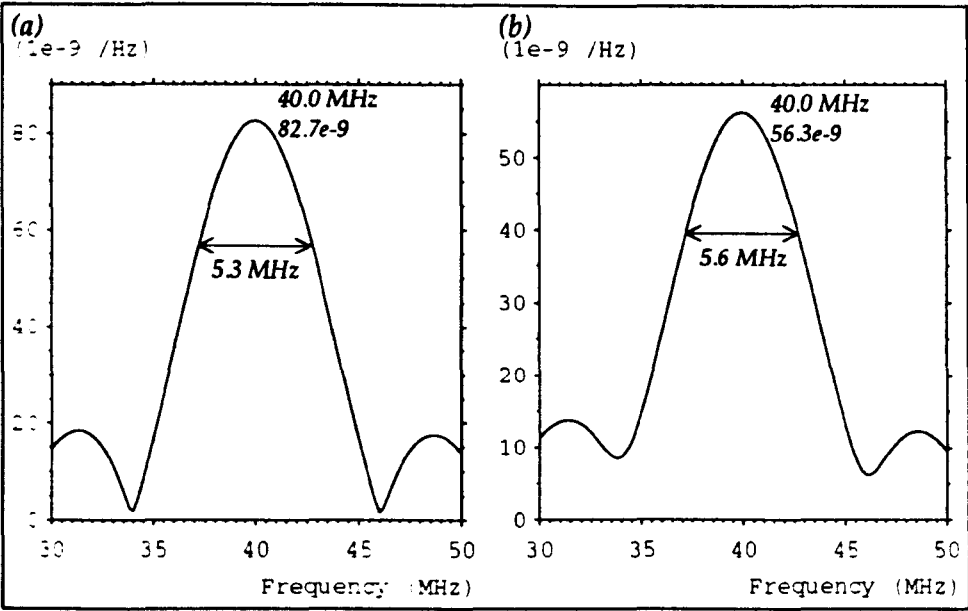


Fig. 7.11 – (a) Damped and (b) undamped sinusoidal signals

The approach adopted was to fit the time domain data to an exponential decay, at the appropriate frequency, and then obtain the Q factor from the decrement. To obtain the decay at a particular frequency,  $f$ , the impulse response is convolved with the complex function  $f_0(t)$ , where

$$f_0(t) = \begin{cases} \exp(j 2 \pi f t) & t < 0 \\ 0 & t > 0 \end{cases}$$

and then the magnitude of the result (at each time) is taken. This gives the response which would be obtained if, after the steady-state has been reached, the source is suddenly removed. The use of a complex exponential function means that a pure exponential decay is obtained rather than a damped sinusoidal signal. It is the same as evaluating the DFT, at each time, for a successively smaller input data window. This means that, because it is only the magnitude which is of interest, the convolution need be no more expensive than a standard DFT.

Simple analysis shows that the convolution of the source function  $f_1(t)$ , as shown in fig. 7.12a, with the truncated exponential decay  $f_2(t)$ , as shown in fig. 7.12b, where  $T = N \Delta t$  and  $N$  is the number of iterations, gives an exponential decay

minus a constant.  $f_1(t)$  is the magnitude of  $f_0(t)$  and  $f_2(t)$  represents the output from the TLM simulation.

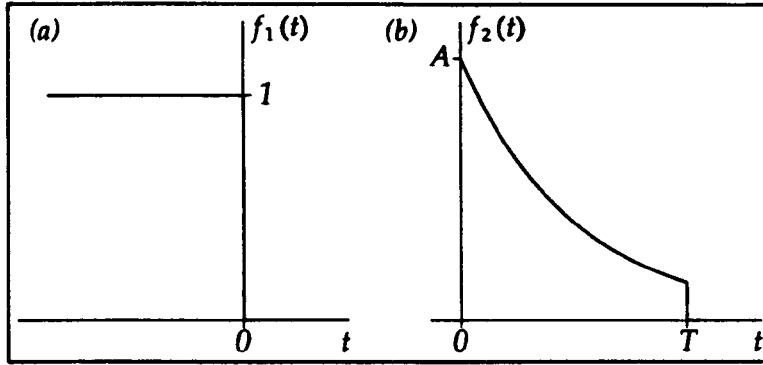


Fig. 7.12 – Source function and truncated exponential decay

$$f_1(t) = \begin{cases} 1 & t < 0 \\ 0 & t \geq 0 \end{cases}$$

$$f_2(t) = \begin{cases} 0 & t < 0 \\ A \exp(-\alpha t) & 0 \leq t \leq T \\ 0 & t > T \end{cases}$$

$$f_3(t) = f_1(t) * f_2(t)$$

$$= \int_t^T \frac{A}{\alpha} \exp(-\alpha \tau) d\tau$$

$$= \frac{A}{\alpha} \{ \exp(-\alpha t) - \exp(-\alpha T) \} \quad \text{for } 0 \leq t \leq T$$

The decrement may be obtained using a least squares fit but the presence of the constant means that  $f_3(t)$  must be differentiated (with respect to time) before this is done. Care must be taken when doing this since  $f_3(t)$  is potentially a noisy signal. Use is made of the fact that the ratio of any two values of the function  $\exp(-\alpha t)$ , for values of  $t$  a constant distance apart, is the same. If the time between the two values is  $t_0$ , then

$$\frac{f_3(t) + k}{f_3(t + t_0) + k} = \frac{\exp(-\alpha t)}{\exp(-\alpha [t + t_0])} \quad \text{where } k = \frac{A}{\alpha} \exp(-\alpha T)$$

$$\Rightarrow f_3(t) = k \{ \exp(\alpha t_0) - 1 \} + \exp(\alpha t_0) f_3(t + t_0)$$

This equation is of the form

$$y = C + R x \quad \text{where } C = k \{ \exp(\alpha t_0) - 1 \}$$

$$\text{and } R = \exp(\alpha t_0)$$

so that linear regression can be performed, where  $C$  is the constant term and  $R$  is the regression coefficient. It is only necessary to evaluate the regression coefficient in order to obtain the decrement.

$$\delta = R^{1/t_0}$$

The  $Q$  factor can then be obtained from

$$Q = \frac{\pi}{\ln \delta}$$

Note that for the higher values of  $Q$  the decrement is close to unity. This is a potential source of error since, for example, for the  $Q$  factor to increase from 200 to 210, the decrement only decreases from 1.0158 to 1.0151.

In order to operate the procedure, a value of  $t_0$  and the number of pairs of values must be selected. The convolution need only be evaluated for the points which are required. The value of  $t_0$  was typically chosen as a multiple of the period of the oscillation, and, where computer resources allowed, all of the data was included. No rules have been developed for the optimum value of  $t_0$  but evaluation of the  $Q$  factor for different values of  $t_0$  (some multiples of the period and others not) shows that the choice is not too critical. However, if  $t_0$  is small the error introduced when taking the difference of two similar values will be large and if  $t_0$  is too large the second value may be swamped by noise.

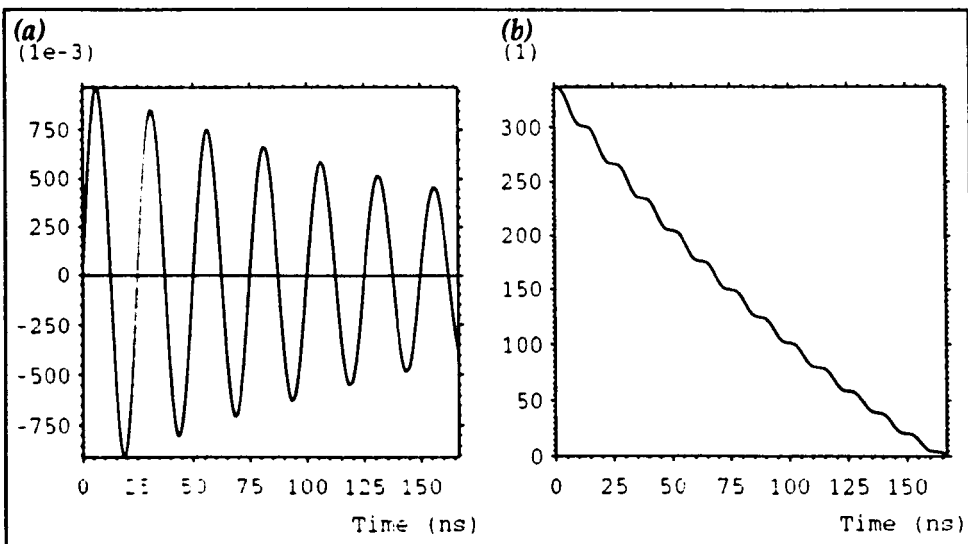


*Fig. 7.13 – (a) Damped sinusoid and (b) magnitude of the convolved signal*

The operation of the method is illustrated for the decaying 40 MHz sinusoidal signal mentioned earlier. The signal is shown in fig. 7.13a and the magnitude



obtained after the convolution is shown in fig. 7.13b. Choosing values of 149 (one period) and 160 for  $t_0$ , and using all the data, gives Q values of 24.9 and 24.8, respectively, compared to the correct value of 25.1.

#### 7.4.2 Validation

The method was evaluated for the first resonance in a screened room of dimensions  $6.1 \times 4.8 \times 2.4 \text{ m}^3$ , modelled with a node spacing of 10 cm and 10000 iterations were performed. The system was excited by an impulse electric field extending along a line from the floor to the ceiling. The reflection coefficient of the walls was varied and comparisons were made with analytical results.

For small losses, where the surface currents are essentially those associated with the loss-free solution, the Q factor of the  $TE_{110}$  mode in a rectangular cavity can be written as [62]

$$Q = \frac{\mu_0 \pi f x_1 y_1 z_1 (x_1^2 + y_1^2)}{R_m [x_1^3 (y_1 + 2 z_1) + y_1^3 (x_1 + 2 z_1)]} \quad (7.1)$$

where  $R_m$  is the resistive part of the surface impedance of the wall. If the wall has conductivity  $\sigma$  and skin depth  $\delta_s$ , then [24 p503]

$$R_m = \frac{1}{\sigma \delta_s}$$

where  $\delta_s = \sqrt{\frac{2}{\omega \mu \sigma}}$

The required link-line reflection coefficient is simply given by

$$\rho_l = \frac{R_m - Z_0}{R_m + Z_0} \quad (7.2)$$

The raw time domain output obtained for a loss-free room and for a room with  $\rho_l = -0.989$  is shown in fig. 7.14 for all 10000 iterations. It is apparent that there is a loss of energy in the second case. The corresponding frequency domain data is shown in fig. 7.15. The amplitude of the peaks is much reduced in the second case but the same resonances can still be identified. The magnitude of the convolved output for five different values of reflection coefficient (ranging from  $-1$  to  $-0.989$ ) is shown in fig. 7.16. For the lossless case, a straight line is obtained but as the losses are increased, the exponential decay becomes more pronounced. Some oscillation is

apparent for all of the curves but it is not significant.

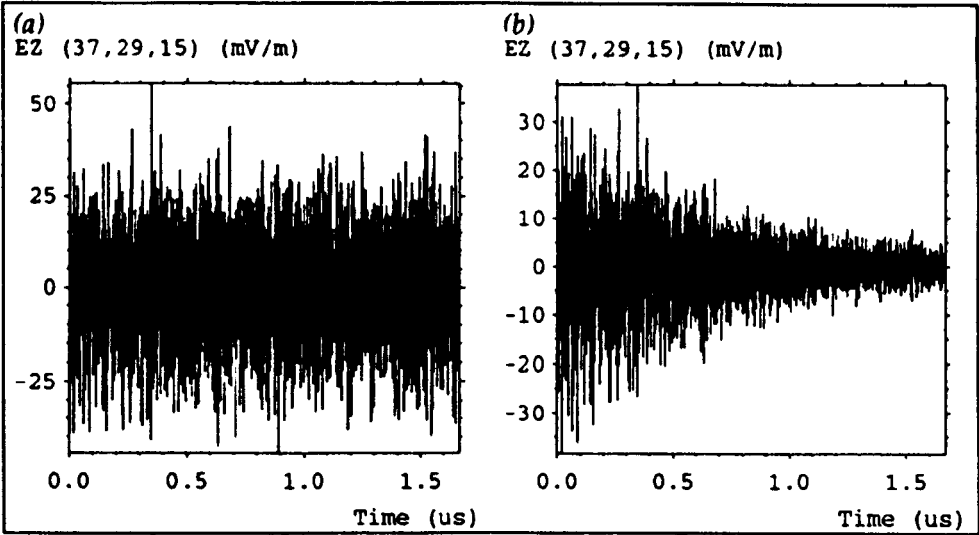


Fig. 7.14 – Time domain data for (a) lossless and (b) lossy systems

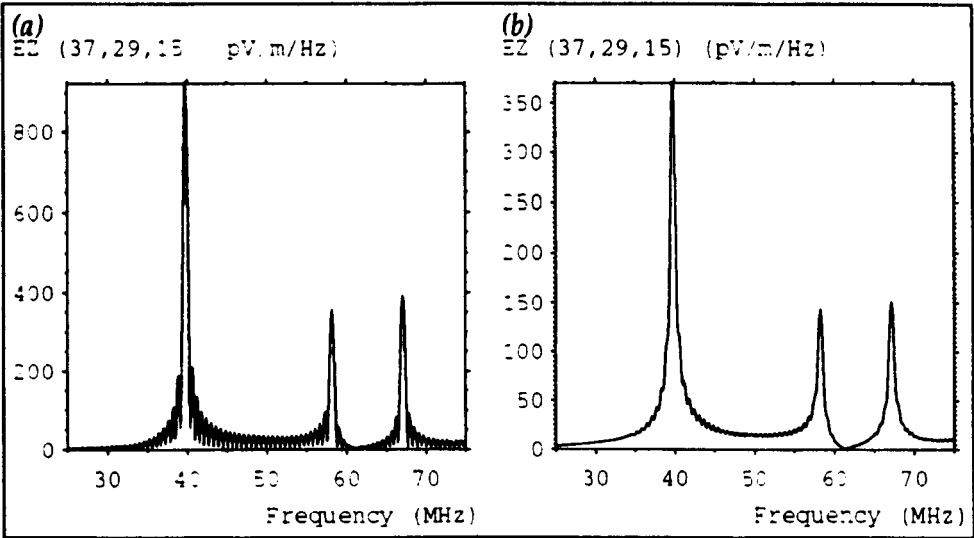


Fig. 7.15 – Frequency domain data for (a) lossless and (b) lossy systems

When greater losses are introduced, the decay in field strength is more rapid and the signal potentially contains a greater noise component. The noise can be reduced by applying a low pass filter before the convolution. This is illustrated in fig. 7.17 for the first 2500 iterations obtained with a reflection coefficient of  $-0.9$ . It is much easier to fit the expected decay curve to the data obtained after filtering.

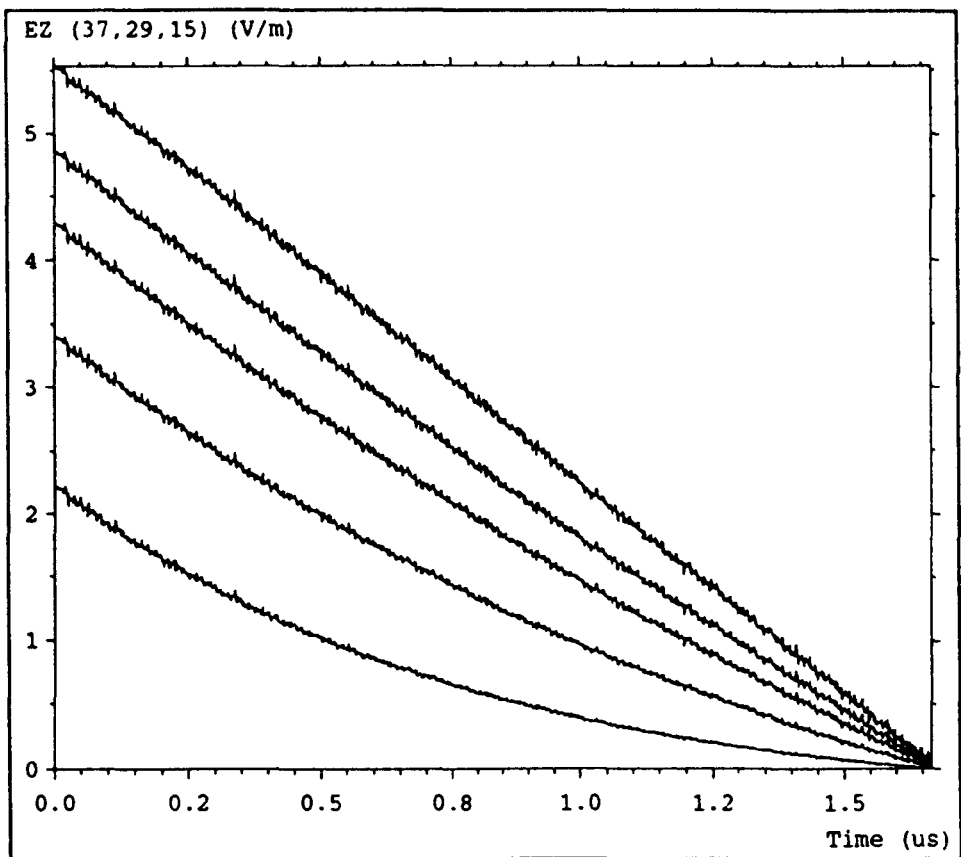


Fig. 7.16 – Magnitude of the convolved signal for various reflection coefficients

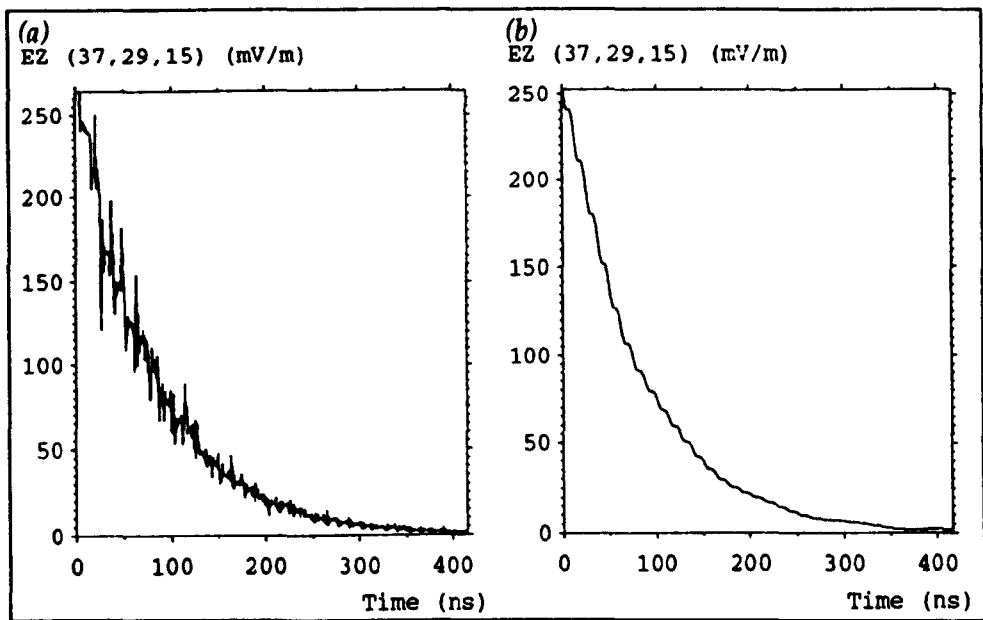


Fig. 7.17 – Magnitude of the convolved signal (a) with and (b) without low pass filter

Results are given below for six different values of reflection coefficient. A 50 MHz low pass filter was used for the more lossy systems. The analytical Q values were calculated from (7.1) at the frequency predicted by TLM, which does not

change when the walls are only slightly lossy. In all cases there is good agreement with the analytical results. In many cases, the Q factor can be obtained with far fewer than 10000 iterations but if the losses are small then sufficient iterations must be performed so that the decay can be observed.

		TLM			Analytical	
$\rho_1$	$R_m$	$f$ (MHz)	$\delta$	Q	$\delta$	Q
-0.99867	0.25	39.7	1.0038	820	1.0040	784
-0.99735	0.50	39.7	1.0078	403	1.0080	392
-0.9947	1.00	39.7	1.0160	198	1.0162	196
-0.989	2.08	39.7	1.0340	94	1.0339	94.3
-0.9	19.8	39.9	1.3735	9.9	1.3713	9.95
-0.8	41.9	40.5	1.9242	4.8	1.9321	4.77

It has been found that the Q factor can be accurately predicted using the proposed method. However, there are difficulties in evaluating very small and very large Q factors. The fitting of the simulation data to the expected decay curve is one area where improvements can be made. Ideally, a method based on Prony’s method in which the complete data set is fitted to a set of damped harmonic signals would be used, if it can be shown to be generally applicable for both moderately damped and highly damped systems.

## 7.5 Room damping

### 7.5.1 Optimum material properties

The addition of RAM inside a screened room results in a reduction of the Q factor and therefore in a more uniform field distribution. Pyramidal RAM can be placed on the walls of the room but at low frequencies it is not very effective unless unrealistically thick layers are used. However, large blocks of RAM can be placed

within the room, at strategic positions, to damp the first few modes, so that damping over the full frequency range is achieved. It is expected that the optimum material properties of the RAM blocks should correspond approximately to those resulting in a similar magnitude of the displacement and conduction currents ( $\sigma \approx \omega\epsilon$ ). It may therefore be possible to select the optimum material properties to suppress certain resonances.

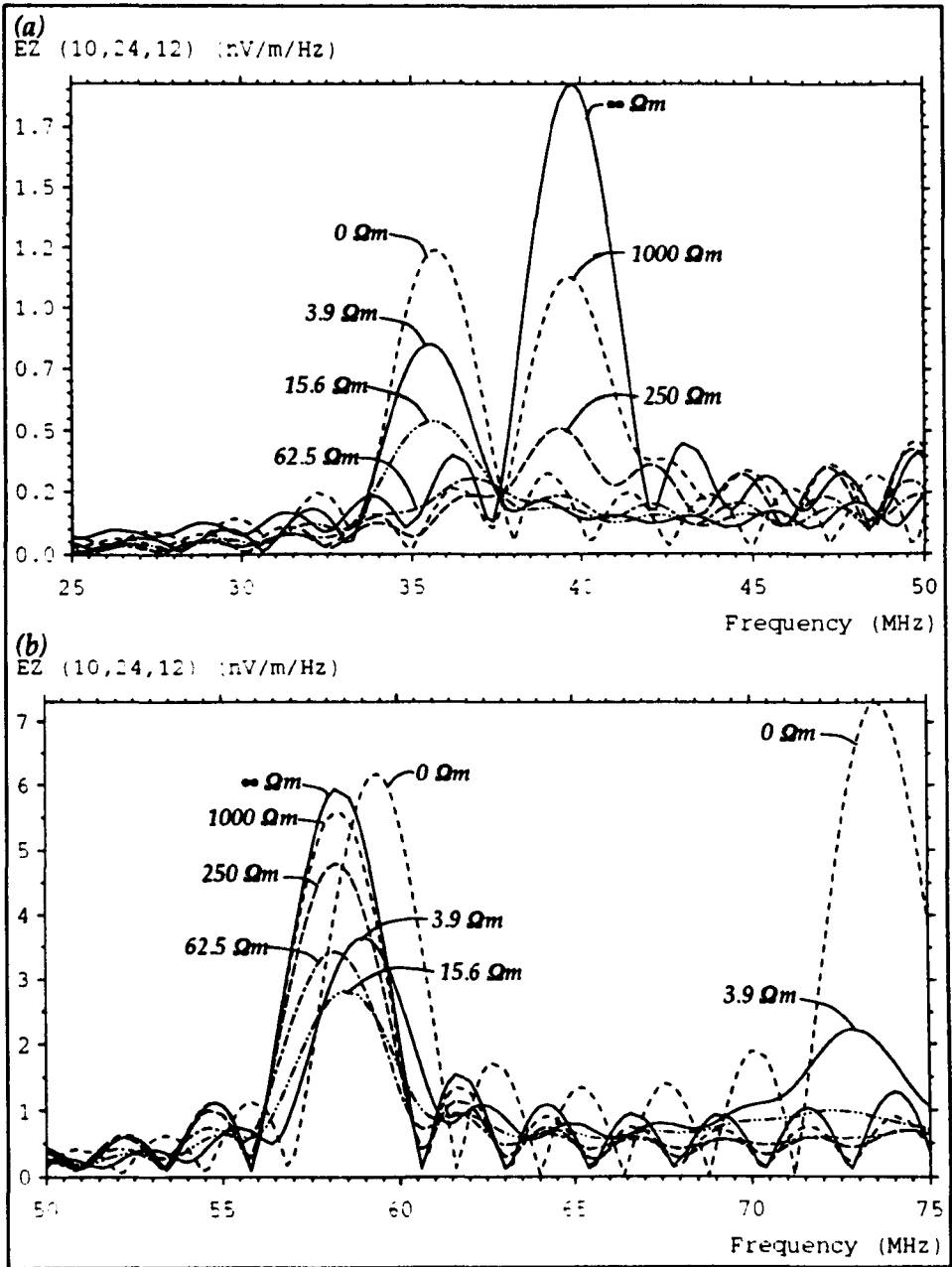


Fig. 7.18 – Varying resistivity for (a) first resonance and (b) second resonance

A series of simulations were performed to determine the optimum resistivity for a 1 m<sup>3</sup> uniform block placed centrally in a screened room. This was done for a

room of dimensions  $6.1 \times 4.8 \times 2.4 \text{ m}^3$ , modelled with a node spacing of 10 cm and 2500 iterations were performed. The system was excited by applying an impulse electric field along a vertical plane 1 m from the end wall and the output was taken at a distance of 1 m from the opposite wall. Separate simulations were performed for each value of resistivity and the DFT was taken for frequency ranges about the first and second resonances. The results are shown in fig. 7.18. For the first resonance, it is apparent that as the resistivity is reduced the amplitude of the peak decreases until it is at a minimum at  $60 \Omega\text{m}$ . If the resistivity is reduced further then a new resonance is established at a lower frequency, reflecting the new room geometry. For the second resonance, the optimum resistivity is lower, at  $16 \Omega\text{m}$ , and as the resistivity is further reduced, the new resonance is shifted up in frequency rather than down. There is found to be little difference in the optimum resistivity if the relative permittivity is increased from unity to 2.5. Analytically, at frequencies of 40 MHz and 58 MHz, the optimum resistivities should be  $450 \Omega\text{m}$  and  $310 \Omega\text{m}$ , respectively. However, the RAM only fills part of the room and its presence will alter the field distribution within the room. In particular, reflections will occur when waves are incident upon the surface of the block.

The optimum resistivity for blocks of different volumes and shapes will be different. However, there is a range of resistivities around the optimum for which damping is good and it would be possible to select material properties which give acceptable damping for a range of configurations. In a practical situation, it is likely that pyramidal RAM would be placed around the block to reduce reflections and this would be expected to change the resistivity which should be used.

### 7.5.2 Actual material properties

When modelling actual RAM blocks, it is difficult to know what material properties to use because measured data varies from sample to sample and the properties may vary within a single block, due to the way in which the material is manufactured. A series of simulations were performed, for uniform blocks, in which the resistivity was varied. The results were then compared to measured data in order to determine the value of resistivity to use in later modelling work<sup>3</sup>. This approach has the advantage, over reflectivity measurements, in that the RAM is

---

<sup>3</sup> The experimental data was supplied by the National Physical Laboratory.

placed in a real environment whereas the reflection is usually obtained for a plane wave incident at a particular angle.

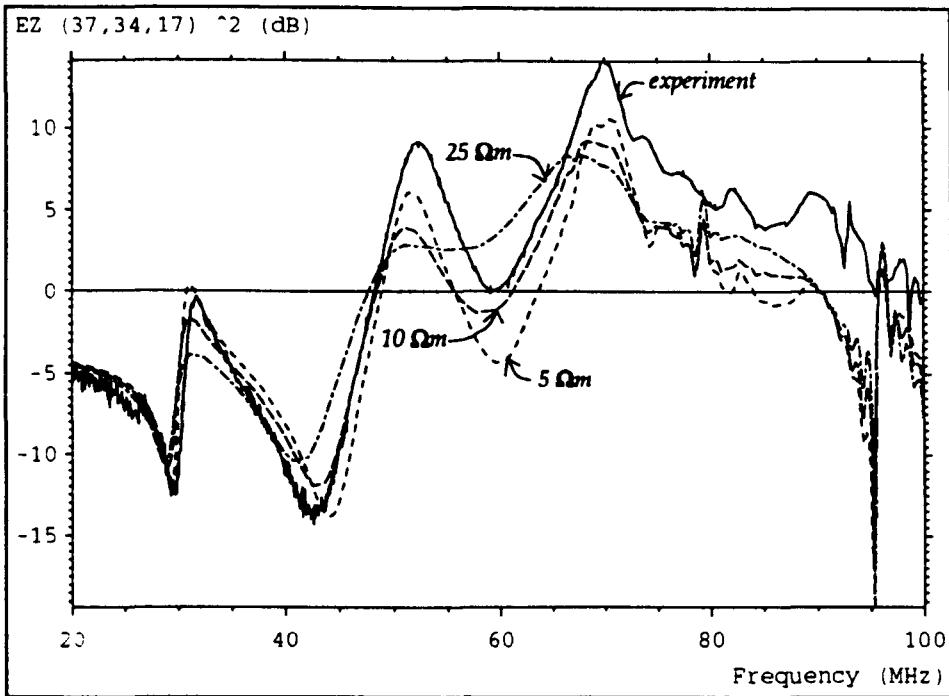


*Fig. 7.19 – Varying resistivity and comparison with experiment*

Simulations were performed for several different volumes of RAM and some of the results obtained for a volume of  $3.0 \times 1.8 \times 1.2 \text{ m}^3$  are shown in fig. 7.19, for a screened room of dimensions  $6.1 \times 4.8 \times 2.4 \text{ m}^3$ . This was modelled with a node spacing of 6 cm and 10000 iterations were performed. The number of iterations was judged to be sufficient by comparing the output of the DFT for input data obtained after 10000 and 20000 iterations. It was found that some peaks were larger, although by no more than 20%, and there was no change in the frequencies of the major features. A small Gaussian voltage source was used to excite the system so that its volume was similar to that of the 10 cm diameter spherical dipole used in the experiment. This enabled a direct comparison to be made between the simulation and experiment. All values were normalised to the equivalent free-space measurement so that the characteristics of the source were eliminated.

The best agreement was obtained for a resistivity of  $5 \Omega\text{m}$ , although this is offset from the experimental data by a few dB at higher frequencies. There are a number of factors which might give rise to this error.

- If the properties of the block do vary throughout its volume then it may not be possible to model it with uniform properties. Also, no account was taken of any frequency dependence.
- A biconical antenna was used as the receiver in the experiment. Such an antenna obtains the average field over its volume rather than the field at a single point (as in the simulation) and its very presence may alter the field distribution in the room.
- The experimental normalisation data was obtained on an open area test site with pyramidal RAM placed on the ground between the transmitter and the receiver. At low frequencies this can only be regarded as an approximation to free-space.

### 7.5.3 Q factor of damped room

The Q factor of a screened room of dimensions  $6.1 \times 4.8 \times 2.4 \text{ m}^3$  was obtained for a node spacing of 10 cm and 10000 iterations were performed. A number of RAM blocks, each measuring  $3.0 \times 0.6 \times 0.6 \text{ m}^3$  were then inserted and the predicted Q factor was compared with experiment <sup>4</sup>.

Experimentally, the Q factors of the first and second resonances were found to be 70 and 67, respectively. The wall reflection coefficient used in the model was selected to be  $-0.985$  (from equations 7.1 and 7.2) so that the same Q factor was obtained for the first resonance. However, the Q factor for the second resonance was then 109. To overcome this, a second set of simulations with a reflection coefficient of  $-0.975$  were used for the second resonance. If a more accurate wall description was used then only a single set of simulations should be required. The results obtained for blocks with resistivities of  $5 \Omega\text{m}$  and  $25 \Omega\text{m}$  are shown below. The value of  $25 \Omega\text{m}$  was obtained as an average of the measured data for pyramidal RAM [63]. The results obtained with  $25 \Omega\text{m}$  blocks are in better agreement with experiment than the  $5 \Omega\text{m}$  blocks. However, all of the simulation results are of the correct order of magnitude. Note that for the moderate levels of damping introduced here, resonant peaks can still be resolved.

---

<sup>4</sup> The experimental data was supplied by the National Physical Laboratory.



Blocks	Freq. (MHz)	Q (5 $\Omega$ m)	Q (25 $\Omega$ m)	Expt. Q
0	39.6	70		70
0	57.2	67		68
1	37.6	42	29	31
1	56.5	29	23	22
2	36.7	35	26	28
2	56.0	24	18	20

### 7.5.4 Optimum RAM arrangement

Ideally, RAM blocks should be placed in the centre of the room, in the position of maximum electric field, so that the first mode is effectively damped. However, in small rooms, the location of the equipment under test and the receiving antenna may require the blocks to be moved from their optimum position. Also, for larger rooms, it may be necessary to damp the first two or three modes if they occur at frequencies below that at which pyramidal RAM on the walls becomes effective and this will require different distributions of blocks.

The first mode in a cavity (the TE<sub>110</sub> mode) has a constant electric field distribution along the shortest dimension. This means that it would be appropriate to place blocks along this direction and centrally with respect to the other two directions. Depending upon the material properties, the field may not penetrate into the centre of the blocks and so hollow blocks can be used, or alternatively, the cross-sectional area can be reduced.

Simulations have been performed for many different arrangements of blocks which provide damping for both vertical and horizontal polarisations and three of these are shown in fig. 7.20. The results obtained when these blocks are placed longitudinally in the system described in §7.5.2 are shown in fig. 7.21 for the vertical polarisation. In all cases, the front surface of the blocks extends 0.6 m over the centre line (with respect to the longest room dimension). It is apparent that six

blocks placed together (each measuring  $3.0 \times 0.6 \times 0.6 \text{ m}^3$ ) gives the worst result. Better results are obtained when five blocks are arranged in a “+” shape because there is more RAM placed along the height of the room and there is no degradation in performance for the horizontal polarisation. The results are slightly better if the centre block is removed to give a “+” shape. This is somewhat unexpected but it can be explained because the electric field can penetrate between the blocks so that greater attenuation is achieved. However, if the blocks are moved further apart then very poor results are obtained because they no longer lie in positions of maximum electric field.

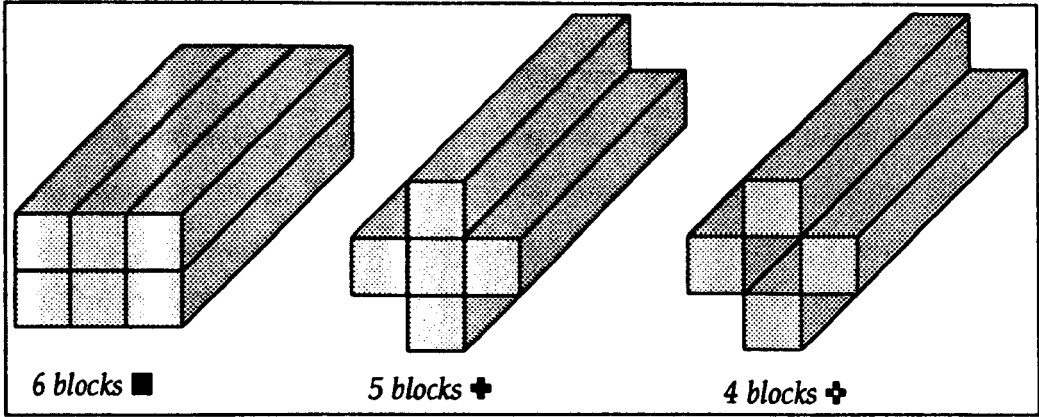


Fig. 7.20 – RAM block arrangements

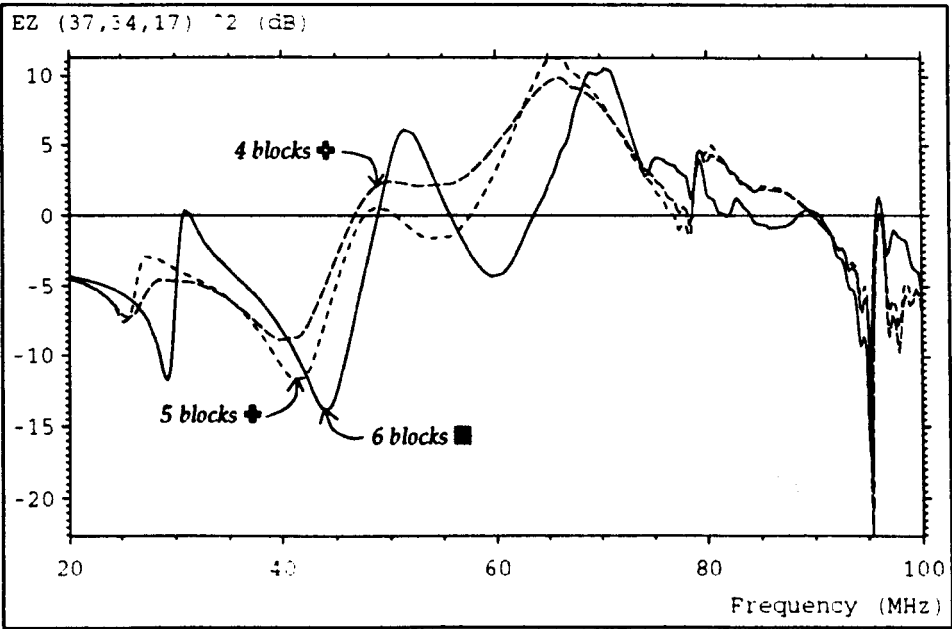
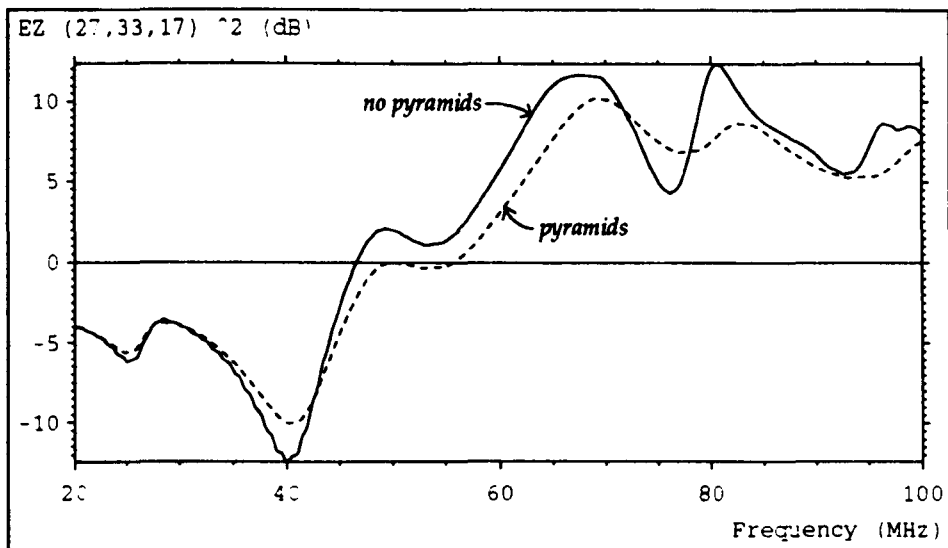


Fig. 7.21 - Damping due to various block arrangements



*Fig. 7.22 – Effect of pyramidal RAM*

The addition of pyramidal RAM improves the high frequency performance. This is illustrated in fig. 7.22 for the case of four blocks in a “+” shape. For one of the curves, pyramidal RAM has been placed behind the receiver and along the end wall. The pyramids have been modelled by plane layers, in which the material properties are varied in proportion to the cross-sectional area, so that they are air-like at the tips and RAM-like at the base. This avoids the need to describe the physical shape of the pyramids within the mesh.

The volume of RAM blocks required can be reduced by placing ferrite tiles on the room walls. These tiles have good absorption at low frequencies but may need to be supplemented by pyramidal RAM at high frequencies so that adequate damping can be obtained over the full frequency range.

## 7.6 Field-to-wire coupling

In this section, a more complicated system is considered in which two 1 m dipoles are placed in a screened room, as shown in fig 7.23<sup>5</sup>. An excitation was applied at the centre of the source dipole and the current was measured at the centre of the slave dipole, which was placed just above a conducting bench. This system represents a typical EMC system in which there is a source of interference (the source dipole), a propagation channel (the screened room) and an interference

<sup>5</sup> This experiment was devised and executed by A. P. Duffy, Department of Electrical & Electronic Engineering, University of Nottingham.

mechanism (coupling to the slave dipole).

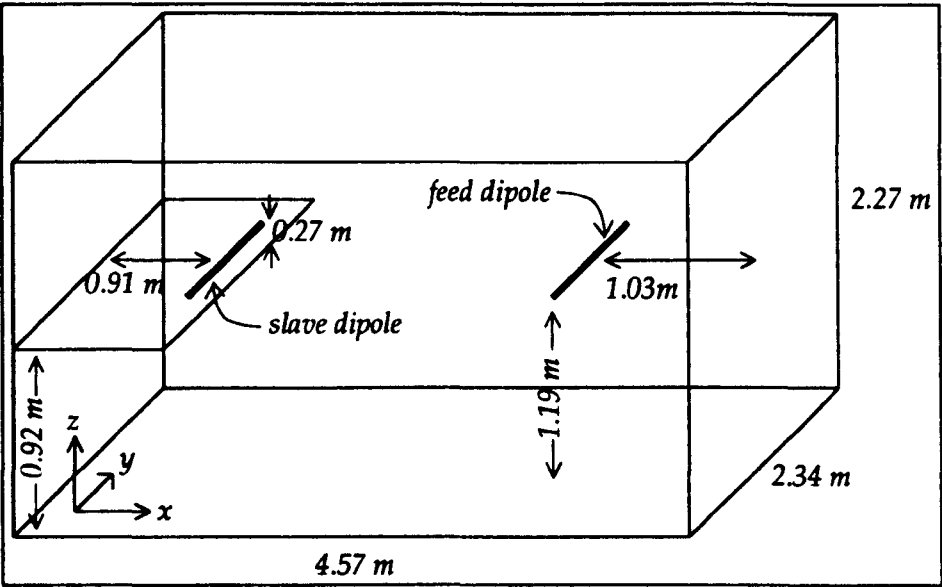


Fig. 7.23 – Dipoles in a screened room

The screened room was modelled with a node spacing of 5 cm and 7500 iterations were performed. The dipoles had a single node cross-section and both the dipoles and the bench were modelled with short-circuit boundaries placed at the mid-point of link-lines. The system was excited by four impulse voltage sources, with  $200\ \Omega$  series resistance, forming the centre of the source dipole. The total source resistance was then  $50\ \Omega$ , which was the same as that used in the experiment. The length of the dipoles was always slightly shorter than the 1 m length used in the experiment so that they could be described with an odd number of nodes, enabling a single node source to be placed at the centre.

The results obtained with a uniform mesh are shown by the solid line in fig. 7.24 over a frequency range 50–150 MHz. For the other curves, a volume of  $5 \times 23 \times 5$  coarse mesh nodes around each of the dipoles was replaced by fine meshes of 1.67 cm and 1 cm node spacing <sup>6</sup>. It can be seen that as the resolution around the wire is increased the peaks increase in frequency. The actual dipole lengths used were 95 cm (for the uniform mesh), 98.3 cm (for the 3:1 mesh) and 99 cm (for the 5:1 mesh) which means that this increase is obtained due to the better description of the dipoles despite small increases in length (which would cause a decrease in frequency). The relative storage and run-time requirements are shown below for

<sup>6</sup> The data from the 3:1 and 5:1 multigrid simulations has been multiplied by 3 and 5, respectively, so that the amplitudes can be directly compared.

these three cases and also for uniform meshes equivalent to the 3:1 and 5:1 multigrid systems. The values for the uniform fine meshes have been estimated because they were too large to run.

	uniform mesh			multigrid mesh	
	5 cm	1.67 cm	1 cm	3:1	5:1
storage	1	3	5	1.29	1.90
run-time	1	9	25	1.51	4.89

The result obtained with the 5:1 multigrid mesh is compared with experiment in fig 7.25. Both curves have been normalised so that the peak values are both unity. This is not an ideal method but it does enable a comparison to be made easily. It can be seen that the main features agree reasonably well. For this reduction ratio, the node spacing (1 cm) is the same as the diameter of the dipoles used in the experiment. Better results are obtained if there is a local reduction in timestep around the dipoles in order to improve the wire description [42].

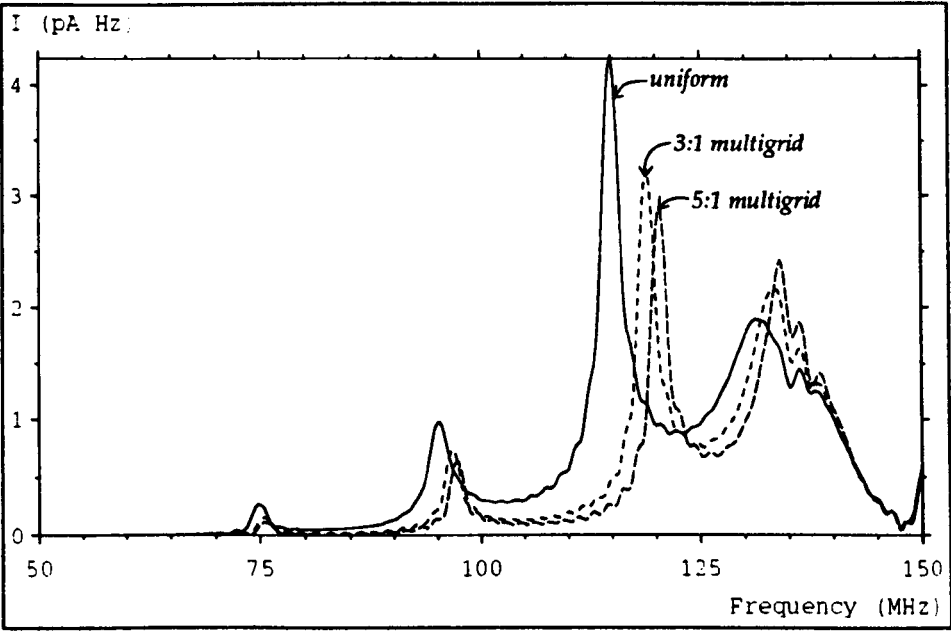
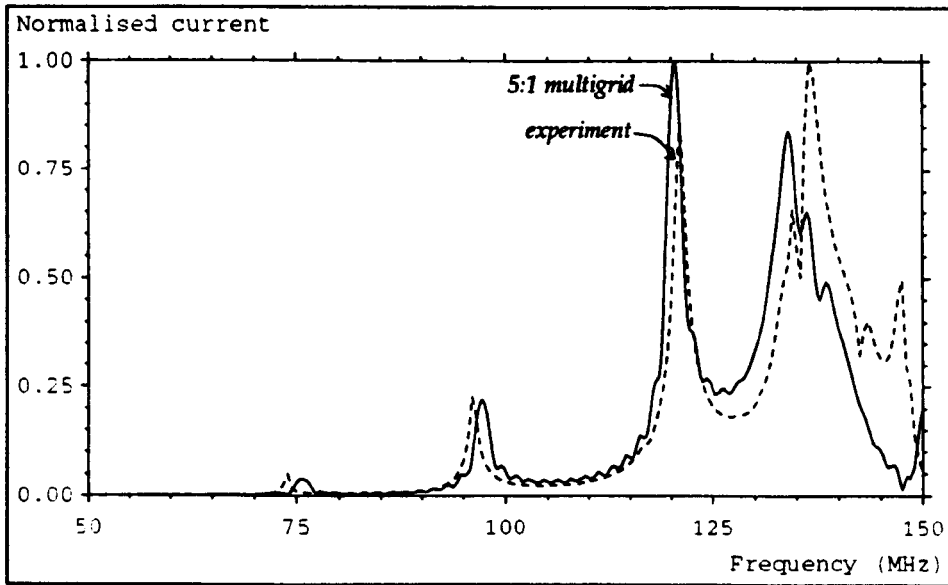
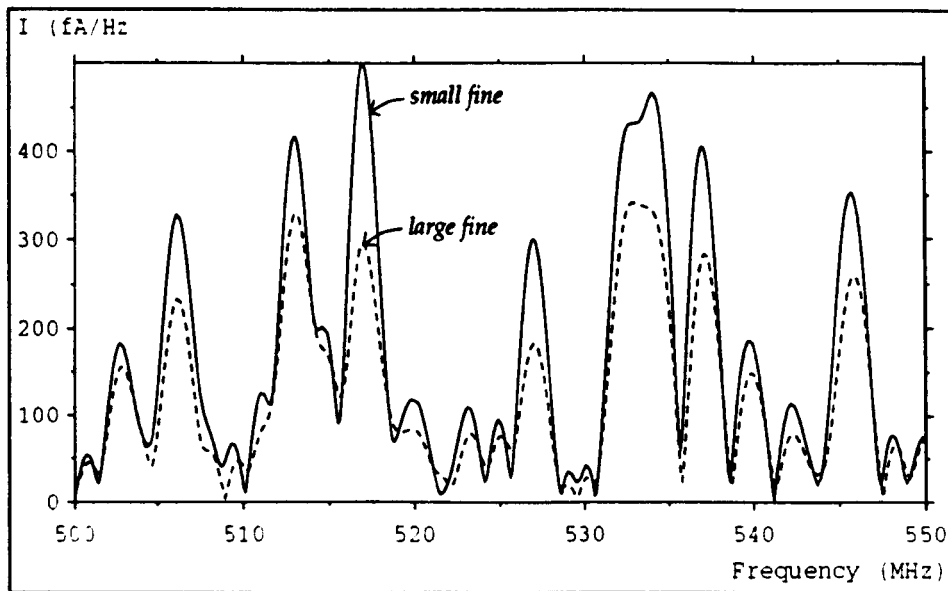


Fig. 7.24 – Effect of increasing resolution



**Fig. 7.25 – Comparison with experiment**



**Fig. 7.26 – Loss of energy due to large fine mesh**

The loss of energy which occurs during the fine→coarse conversion in a multigrid system can be investigated by increasing the volume of the fine mesh region. This is illustrated for a 3:1 reduction in fig. 7.26, where the volume of each fine mesh region has been increased from 15×69×15 nodes to 15×135×75 nodes. The fine mesh then extends across most of the width of the room and across most of the distance from the bench to the ceiling. Very little difference is observed below 150 MHz and so the frequency range 500→550 MHz is shown. It is apparent that there is considerable attenuation. In any lossless system it would be wise to avoid high reduction ratios and to keep the fine mesh regions as small as possible.

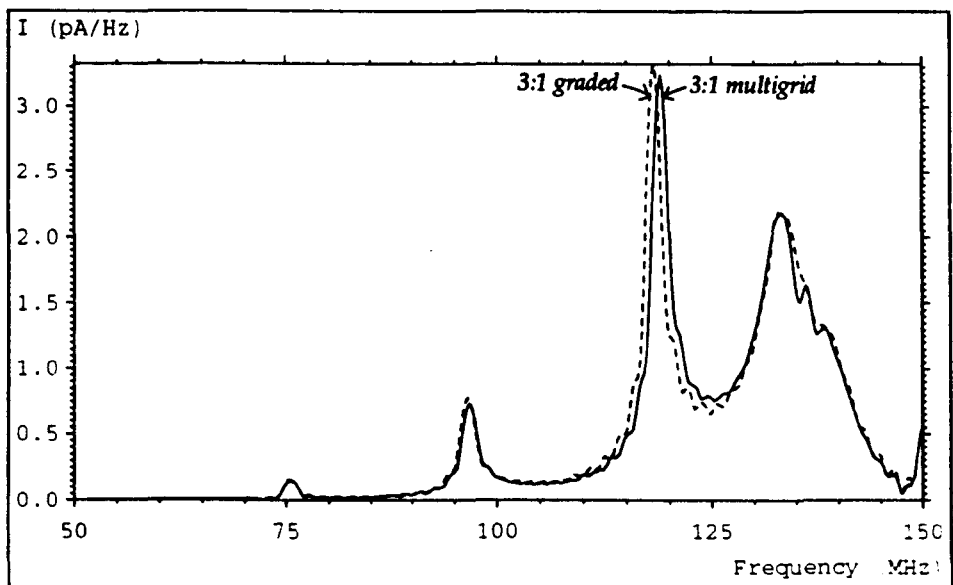


*Fig. 7.27 – Comparison of multigrid and graded mesh models*

A graded mesh can also be used to model this system. A comparison between the 3:1 multigrid mesh and a graded mesh is shown in fig. 7.27. For the graded mesh, the node dimensions normal to the dipoles have been reduced to 1.67 cm (the same as for the multigrid case). The grading used, moving out from each dipole, was 1×1.67 cm, 2×2 cm, 2×3 cm then 5 cm. The node dimensions parallel to the dipole were mainly kept constant but grading was applied so that the source at the centre of the dipole was described by a cubic node and so that the length of the dipole was exactly the same as in the multigrid simulation. It can be seen that the agreement is excellent, both in frequency and amplitude, although some differences are observed at frequencies above 150 MHz. The big disadvantages of the graded mesh are the additional storage requirement (for mesh parameters, stub voltages and additional nodes) and the fact that the same small timestep must be used throughout the entire problem space. A comparison of the computer resources is given below.<sup>7</sup>

	3:1 multigrid	3:1 graded
storage	1.29	2.25
run-time	1.51	7.36

<sup>7</sup> Further details on computer resources can be found in appendix 4.

## 7.7 TEM cell

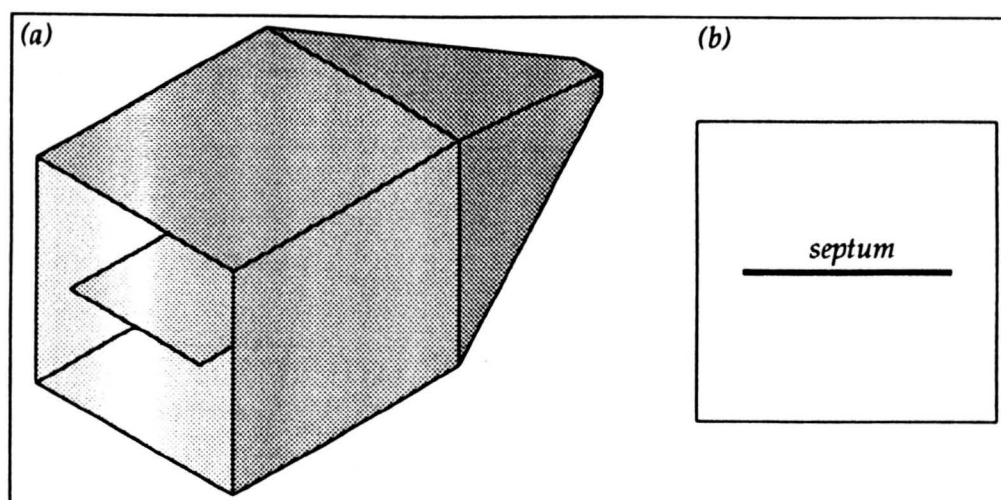


Fig. 7.28 – TEM cell

A transverse electromagnetic (TEM) cell is a section of rectangular coaxial transmission-line (typically  $50\ \Omega$ ) tapered at each end so that it can be connected to standard cables [64]. A cut-away view is shown in fig. 7.28a and a cross-sectional view is shown in fig. 7.28b. The centre conductor, or *septum*, is a flat sheet of metal supported by dielectric rods in the centre of the cell. The TEM cell is suitable for both radiated electromagnetic susceptibility testing and measuring radiated emissions and it can be used over a frequency range extending from d.c. to an upper limit determined by resonances and the propagation of additional modes.

A property of the TEM mode is that the electric field in the transverse plane satisfies Laplace's equation,  $\nabla^2 V = 0$ . This means that the transverse electric field can be obtained from the related static problem in 2-dimensions. This can be done numerically using a 2-dimensional TLM code or a 3-dimensional code can be used if open-circuit boundaries are placed above and below the plane. This has been done for a TEM cell with a cross-section of  $50 \times 50\text{ cm}^2$  and a 42 cm wide septum so that the results could be compared with those obtained using conformal mapping techniques by Tippet and Chang [65]. Short-circuit boundaries were used to represent the metal of the structure and the system was excited by applying an impulse electric field from the top and bottom walls to the septum. The result was obtained as a time average of 10000 iterations (see §4.2.1). The agreement with the analytical results is acceptable considering the fact that the septum thickness was



not modelled accurately.

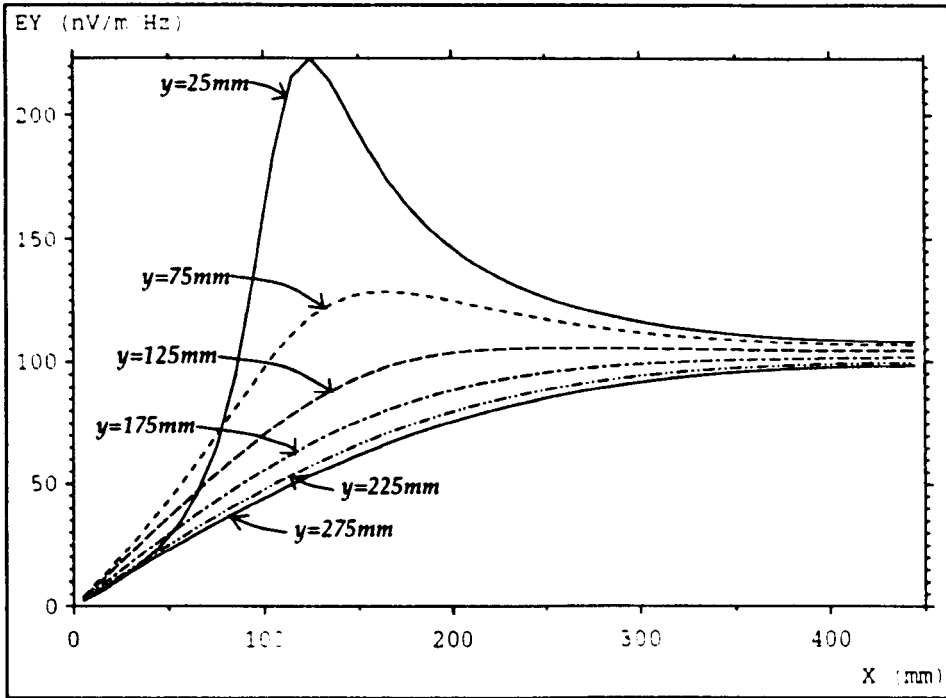


Fig. 7.29 – Vertical component of electric field at various heights above septum

For the remainder of this section a 90 cm long TEM cell of cross-section  $90 \times 60 \text{ cm}^2$  with a 68 cm septum has been used. This cell has a working bandwidth of 180 MHz. The vertical component of the electric field, extending from the left wall to the centre of the septum is shown for various heights above the septum in fig 7.29. A 3-dimensional model may be constructed by placing matched boundaries at the ends of the cell. This system may be excited by applying an impulse electric field on link-lines parallel to the required direction of propagation on a plane adjacent to one of the ends. A plane wave is not easily established in this system so 4000 iterations have been performed and a 500 point window has been applied to reduce the effect of the noise. The transverse components of the electric field at an off-centre output point (normalised so that the vertical component is unity at d.c.) are shown for three different excitations in fig. 7.30. In the first case, the vertical component of the electric field extends from the top and bottom walls to the septum (with opposite signs above and below the septum) but it is placed at the centre of the septum only. In the second case, the excitation extends across the width of the septum and in the third case both transverse components are excited with the steady-state solution obtained from the 2-dimensional model. The

response is essentially flat for the third case but features are present for the other cases. These features are highly dependant on the length of the cavity. A comparison is made in fig. 7.31, for the vertical component, in cells of length 0.9 m and 1.8 m with the excitation extending across the width of the septum. For the longer cell, a resonant peak can be identified and there is very little variation below this frequency. The field distribution at d.c. throughout the volume of the cell is independent of the excitation used but exciting with the steady-state solution means that a shorter cavity can be used. In this case, some disturbance is introduced in the vicinity of the excitation but it does not extend significantly into the cavity.

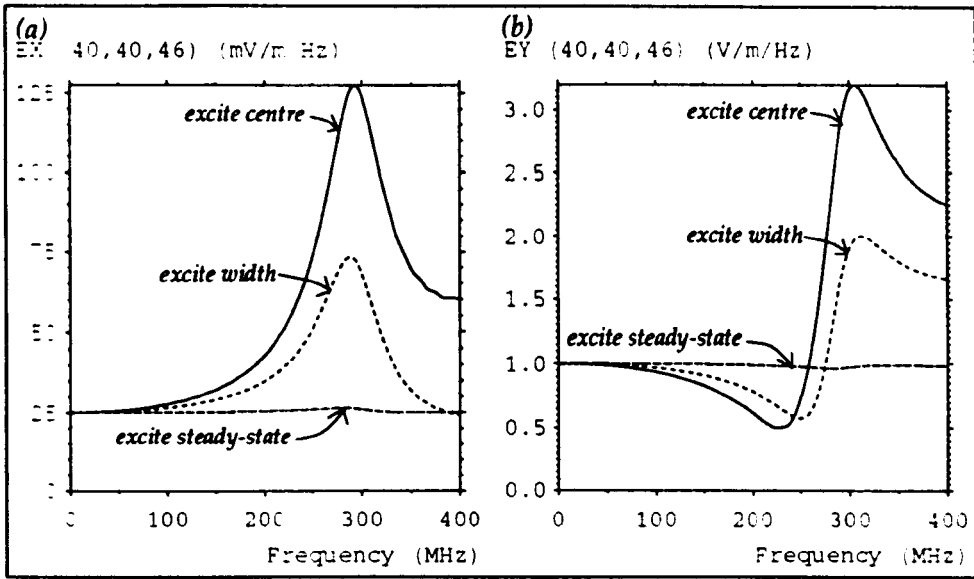


Fig. 7.30 – (a) Horizontal and (b) vertical electric field for different excitations

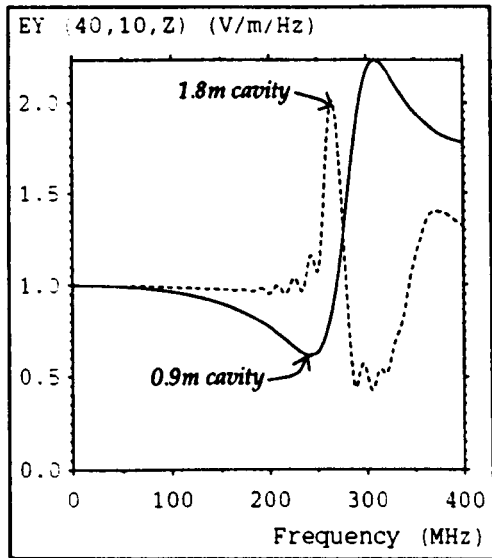


Fig. 7.31 – Effect of changing length of cavity

A 10 cm spherical dipole has been modelled inside a TEM cell to investigate whether it has a significant effect on the field distribution. The transverse components of the electric field are shown for planes parallel to the direction of propagation in fig. 7.32, for the case when the steady-state excitation has been applied. The noise observed in the first plot is an artefact of the excitation. The ratio between the vertical component of the field with and without the dipole present is shown in fig. 7.33 for a transverse plane passing through the centre of the dipole. There is a local field variation in the vicinity of the dipole but the bulk of the field remains unaffected which means that it is reasonable to use a TEM cell to calibrate antennas which are of similar size to the spherical dipole.

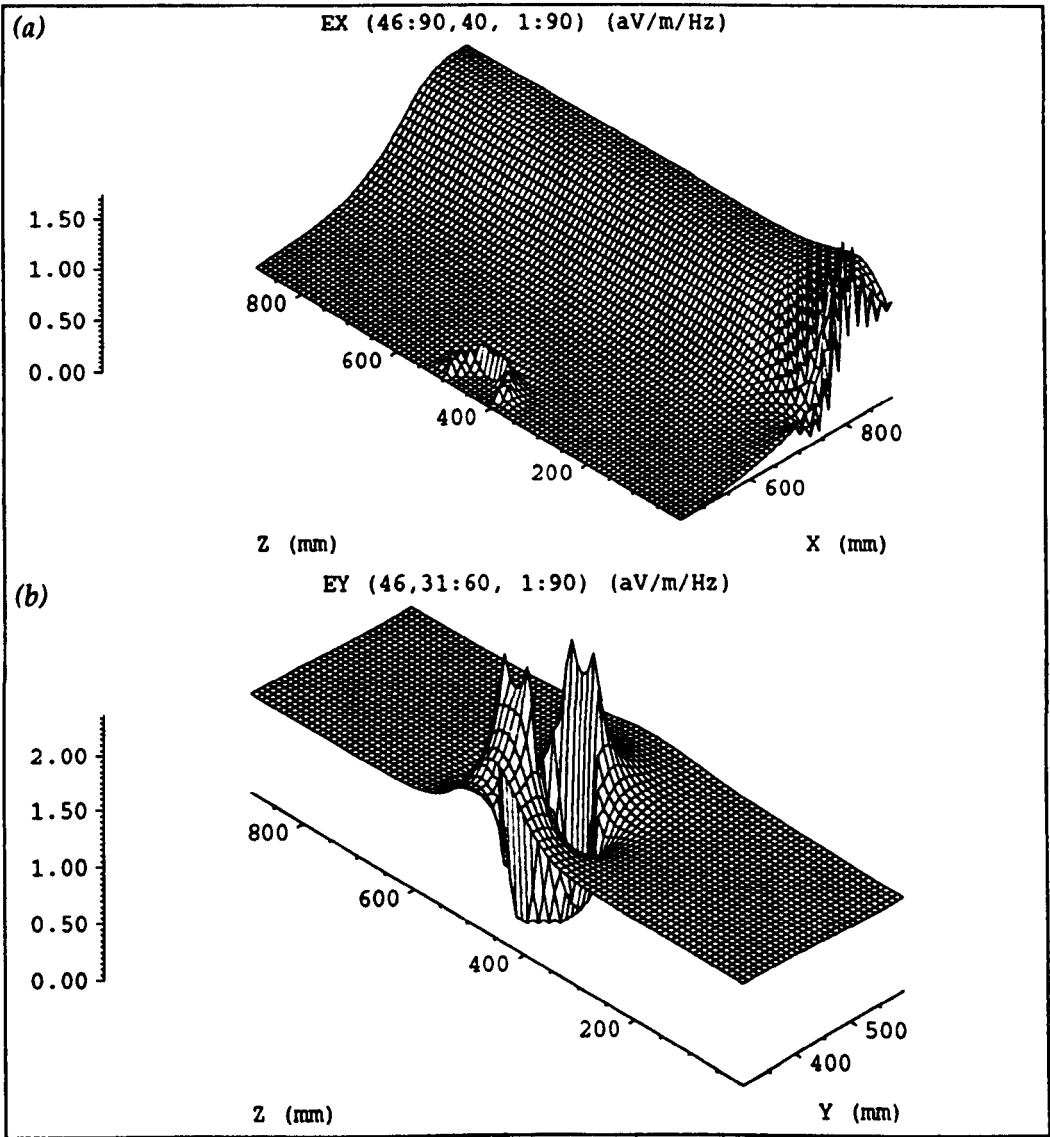
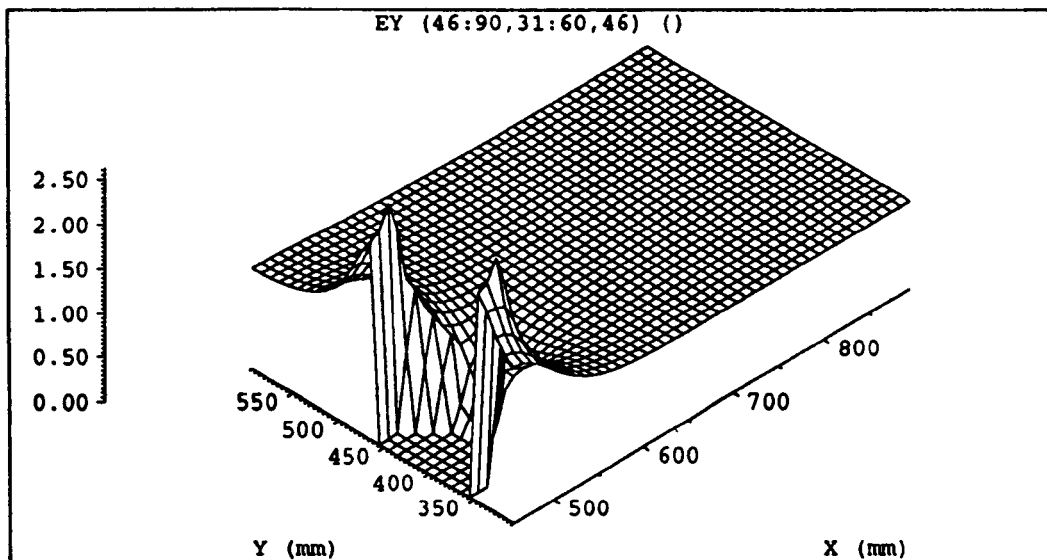


Fig. 7.32 – (a) Vertical and (b) horizontal electric field in presence of spherical dipole



*Fig. 7.33 – Ratio of the vertical electric field with and without spherical dipole*

# Chapter 8

## Unbounded Systems

### 8.1 Wire antennas

An antenna can be regarded as the structure associated with the region of transition between a guided wave and a free-space wave, or *vice-versa* [66 p17]. In TLM, a metal structure can be made to behave as a radiating antenna by exciting a current in it. This can be done by means of voltage or current sources or by applying a magnetic field loop around the antenna (Ampère's law). In this section, results are presented for tests performed on a linear antenna, or *dipole*, in free-space.

Originally, the TLM method was used in the analysis of waveguide and cavity resonator type problems and proper open boundary conditions were not investigated. Matched boundaries can be used as an approximation; they act as perfect absorbing boundaries for waves which are normally incident (see §5.12). In 2-dimensions, if a wave is incident at an angle  $\theta$  (to the normal), then the terminating impedance must be multiplied by a factor  $1/\cos\theta$ , and the resulting variable reflection coefficient has been coupled to an algorithm to predict the angle of the incident wave [67]. Absorbing boundaries have the disadvantage that if they are placed in the near field they remove all the energy that is incident upon them rather than just the radiated component. More general boundary conditions, based on those used in the finite difference time domain method have also been implemented [68,69]. An alternative method has been suggested in which pulses passing through the boundary plane are convolved with the impulse response of a perfect open boundary but, except for very simple cases, the storage requirement is excessive [70]. For the work presented in this chapter only simple matched boundary conditions have been used. Provided care is taken, in particular that the boundaries are distant from the region of interest, these boundaries have been found to be adequate for the systems considered. The space between the region of interest and the boundaries is often termed "whitespace".

Short-circuit nodes and short-circuits placed at the mid-point of link-lines can both be used to describe wire-like features within the TLM mesh. In order to reduce computer requirements to acceptable limits, it is desirable to model wires with a single node cross-section. However, there are problems with the circumferential communication of pulses around the wire, in particular, there is no direct communication between the corner nodes and the wire itself, and this leads to inaccurate results (see §5.11). A method has been proposed in which an additional "corner stub" is added to the node [71] but a more satisfactory approach is to introduce a local reduction in timestep around the wire in order to directly reduce the communication delay [42]. Another unsatisfactory aspect is that the modelled wire diameter is indeterminate. Tests have been performed to obtain the effective diameter indirectly from the inductance or capacitance of the wire inside a square conduit but different answers are produced by the two methods [72]. It is only when several nodes are used across the diameter that the modelled diameter can be specified with any accuracy, and this cannot be done in the majority of cases. An alternative approach to the modelling of wires is to use thin wire models, which allow wire diameters smaller than the node spacing to be used and these methods appear to give good results [73,74,75]. A diakoptic method has also been suggested in which pre-solved wire structures are inserted into the model [76]. For the work presented in this chapter, only simple short-circuit nodes and short-circuits on link-lines have been used.

A series of tests were performed to investigate the differences between using short-circuit nodes and short-circuits placed on link-lines for a 1.05 m (21 $\lambda$ ) antenna placed in the centre of a 51 $\times$ 51 $\times$ 71 node mesh with 5 cm node spacing, surrounded by matched boundaries. The parallel component of the electric field at a distance of 0.5 m and the current at the centre of the dipole<sup>1</sup> are shown in fig. 8.1 over a frequency range 0 $\rightarrow$ 500 MHz for the two models. The current can be calculated directly from the voltage pulses adjacent to the short-circuits or indirectly from the magnetic field using Ampère's law. In the latter case, a *tight* loop must be used so that there is no significant  $\frac{\partial D}{\partial t}$  term. For both models, an impulse current was applied on the centre node only and the results have been

<sup>1</sup> It is necessary to apply a window function prior to the DFT to obtain the current output coincident with the excitation.

normalised so that the DFT of the excitation pulse alone would be unity. It is apparent that the resonances, when the wire is behaving as  $\lambda/2$  and  $3\lambda/2$  dipoles, occur at slightly higher frequencies when short-circuits on link-lines are used. However, in both cases, the frequencies are much lower than the expected analytical resonances for an infinitesimally thin dipole, which occur at 143 MHz and 428 MHz. This is due to the fact that the dipole is not thin, as well as to the pulse communication problem mentioned earlier. This error does not preclude the use of the antenna as an arbitrary radiator.

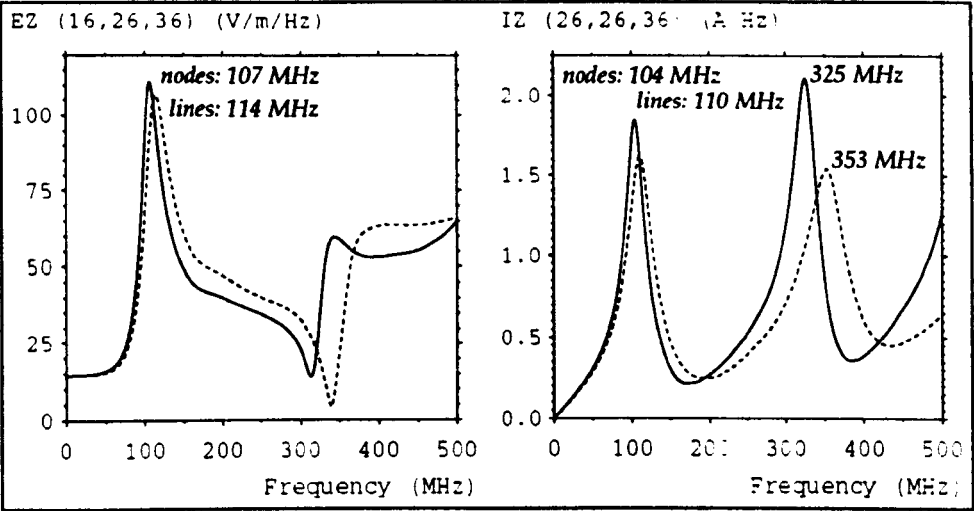


**Fig. 8.1 – Electric field and current for central excitation**

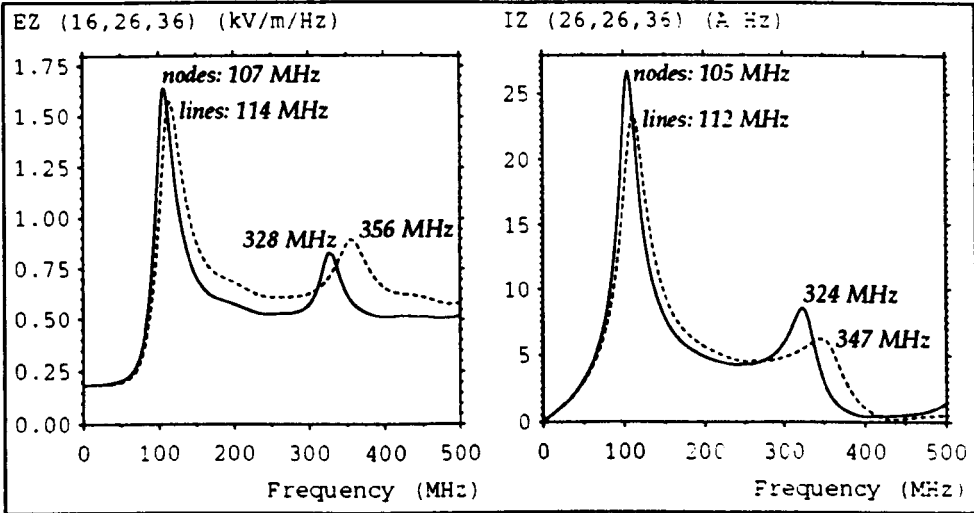
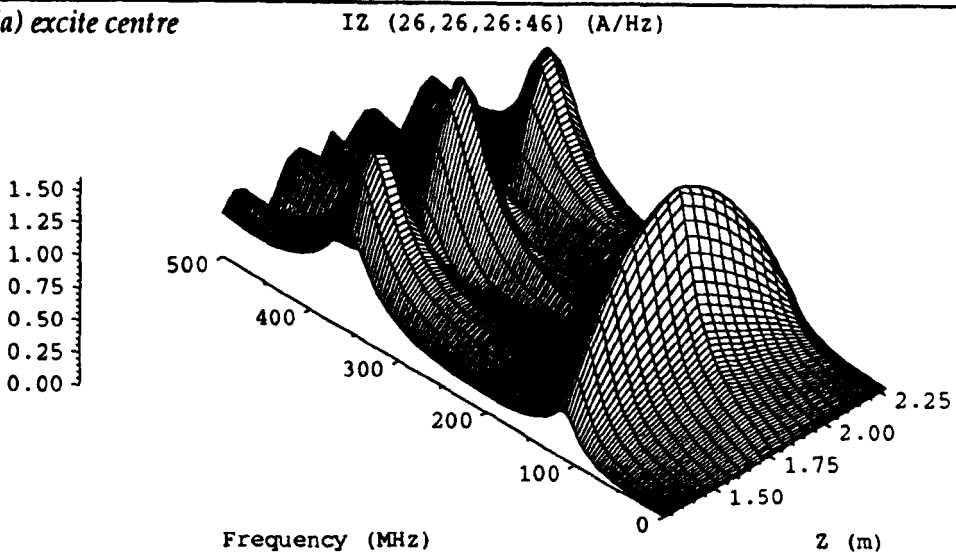
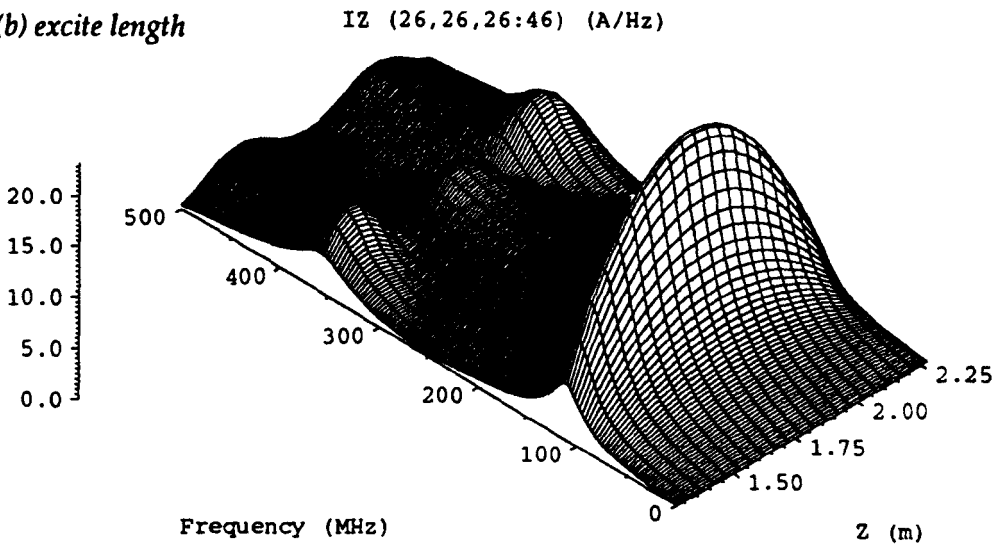


**Fig. 8.2 – Electric field and current for excitation along the length**

(a) excite centre



(b) excite length



(c) length÷centre

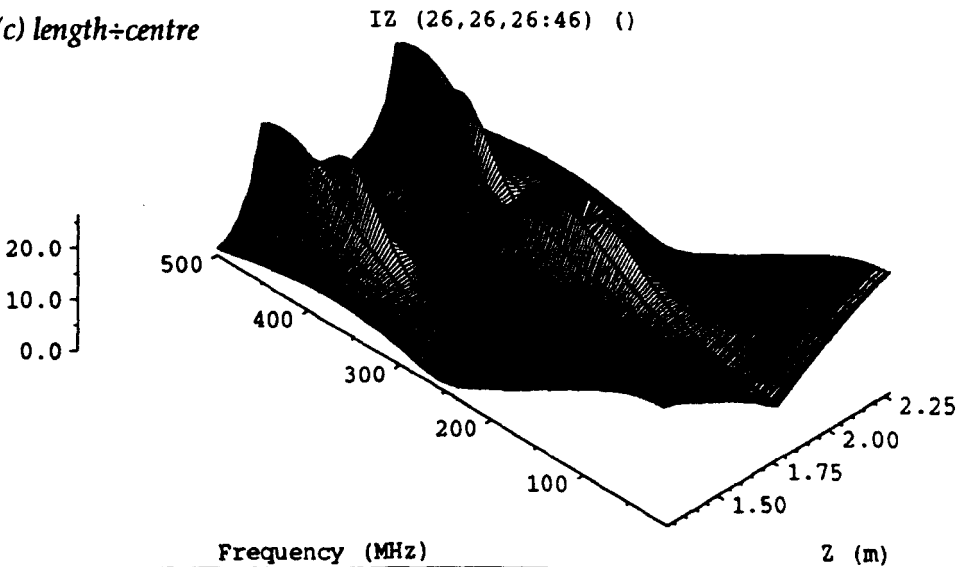


Fig. 8.3 – Current along the length of the dipole



Fig. 8.2 shows the corresponding graphs for the case when both dipoles are excited by a uniform impulse current extending along their full length. The resonant frequencies are similar to the previous cases but the relative energy in each of the resonances is different. Electric field maxima are apparent for the  $3\lambda/2$  resonance although they are not observed for central excitation. This is not unreasonable since the electric field at the output point will depend upon the relative phases of the contributions from each segment of the dipole. A peak will only be observed if the off-resonant current distribution is such that constructive interference does not cause the output field to be increased.

The current distribution along the length of the dipole is plotted against frequency for a dipole constructed from short-circuits on link-lines, for central excitation in fig. 8.3a and for excitation along the length in fig. 8.3b. The ratio between these two plots is shown in fig. 8.3c. It is interesting to note that at the two resonant frequencies, the ratio is approximately constant, which means that the resonant current distribution is independent of the excitation. In summary, it can be stated that short-circuits on link-lines provide a better wire description than short-circuit nodes. Excitation at the centre is physically more meaningful than exciting along the length since this is the way it is generally done in reality, but the second method can be used if required.

In order to model a dipole in free space, it is only really necessary to model one eighth of the problem space if symmetry is exploited. This can be done by placing a short-circuit boundary at the mid-point of the dipole and open-circuits passing through the dipole cross-section, as shown in fig. 8.4. The disadvantage of this is that the minimum cross-section is increased to  $2 \times 2$  nodes and the dipole must be an even number of nodes long. Results are shown in fig. 8.5 for a 1.1 m dipole described in a 5 cm mesh and in a 2.5 cm mesh. In the first case, the cross-section is  $2 \times 2$  nodes and in the second case, cross-sections of  $2 \times 2$  and  $4 \times 4$  nodes have been used. The  $4 \times 4$  dipole in the 2.5 cm mesh represents the same physical system as the  $2 \times 2$  dipole in the 5 cm mesh, but the resonant frequencies are slightly higher (102→105 MHz and 341→349 MHz) due to the better description of the  $4 \times 4$  dipole. The  $2 \times 2$  dipole in the 2.5 cm mesh has half the diameter and so higher frequencies would be expected.

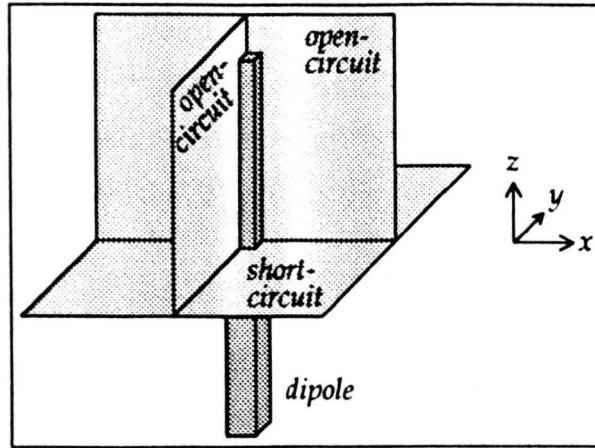


Fig. 8.4 – Exploiting symmetry

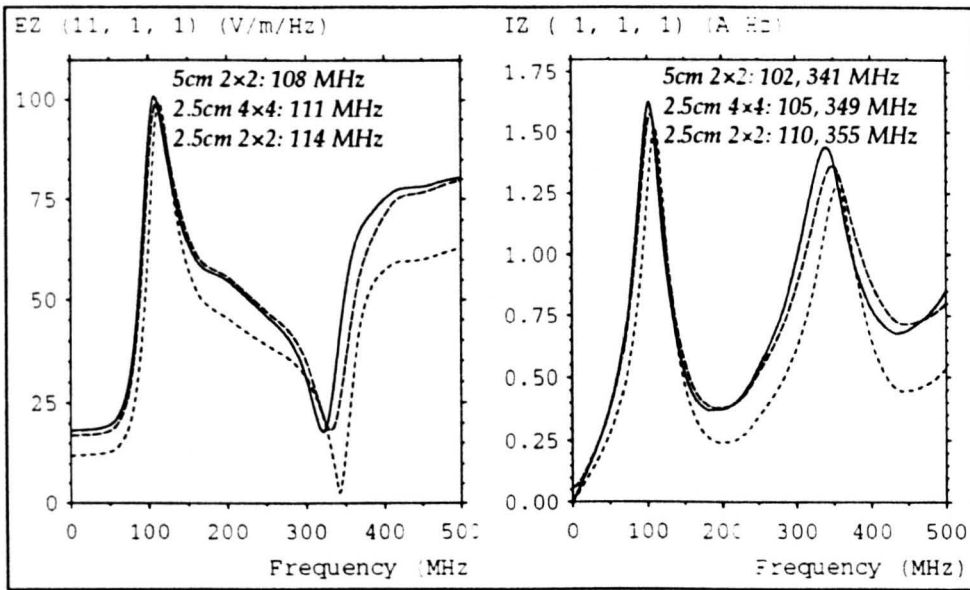


Fig. 8.5 – Electric field and current for dipoles of different cross-section.

To assess the effect of the imperfect boundary conditions, the size of the mesh was reduced from  $26 \times 26 \times 36$  to  $16 \times 16 \times 26$  nodes ( $\Delta l = 5\text{cm}$ ). The results are shown in fig. 8.6. Moving the boundaries inward produces some error at frequencies around the first resonance but at higher frequencies, where the electrical distance to the boundary is greater, there is little effect. No significant changes are observed if the boundaries are moved further away.

The electric field in the volume around the dipole can be conveniently observed by calculating the field on a plane at a specific frequency. The field profile on two orthogonal planes is shown in fig. 8.7 for the first resonance (131 MHz). Only one quarter of each plane is shown. The contours are lines of constant electric field magnitude plotted with a log. scale. The dipole has been modelled in a 1 cm

fine mesh and the field is shown in a 4 cm mesh extending by 28 m in each direction. An 8 cm coarse mesh has been placed around the other meshes to move the boundaries to a distance of 48 m from the dipole. In the X-Y plane, a series of concentric circles are produced and the main lobe can be seen extending towards the right in the X-Z plane.

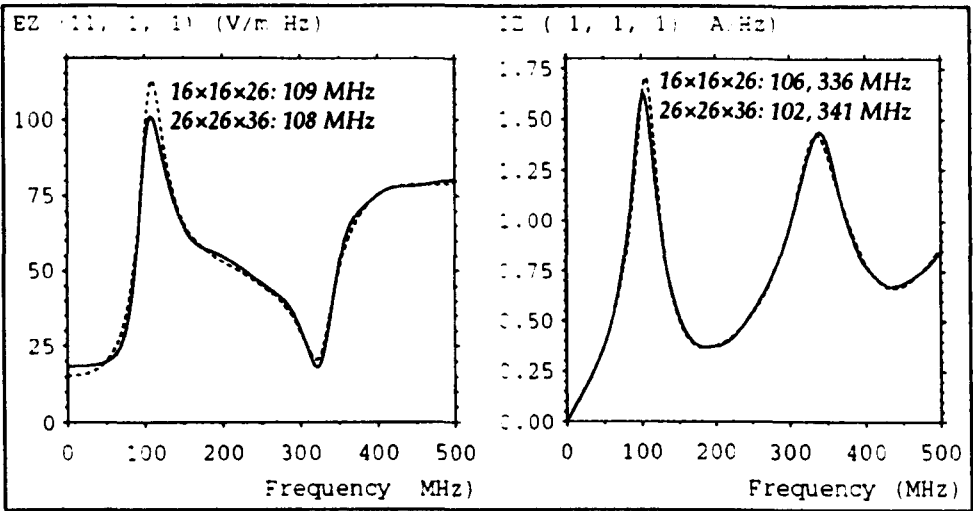


Fig. 8.6 – Effect of boundaries

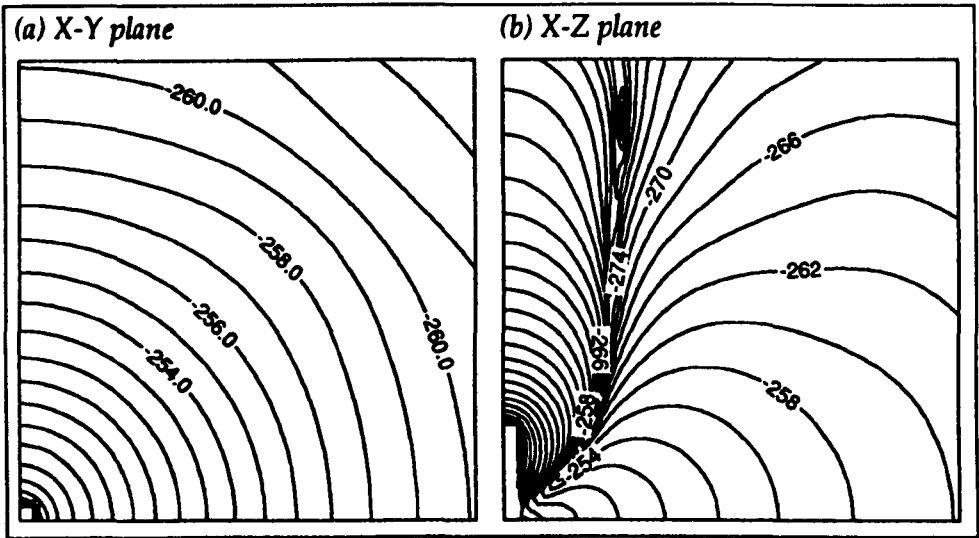


Fig. 8.7 – Electric field around a dipole

## 8.2 Slot antennas

A slot antenna can be considered as the complementary form of a wire antenna. This follows from an extension of Babinet’s principle which states that the complementary antenna is obtained by replaced all of the metal in the plane of the dipole by air, and *vice-versa*, and by exchanging the electric and magnetic field

quantities [66 pp632–635]. A slot antenna equivalent to a 1 m dipole can be constructed from an infinite plane by cutting a thin hole 1 m in length. In TLM, an infinite plane can be approximated by a finite plane, provided that its dimensions are large compared with the dimensions of the slot. Generally, it is only the radiation emanating from one side of the slot which is of interest and in this case the space on the other side can be truncated with a matched boundary.

In fig. 8.8, the electric field at a point 0.9 m from a  $100 \times 10 \text{ cm}^2$  slot is shown for four different cases, when the distance behind the slot to the matched boundary is varied from 0.1 m to 1.5 m. The region in front of the slot was modelled with a  $60 \times 51 \times 29$  node mesh with a 10 cm node spacing. The short-circuit plane was modelled by short-circuits at the mid-point of link-lines and the slot was excited by an impulse electric field across the slot extending along the length. It can be seen that if the matched boundary is placed directly behind the slot, a significant amount of energy is absorbed rather than being radiated. The boundary needs to be at least 1.5 m away to minimise the effect on the first resonance but this distance can be reduced for the second resonance.

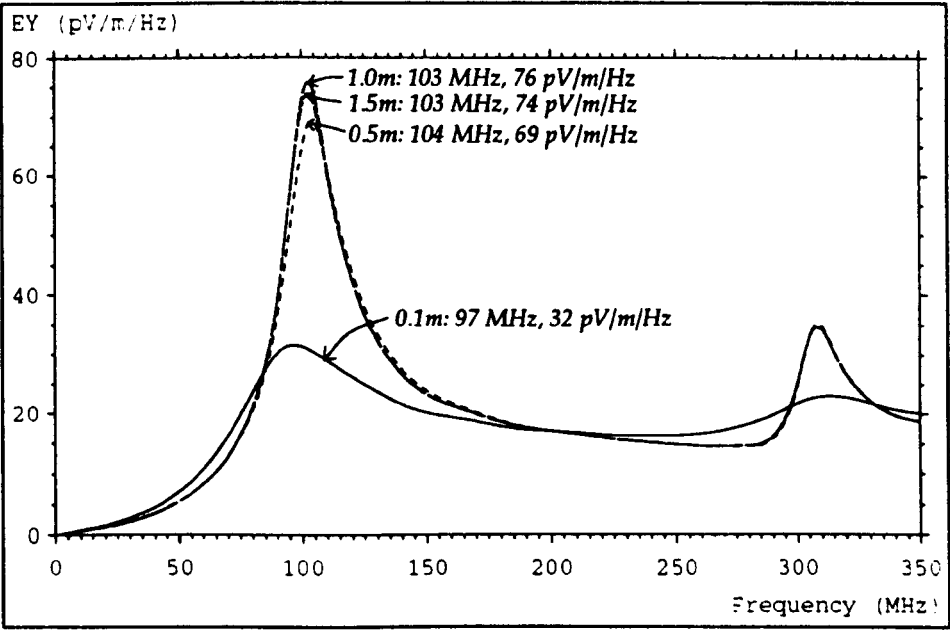


*Fig. 8.8 – Effect of matched boundary on electric field produced by slot*

The differences obtained when the plane is modelled by short-circuit nodes rather than short-circuits on link-lines are shown in fig. 8.9. The field magnitudes are different because different excitations were used: node excitation for the short-

circuit nodes and link-line excitation for short-circuits on link-lines. Slightly higher frequencies are obtained with the short-circuit nodes, in contrast to the wire antenna. The corresponding graphs obtained when the slot is excited at the centre only are shown in fig. 8.10. In this case, the second resonance is more pronounced.

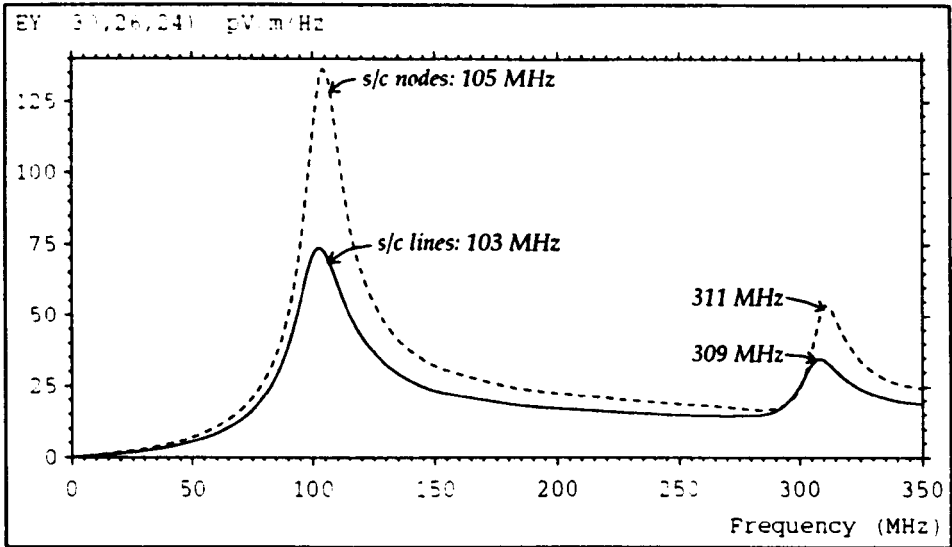


*Fig. 8.9 – Short-circuit nodes and short-circuits on link-lines, excite length*

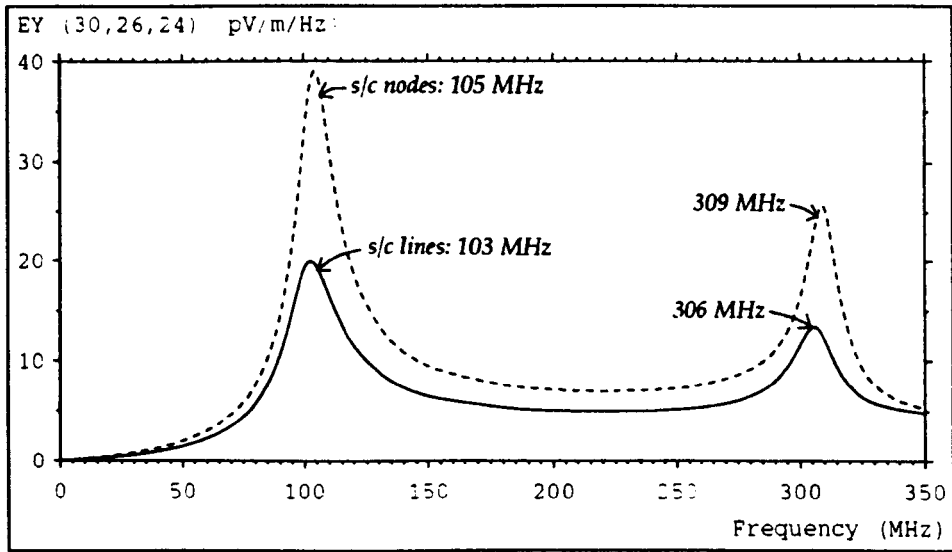


*Fig. 8.10 – Short-circuit nodes and short-circuits on link-lines, excite centre*

A fat slot, measuring  $16\times4\text{ cm}^2$  has also been investigated. This slot is used with the simulated device under test described in §8.6. It has been modelled at various resolutions with the multigrid technique. It is necessary that the fine mesh encloses a number of nodes around the slot for the increase in resolution to be observed. Symmetry was exploited when the slot dimensions were an even number of nodes. In all cases, a central excitation of minimum width was used and the

amplitude of the results has been normalised to an equivalent coarse mesh excitation. The results obtained with node spacings of 4 cm, 2 cm, 1 cm and 0.5 cm are shown in fig. 8.11. It is apparent that the frequencies of maximum amplitude do not converge quickly as the resolution is increased. However, the slot exhibits a very low Q resonance and the shape of the curves obtained with 1 cm and 0.5 cm node spacings are similar.

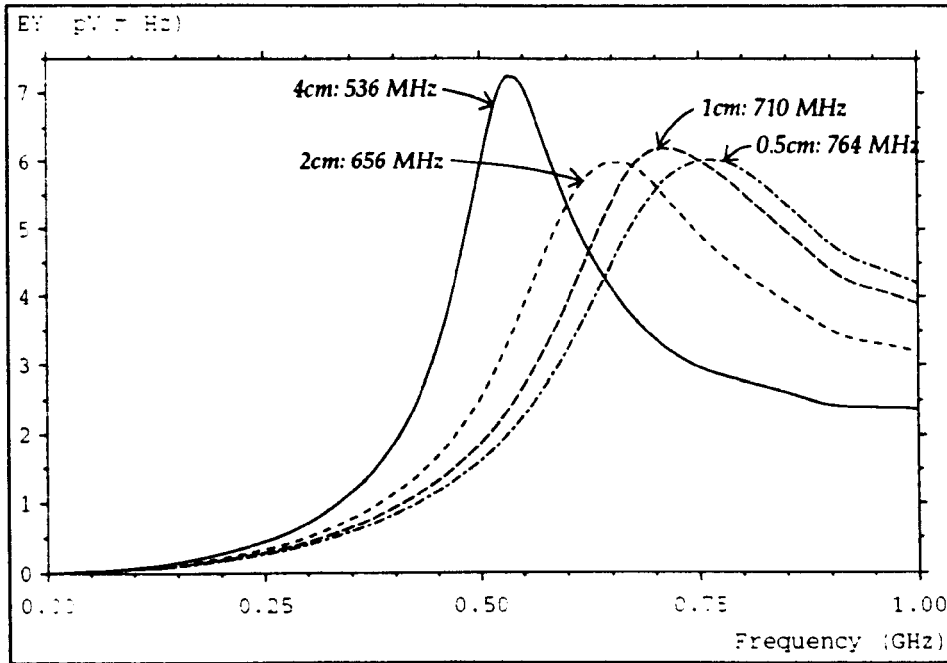


Fig. 8.11 – Effect of resolution on a fat slot

### 8.3 Spherical dipole

A spherical dipole (SD) can be used as an unintrusive transmitting or receiving device because it can be made small compared with the wavelength, with no trailing conducting wires which might disturb the field. The particular SD considered in this section consists of a 10 cm diameter sphere with a 0.3 cm equatorial gap. An optical link is used to connect the SD to the outside world and the internal electronics is powered by batteries. Below 200 MHz, the diameter is at most one fifteenth of a wavelength and it can be regarded as an elemental electric dipole source [77]. The SD can be used up to 1 GHz but its size is then an appreciable fraction of the wavelength.

A “staircase” approximation was used to represent the SD in a uniform rectangular mesh. The effects of such an approximation are not precisely known

but the results obtained for different node sizes indicate that they are not significant for the types of problem considered. For simplicity, short-circuit nodes were used rather than short-circuits on link-lines. Both solid and hollow spheres were considered. Short-circuit nodes were placed on nodes which met the following conditions

$$d < r + 0.6 \qquad \text{for solid dipole}$$

$$r - 0.6 < d < r + 0.6 \qquad \text{for hollow dipole}$$

where  $d$  is the distance, in nodes, between the test node and the centre of the sphere (which need not be at the centre of a node) and  $r$  is the required radius of the sphere in nodes (which need to be an integer). A value of 0.6 was used, rather than 0.5, to make certain that the hollow sphere contained no holes. A gap, typically one node in width was established to separate the two hemispheres. A 50 Ω lossy node was placed at the centre of the sphere and this was excited by an impulse magnetic field on the adjacent link-lines. Various sections through a hollow SD with a linear feed are shown in fig. 8.12, for a node spacing of 1 cm.

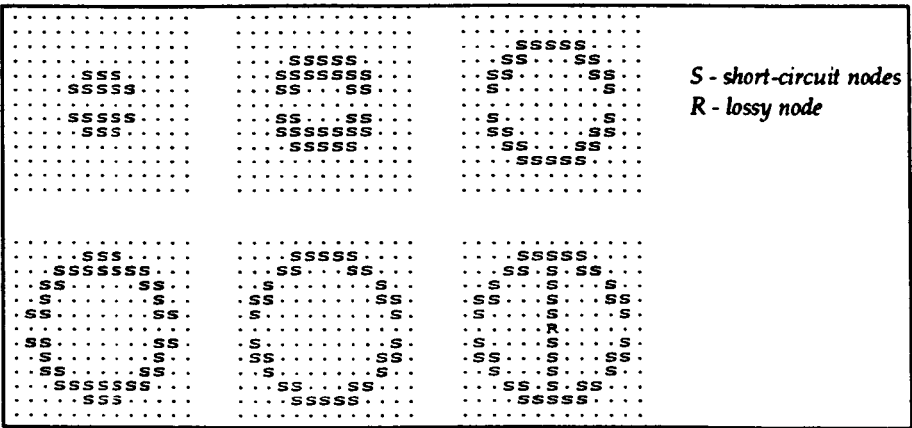


Fig. 8.12 – Spherical dipole model

To assess the effect of mesh resolution and gap width on the response obtained from a solid SD, a number of simulations were performed (some using the multigrid technique) in which the node spacing was reduced from 2 cm to 0.5 cm. Typical results are shown in fig. 8.13 for two components of the electric field. The gap width was a single node in all cases. The curves have been normalised so that the mean value in the range 0→1 GHz is the same, to account for the change in volume of the excitation and the physical gap width. It can be seen that the shape of

the curves does not vary significantly from 1 cm to 0.5 cm and so modelling the SD with a 0.5 cm mesh should give reasonable results.

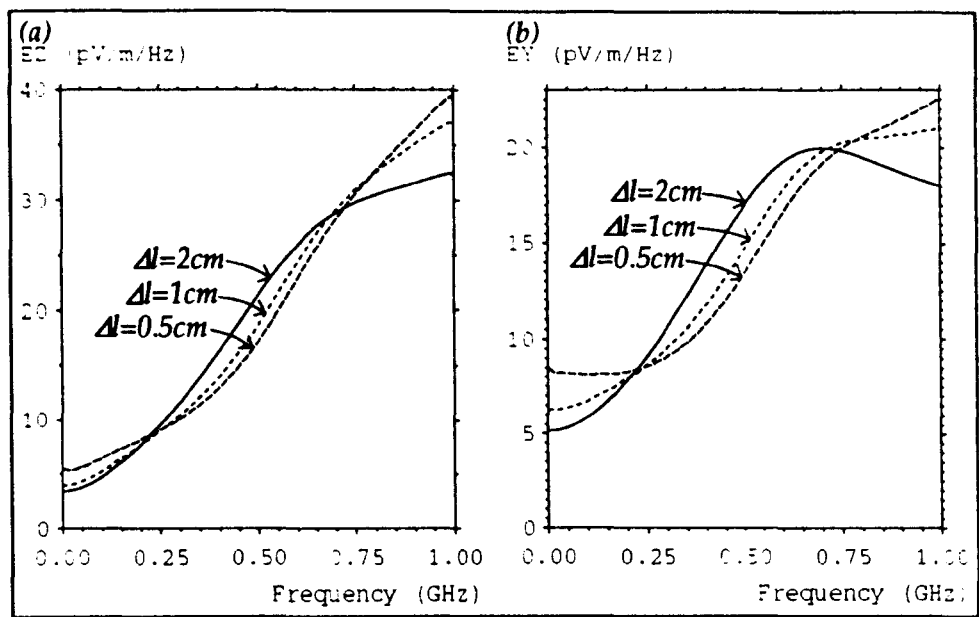


Fig. 8.13 – Effect of resolution on spherical dipole model

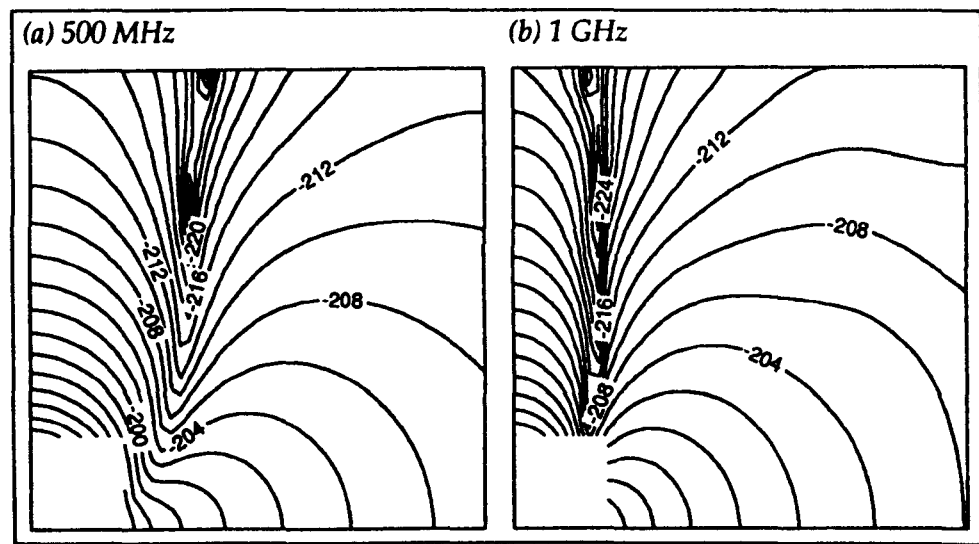


Fig. 8.14 – Electric field around spherical dipole

The field profile around a solid SD is shown in fig. 8.14 at frequencies of 500 MHz and 1 GHz. The output plane is parallel to the SD axis and symmetry has been exploited so that only one quarter of the plane is shown. The plane extends by 50 cm from the centre of the SD in each direction. The contours are lines of constant electric field magnitude plotted with a log. scale. In the equatorial plane, a series of concentric circles are produced. The SD was modelled in a  $20^3$  mesh with  $\Delta l=0.5\text{cm}$ , the field is shown in a  $50^3$  mesh with  $\Delta l=1\text{cm}$  and matched boundaries are placed



around a  $50^3$  coarse mesh with  $\Delta l=2\text{cm}$ .

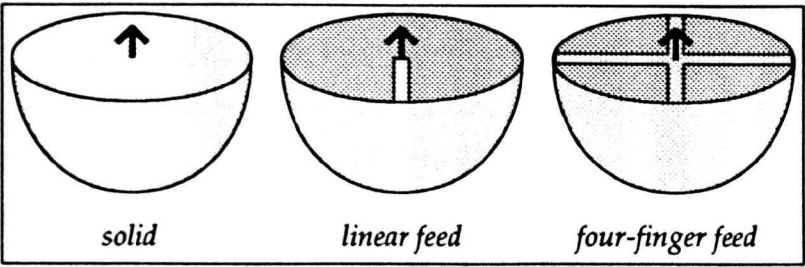


Fig. 8.15 – Different feed arrangements

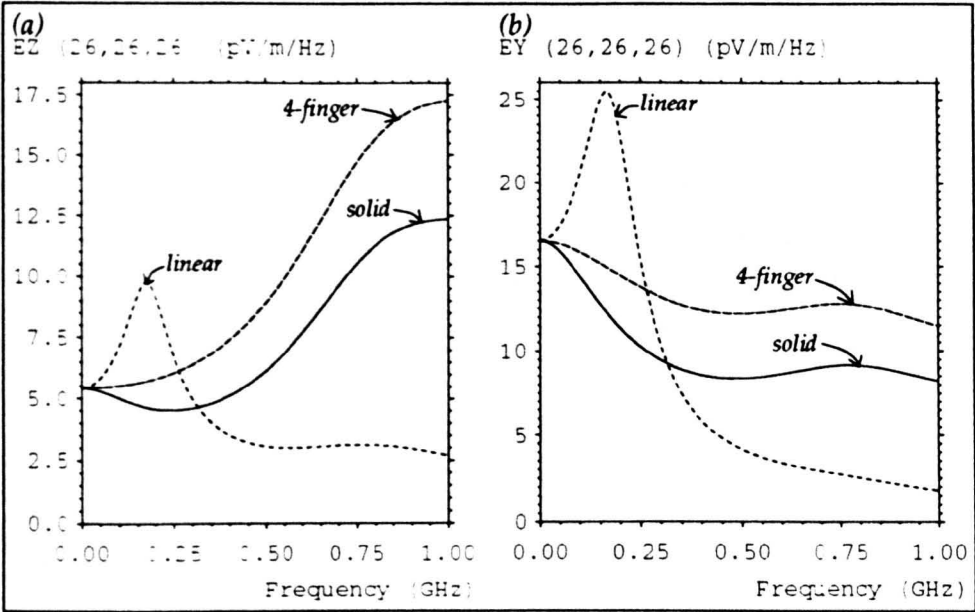
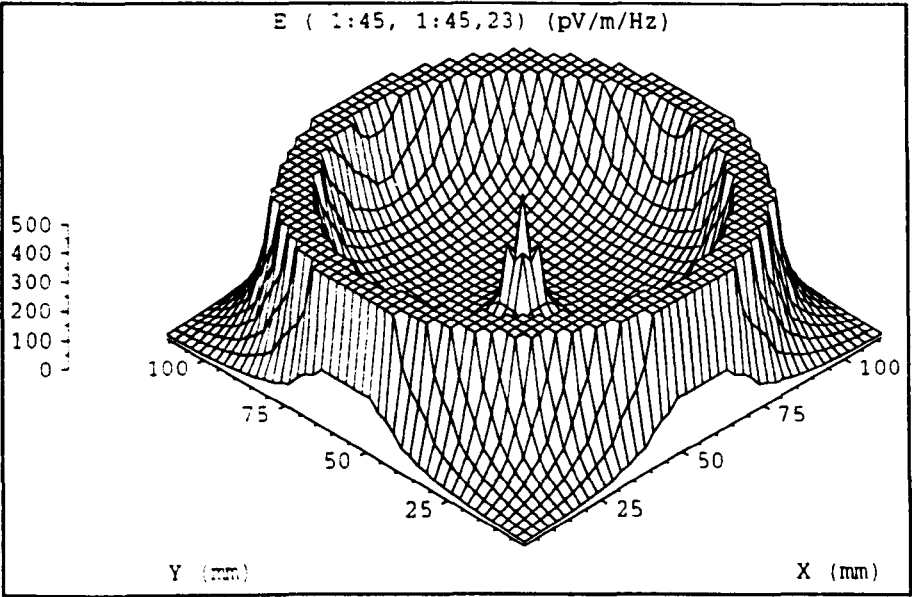


Fig. 8.16 – Electric field due to different feed arrangements

It would be expected that the constructional details of the SD would have a significant effect on its properties. It is obviously not possible to exactly model the circuits, wires and batteries inside the SD in any detail. However, three different configurations were studied to assess the effect of different feed arrangements. These arrangements, shown in fig. 8.15, consisted of a solid SD, a hollow SD with north-south linear feed and a hollow SD with an equatorial four-finger feed (with the fingers in each hemisphere aligned). The component of the electric field parallel to the SD axis is shown in fig. 8.16a, for the three cases, and an orthogonal component is shown in fig. 8.16b. The output point is 13 cm from the centre of the SD, offset by 7.5 cm in each direction, and a  $81^3$  mesh with  $\Delta l=0.5\text{cm}$  has been used. It is apparent that a peak is observed with the linear feed. To investigate this peak, the resolution was increased to 0.25 cm and the field inside the sphere was considered. The peak is only observed for the linear feed when there is a gap

between the two hemispheres. The field profile at 115 MHz is shown in fig. 8.17 on the equatorial plane for the case of a single node gap. No resonant structure is observed in the field and this is as expected since the SD diameter corresponds to a frequency of 3 GHz. The peak may be due to some form of LC oscillation. It is apparent that the hollow SD with linear feed exhibits complicated behaviour. In practice, the SD can never be completely hollow and so the solid SD or hollow SD with four-finger feed should be more realistic models.



*Fig. 8.17 – Field profile inside a spherical dipole with linear feed*

A particular area of concern in the modelling of the SD is the use of only a single node to define the gap width. Ideally, many nodes should be used so that waves travelling out of and into the SD can be described adequately. To assess the implications of using such a coarse description, the output at the centre of the SD was recorded when a plane wave, polarised parallel to the SD axis, was incident. The plane wave was formed in a  $81^3$  mesh with appropriate boundary conditions to allow perfect propagation (see §4.6.1). This system has the advantage that the excitation is independent of the mesh resolution (which is not the case if the magnetic field is applied around a single node). The TEM mode will propagate from d.c. upwards but at higher frequencies additional modes will be present. In a mesh with a constant number of nodes in each direction, these modes will occur first for larger values of node spacing. The results obtained for a hollow SD with linear feed for mesh resolutions of 1 cm and 0.5 cm are shown in fig. 8.18. In the

second case, gaps widths of one and two nodes were used. It can be seen that the frequency of the maximum is a function of the gap width rather than the node spacing. This suggests that, although far from ideal, it is acceptable to use a single node gap.

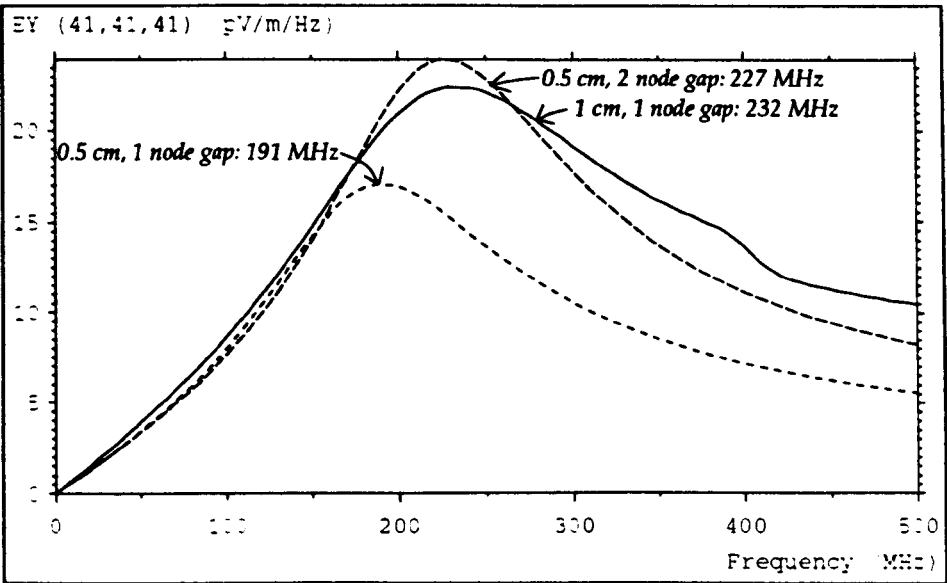


Fig. 8.18 – Effect of resolution and gap width

### 8.4 Radiation resistance

The radiation resistance is a conceptual quantity which relates the current in an antenna to the radiated power. It is not associated with any physical resistance in the antenna but is a resistance coupled from the antenna and its environment to the antenna terminals [66 p20]. It is defined by

$$R_r = \frac{P}{I_{rms}^2}$$

where  $P$  is the radiated power and  $I_{rms}$  is the rms current through the antenna terminals. In TLM,  $R_r$  can be obtained directly from this expression in the same way that it is calculated analytically. The current at the excitation point can be readily obtained either directly from the voltage pulses or indirectly via Ampère’s law. The radiated power can be obtained by summing the real part of the Poynting vector over any closed surface enclosing the antenna. It is convenient to construct this surface from a set of planes passing though the mid-point of link-lines, so that corners do not have to be considered. It is then appropriate to express the radiated power directly in terms of voltage pulses rather than field quantities. The electric

and magnetic fields on a link-line are given by (for the 12-port and stub-loaded nodes)

$$E = -\frac{1}{\Delta l}(V_1 + V_2) \quad \text{and} \quad H = \pm \frac{1}{Z_0 \Delta l}(V_1 - V_2)$$

where  $V_1$  and  $V_2$  are the voltage pulses from adjacent nodes (which may be either incident or scattered). The Poynting vector, at a particular frequency, is given by

$$\underline{S} = \underline{E} \times \underline{H}^*$$

where  $\underline{E}$  and  $\underline{H}$  are complex quantities output from a DFT and  $*$  indicates the complex conjugate. The radiated power over the surface area of a single link-line, due to one polarisation, can be written as

$$P_i = \frac{\Delta l^2}{2} \text{Re}(\underline{E} \times \underline{H}^*)$$

where  $E$  and  $H$  are peak quantities. In terms of the voltage pulses

$$\begin{aligned} P_i &= \frac{1}{2Z_0} (V_{out} V_{out}^* - V_{in} V_{in}^*) \\ &= \frac{1}{2Z_0} (|V_{out}|^2 - |V_{in}|^2) \end{aligned}$$

where  $V_{out}$  is the voltage pulse travelling out of the surface and  $V_{in}$  is the pulse travelling into the surface. The total radiated power is then obtained by summing both polarisations over all planes.

$$P = \sum_i P_i$$

If the voltage pulses and the current are both evaluated as peak quantities then the radiation resistance can be written as <sup>2</sup>

$$R_r = \frac{\sum (|V_{out}|^2 - |V_{in}|^2)}{Z_0 I^2}$$

A useful check to ensure that sufficient iterations have been performed is to consider two surfaces placed at different distances from the antenna; the power flow through each should be the same. Alternatively, the power flow through a plane which is expected not to radiate can be monitored to ensure that this is the case.

<sup>2</sup> If the DFT contains a  $\Delta l$  multiplier (see §3.1) then it is important to ensure that  $\Delta l^2$  is included in  $|V|^2$  as well as in  $I^2$ .

The radiated power must be calculated in the frequency domain and separate DFT's must be performed for each polarisation and for each point on the surface. For a large surface, the volume of time domain data may be excessive and it may be necessary to maintain running sums for the DFT's within the main calculation, rather than outputting the time domain data to be processed later. In any case, the radiated power will be the same through any surface and it would be sensible to choose the smallest possible surface in order to reduce the storage requirement. However, it would be advisable to leave some gap between the antenna and the surface in case there are any numerical errors resulting from summing the reciprocating energy in the near field. Alternatively, an appropriate window function can be used prior to the DFT. If the power is to be calculated at a large number of frequencies then it may be possible to reduce the storage requirement by evaluating the DFT for a number of adjacent nodes together, assuming that there is negligible phase difference between them. An alternative method of calculating the radiated power would be to sum the power dissipated in all lossy components in the system. For example, the power radiated by a single antenna surrounded by a matched boundary is equal to the power dissipated in the boundary. However, the number of DFT's required for all lossy components is likely to exceed the number needed for a small surface placed directly around the antenna.

To validate the method, a 1 m dipole was modelled with short-circuits on link-lines in a  $50^3$  mesh with  $\Delta l=2\text{cm}$ . Symmetry was exploited so that the dipole cross-section was  $2\times 2$  nodes. The dipole was excited by a Gaussian voltage source at its centre and the power flow through a surface placed at a distance of one node was obtained. The current at the dipole centre and the power flow were then multiplied by appropriate constants to give the total current and power for a dipole with no symmetry planes. The total power flow is shown in fig. 8.19a. The only significant contribution comes from voltage pulses polarised along the axis of the dipole (on planes parallel to the axis). The current is shown in fig. 8.19b and the radiation resistance is shown in fig. 8.19c. The analytical radiation resistance of a thin centre-fed half-wave dipole with a sinusoidal current distribution is  $73\ \Omega$  [66 p227]. The values obtained at the current maximum and at the power maximum are  $54\ \Omega$  and  $63\ \Omega$ , respectively, and the analytical value is achieved at a frequency of 132 MHz. It can be stated that there is good agreement, given the inadequacies of

the dipole model.

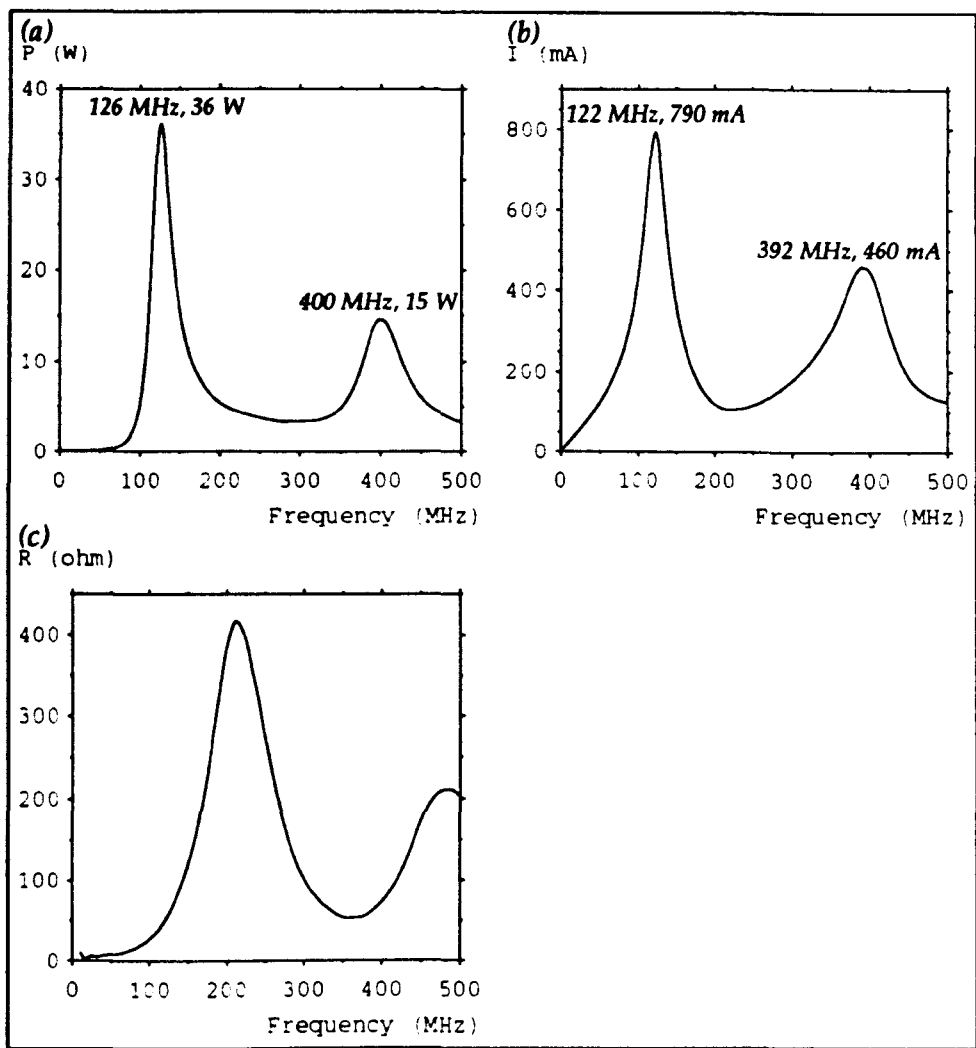
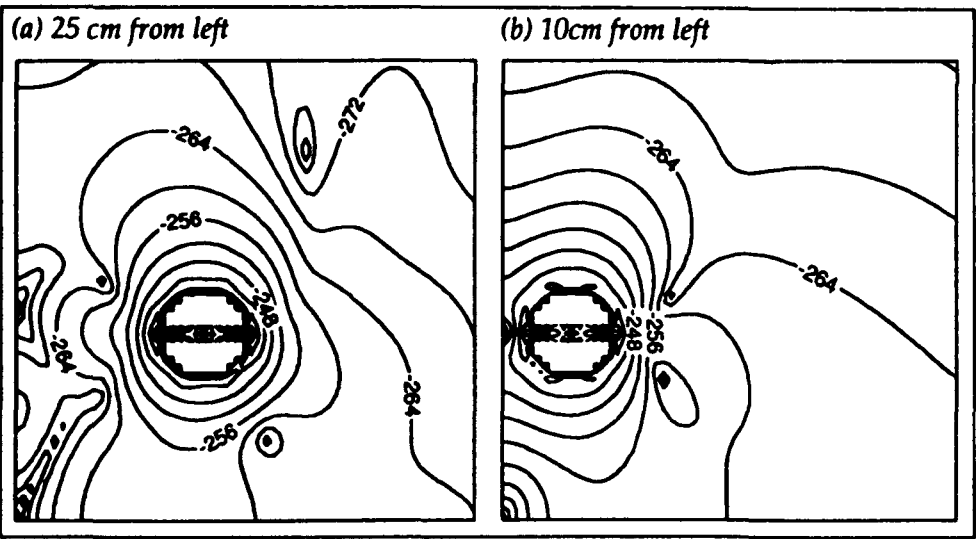


Fig. 8.19 – Power, current and radiation resistance for a linear dipole

### 8.5 Proximity effects

EMC measurements are subject to errors and uncertainties due to the non-ideal measurement environment. A particular type of uncertainty is caused by changes in the calibration of antennas used in such environments, which results in measurements done under supposedly similar conditions exhibiting substantial differences. Antennas are often used in close proximity to conducting surfaces, such as screened room walls and equipment cabinets, and it is important to determine their effect on the operation of the antenna. The effect of conducting surfaces on the magnitude of the electric field around a 10 cm spherical dipole is shown in fig. 8.20, at a frequency of 500 MHz. Short-circuits have been placed along

the bottom and left edges. In fig. 8.20a the SD is 25 cm from each surface and in fig. 8.20b the distance to the left edge is reduced to 10 cm.



*Fig. 8.20 – Effect of a conducting corner on the field around a spherical dipole*

To get a quantitative measure of the effect of conducting surfaces, it is possible to observe the field at a point when the distance between the surface and the antenna is varied. The disadvantage of this is that constructive and destructive interference from multiple reflection paths result in a confusing output. A more satisfactory approach is to observe changes in radiation resistance. The change in radiation resistance of a horizontally polarised half-wave dipole can be predicted analytically [66 pp461–467] and this can be used to verify the predictions made using TLM. A 1.1 m dipole was modelled in a 10 cm mesh with matched boundaries placed at a distance of 7.5m from the antenna (using the multigrid technique). The height of the dipole above a 16×15 m<sup>2</sup> ground plane was varied from 0.6→2.4 m and free-space conditions were also considered. The current and radiation resistance are shown in fig. 8.21. The relative amplitudes of the power curves are similar to those of the current curves. The radiation resistance is compared with analytical results below, at frequencies corresponding to the first electric field maximum (102 MHz) and also the analytical resonant frequency (136 MHz). The numbers in parentheses give the relative radiation resistance with respect to the free-space value.

distance (m)	analytical	TLM @ 102 MHz	TLM @ 136 MHz
$\infty$	72 $\Omega$	55 $\Omega$	164 $\Omega$
0.6	94 $\Omega$ (1.31)	67 $\Omega$ (1.22)	215 $\Omega$ (1.31)
1.2	62 $\Omega$ (0.86)	60 $\Omega$ (1.09)	132 $\Omega$ (0.80)
1.8	82 $\Omega$ (1.14)	45 $\Omega$ (0.82)	181 $\Omega$ (1.10)
2.4	71 $\Omega$ (0.99)	63 $\Omega$ (1.15)	154 $\Omega$ (0.94)

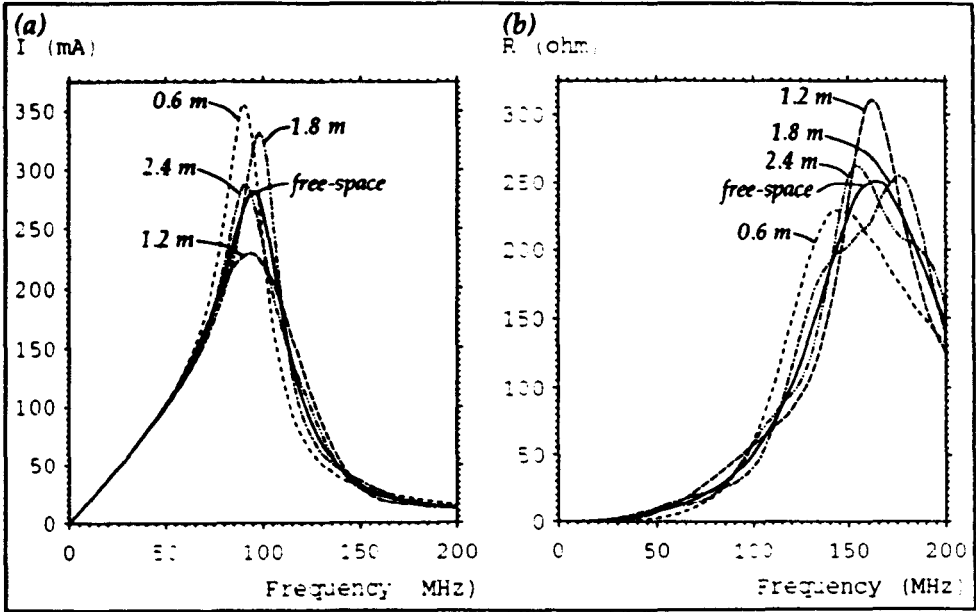
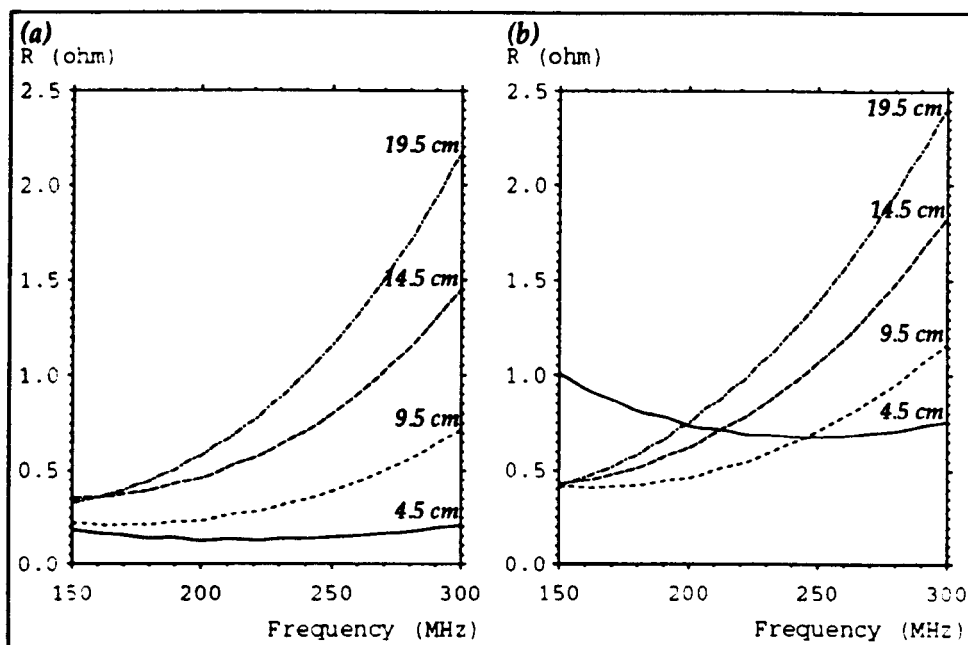


Fig. 8.21 – Current and radiation resistance for dipole above ground plane

The TLM free-space result at 102 MHz is worse than that predicted in §8.4 due to the poorer dipole description and this is reflected in the values obtained with the ground plane. The absolute values are of the correct order of magnitude but the relative radiation resistance is completely erroneous. At 136 MHz, the absolute radiation resistance is too large but the relative radiation resistance is in good agreement with the analytical result. This to be expected since the change in radiation resistance is a function of the electrical distance to the ground plane at the analytical resonant frequency rather than at the observed resonant frequency. The results indicate that it should be possible to observe trends even for a crude antenna model, although the absolute values may be inaccurate.





**Fig. 8.22 – Short-dipole above (a) a ground plane (b) a conducting edge**

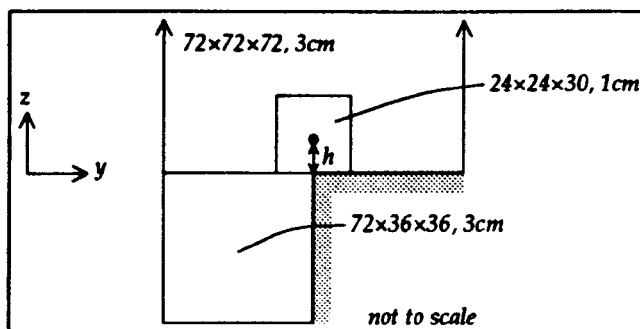


**Fig. 8.23 – Configuration used to place dipole above an edge**

A spherical dipole can be approximated by a linear dipole operating well below its first resonance, for frequencies within its operating range. A horizontally polarised 11 cm linear dipole was modelled with a 1 cm mesh and the height above the ground plane was varied from 4.5 cm to 19.5 cm. A 3 cm coarse mesh was placed around the 24×24×30 fine mesh so that the matched boundaries were at least 1 m from the antenna. The results for radiation resistance are shown in fig. 8.22a. There is very little power radiated below 150 MHz and so the radiation resistance is likely to be in some error below this frequency. The current is largely unaffected by the ground plane, except for the closest case. It is apparent that as the dipole approaches the ground the radiation resistance decreases, which is the expected result. The dipole has also been modelled above a conducting edge, as shown in fig. 8.23 and the results are shown in fig. 8.22b. The radiation resistance is greater than

for the infinite ground plane and this increase is more noticeable for the smaller heights.

Simulations have been performed to determine the change in radiation resistance of the spherical dipole model used in §8.3. The SD was modelled in a  $27^3$  fine mesh of 0.5 cm node spacing and this was placed within, for the free-space simulation, a  $81^3$  coarse mesh of 1.5 cm node spacing. A ground plane was then incorporated into the model and this was placed at distances of 9.5 cm, 14 cm and 20 cm from the centre of the dipole. The radiated power was obtained in the coarse mesh in order to reduce the storage requirement. The results are shown in fig. 8.24a for a plane parallel to the dipole axis and in fig. 8.24b for a normal plane. It is apparent that greater variations are observed in the first case. It is unlikely that the radiation resistance of a real SD would have exactly the calculated values since the feed arrangement and internal components were not modelled accurately. In addition, the ground plane used in the model may not have been large enough to approximate an infinite ground plane. However, the observed trend that variations from the free-space value decrease with increasing spacing and that greater variations are observed for a plane parallel to the dipole axis should still be true.

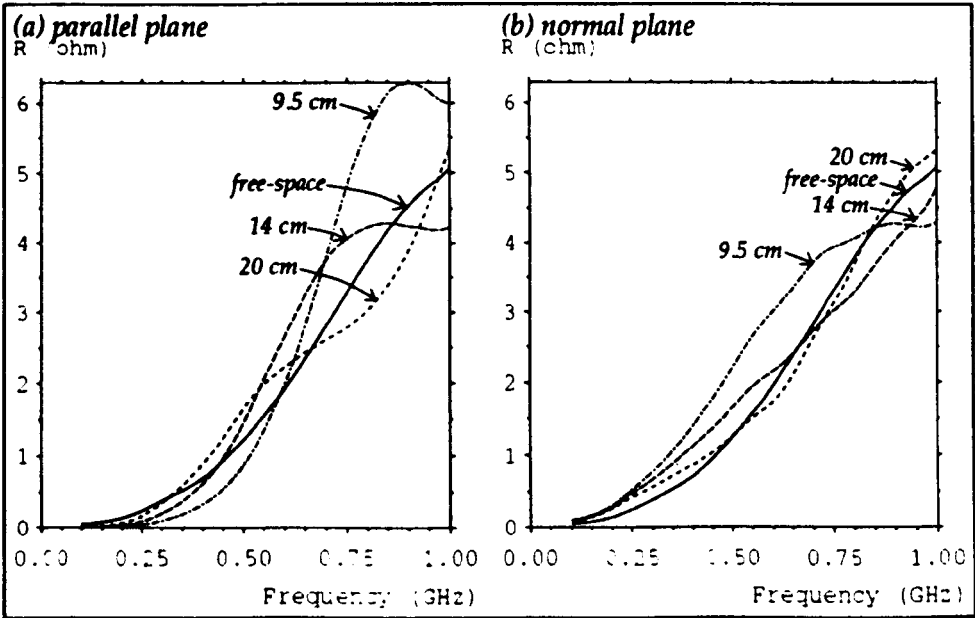


Fig. 8.24 – Radiation resistance of a spherical dipole

## 8.6 Simulated device under test

In order to investigate the measurement of the emission from real equipment, a simulated device under test (DUT) was constructed<sup>3</sup>. The DUT measures  $48 \times 48 \times 12$  cm<sup>3</sup> and is designed to imitate, in a simplified manner, the way in which real electronic devices would radiate into either free-space or a screened room. The dimensions are similar to those of standard 19" rack equipment. It consists of a brass box which can be made to radiate in a number of ways by removing panels to reveal slots (slot modes) or by adding panels parallel to existing surfaces (gap modes). The two modes considered in this section are shown in fig. 8.25. For the front slot mode, a  $16 \times 4$  cm<sup>2</sup> slot is revealed in one of the side panels and it is excited by a voltage applied across the centre. For the top gap mode, an additional panel is placed 4 cm above the top panel, supported on dielectric spacers, and the excitation is applied centrally between the two panels. An optical link is used to connect the DUT to the external environment and the internal electronics is powered by batteries.

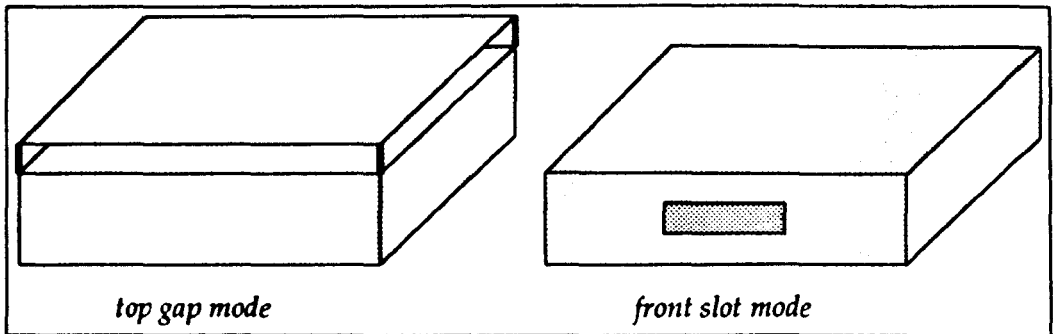


Fig. 8.25 – DUT

The vertical component of the electric field at a distance of 80 cm from the front of the DUT is shown in fig. 8.26 for the top gap mode, with the DUT in free-space. A 4 cm uniform mesh of  $76 \times 68 \times 38$  nodes was used as well as a multigrid mesh in which the DUT was described in a 2cm fine mesh of  $40 \times 26 \times 20$  nodes. One symmetry plane was exploited. It is apparent that as the resolution is increased the frequency of the features shifts up, although the overall shape remains unchanged. The field obtained at a distance of 32 cm for the front slot mode is shown in fig. 8.27. A smaller mesh was used so that a 2 cm uniform fine mesh could be compared

<sup>3</sup> The DUT was designed and built at the University of York.

with the multigrid result. Three results are shown in the graph: a  $44 \times 35 \times 22$  4 cm uniform mesh, a  $88 \times 70 \times 44$  2 cm uniform mesh and a 4:1 multigrid mesh with a  $80 \times 44 \times 40$  1 cm fine mesh region. Essentially the same result was obtained with a 2:1 reduction ratio and 2 cm coarse mesh as for the 4:1 reduction ratio and 4 cm coarse mesh, although some small differences were obtained above the  $10\Delta l$  limit of the coarse mesh (750 MHz). It can be seen that as the resolution is increased there are changes in the shape of the response as well as a shift in frequency. In particular, the central peak is resolved into two peaks for 2 cm resolution but returns to one peak for 1 cm resolution. These results suggest that for accurate modelling of the slot mode at high frequencies, the resolution must be increased further.

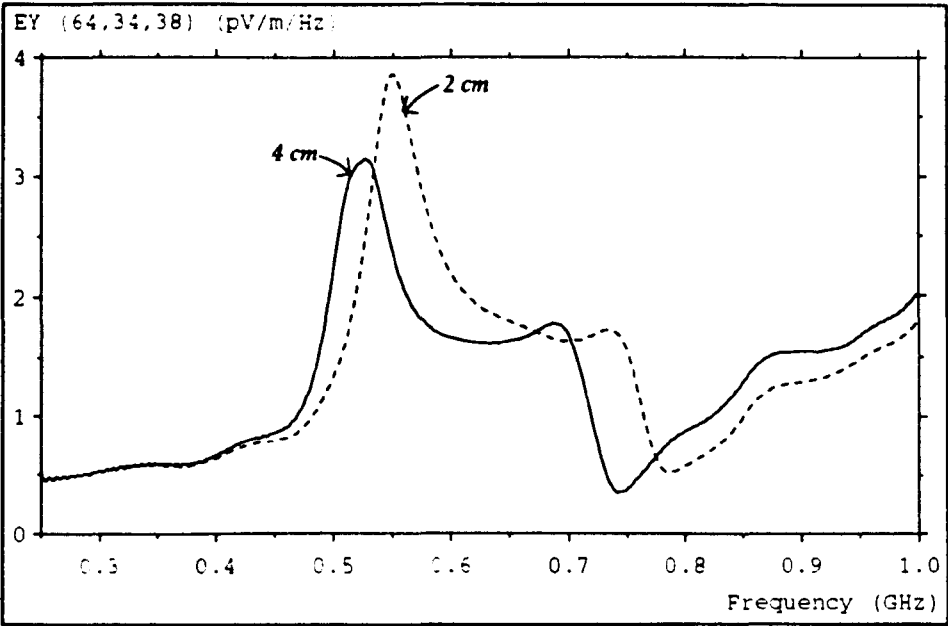


Fig. 8.26 – Top gap mode

The magnitude of the vertical component of the electric field is shown in fig. 8.28 at four different frequencies on a horizontal plane passing through the DUT. In this case, the DUT is operating in its top gap mode and it is placed 4 cm above a ground plane. Symmetry was exploited in the model but the full plane is shown in the figure. The plane extends by 2.5 m in each direction and the 2 cm fine mesh around the DUT is shown blank. It can be seen that at low frequencies the DUT radiates uniformly but the field pattern becomes more complex as the frequency is increased.

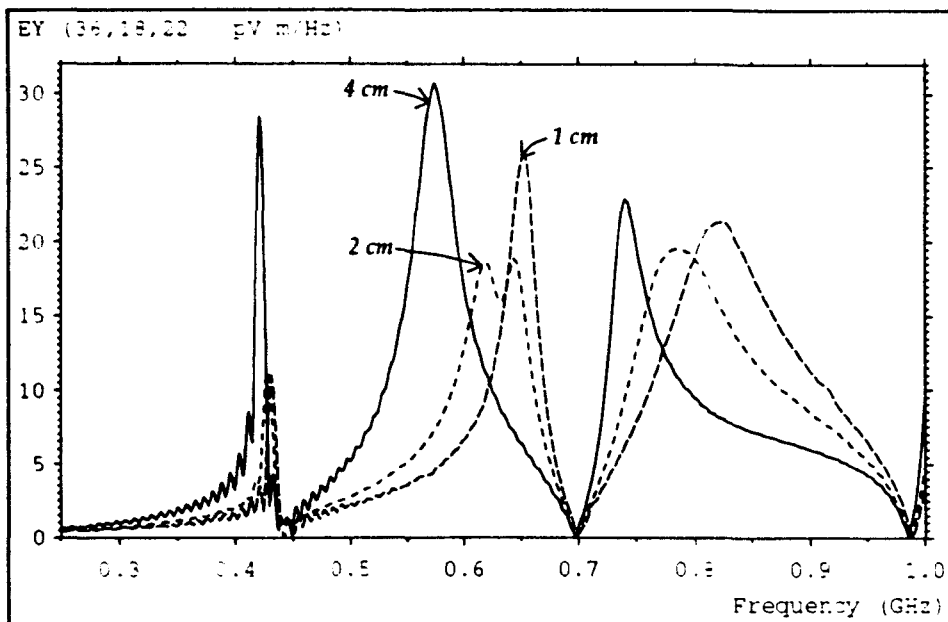


Fig. 8.27 – Front slot mode

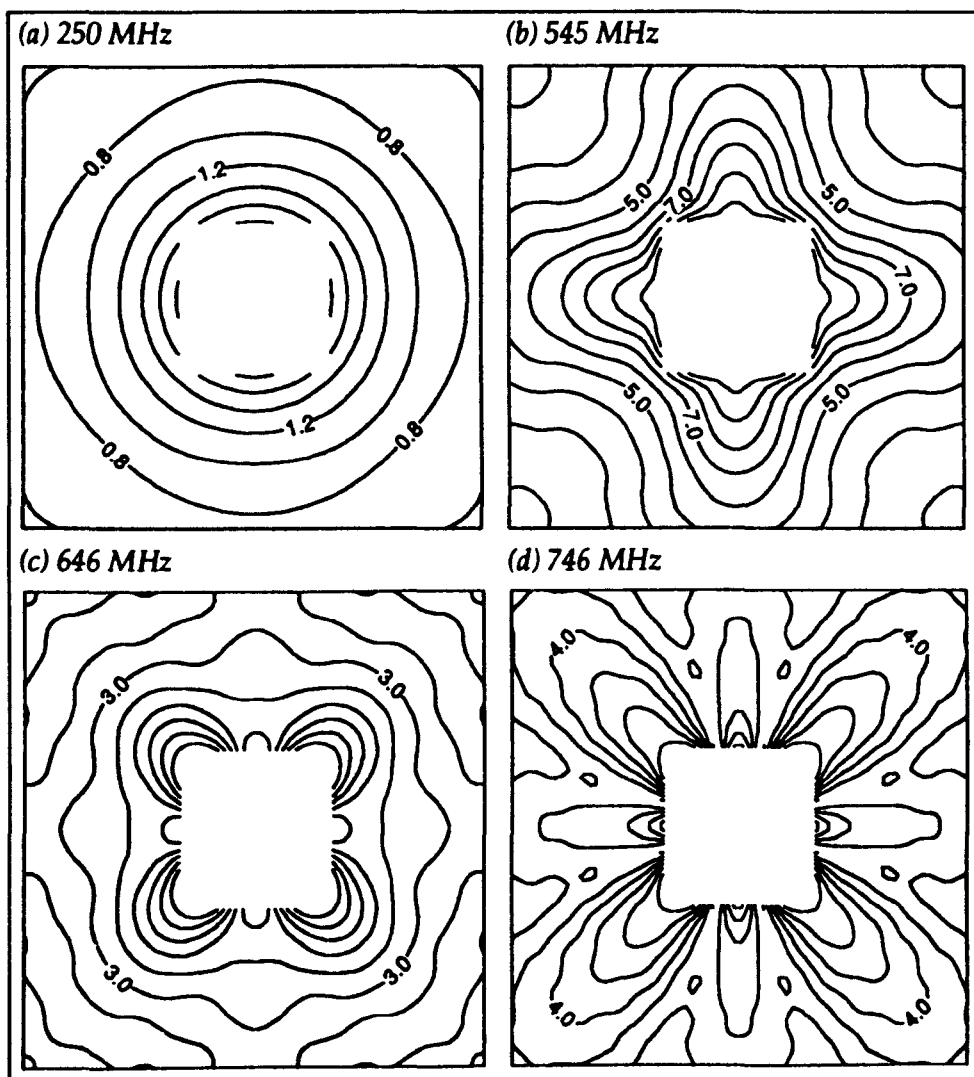
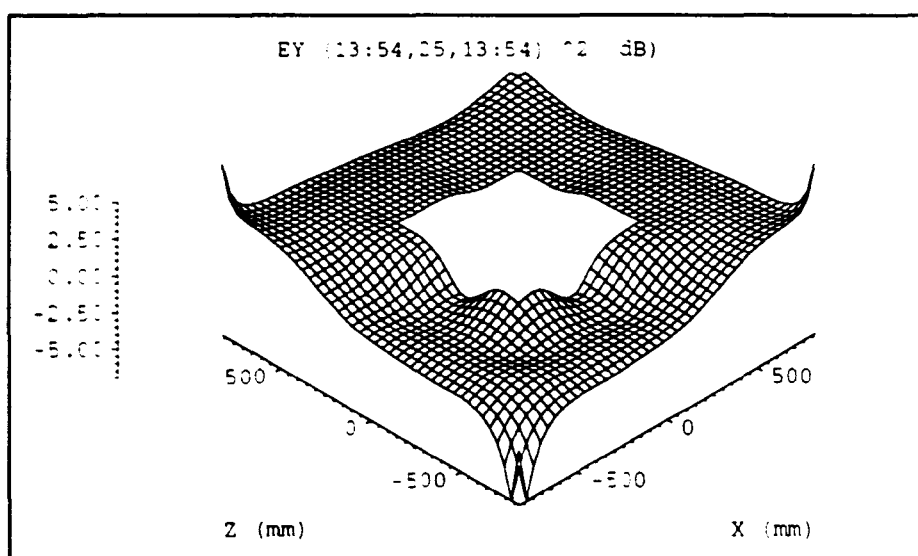


Fig. 8.28 – Field profile for top gap mode

The effect of a cable on the radiation properties of the DUT can be readily investigated for the simple case of a straight wire. Consider the DUT top gap mode with the DUT placed 1 m above a ground plane. A vertical cable with a  $2 \times 2 \text{ cm}^2$  cross-section was attached from one corner of the DUT to the ground plane. The ratio (in dB) of the vertical component of the electric field with and without the cable present is shown in fig. 8.29 on a horizontal plane passing through the DUT, at a frequency of 550 MHz. The field observed at distances of 0.5 m and 1 m is shown in figs. 8.30a and 8.30b, respectively. For the point closest to the DUT, the response is dominated by direct radiation from the gap. When the output is 1 m from the DUT, more significant variations are obtained.



*Fig. 8.29 – Ratio of field with and without attached cable*

## 8.7 Electromagnetic properties of a vehicle body

The incorporation of electronic systems into road vehicles has meant that the EMC aspects of the design of the vehicle body must be considered. This is particularly important for safety critical functions such as anti-lock braking, steering, suspension and collision avoidance systems [78]. The internal environment of the car can be described as a leaky metallic cavity which is loaded with a variety of materials, such as engine parts, seating and passengers. Vehicle bodies are not generally designed with electromagnetic considerations in mind and so it is not a simple matter to make an assessment of their electromagnetic characteristics. Numerical simulation has the potential to give a complete picture of

the electromagnetic interactions in a complex vehicle environment.

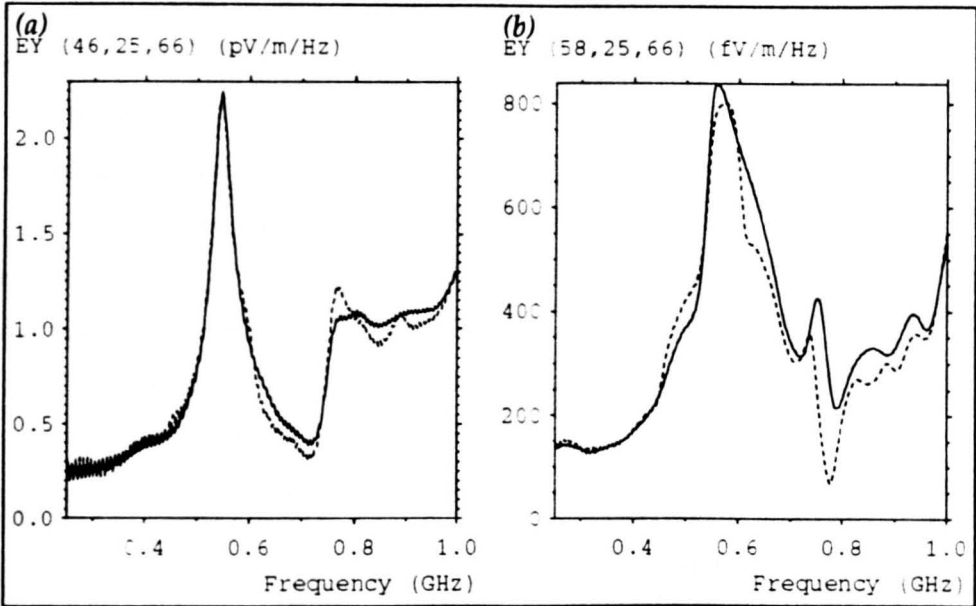


Fig. 8.30 – Electric field with and without attached cable

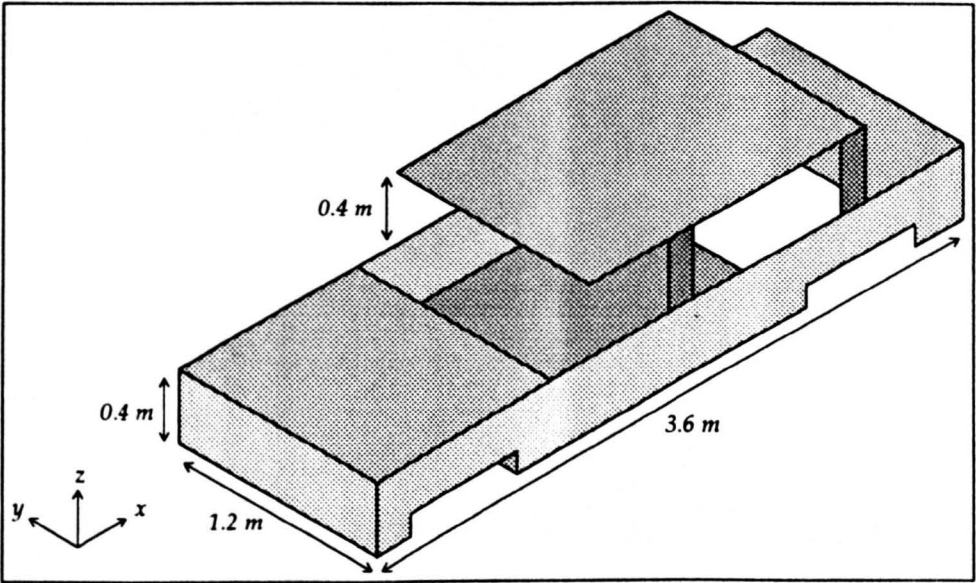


Fig. 8.31 – Car model

In this section, the simplified car model shown in fig. 8.31 is considered. Simulations have been performed to determine the field strength inside the car due to an external excitation for the case when the car is on an open area test site. The car was modelled within a 5 cm mesh of  $132 \times 60 \times 39$  nodes and a 15 cm mesh of  $84 \times 60 \times 53$  nodes was used to move the matched boundaries away from the region of interest. The car was placed just above a ground plane, which was assumed perfectly conducting, and it was illuminated by a short dipole placed 1 m from the

front. A typical result is shown in fig. 8.32a, where the vertical component of the electric field is plotted on a horizontal plane just above the level of the bonnet, at a frequency of 175 MHz. The region of high field strength, which has been clipped, marks the location of the dipole. The ratio of the field strength with and without the car present is shown in fig. 8.32b. It is apparent that the field strength in certain locations is almost four times as great as the free-space value. The locations of maximum field strength will be a function of frequency as well as position. The same ratio is shown in fig. 8.33 plotted against distance and frequency along a line parallel to and passing through the car. Such plots enable the designer to locate potential trouble spots and the data can be generated from a single TLM run.

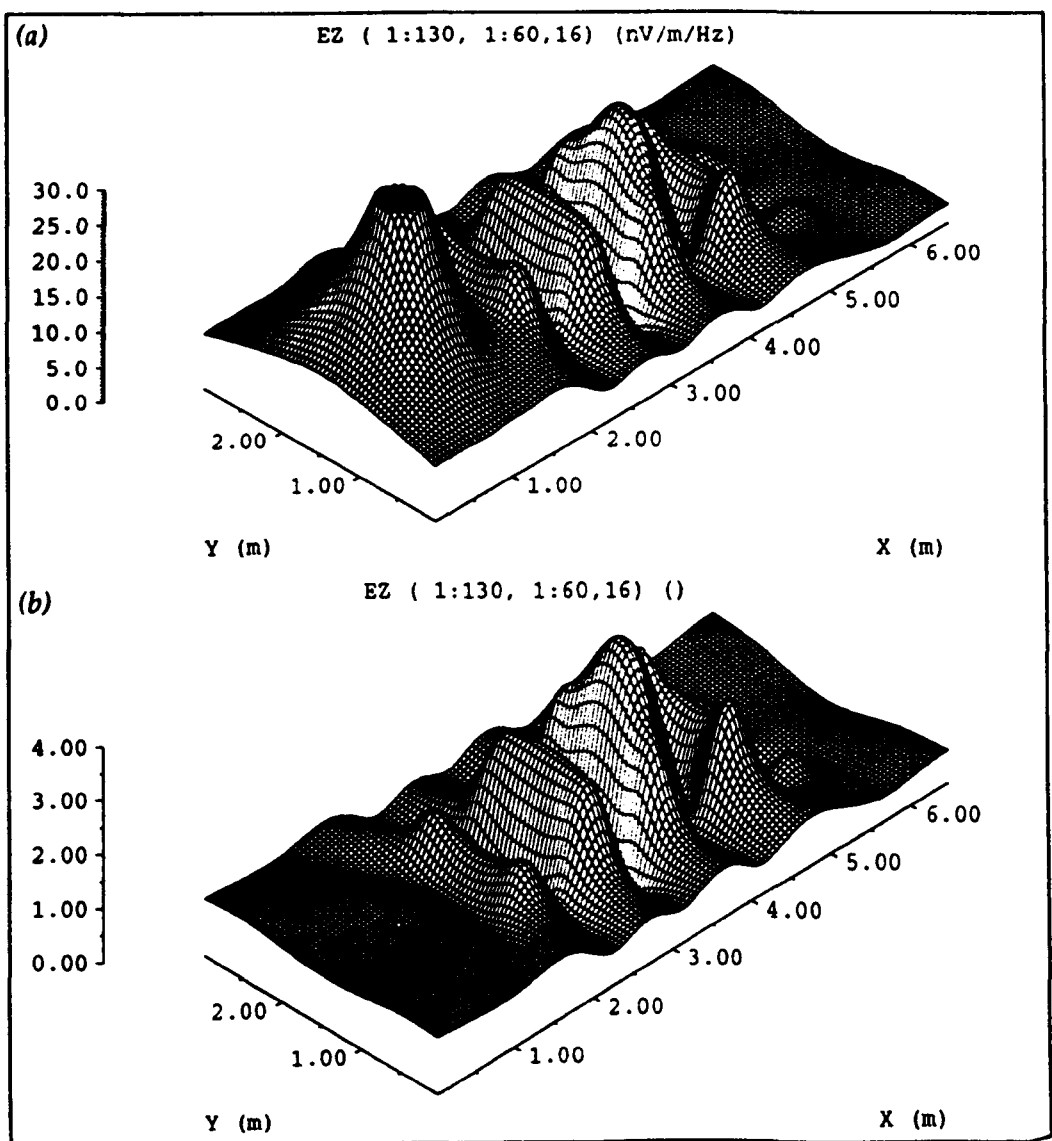
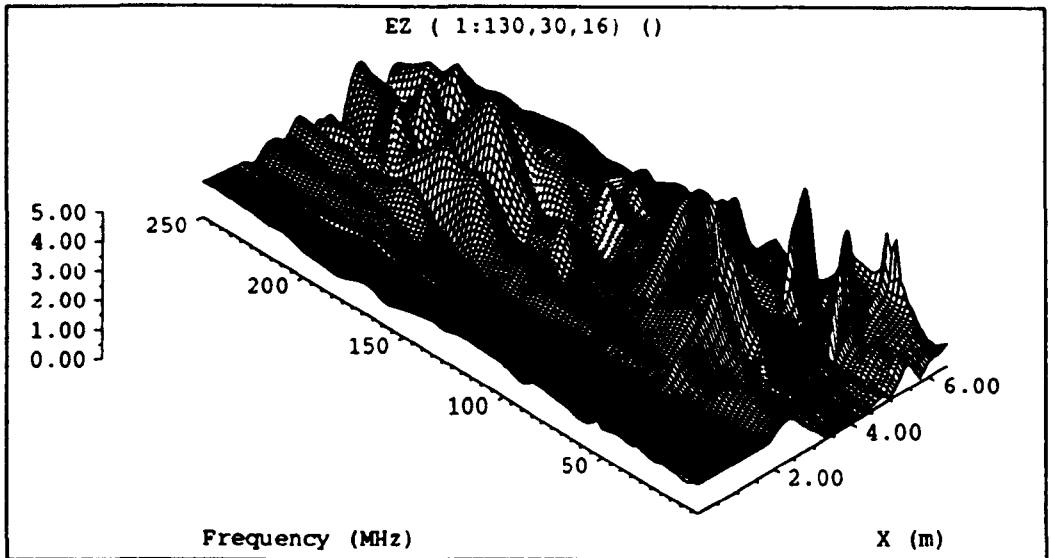


Fig. 8.32 – Electric field on a horizontal plane





*Fig. 8.33 – Field variation with position and frequency*

Results have been presented for the field strength produced inside a car body made up from perfectly conducting plane surfaces. The complexity of the car model can be increased so that it involves more complex shapes and so that the effect of passengers or other vehicles can be investigated. However, of greater use, as far as susceptibility is concerned, is a knowledge of the currents induced by the incident field. TLM has been used to obtain such information with some success [79].

## 8.8 Current induced by a simplified table top device

The problem considered in this section is representative of a class of electromagnetic problems that arise when attempting to predict the level of electromagnetic interference from a small table-top computing device [80]. The configuration is shown in fig 8.34 and the objective is to determine the current induced in the base of the long wire due to a source placed on the table. The system consists of a 1 m vertical wire attached to a thin plate measuring  $50.4 \times 29.4 \text{ cm}^2$ , above a ground plane. Above the plate, a wire either extends vertically by 15.8 cm or is bent so that it measures 2.3 cm vertically and 13.5 cm horizontally. This system has proved to be difficult to solve by numerical means because of the requirement to simultaneously represent thin metal surfaces and a thin electrically long wire in an unbounded volume [81].

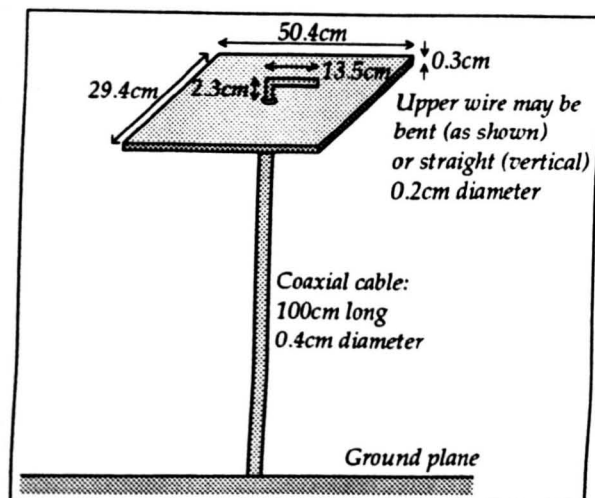
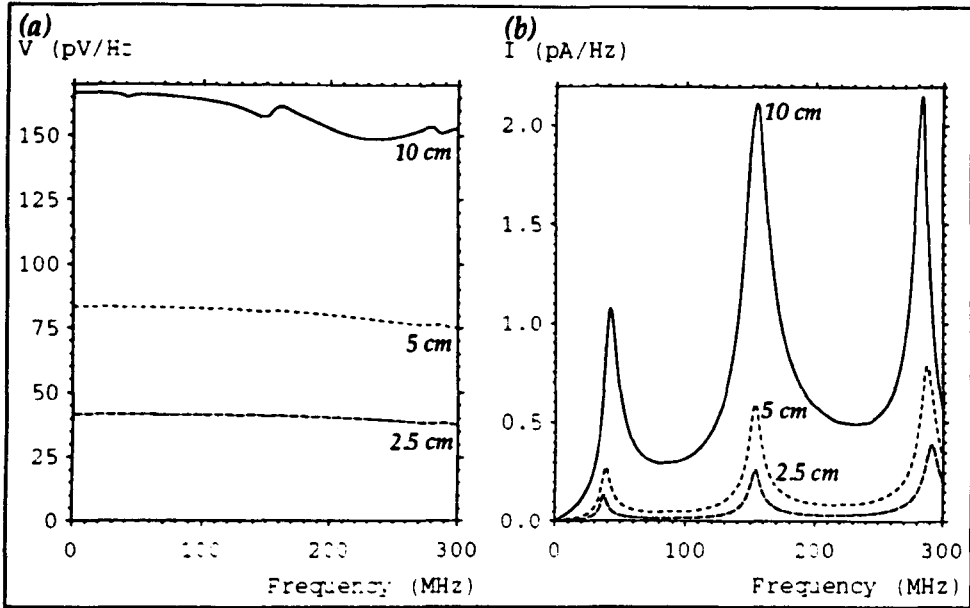


Fig. 8.34 – Simplified table top device

The system has been modelled using a large coarse mesh with 10 cm node spacing and both the multigrid and graded mesh techniques have been used to increase the resolution in the region of interest. The metal of the structure was modelled with short-circuits at the mid-point of link-lines and the open boundary conditions were approximated by matched boundaries. Symmetry was not exploited so that the bent wire could be considered and also so that a single node cross-section could be used for the wire. The source, which was used to connect the plate to the top wire, was modelled by four impulse voltage sources, each with  $200\ \Omega$  series resistance, arranged around the centre node. The output was taken as the sum of currents in the four short-circuits at the base of the long wire. 2000 iterations were performed, with respect to the coarse node spacing, to allow the signal at the output to reach a steady state.

The multigrid models were based on a  $90 \times 90 \times 45$  node coarse mesh so that the boundaries were 3.3 m away from the nearest part of the structure. Two fine mesh regions were used: one measuring  $0.4 \times 0.4 \times 0.9\ \text{m}^3$  was placed around the long wire and the other, measuring  $1.0 \times 1.0 \times 0.4\ \text{m}^3$ , was placed around the plate and the top wire. The source voltage and the current for the straight wire are shown in figs. 8.35a and 8.35b, respectively, for a uniform mesh and for 2:1 and 4:1 multigrid meshes. The value of the source voltage is approximately that which would be expected for a single impulse (i.e. equal to  $\Delta t$ ) although there are fluctuations in the vicinity of the resonances. The same results are shown in fig. 8.36 with a log. scale (in dB above  $1\ \mu\text{A}$ ) normalised to unit source voltage.



**Fig. 8.35 – Source voltage and current for the multigrid models**

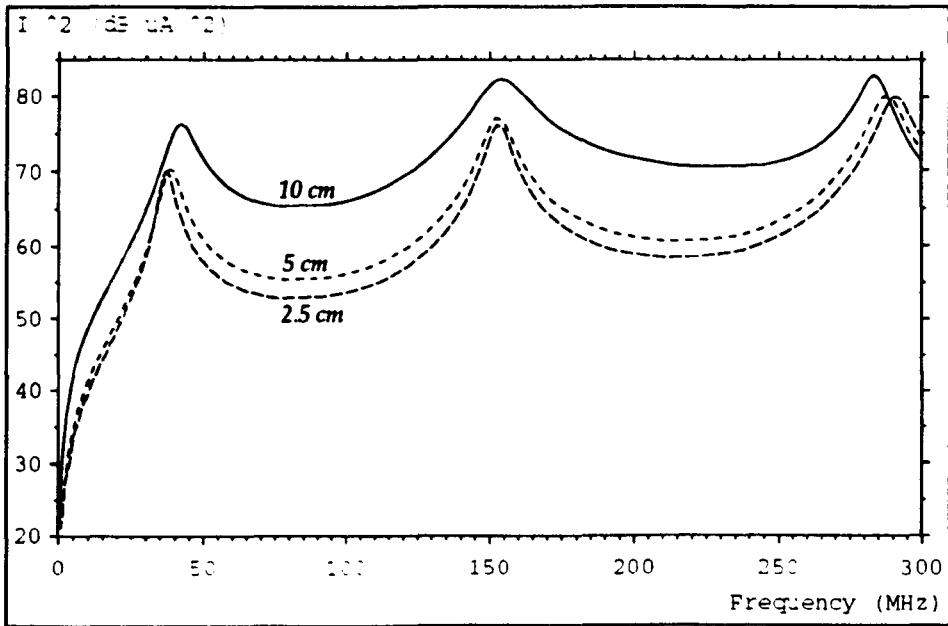


**Fig. 8.36 – Normalised current for the multigrid models**

The graded mesh models were based on a  $81 \times 81 \times 57$  node mesh with 10 cm as the largest node dimension. The results for a uniform mesh and for two different grading schemes are shown in fig. 8.37. In the first scheme, the node dimensions were reduced to 2 cm around the top wire and long thin nodes were used to describe the 1 m wire. The node dimensions in the two directions normal to the long wire were equal and symmetrical about the wire, as follows

32×10cm, 7cm, 4×5cm, 4cm, 3cm, 3×2cm, 3cm, 4cm, ...

The dimensions parallel to the wire were

9×8cm, 2×6cm, 2×4cm, 2×3cm, 2×2cm, 2×3cm, 2×4cm, 6cm, 8cm, 34×10cm

In the second scheme, the node dimensions normal to the wire were reduced to 1 cm and the dimensions parallel to the wire were unchanged

31×10cm, 7cm, 4×5cm, 3.5cm, 2.5cm, 2cm, 1.5cm, 1cm, 1.5cm, 1cm, 1.5cm, ...

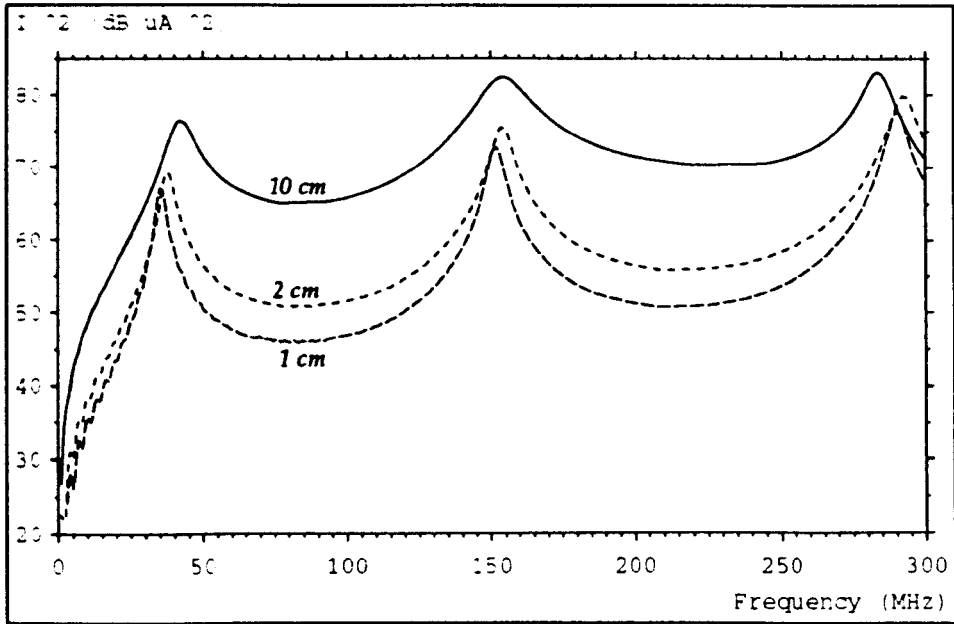


Fig. 8.37 – Normalised current for the graded mesh models

The graded mesh models were more expensive than the multigrid models in both storage and run-time even though they contained roughly the same number of nodes <sup>4</sup>. Another disadvantage is that additional grading must be applied to describe the bent wire. Higher reduction ratios have been applied with the graded mesh since there is no obvious limit to the smallest node dimension, other than that of prohibitive run-time. The same is not necessarily true for the multigrid technique but further work is needed here.

Comparisons with experiment are shown in figs. 8.38a and 8.38b for the straight and bent wire, respectively <sup>5</sup>. The frequency extends from 1 MHz to 100 MHz on a log. scale. The 4:1 multigrid scheme mentioned earlier was used with the addition of a 32×8×16 node fine mesh of 1.25 cm node spacing, placed around the top wire. There is reasonable agreement, at higher frequencies, considering the fact

<sup>4</sup> Further details on computer resources can be found in appendix 4.

<sup>5</sup> The experimental data was obtained from [80].

that the wire diameters and plate thickness were not modelled accurately. Further development of the method should enable the exact dimensions to be used.

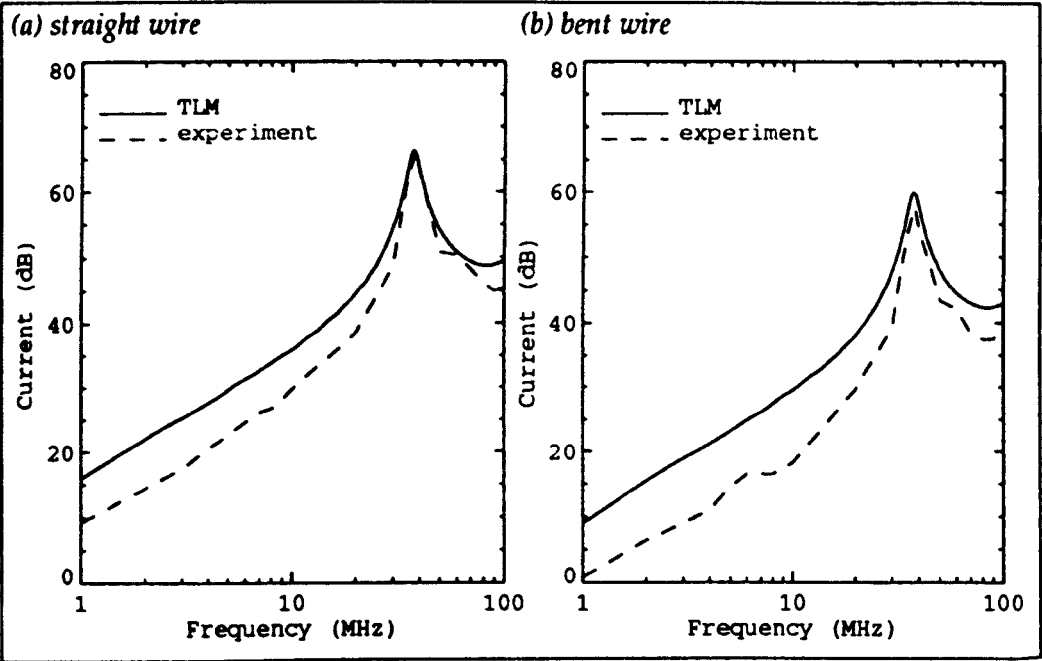


Fig. 8.38 – Comparison with experiment

# **Chapter 9**

## **Discussion and Conclusions**

### **9.1 Numerical modelling method**

The inevitable question which arises from this work is "Can I use TLM to solve realistic EMC problems and how does it compare with other methods?". The first part of the question will be dealt with in §9.3, where a review of the results is presented. As regards the second part of the question, it is beyond the remit of this thesis to give a full and unbiased comparison of all the different modelling methods; the work here has concentrated on the development and application of a single method. However, it is appropriate to make some comments based on the experience gained using TLM over a number of years. Ultimately, the choice of modelling method may well depend upon what the user is used to and it would be reasonable to use a method which is not ideally suited to a particular application if such a code is available and the user is experienced in its use.

Much emphasis is placed on the fact that the TLM method has a physical interpretation. This means that, for example, to place a voltage source into the mesh, the relevant equations can be found directly from transmission-line theory and there is no need to get involved with abstract mathematics. Such an approach is fine for the electrical engineer but TLM is applied in other areas, such as heat diffusion and acoustics, and here the transmission-line analogy may not be so appropriate. However, the basic premise that it is more appropriate to solve a discrete system exactly rather than solving a continuous system approximately is still valid. From an end-user point of view, a physical interpretation is less important since the requirement is to enter a problem definition and obtain the results with little or no interaction. This view is dangerous, unless appropriate safeguards are built into the system, because it is important to appreciate the sorts of problems which can be realistically tackled, and the nature and significance of any errors.

A criticism often directed at differential modelling methods is that they obtain a solution by a crude "brute force" approach. For other methods, the user

has to perform some manipulation of equations or has to have some knowledge of the expected behaviour of the system in order to define the problem, and it is then suggested that the user has a better understanding of the underlying mechanisms at work. This may well be true, to a certain extent, and indeed it is possible, for example, to obtain the resonant frequencies in a cavity of complex shape with no appreciation of how multiple reflections combine to produce the standing wave pattern. However, such an understanding of the basic processes may not be necessary and it is always possible to perform further investigations if required, for example, by obtaining the field profile at the resonant frequency. In fact, it can be regarded as an advantage not to need to know anything about how a system will respond. For example, to obtain the radiation pattern around an antenna, the antenna can be excited by a simple impulse excitation at a point and the model automatically takes care of the current distribution and the resonant frequencies. To solve the same system by other means it may be necessary to assume the current distribution. It is remarkable how the repeated application of a simple procedure over a large number of points produces such a diversity of results.

One of the features of a differential time domain method is that output information is available at all points in the mesh throughout the entire simulation time. Most of this information will never be used directly but it is necessary to obtain the solution throughout the entire mesh even for a single output point (neglecting nodes which cannot have any influence on the output due to finite propagation time). The conventional method in TLM is to follow the propagation of all pulses in the mesh. Some success has been achieved by performing a limited number of "random walks" for single pulses [82] and there may be other methods of reducing the quantity of information which must be processed.

The TLM method is strongly related to the finite difference time domain (FDTD) method and comparisons concerning accuracy and efficiency are unavoidable. It has been shown that the 3-dimensional expanded TLM node can be operated in such a way that it produces identical numbers to the FDTD approach [83] but it requires greater computer resources in terms of both run-time and storage [84]. However, the SCN is more accurate than the expanded node [85]. The storage requirement for FDTD is six quantities per node (giving the electric and

magnetic fields in each direction) but twelve quantities are required for the SCN (12-port node). It is not clear, at this time, whether results obtained using the SCN are sufficiently better than those obtained using FDTD to justify the greater computer resources. However, the fact that twelve quantities are available means that there is considerable flexibility in the way excitation is applied and outputs are taken. For example, all six field quantities can be taken at the same point (at a node) or at different points (on a link-line) and other quantities such as current, charge and energy can all be directly obtained.

## **9.2 Development of the TLM method**

In its basic form, the TLM method is intrinsically suited to EMC problems and so no development is needed to model simple EMC systems. However, to model more complex systems and to properly interpret results additional features have to be added and a knowledge has to be gained of the nature of the results which can be expected.

The scattering matrices of the 12-port node, the stub-loaded node and the hybrid node have been derived from first principles. Although this does not add any new functionality to the method, it does expose some properties of the node which are not immediately apparent from the scattering matrix. For example, it has been found that the contribution to the electric and magnetic field at a node from each of the two pairs of orthogonal link-lines is the same. Analysis of the node in this way may lead to a better understanding of the relationship between TLM and the FDTD method. The use of matrix notation does allow the scattering and connection processes to be written in a concise manner but it is not well suited to gaining a proper understanding of the scattering procedure nor is it suited to direct implementation. This first point is especially true if the rows and columns are ordered in an arbitrary manner because the symmetry of the scattering matrix cannot then be readily appreciated. Assigning names to the ports rather than numbers means that the ports can be identified directly without having to refer to a diagram.

It is important to inspect the time domain output from a simulation before applying any post-processing operations. If the data contains a significant high



frequency component then a suitable window function must be applied but if a window is applied unnecessarily it will reduce the accuracy of the results. It is possible, to a certain extent, to identify problems after the DFT, particularly if there is a strong *sinc* presence, but in other cases (example 1 in §3.2) it may not be apparent that anything is wrong. This is especially true if the data is plotted with a log. scale.

Outputs and excitation can be positioned either on nodes or on link-lines and, generally, the two can be used interchangeably. However, there are advantages in using nodes when several field components are required at the same point and in using link-lines when the field over a surface or the energy is considered. A problem has been identified with exciting the field on a node in the presence of stubs. This has not presented any difficulty for the work presented here since systems have always been excited in free-space and when a graded mesh has been used the excitation has been applied in the region of smallest node dimensions (where there are no stubs). However, this is something which needs further investigation.

When presented with a system, a choice has to be made on whether to excite in a completely general way or in a more restrictive way. For example, placing a source at a single point in a cavity will excite many modes but only a limited set of modes will be excited if sources are placed on a plane, or, if a TEM cell is excited by the steady-state field distribution over a plane then only the TEM mode will propagate. The decision will be based upon the particular aspect of the system which is to be investigated.

A significant proportion of the work has concentrated on the development of the multigrid method and a high degree of success has been achieved. Considerable effort was expended in trying to enforce conservation of both charge and energy across the interface but it appears that explicitly imposing energy conservation is unnecessary. There is an inevitable loss of energy when information is passed from the fine mesh to the coarse mesh but this can be insignificant even in closed systems when no other losses are present. The multigrid technique has been used to increase the mesh resolution in regions where fine features are present and also to move imperfect numerical boundaries away from the region of interest.

The multigrid method is an alternative to the graded mesh method and it is therefore appropriate to compare the two. For all of the systems considered, where the same maximum resolution has been used for both methods, the multigrid technique has been found to be the most efficient although the results are of similar accuracy. However, greater resolutions have been applied with the graded mesh because of concerns over the maximum reduction ratio that can safely be applied with the multigrid technique. In fact, both the ratio between adjacent node dimensions for the graded mesh and the overall multigrid reduction ratio may both have allowed an excessive safety margin. No guidelines are available, at this time, to give the likely errors due to specific grading schemes. The use of a graded mesh is likely to be more efficient if non-cubic nodes can be used and there is always the possibility of using a cylindrical or spherical coordinate system. Ultimately, a combined graded and multigrid technique may provide the best solution.

A method has been developed for running a very large single mesh problem where the storage requirement exceeds the available physical memory. In principle, a uniform mesh could be used instead of a graded or multigrid mesh, at least for small reduction ratios, provided that sufficient processor power and disk space are available. However, modern computer workstations can be fitted with sufficient memory to keep them occupied for significant periods of time and, realistically, the method will only be practical when the required storage is only slightly larger than the available memory.

Guidance has been given on how to improve the storage and run-time efficiency of a TLM simulation program although it has not been the aim of this work to describe in detail how such a program should be written. Efficient code is important even when high performance computers are available because there will always be the requirement to solve larger problems more quickly. Some effort has been expended on defining problems in a user-friendly manner but there are significant improvements to be made here, particularly in the area of graphical user interfaces. It is tedious to define both multigrid and graded mesh problems when many meshes and complicated grading schemes are used.

### 9.3 Application of the TLM method

One of the first problems to be tackled using the TLM method was that of predicting the resonant frequencies of a cavity. The frequencies obtained agree very well with analytical values and results have been presented which confirm this. Results have been presented to show the effect of a conducting bench on the resonances inside an unlined screened room. Inspection of the field profiles shows that the bench causes distortion of the existing modes as well as introducing completely new bench specific resonances. The resonant frequencies have been compared with experiment and there is good agreement. Simulations have also been performed to assess the effect of small changes in position when measurements are made in an unlined screened room and, as expected, greater variations are experienced at higher frequencies. Numerical modelling is an ideal tool to perform such investigations because it is possible to vary a single parameter with all other parameters kept constant.

The Q factor is a useful measure of the level of damping in a system. A method has been developed which enables the Q factor to be obtained from the time domain data at a single output point. This involves convolution in the time domain and, for lightly damped systems, it is necessary to process the data produced from a large number of iterations for any decay to be observed. It is possible to evaluate the convolution for a limited number of points but this should only be done if insufficient computer resources are available. The fitting of the convolved signal with the expected decay curve was done in a relatively crude manner and this is one area in which improvements can be made. Values of the Q factor obtained by this method for an empty cavity with lossy walls are in good agreement with analytical results.

A large number of simulations have been undertaken to investigate the damping of the first few resonances in a screened room using radiation absorbing material (RAM). Tests have been performed to determine the optimum material properties of a uniform RAM block placed in the centre of the room to damp a specific resonance. Simulations have also been performed to determine the actual material properties of a RAM block by measuring room damping experimentally.

Some degree of room damping is essential if repeatable measurements are to be made and work has been carried out to determine the optimum arrangement of RAM blocks to achieve the desired level of damping with minimum RAM volume. A simple model for pyramidal RAM has also been incorporated. There is a good level of agreement between TLM and experiment but it may be necessary to introduce some frequency dependence into the model if the results are to be used over a large frequency range.

Some work has been undertaken to investigate an alternative measurement environment — the TEM cell. TLM has been used to determine the field in the centre of the cell both with and without a test object. A model incorporating the tapered ends could be used to perform a more detailed analysis.

Simple wire and slot antennas have been modelled because it is important to understand simple devices before moving on to more complex ones. Accurate modelling of fine features, such as wires, is a non-trivial task. Even to model quite a fat slot it is necessary to use a description many nodes across. However, if the antenna is to be used as an arbitrary radiator or if the resonant frequencies are not important then simple models can be used. A spherical dipole antenna has also been modelled and the impact of using different feed arrangements has been investigated. Although it is not possible to model the interior of the SD exactly, it is possible to make predictions on likely trends.

A method has been presented for determining the radiation resistance of an arbitrary antenna. This is done by measuring the current at the feed point and the power radiated through an arbitrary surface. All of the necessary information can be extracted from a single TLM run. Comparisons with the analytical result for a half-wave dipole have been hampered by the crude dipole model but if a very fine mesh is used the result is similar to the expected value. The radiation resistance has been used as a measure of the effect of proximity to conducting surfaces. Such effects are important if measurement antennas are placed near to equipment cabinets or screened room walls. Both linear and spherical dipole antennas have been considered.

All of the results mentioned so far have been concerned with characterisation of the measurement environment. Simulations have also been performed for more general EMC systems. The coupling between two dipoles in an unlined screened room has been modelled and good agreement has been obtained with experimental results. It was also shown that when similar node dimensions were used with the multigrid and graded mesh techniques, essentially the same result was obtained. The radiation properties of a simplified device under test have been modelled. A greater resolution needs to be applied for accurate results to be obtained but it has been possible to show approximately how the device radiates. Simulations have been performed to assess the effect of the vehicle body on an incident field. The results show that significant increases in field strength occur at certain positions and at certain frequencies. Finally, the current induced in a wire by a table-top device has been investigated. Reasonable agreement with experiment has been obtained considering that the wire diameters and plate thickness were not modelled accurately.

## **9.4 Future work**

Suggestions for further work have been made throughout this thesis but some of the more important recommendations are repeated here. The fundamental operation of the TLM method needs to be thoroughly investigated. This needs to be done, in part, so that the multigrid method can be fully understood and also so that, for example, the correct way of exciting a node with stubs can be found. More work needs to be done on the multigrid method to determine the maximum reduction ratios that can be employed and on whether an improved conversion method can be derived. The multigrid and graded mesh techniques need to be combined so that the advantages of both can be exploited. A comparison of the TLM multigrid method with the multigrid methods used in finite difference schemes may also be useful.

As far as modelling EMC systems is concerned, the requirements are principally for good open boundary descriptions and methods for accurately describing thin sheets and wires. Some of the results have suffered from insufficient resolution and these could be improved upon by using such fine descriptions. It

would also be useful to assess the effect of using a “staircase” approximation to a sphere by comparing with a model defined in spherical coordinates.

## **9.5 Overall conclusions**

TLM has been successfully applied to a number of EMC problems. The applications have concentrated on characterisation of EMC measurement environments as well as on some more general systems but the same methods could be used in other areas. A multigrid method has been developed and significant reductions in computer resources over those required for a graded mesh have been experienced. The TLM method has proved to be very useful and its physical interpretation means that new features can easily be added. The inevitable increase in computer power in the future will allow TLM to be used for more complex and realistic systems.

# References

1. A. C. Marvin, "New developments in EMC education", *Proc. of the 10th International Zurich Symposium on Electromagnetic Compatibility*, 9–11 March 1993, pp 403–406.
2. R. M. Showers, "Influence of IEC work on national electromagnetic compatibility standards", *ibid.*, supplement pp 7–12.
3. H. K. Mertel, "Military EMC standardization", *ibid.*, supplement pp 13–30.
4. D. N. Heirman, "Commercial EMC standards in the United States", *ibid.*, supplement pp 31–43.
5. D. Hadlock, P. Szerszen, J. Williams, E. Patrick, T. Waltemyer and I. Kohlberg, "Biological effects of large unbounded shielded and unshielded electromagnetic pulse simulators", *ibid.*, pp 15–18.
6. C. E. Brench, "Optimizing EMI shield design with numerical techniques", *Proc. of the 8th Annual Review of Progress in Applied Computational Electromagnetics (ACES)*, Monterey, CA, USA, 16–20 March 1992, pp 435–440.
7. R. J. Cook, "Requirement for the origination of a draft emission calibration procedure, final report for stage II", MoD contract report, January 1992, Division of Electrical Science, National Physical Laboratory.
8. R. J. Cook, P. S. Bansal and M. J. Alexander, "The measurement of field strength in a screened enclosure", *Proc. 8th Int. Conf. on Electromagnetic Compatibility*, Edinburgh, 21–24 September 1992, IEE Conf. Publ. 362, pp 256–262.
9. P. Hammond, "Some thoughts on the numerical modelling of electromagnetic processes", *Int. J. Numerical Modelling*, 1988, 1 (1), pp 3–6.
10. E. K. Miller, "A selective survey of computational electromagnetics", *IEEE Trans. Antennas and Propagation*, 1988, 36 (9), pp 1281–1305.
11. D. P. Johns, A. J. Wlodarczyk, A. Mallik and C. Christopoulos, "New TLM technique for steady-state field solutions in three dimensions", *Electron. Lett.*, 1992, 28 (18), pp 1692–1694.

12. N. J. Carter, "The role of electromagnetic modelling in aircraft clearance — a customer's viewpoint", *IEE Colloquium: Does electromagnetic modelling have a role in EMC design*, London, 4 February 1993.
13. M. Hook, "The use of large electromagnetic computer models in EMC applications", *ibid.*.
14. W. J. R. Hoefer, Editorial, *Int. J. Numerical Modelling*, 1989, 2 (4), pp 189–190.
15. P. B. Johns, "A new mathematical model to describe the physics of propagation", *The Radio and Electronic Engineer*, 1974, 44 (12), pp 657–665.
16. P. B. Johns, "The art of modelling", *Electronics and Power*, 1979, 25 (8), pp 565–569.
17. S. Akhtarzad and P. B. Johns, "Solution of Maxwell's equations in three space dimensions and time by the TLM method of analysis", *Proc. Inst. Elec. Eng.*, 1975, 122, pp 1344–1348.
18. P. Saguet and E. Pic, "Utilization d'un nouveau type de noeud dans la méthode TLM en trois dimensions", *Electron. Lett.*, 1982, 18, pp 478–480.
19. P. B. Johns, "A symmetrical condensed node for the TLM method", *IEEE Trans. MTT*, 1987, MTT-35, pp 370–377.
20. J. Mlakar, "Lumped circuit symmetrical TLM node", *Electron. Lett.*, 1992, 28 (5), pp 497–498.
21. A. J. Wlodarczyk, "Representation of symmetrical condensed TLM node", *Electron. Lett.*, 1992, 28 (18), pp 1686–1687.
22. C. Christopoulos, "Conservation of flux linkage", private communication, University of Nottingham, 23rd December 1992.
23. E. A. Guillemin, "Theory of Linear Physical Systems", John Wiley and Sons Inc., 1963, pp 137–140.
24. R. E. Collin, "Foundations for Microwave Engineering", 2nd edition, McGraw-Hill, 1992.
25. P. Naylor and R. A. Desai, "New three dimensional symmetrical condensed lossy node for solution of electromagnetic wave problems by TLM", *Electron. Lett.*, 1990, 26, pp 492–494.



26. F. J. German, G. K. Gothard and L. S. Riggs, "Modelling of materials with electric and magnetic losses with the symmetrical condensed TLM method", *Electron. Lett.*, 1990, 26, pp 1307–1308.
27. J. F. Dawson, "Improved magnetic loss for TLM", *Electron. Lett.*, 1993, 29 (5), pp 467–468.
28. P. Naylor and R. Ait-Sadi, "Simple method for determining 3-D TLM nodal scattering in nonscalar problems", *Electron. Lett.*, 1992, 28, pp 2353–2354.
29. S. Wright, "The application of transmission-line modelling implicit and hybrid algorithms to electromagnetic problems", Ph.D. Thesis, 1988, University of Nottingham.
30. R. H. Voelker and R. J. Lomax, "A finite-difference transmission line matrix method incorporating a non-linear device model", *IEEE Trans. MTT*, 1990, MTT-38, pp 302–312.
31. R. Scaramuzza and A. J. Lowery, "Hybrid symmetrical condensed node for the TLM method", *Electron. Lett.*, 1990, 26, pp 1947–1949.
32. F. J. German, G. K. Gothard, L. S. Riggs and P. M. Goggans, "The calculation of radar cross-section (RCS) using the TLM method", *Int. J. Numerical Modelling*, 1989, 2 (4), pp 267–278.
33. S. M. Kay, "Modern Spectral Estimation, Theory and Applications", Prentice Hall, 1988, Chapter 4.
34. P. B. Johns, "Application of the transmission-line matrix method to homogeneous waveguides of arbitrary cross-section", *Proc. Inst. Elec. Eng.*, 1972, 119 (8), pp 1086–1090.
35. J. D. Wills, "Spectral estimation for the transmission-line matrix method", *IEEE Trans. MTT*, 1990, MTT-38 (4), pp 448–451.
36. W. J. R. Hoefer, "Time domain electromagnetic simulation for microwave CAD applications", *IEEE Trans. MTT*, 1992, MTT-40 (7), pp 1517–1527.
37. Z. Bi, Y. Shen, K. Wu and J. Litva, "Fast finite-difference time-domain analysis of resonators using digital filtering and spectrum estimation techniques", *IEEE Trans. MTT*, 1992, MTT-40 (8), pp 1611–1619.

38. K. S. H. Lee (ed.), "EMP Handbook: Principles, Techniques and Reference Data", sponsored by the Department of Electrical and Computer Engineering, University of New Mexico, July 1983, pp 297–302.
39. B. P. Lathi, "Modern Digital and Analog Communication Systems", Holt-Saunders, 1983, p 80.
40. K. Kunz and R. Luebbers (Pennsylvania State University), "An introduction to FDTD and its applications", course notes, 16 March 1992, 8th Annual Review of Progress in Applied Computational Electromagnetics (ACES), Monterey, CA, USA.
41. J. L. Herring, "Transmission-line modelling in electrodynamics", M.Eng. Dissertation, University of Nottingham, 1989, Chapter 3.
42. A. P. Duffy, T. M. Benson, C. Christopoulos and J. L. Herring, "New methods for accurate modelling of wires using TLM", *Electron. Lett.*, 1993, **29** (2), pp 224–226.
43. H. Meliani, D. de Cogan and P. B. Johns, "Use of orthogonal curvilinear meshes in TLM models", *Int. J. Numerical Modelling*, 1988, **1** (4), pp 221–238.
44. R. Scaramuzza, P. Naylor and C. Christopoulos, "Numerical simulation of field-to-wire problems using transmission-line modelling", *Proc. Int. Conf. on Computation in Electromagnetics*, London, 25–27 November 1991, IEE Conf. Publ. 350, pp 63–66.
45. M. J. Berger, "On conservation at grid interfaces", *Society for Industrial and Applied Mathematics (SIAM) J. Numer. Anal.*, 1987, **24** (5), pp 967–984.
46. P. B. Johns and R. L. Beurle, "Numerical solution of 2-dimensional scattering problems using a transmission-line matrix", *Proc. Inst. Elec. Eng.*, 1971, **118** (9), pp 1203–1208.
47. S. Akhtarzad and P. B. Johns, "Generalised elements for t. l. m. method of numerical analysis", *Proc. Inst. Elec. Eng.*, 1975, **122** (12), pp 1349–1352.
48. P. B. Johns and K. Akhtarzad, "The use of time-domain diakoptics in time discrete models of fields", *Int. J. for Numerical Methods in Engineering*, 1981, **17**, pp 1–14.

49. P. B. Johns and K. Akhtarzad, "Time-domain approximations in the solution of fields by time domain diakoptics", *Int. J. Numerical Methods in Engineering*, 1982, 18, pp 1361–1373.
50. P. Naylor and C. Christopoulos, "A comparison between the time-domain and the frequency-domain diakoptic methods for solving field problems by transmission-line modelling", *Int. J. Numerical Modelling*, 1988, 2 (1), pp 17–30.
51. P. Saguet, "The 3D transmission-line matrix method: theory and comparison of the processes", *Int. J. Numerical Modelling*, 1989, 2 (4), pp 191–201.
52. R. Ait-Sadi, A. J. Lowery and B. Tuck, "Combined fine-coarse mesh transmission-line modelling method for diffusion problems", *Int. J. Numerical Modelling*, 1990, 3 (2), pp 111–126.
53. S. H. Pulko, I. A. Halleron and C. P. Phizacklea, "Substructuring of space and time in TLM diffusion applications", *Int. J. Numerical Modelling*, 1990, 3 (3), pp 207–214.
54. P. M. Poman, E. Channabasappa and W. J. R. Hoefer, "Transmission line matrix method on massively parallel processor computers", *Proc. of the 9th Annual Review of Progress in Applied Computational Electromagnetics (ACES)*, Monterey, CA, USA, 22–26 March 1993, pp 467–474.
55. D. Pompei and R. Vasta, "Implementation of TLM on a connection machine — example from printed antenna simulations", *IEE Colloquium on developments in transmission-line modelling*, Nottingham, 2 April 1993, pp 7/1–7/3.
56. C. E. Tong and Y. Fujino, "An efficient algorithm for transmission line matrix analysis of electromagnetic problems using the symmetrical condensed node", *IEEE Trans. MTT*, 1991, MTT-39 (8), pp 1420–1424.
57. L. J. Kenah, R. E. Goldenberg and S. F. Bate, "Version 4.4 VAX/VMS Internals and Data Structures", Digital Press, 1988, Part IV (memory management).
58. J. R. Marek and J. MacGillivray, "A method for reducing run-times of out-of-core FDTD problems", *Proc. of the 9th Annual Review of Progress in Applied Computational Electromagnetics (ACES)*, Monterey, CA, USA, 22–26 March 1993, pp 344–351.

59. T. H. Hubing and G. K. Bhat, "Using commercial CAD packages to interface with 3D EM modeling codes", *Proc. of the 8th Annual Review of Progress in Applied Computational Electromagnetics (ACES)*, Monterey, CA, USA, 16–20 March 1992, pp 607–610.
60. Defence Standard 59-41, Part 1, Issue 4, June 1988, Ministry of Defence.
61. P. S. Bansal, M. J. Alexander and R. J. Cook, "Investigation of the effects of a conducting bench in screened room emission measurements 30 MHz to 300 MHz", MoD contract report, October 1992, Division of Electrical Science, National Physical Laboratory.
62. J. D. Kraus, "Electromagnetics", 3rd edition, McGraw-Hill, 1985, pp 600–603.
63. "R. A. M. Pyramids", report E. Mat 3699, Electrical Materials and Production Processes Branch, Directorate General of Defence Quality Assurance, Procurement Executive, Ministry of Defence, 19 May 1939.
64. M. L. Crawford and J. L. Workman, "Using a TEM cell for EMC measurements of electronic equipment", National Bureau of Standards (USA), Technical note 1013, July 1981.
65. J. C. Tippet and D. C. Chang, "Radiation characteristics of electrically small devices in a TEM cell", *IEEE Trans. EMC*, 1976, EMC-18 (4), pp 134–140.
66. J. D. Kraus, "Antennas", 2nd edition, McGraw-Hill, 1983.
67. N. R. S. Simons and E. Bridges, "Method for modelling free space boundaries in TLM simulations", *Electron. Lett.*, 1990, 26 (7), pp 453–455.
68. N. R. S. Simons and E. Bridges, "Application of the TLM method to two-dimensional scattering problems", *Int. J. Numerical Modelling*, 1992, 5, pp 93–110.
69. J. A. Morente, J. A. Portí and M. Khalladi, "Absorbing boundary conditions for the TLM method", *IEEE Trans. MTT*, 1992, MTT-40 (11), pp 2095–2099.
70. Eswarappa, H. I. Costache and W. J. R. Hoefer, "Transmission line matrix modeling of dispersive wide-band absorbing boundaries with time-domain diakoptics for S-parameter extraction", *IEEE Trans. MTT*, 1990, MTT-38 (4), pp 379–385.

71. U. Mueller, P. P. M. So and W. J. R. Hoefer, "The compensation of coarseness error in 2D TLM modeling of microwave structures", *IEEE MTT-S Digest*, 1992, pp 373–376.
72. P. Naylor, "Coupling between electromagnetic waves and wires using transmission-line modelling", Ph.D. Thesis, 1986, University of Nottingham.
73. P. Naylor and C. Christopoulos, "A new wire node for modeling thin wires in electromagnetic field problems solved by transmission line modeling", *IEEE Trans. MTT*, 1990, MTT-38 (3), pp 328–330.
74. A. J. Wlodarczyk and D. P. Johns, "New wire interface for graded 3-D TLM", *Electron. Lett.*, 1992, 28 (8), pp 728–729.
75. J. A. Porti, J. A. Morente, M. Khalladi and A. Gallege, "Comparison of thin-wire models for TLM method", *Electron. Lett.*, 1992, 28 (20), pp 1910–1911.
76. P. Naylor, C. Christopoulos and P. B. Johns, "Coupling between electromagnetic fields and wires using transmission-line modelling", *IEE Proc. Pt. A*, 1987, 134 (8), pp 679–686.
77. A. C. Marvin and G. Simpson, "Screened room radiated emission measurements; a preliminary calibration procedure for the frequency range 1 MHz to 30 MHz", *Proc. of the 5th British Electromagnetic Measurements Conf.*, Malvern, UK, 11–14 November 1991, pp 35/1–35/5.
78. C. Christopoulos, A. Mallik, P. Naylor and P. B. Johns, "Computer simulation in EMC design and testing of vehicles", *Proc. of the 18th International Symposium on Automotive Technology and Automation*, Florence, Italy, 30 May – 3 June 1988, paper 88125.
79. P. Naylor and C. Christopoulos, "Coupling between electromagnetic fields and multimode transmission systems using TLM", *Int J. Numerical Modelling*, 1989, 2 (4), pp 227–240.
80. T. H. Hubing, "Calculating the currents induced on wires attached to opposite sides of a thin plate", *The ACES Collection of Canonical Problems Set 1*, special publication of the Applied Computational Electromagnetics Society (ACES), ed. H. A. Sabbagh, pp 9–13.

81. T. H. Hubing, "Numerical techniques for EMI source modeling: a review of progress", *Proc. of the 8th Annual Review of Progress in Applied Computational Electromagnetics (ACES)*, Monterey, CA, USA, 16–20 March 1992, pp 413–417.
82. T. R. Rowbotham and P. B. Johns, "Waveguide analysis by random walks", *Electron. Lett.*, 1972, 8 (10), pp 251–253.
83. P. B. Johns, "On the relationship between TLM and finite-difference methods for Maxwell's equations", *IEEE Trans. MTT*, 1987, MTT-35 (1), pp 60–61.
84. M. Celuch and W. K. Gwarek, "Comparative study of the time-domain methods for the computer analysis of microwave circuits", *Proc. Int. Conf. on Computation in Electromagnetics*, London, 25–27 November 1991, IEE Conf. Publ. 350, pp 30–34.
85. R. Allen, A. Mallik and P. Johns, "Numerical results for the symmetrical condensed TLM node", *IEEE Trans. MTT*, 1987, MTT-35 (4), pp 378–382.

# Publications

Parts of the work in this thesis have been presented in several publications, which are as follows:

1. J. L. Herring and C. Christopoulos, "The vehicle body as an electromagnetic shield — numerical simulation for emission and susceptibility studies", *Proc. of the 7th Int. Conf. on EMC*, University of York, UK, 28–29 August 1990.
2. J. L. Herring, P. Naylor and C. Christopoulos, "Transmission-line modelling in electromagnetic compatibility studies", *Int. J. Numerical Modelling*, 1991, 4, pp 143–152.
3. J. L. Herring and C. Christopoulos, "Multigrid transmission-line modelling method for solving electromagnetic field problems", *Electron. Lett.*, 1991, 27, pp 1794–1795.
4. C. Christopoulos, J. L. Herring and R. A. Scaramuzza, "Electromagnetic simulation using TLM modelling", *IEE Colloquium on Transmission-Line Matrix Modelling*, London, 18 October 1991.
5. J. L. Herring and C. Christopoulos, "Numerical simulation for better calibration and measurements", *Proc. of the 5th British Electromagnetic Measurements Conf.*, Malvern, UK, 11–14 November 1991, pp 37/1–37/4.
6. C. Christopoulos and J. L. Herring, "Developments in the transmission-line modelling (TLM) method", *Proc. of the 8th Annual Review of Progress in Applied Computational Electromagnetics (ACES)*, Monterey, CA, USA, 16–20 March 1992, pp 523–530.
7. J. L. Herring, A. P. Duffy, T. M. Benson and C. Christopoulos, "A transmission-line modelling (TLM) study of screened room behaviour", *IEE Colloquium on Radiated Environment Test Facilities*, London, 2 June 1992.
8. A. P. Duffy, J. L. Herring, T. M. Benson and C. Christopoulos, "The application of TLM to EMC design", *IEE Colloquium: Does electromagnetic modelling have a role in EMC design*, London, 4 February 1993.

9. A. P. Duffy, J. L. Herring, T. M. Benson and C. Christopoulos, "The application of the transmission-line modelling (TLM) method to the simulation of propagation and coupling inside conducting enclosures", *Proc. of the 10th International Zurich Symposium on Electromagnetic Compatibility*, 9–11 March 1993, pp 445–449.
10. J. L. Herring and C. Christopoulos, "The application of different meshing techniques to EMC problems", *Proc. of the 9th Annual Review of Progress in Applied Computational Electromagnetics (ACES)*, Monterey, CA, USA, 22–26 March 1993, pp 755–762.
11. A. P. Duffy, J. L. Herring, T. M. Benson and C. Christopoulos, "Comparison of TLM simulations and experiment in EMC problems", *IEE Colloquium on Developments in Transmission-Line Modelling*, Nottingham, 2 April 1993, pp 4/1–4/3.
12. C. Christopoulos and J. L. Herring, "The application of transmission-line modelling (TLM) to electromagnetic compatibility problems", accepted for publication *IEEE Trans. EMC, Special Issue on EMC Applications of Numerical Techniques*.



# Appendices

## A.1 Conservation of flux linkage

The concept of conservation of flux linkage was introduced to overcome the problem of associating a loop current with the node, without an equivalent circuit. The concept of charge conservation is a familiar one and can be expressed as

$$\Delta t \sum_n (Y_{0n} V_n^i) = \Delta t \sum_n (Y_{0n} V_n^r)$$

$$\text{or } \sum_n (C_n V_n^i) = \sum_n (C_n V_n^r)$$

where  $C_n$  is the capacitance associated with each of the transmission-lines. By analogy, it is reasonable to expect that the total magnetic flux linked with the incident pulses is equal to the total magnetic flux linked with the scattered pulses. This can be expressed as

$$\sum_n (L_n I_n^i) = \sum_n (L_n I_n^r)$$

where  $L_n$  is the inductance associated with each of the transmission-lines. Two examples will now be considered to show how simple transmission-line problems can be solved using the concepts of conservation of charge and magnetic flux linkage.

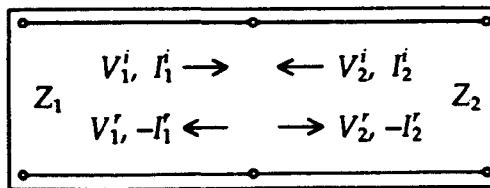


*Fig. A.1 – Impedance discontinuity*

Consider the voltage pulses reflected from an impedance discontinuity in a transmission-line, as shown in fig. A.1. If  $V_1^i$  and  $V_2^i$  are the incident pulses, on transmission-lines with capacitance  $C_1$  and  $C_2$ , respectively, then charge conservation gives

$$C_1 V_1^i + C_2 V_2^i = C_1 V_1^r + C_2 V_2^r$$

writing  $C_1 = \Delta t / Z_1$  and  $C_2 = \Delta t / Z_2$  gives

$$\frac{V_1^i}{Z_1} + \frac{V_2^i}{Z_2} = \frac{V_1^r}{Z_1} + \frac{V_2^r}{Z_2} \quad (\text{A.1})$$

If the inductances associated with the transmission-lines are  $L_1$  and  $L_2$ , then conservation of flux linkage gives

$$L_1 I_1^i - L_2 I_2^i = L_1 I_1^r - L_2 I_2^r$$

writing  $L_1 = Z_1 \Delta t$ ,  $L_2 = Z_2 \Delta t$  and expressing in terms of voltage pulses gives

$$V_1^i - V_2^i = -V_1^r + V_2^r \quad (\text{A.2})$$

Solving equations (A.1) and (A.2) gives the expected result

$$V_1^r = \left( \frac{Z_2 - Z_1}{Z_1 + Z_2} \right) V_1^i + \left( \frac{2 Z_1}{Z_1 + Z_2} \right) V_2^i$$

$$V_2^r = \left( \frac{2 Z_2}{Z_1 + Z_2} \right) V_1^i + \left( \frac{Z_1 - Z_2}{Z_1 + Z_2} \right) V_2^i$$

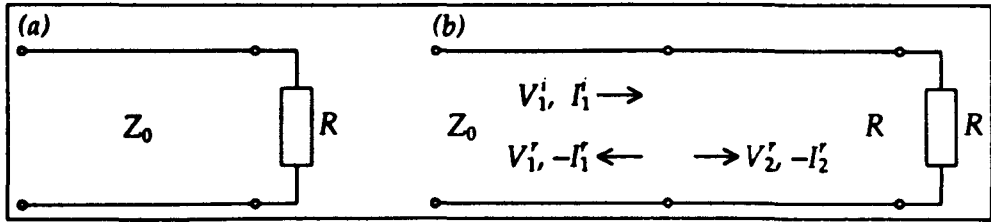


Fig. A.2 – Terminated transmission-line

A transmission-line with a resistive load, as shown in fig. A.2a, can also be solved in this way, by replacing the resistor with a stub of characteristic impedance,  $R$ , as shown in fig. A.2b. If  $V_1^i$  and  $V_1^r$  are the incident and reflected voltage pulses on the transmission-line and  $V_2^r$  is the voltage pulse reflected into the stub (there is no incident pulse) then conservation of charge gives

$$\frac{V_1^i}{Z_0} = \frac{V_1^r}{Z_0} + \frac{V_2^r}{R} \quad (\text{A.3})$$

Conservation of flux linkage gives

$$V_1^i = -V_1^r + V_2^r \quad (\text{A.4})$$

Eliminating  $V_2^r$  from (A.3) and (A.4) gives the required result

$$V_1^r = \left( \frac{R - Z_0}{R + Z_0} \right) V_1^i$$

The justification for expecting conservation of magnetic flux linkage follows from Maxwell's equations, which state that the integral of the magnetic flux

density,  $\underline{B}$ , over a closed surface is zero.

$$\oint \underline{B} \cdot d\underline{S} = 0 \quad (\text{A.5})$$

Consider, in 2-dimensions, a surface enclosing a number of transmission-lines, as shown in fig. A.3. The magnetic field is forced to be zero everywhere except between the wires (planes in 3-dimensions) of each transmission-line. This restriction implies that all elements in the system are replaced by transmission-lines. Resistors must be replaced by transmission-lines which are either infinitely long or are terminated with a matched load placed outside the surface of interest. The flux linked with each transmission-line,  $\lambda_n$ , can be written as

$$\lambda_n = \iint \underline{B}_n \cdot d\underline{S}_n$$

Equation (A.5) can then be written as a sum of flux linkages.

$$\sum_n \lambda_n = 0$$

The flux linkage can then be written in terms of inductance and current.

$$\sum_n L_n I_n = 0$$

The current can then be expressed in terms of incident and reflected pulses.

$$\sum_n L_n (I_n^i - I_n^r) = 0$$

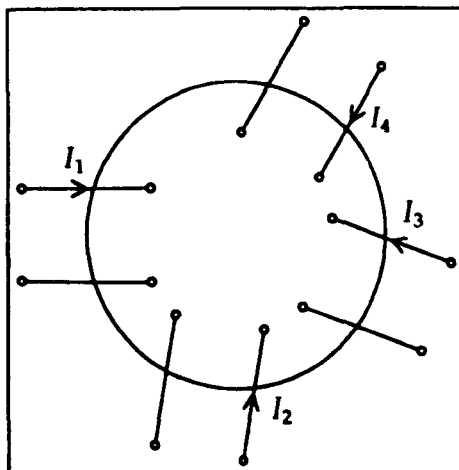


Fig. A.3 – Transmission-lines passing through a surface

## A.2 Optimised paging

In this section, the optimised paging algorithm mentioned in §6.4 is described in more detail. The mesh is assumed to be divided into two regions along the z-axis.

The main features of the algorithm are given below in Pascal.

```
zdiv:=(zmax+region_iterations+1)/2;
for t1:=1 to iterations/region_iterations do
begin
  for t2:=1 to region_iterations do
  begin
    for z:=1 to zdiv-t2 do
      scatter(z);
    for z:=1 to zdiv-t2 do
    begin
      connectxy(z);
      if (z<zdiv-t2) then connect(z)
    end
  end;
  for t2:=1 to region_iterations do
  begin
    for z:=zdiv-t2+1 to zmax do
      scatter(z);
    for z:=zdiv-t2 to zmax do
    begin
      if (z>zdiv-t2) then connectxy(z);
      if (z<zmax) then connectz(z)
    end
  end
end;
```

The nodes in the z direction are numbered 1, 2, 3, ..., zmax-1, zmax. The following symbols have been used:

<b>region_iterations</b>	the number of iterations to perform in each region
<b>zdiv</b>	the z coordinate of the first plane of nodes wholly contained in the second region
<b>iterations</b>	the total number of iterations
<b>scatter</b>	a procedure which scatters pulses on a plane of nodes with the given z coordinate.

<b>connectxy</b>	a procedure which connects between link-lines parallel to the $x$ - and $y$ -axes, over a plane with the given $z$ coordinate.
<b>connectz</b>	a procedure which connects between link-lines parallel to the $z$ -axis (nodes $z$ and $z + 1$ ), over a plane with the given $z$ coordinate.

Other features can be added to the method: features at nodes should use the range of coordinates specified for the scatter procedure and features on link-lines should use the range of coordinates specified for the connect procedures.

### A.3 Graded mesh parameters

Generally, for a graded mesh simulation, the user specifies the node dimensions and the mesh parameters are calculated automatically. This means that the user will often have no feel for the values of link-line and stub admittances used. In this section, the mesh parameters for the hybrid node are shown graphically for one of the simulations performed in §8.8, on a  $X$ - $Z$  plane passing through the smallest node dimension in the  $y$ -direction. The node dimensions in each direction are given below.

**X:** 32×10cm, 7cm, 4×5cm, 4cm, 3cm, 3×2cm, 3cm, 4cm, 4×5cm, 7cm, 32×10cm

**Y:** 2cm

**Z:** 9×8cm, 2×6cm, 2×4cm, 2×3cm, 2×2cm, 2×3cm, 2×4cm, 6cm, 8cm, 34×10cm

The maximum permissible timestep for each node is shown in fig. A.4a. The overall timestep is usually chosen to be the minimum of these values for the entire mesh but a smaller value can be used if required. The normalised link-line admittance for link-lines contributing to the  $y$ -component of the magnetic field is shown in fig. A.4b and the corresponding stub admittance is shown in fig. A.4c. Note that the first and last plots have been inverted (multiplied by  $-1$ ) so that the detail can be seen more clearly. It can be seen that the timestep is determined by the smallest node spacing and in this region the stub admittance is zero. In regions near the corners, where the dimensions of the nodes in the  $x$ - and  $z$ -directions are large compared with the  $y$ -dimension, the link-line admittance is low and the stub admittance is high.

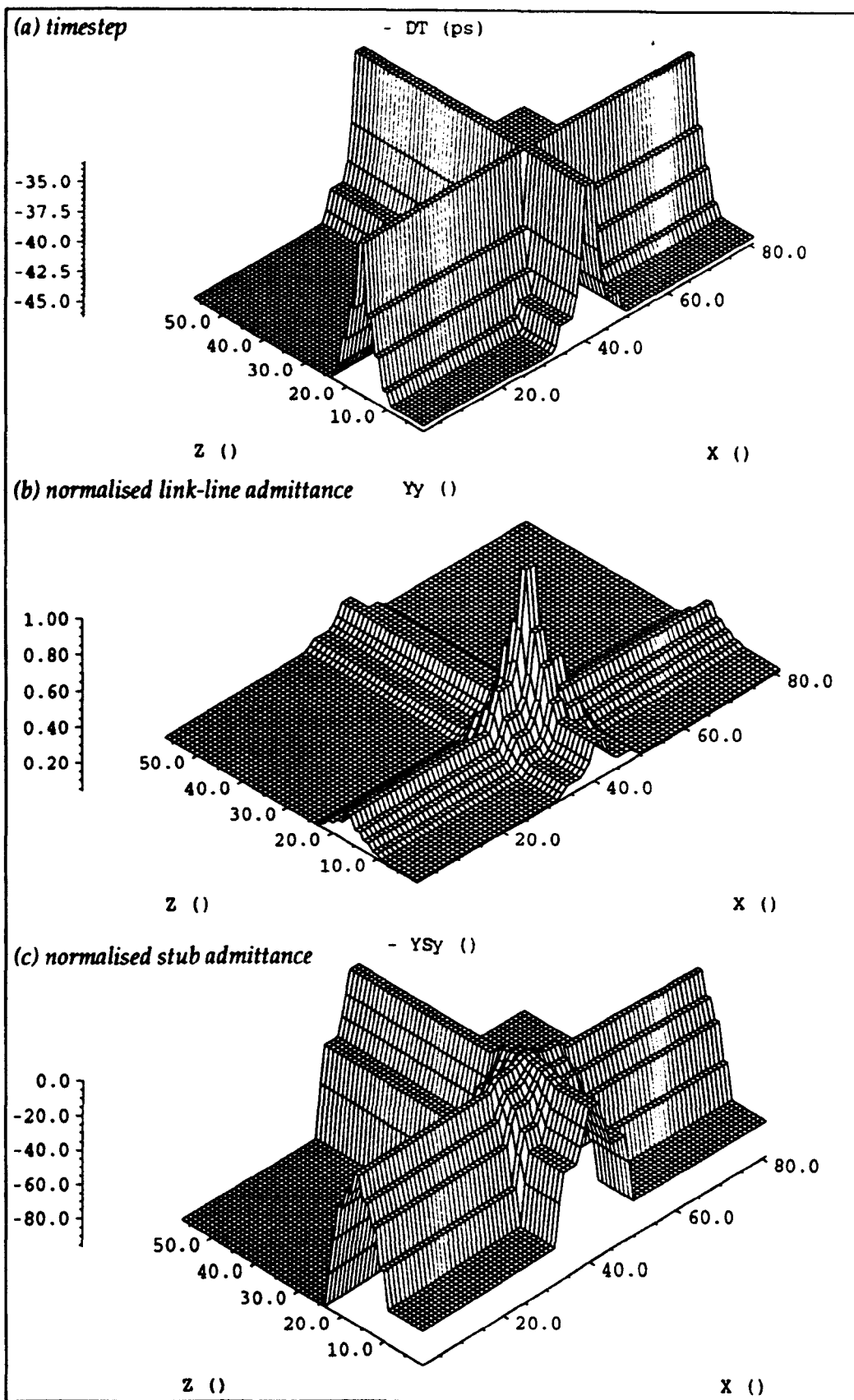


Fig. A.4 – Mesh parameters for graded mesh using the hybrid node

## A.4 Computer resources

In this section, the computer resources required to run realistic EMC problems are presented. Obviously, with the current rate of progress in computer technology, these figures will quickly become out of date but they give an indication of the sorts of problems which can be tackled using moderately powerful computer workstations at the present time. The simulations were performed on a Hewlett-Packard 710 workstation with the following specification:

processor	PA-RISC 1.1
operating system	HP-UX 8.07
clock speed	50 MHz
memory	48 Mbyte
SPECmarks	49
integer performance	57 MIPS
floating point performance	12 MFLOPS

The simulation program was written in ANSI C and used single precision real numbers. The storage and run-time requirements for the graded mesh will depend upon whether mesh parameters and scattering coefficients are stored or recalculated on each iteration. In this case, the mesh parameters were stored but the scattering coefficients were recalculated.

### Field-to-wire coupling (§7.6)

#### i) multigrid mesh

mesh:  $91 \times 47 \times 45$  (5cm),  $15 \times 69 \times 15$  (1.67cm),  $15 \times 69 \times 15$  (1.67cm)

nodes: 223 515

iterations: 7 500 (coarse mesh)

scattering operations: 2 142 112 500

memory: 11.8 Mbyte (65 536 text, 12 288 000 data, 12 288 stack)

CPU time: 4 hours, 1 min., 26 sec.

average time: 6.8  $\mu$ s/node/iteration

**ii) graded mesh**

mesh: 103 $\times$ 53 $\times$ 51 ( $\Delta l_{max}$ =5cm,  $\Delta l_{min}$ =1.67cm)

nodes: 278 409

iterations: 22 500

scattering operations: 6 264 202 500

memory: 23.1 Mbyte (69 632 text, 24 150 016 data, 12 288 stack)

CPU time: 23 hours, 3 min., 48 sec.

average time: 13.3  $\mu$ s/node/iteration

**Current induced by a simplified table top device (§8.8)**

**i) multigrid mesh**

mesh: 90 $\times$ 90 $\times$ 45 (10cm), 16 $\times$ 16 $\times$ 36 (2.5cm), 40 $\times$ 40 $\times$ 16 (2.5cm)  
32 $\times$ 8 $\times$ 16 (1.25cm)

nodes: 403 412

iterations: 2000 (coarse mesh)

scattering operations: 1 073 064 000

memory: 20.2 Mbyte (65 536 text, 21 086 208 data, 12 288 stack)

CPU time: 2 hours, 2 min., 49 sec.

average time: 6.9  $\mu$ s/node/iteration

**ii) graded mesh**

mesh: 81 $\times$ 81 $\times$ 57 ( $\Delta l_{max}$ =10cm,  $\Delta l_{min}$ =1cm)

nodes: 373 977

iterations: 20 000

scattering operations: 7 479 540 000

memory: 30.2 Mbyte (69 632 text, 31 617 024 data, 12 288 stack)

CPU time: 26 hours, 51 min., 50 sec.

average time: 12.9  $\mu$ s/node/iteration



## A.5 List of programs

A substantial volume of code has been written to perform the work described in this thesis. The more recent code has been written in C and, to reduce duplication of source code, each program has been linked with one or more libraries of common functions. The most important programs are listed below.

### Pre-processing programs

TLM04	read problem definition (see §6.5.2) and process standard features
MTLM02	process multigrid features
GRAD01	process graded mesh features
SDIP04	add spherical dipole definition

### Simulation programs

TLM3D01	uniform mesh
MTLM3D01	multigrid mesh
HTLM3D01	graded mesh using the hybrid node

### Post-processing programs

To perform the required post-processing operations, the emphasis has been on generating a large number of programs which perform relatively simple tasks. The data output from the simulation is passed through a number of these programs to produce the required result. The advantage of this approach is that each program can be fully tested. The main disadvantage is that it is tedious to perform more complex operations.

BPF01	band pass filter
CLIP02	clip data to specified limits
CMPLX02	convert complex data to real data
CMPLX03	obtain complex conjugate
COMB02	evaluate arbitrary arithmetic expressions involving constants and input data
COMP01	compare two data files
COMP02	compare many data files

DB03	convert to dB
EDIT01	change range of axes
FT04	perform Fourier transform
LPF02	low pass filter
PEAK02	obtain minima and maxima
Q01	calculate Q factor
REDUCE01	remove excess data points
REMAP01	map data onto a new set of axes
SCALE01	apply scale factors
SUM02	calculate sum with respect to specified axis
WIND03	apply window function
VECT02	transform vector data

## **Graph plotting programs**

A number of graph plotting programs have been written which can be used to plot data on a VDU or to generate hardcopy output. These have been written to meet two needs: (i) for everyday use it is useful to be able to plot graphs quickly with all relevant information on what the data is automatically included (ii) for presentation purposes a greater degree of control is required. Use has also been made of commercial packages to obtain the graphs with log. axes and the contour plots.